



HAL
open science

Simulations numériques directes de couches limites turbulentes hypersoniques avec des effets thermochimiques de non-équilibre

Donatella Passiatore

► **To cite this version:**

Donatella Passiatore. Simulations numériques directes de couches limites turbulentes hypersoniques avec des effets thermochimiques de non-équilibre. Energie électrique. HESAM Université; Politecnico di Bari. Dipartimento di Ingegneria Meccanica e Gestionale (Italia), 2021. Français. NNT : 2021HESAE069 . tel-03687597

HAL Id: tel-03687597

<https://pastel.hal.science/tel-03687597>

Submitted on 3 Jun 2022

HAL is a multi-disciplinary open access archive for the deposit and dissemination of scientific research documents, whether they are published or not. The documents may come from teaching and research institutions in France or abroad, or from public or private research centers.

L'archive ouverte pluridisciplinaire **HAL**, est destinée au dépôt et à la diffusion de documents scientifiques de niveau recherche, publiés ou non, émanant des établissements d'enseignement et de recherche français ou étrangers, des laboratoires publics ou privés.

ÉCOLE DOCTORALE SCIENCES ET MÉTIERS DE L'INGÉNIEUR

Laboratoire DynFluid - Campus de Paris

THÈSE

présentée par : **Donatella PASSIATORE**
soutenue le : **09 décembre 2021**

pour obtenir le grade de : **Docteur d'HESAM Université**

préparée à : **École Nationale Supérieure d'Arts et Métiers**
Spécialité : **Génie mécanique**

**Direct Numerical Simulations of hypersonic turbulent boundary layers
with thermochemical non-equilibrium effects**

THÈSE dirigée par :
Mme CINNELLA Paola

et co-encadrée par :
M. PASCAZIO Giuseppe, M. SCIACOVELLI Luca

Jury

| | | |
|------------------------------|--|--------------|
| M. Thierry MAGIN | Professeur, University of Liège | Président |
| M. Eric GARNIER | Directeur de recherche HDR, Onera | Rapporteur |
| M. Gianluca IACCARINO | Professeur, Stanford University | Rapporteur |
| Mme Taraneh SAYADI | Maître de Conférences HDR, Sorbonne Université | Examinatrice |
| Mme Paola CINNELLA | Professeur, Sorbonne Université | Examinatrice |
| M. Giuseppe PASCAZIO | Professeur, Politecnico di Bari | Examineur |
| M. Luca SCIACOVELLI | Maître de Conférences, ENSAM Paris | Examineur |



Politecnico
di Bari

Department of Mechanics, Mathematics and Management
MECHANICAL AND MANAGEMENT ENGINEERING
PH.D. PROGRAM
SSD: ING-IND/06 - FLUID DYNAMICS

Final dissertation

**Direct Numerical Simulations of hypersonic
turbulent boundary layers with thermochemical
non-equilibrium effects**

by
DONATELLA PASSIATORE

Referees:

Prof. Gianluca IACCARINO
Dr. Ing. Eric GARNIER

Supervisors:

Prof. Giuseppe PASCAZIO
Prof. Paola CINNELLA
Dr. Ing. Luca SCIACOVELLI

*Coordinator of the Ph.D. Program:
Prof. Giuseppe P. Demelio*

Course XXXIV, 01/11/2018 - 31/10/2021

I'm burnin' through the sky, 2000 DEGREES
That's why they call me Mister Fahrenheit
I'm travelling at the speed of SOUND
I wanna make a HYPERSONIC woman of you.

Freddie Mercury

Acknowledgments

I wish to express my sincere gratitude to Prof. Pascazio and Prof. Cinnella for their guidance and support during this project. Each inspiring discussion has always been an occasion to learn something new and to improve myself and my work. The passion that I found myself naturally including in this project has been dictated by a harmonious and fruitful work environment and I am deeply grateful for this.

I would like to express special thanks to Dr. Ing. Sciacovelli for accompanying me during this period. He has been capable to provide me the right tips to overcome most of the obstacles. Without his guidance and knowledge I would not have been able to achieve this result and part of my today scientific personality is because of him. I feel deeply honored to have been his first Ph.D. student.

Last but not least, I wish to thank all the people that, both from a scientific and personal point of view, have contributed for me to conclude this wonderful three-year journey.

ACKNOWLEDGMENTS

Résumé étendu

Introduction

L'étude des écoulements hypersoniques suscite un grand intérêt, tant du point de vue de l'ingénierie que du point de vue académique. Le domaine de l'aéronautique est à l'origine de cet intérêt, mais récemment des concepts de véhicules hypersoniques innovants poussent l'homme vers de nouveaux domaines inexplorés, nécessitant une connaissance et une maîtrise toujours plus grandes du domaine hypersonique. Tout véhicule en vol à une vitesse hypersonique génère une onde de choc, qui entraîne des changements brusques dans les propriétés de l'écoulement. L'énorme quantité d'énergie cinétique de l'écoulement incident est convertie en énergie interne lorsque le gaz traverse l'onde de choc et la température s'élève dangereusement dans la région située entre le choc et la surface du véhicule, ce qui entraîne une dissociation moléculaire et une excitation vibrationnelle. Une connaissance précise des conditions d'écoulement en aval du choc est cruciale pour concevoir le système de protection thermique et éviter un échauffement aérodynamique excessif. Dans une telle situation, l'érosion ou l'ablation du bouclier thermique pourrait induire une transition de l'écoulement d'un régime laminaire à un régime turbulent. Les charges thermiques et mécaniques augmentent considérablement dans un écoulement entièrement turbulent, atteignant un pic plus ou moins élevé dans la région de transition; pour cette raison, l'évaluation a priori de la zone de transition est importante. Malheureusement, la turbulence compressible et le régime transitoire dans des conditions de haute enthalpie sont des phénomènes physiques qui ne sont pas encore bien compris; le lien entre les effets de haute température et les écoulements turbulents est un domaine de recherche encore plus inexploré. En général, le scénario turbulent est très préoccupant pour les véhicules civils et militaires volant à des altitudes relativement basses (associées à des nombres de Reynolds élevés en raison de densités plus importantes); une meilleure compréhension de ce régime est essentielle pour permettre aux véhicules de voler à des vitesses toujours plus élevées (régime hypersonique) et à des altitudes plus basses (régime turbulent). D'un point de vue technique, un avion est fondamentalement conçu pour tolérer certaines charges. Les estimations de ces charges sont dérivées de mesures expérimentales ou de simulations numériques qui fournissent les quantités macroscopiques nécessaires au choix de la forme, du poids et des matériaux du corps. Cependant, dans le domaine de l'aérothermodynamique, les propriétés macroscopiques sont étroitement liées à la nature microscopique du gaz. C'est l'une des principales raisons pour lesquelles les écoulements à haute température requièrent une attention particulière, car des effets thermo-chimiques spécifiques sont déclenchés par les hautes températures impliquées: des réactions chimiques et des phénomènes d'excitation vibrationnelle peuvent se produire et donner lieu à des conditions de non-équilibre. Ces aspects sont détaillés ci-dessous.

L'énergie interne d'une molécule générique est composée de différentes formes (ou modes) d'énergie: translationnelle, rotationnelle, vibrationnelle et électronique. Dans des conditions normales (tempéra-

tures inférieures à 800 K), les niveaux d'énergie translationnelle et rotationnelle sont entièrement excités et prévalent sur les niveaux vibrationnels. Pour des températures plus élevées, l'énergie vibrationnelle des molécules devient importante et modifie les propriétés du gaz. Pour un mélange de gaz, dont les modes vibrationnels des molécules sont excités, l'équation d'état doit tenir compte du comportement caloriquement imparfait. Par conséquent, dans ces conditions, l'air est un mélange de gaz thermiquement parfaits et caloriquement imparfaits. Si la température augmente encore, au-delà de 2000 K, des processus chimiques se produisent: O_2 commence à se dissocier et il est complètement épuisé à 4000 K quand, à son tour, la dissociation de N_2 commence. Pour des températures encore plus élevées (c'est-à-dire au-dessus de 9000 K), la plupart du N_2 est dissocié et des processus d'ionisation se produisent. Les processus que nous venons de décrire se produisent principalement par des collisions moléculaires, qui nécessitent un certain temps (fini) pour avoir lieu. Si le temps caractéristique de ces phénomènes est comparable au temps caractéristique de l'écoulement (c'est-à-dire que $\tau/\tau_{\text{flow}} \approx 1$), on dit que l'écoulement est dans un état de non-équilibre chimique et/ou thermique. Dans le cas d'un non-équilibre thermo-chimique simultané, il existe un couplage étroit entre les taux de relaxation thermique et les taux de réaction chimique. Par exemple, on s'attend à ce que les molécules excitées vibrationnellement se dissocient plus rapidement, car elles nécessitent moins d'échange d'énergie lors des collisions.

Ces dernières années, des progrès importants ont été réalisés dans l'étude des écoulements à grande vitesse. La plupart des études détaillées sont basées sur les résultats de simulations numériques, car la réalisation d'expériences dans les conditions d'intérêt est généralement coûteuse, voire irréalisable. Les simulations numériques à haute fidélité peuvent être un outil puissant pour compléter les données expérimentales disponibles, en particulier les résultats concernant les écoulements turbulents qui sont généralement rares. L'une des configurations classiques pour étudier les écoulements turbulents pariétaux compressibles est la couche limite, qui peut être considérée comme une vue rapprochée d'une petite région du fuselage d'un véhicule.

La contribution de cette thèse est donc d'étudier les effets thermo-chimiques dans les couches limites hypersoniques au moyen de simulations numériques directes, assurant la résolution de toute la gamme active des échelles temporelles et spatiales. L'objectif est de fournir une grande quantité de données précises qui peuvent donner accès à différentes quantités instantanées et statistiques, permettant des analyses approfondies de la nature de la turbulence, des effets de compressibilité, de la topologie de l'écoulement ou de l'interaction turbulence/thermo-chimique et permettant le développement de modèles de turbulence plus précis.

Equations et méthode numérique

Dans le présent travail, nous analysons un mélange gazeux composé de N_2 , O_2 , NO , O et N , dont la nature est décrite par les équations tridimensionnelles compressibles de Navier–Stokes pour des écoulements réactifs multi-espèces et thermiquement hors équilibre (Gnoffo *et al.*, 1989). Le comportement du gaz est modélisé par la formulation “Translational-Rotational-Vibrational” (TRV), qui donne l'expression de l'enthalpie de l'espèce; la loi de Dalton décrit la pression du mélange et donne l'expression de l'équation d'état thermique. Pour fermer le système, l'expression des modèles thermo-physiques décrivant la viscosité, les conductivités thermiques et les coefficients de diffusion de masse doit être spécifiée. Dans les simulations suivantes, la viscosité et les conductivités thermiques des différentes espèces sont décrites par les relations de Blottner *et al.* (1971) et la correction d'Eucken (Hirschfelder & Curtiss, 1969). Les propriétés du mélange sont évaluées à partir des règles de mélange

de Wilke (1950). Quant aux coefficients de diffusion, la loi de Fick a été utilisée pour décrire le phénomène de diffusion de masse; un coefficient équivalent a été utilisé pour la diffusion de chaque espèce individuelle dans le mélange (Hirschfelder *et al.*, 1954). Pour conclure, il est nécessaire de fournir une expression pour les termes sources apparaissant dans les équations de conservation pour les espèces individuelles et l'équation de conservation pour l'énergie vibrationnelle moyenne des trois molécules. Pour cela, le modèle à deux températures de Park a été utilisé (Park, 1988).

Les équations de Navier-Stokes sont intégrées numériquement à l'aide d'un schéma de différences finies centrées d'ordre élevé (Sciacovelli *et al.*, 2021). Les flux convectifs sont discrétisés au moyen d'un schéma d'ordre dix, tandis que les termes visqueux sont discrétisés au moyen de différences finies standard d'ordre quatre. Un schéma centré a une nature purement dispersive; pour cette raison, afin d'assurer la robustesse numérique, une stratégie basée sur l'ajout d'une dissipation artificielle adaptative est adoptée. Celle-ci est basé sur une combinaison d'un terme de dissipation d'ordre neuf et d'un terme de capture de choc d'ordre inférieur. Un senseur de choc hautement sélectif est utilisé pour déclencher la capture des chocs à proximité immédiate des discontinuités d'écoulement. L'intégration temporelle est effectuée au moyen d'un schéma Runge-Kutta d'ordre trois (Gottlieb & Shu, 1998).

Couche limite turbulente hypersonique sur une paroi plane adiabatique

Dans cette section, on analyse une couche limite hypersonique qui se développe sur une paroi plane adiabatique dans des conditions chimiques de non-équilibre. L'analyse qui suit est divisée en deux parties. Dans un premier temps, nous nous concentrons sur les régions laminaire et de transition; ensuite, l'influence du non-équilibre chimique sur la région de turbulence pleinement développée est évaluée, grâce également à la comparaison avec les résultats d'une simulation avec l'hypothèse du mélange gelé. Pour les deux analyses, les conditions thermodynamiques sont similaires à celles adoptées dans plusieurs études de stabilité (Malik & Anderson, 1991; Hudson *et al.*, 1997; Perraud *et al.*, 1999; Franko *et al.*, 2010; Marxen *et al.*, 2014; Miró Miró *et al.*, 2018); en particulier, les valeurs imposées pour l'écoulement non perturbé sont $M_\infty = 10$, $T_\infty = 350$ K e $p_\infty = 3596$ Pa. L'écoulement est laminaire dans la région d'entrée du domaine de calcul, où l'air est caractérisé par sa composition standard ($Y_{O_2}=0.233$ e $Y_{N_2}=0.767$).

Un mode Mack est excité avec une forte amplitude afin de promouvoir une transition "second-mode", qui s'avère être la plus instable dans le régime hypersonique. La présente simulation comprend la région laminaire et la région de transition, intégrant la région de croissance linéaire des perturbations, la zone d'interaction entre les modes secondaires et la rupture non linéaire en turbulence. Le type de scénario de transition généré donne lieu, pour la première fois dans la littérature, à une transition du type "second-mode" sousharmonique. En fait, bien qu'un mode de Mack (bidimensionnel et haute fréquence) soit excité avec une amplitude significative par rapport aux modes secondaires, le processus de transition n'est pas régi par le mode fondamental. Les modes sousharmoniques bidimensionnels et obliques sont naturellement sélectionnés et amplifiés, drainant l'énergie du mode fondamental. En allant vers les derniers stades de la transition, des modes stationnaires apparaissent, provoquant une distorsion du champ moyen. L'interaction des modes bidimensionnels et obliques conduit à la formation de tourbillons "en lambda". L'analyse modale et la description des vues instantanées de l'écoulement confirment que le scénario de transition présente des similitudes remarquables, au moins en termes qualitatifs, avec la transition de type H pour les écoulements incompressibles (Herbert, 1988). Dans un scénario de type H , des structures en forme de lambda apparaissent et s'organisent de manière parfaitement décalée; de plus, cette voie est caractérisée par l'amplification des modes sub-

harmoniques. Des analyses supplémentaires sont prévues en perspective, afin de clarifier ce scénario, plus particulièrement pour les phases finales de la transition, afin d'étudier comment l'instabilité des tourbillons en λ ainsi que la prédominance des modes stationnaires, mènent au régime pleinement turbulent. En outre, une comparaison avec un scénario sans réactions chimiques est également prévue.

Dans ce qui suit, nous nous concentrons sur la région turbulente dans le but de comprendre si, et dans quelle mesure, le non-équilibre chimique modifie la turbulence compressible confinée. La configuration de plaque plane quasi-adiabatique, bien que très idéalisée, nous permet d'étudier l'influence de valeurs de température extrêmement élevées dans la région proche de la paroi, qui revêt une importance extrême pour la conception des véhicules. Le principal effet de la dissociation des gaz est de changer la composition du mélange proche de la paroi, dans la région située entre la sous-couche visqueuse et le "buffer layer", modifiant ainsi les propriétés thermophysiques du fluide. En outre, les réactions chimiques endothermiques drainent l'énergie de l'écoulement dans la région où la turbulence est produite, ce qui entraîne une intensité turbulente légèrement inférieure et une réduction des fluctuations de température d'environ 10%. Les faibles valeurs observées pour les nombres moyens de Damköhler des espèces indiquent que la dissociation chimique est beaucoup plus lente que l'échelle de temps caractéristique de l'écoulement, c'est-à-dire que l'écoulement n'est pas loin des conditions d'écoulement dit "gelé", dans lesquelles la composition reste constante. Dans cette situation, les principales différences par rapport à un écoulement avec chimie gelée sont observées pour les quantités thermodynamiques; en revanche, la présence de réactions chimiques ne modifie pas sensiblement les quantités dynamiques ou les spectres turbulents. Les données fournies par cette simulation ont également été utilisées pour évaluer certaines hypothèses de modélisation classiques dérivées de la théorie Strong Reynolds Analogy (SRA). Il est démontré que cette dernière reste généralement valable. Les hypothèses d'un nombre de Prandtl turbulent constant et d'un nombre de Schmidt turbulent constant, classiquement utilisées pour modéliser le transport turbulent de chaleur et le transport turbulent de masse, fournissent une approximation acceptable dans certaines conditions.

Couche limite turbulente hypersonique sur une paroi plane refroidie

Dans cette section, le lien entre la turbulence et les effets de non-équilibre thermique et chimique est analysé. La configuration étudiée est une couche limite sur une paroi plane refroidie. Les propriétés de l'écoulement non perturbé correspondent aux conditions en aval du choc oblique généré par un dièdre avec un angle de demi-ouverture de 6° volant à Mach 20, à une altitude d'environ 36 km. Dans ces conditions, l'écoulement se trouve dans un état de non-équilibre vibrationnel, tandis que l'activité chimique reste relativement faible.

Afin de quantifier le non-équilibre thermique, un nombre de Damköhler vibrationnel est défini, basé sur plusieurs échelles de temps caractéristiques de l'écoulement. Les résultats montrent que, à l'exception de la région proche de la paroi où l'écoulement est gelé d'un point de vue vibrationnel, de fortes conditions de non-équilibre thermique persistent jusqu'au bord de la couche limite. L'azote moléculaire semble être responsable du non-équilibre thermique, car sa température caractéristique est suffisamment élevée pour provoquer des taux de relaxation faibles. L'excitation vibrationnelle est largement causée par le mélange turbulent, comme observé par le couplage étroit avec les événements de balayage et d'éjection associés avec les structures tourbillonnaires de proche paroi. Les fluctuations de vitesse entraînent l'air plus froid des régions extérieures vers la paroi ou l'air plus chaud loin de la couche intérieure. Les modes roto-translotionnels s'adaptent rapidement à ces importantes fluctuations de

température, contrairement aux modes vibrationnels. Au niveau macroscopique, la conséquence directe est que la température vibrationnelle est en retard sur la température translationnelle jusqu'à la première moitié de la zone logarithmique; à partir de là, l'écoulement passe à un état de surexcitation vibrationnelle qui se maintient jusqu'au bord de la couche limite. L'inspection des bilans énergétiques vibrationnels confirme que le transport turbulent joue un rôle fondamental. En suivant les stratégies habituelles de modélisation RANS, on peut définir un nombre de Prandtl vibrationnel turbulent qui prend des valeurs proches de l'unité pour la majeure partie de la couche limite. Les statistiques de second ordre montrent que les tensions de Reynolds sont qualitativement similaires à celles observées dans des conditions de basse enthalpie; de plus, la condition de paroi isotherme conduit à un profil de température fluctuant non monotone caractérisé par deux pics. Au contraire, les fluctuations de la température vibrationnelle présentent des profils monotones croissants en raison des conditions de non-équilibre marquées existant dans le "buffer-layer". Les analyses des effets de compressibilité ont montré que les mouvements de forte dilatation se trouvent principalement près de la paroi, les fortes compressions étant légèrement plus probables que les fortes expansions. Il n'existe pas de relation directe entre les compressions/expansions et la sous-excitation/surexcitation vibrationnelle, contrairement à ce qui a été observé pour la turbulence non confinée, mais on peut conclure qu'en général les événements de forte compressibilité augmentent indirectement le non-équilibre thermique.

Conclusions

Les résultats présentés dans cette thèse représentent une contribution à la connaissance de la turbulence confinée compressible des écoulements hypersoniques et donnent un aperçu de certains phénomènes physiques qui coexistent dans la dynamique des gaz à haute vitesse. Les écoulements turbulents de gaz à haute enthalpie représentent un domaine de recherche important pour de nombreuses applications. À cette fin, une étude numérique a été menée sur l'influence des effets de haute température déclenchés par les conditions hypersoniques sur les écoulements d'air turbulent. Notre étude porte sur les écoulements autour des véhicules hypersoniques présentant les caractéristiques suivantes: i) le nombre de Mach est suffisamment élevé pour maintenir des conditions hypersoniques en aval de l'onde de choc détachée en amont du véhicule; ii) en conséquence, l'énergie thermique augmente de manière à déclencher des effets de relaxation chimique et vibrationnelle et l'air se comporte comme un mélange réactif d'azote, d'oxygène et de monoxyde d'azote; iii) le nombre de Reynolds est tel que l'écoulement est dans un régime principalement turbulent. Afin d'avoir une idée des mécanismes sous-jacents à ces écoulements, nous avons réalisé une étude numérique d'une couche limite sur une plaque plane; des configurations de plaques adiabatiques et refroidies ont été étudiées, du régime laminaire au régime entièrement turbulent.

La turbulence compressible confinée des gaz à haute température présente certaines similitudes avec les configurations dans des conditions cryogéniques. Malgré les températures élevées atteintes, l'activité chimique est relativement lente par rapport à l'évolution de l'écoulement. Ceci se traduit par un couplage faible entre les phénomènes chimiques et la dynamique de l'écoulement, conduisant à des vitesses moyennes et des profils d'intensité turbulente similaires à ceux rencontrés dans les écoulements hypersoniques à faible enthalpie, lorsqu'ils sont correctement mis à l'échelle avec des quantités semi-locales. Pour la même raison, la transition vers le régime turbulent reste qualitativement similaire à celle attendue pour un gaz parfait non réactif; la redistribution de l'énergie modale due au changement de composition du mélange est la différence la plus significative. En revanche, la partie de l'énergie drainée pour déclencher les phénomènes de dissociation entraîne une réduction globale des fluctuations

turbulentes et de la température. L'autre aspect à prendre en compte est la modification des propriétés thermophysiques due à la variation des fractions massiques des espèces; les propriétés de transport et les propriétés thermodynamiques peuvent s'écarter considérablement de leurs valeurs gelées, ce qui modifie l'importance relative des flux diffusifs par rapport aux flux turbulents. Dans l'ensemble, le mélange turbulent et la diffusion moléculaire redistribuent le gaz dans le domaine et influencent sa composition. En même temps, pour les configurations refroidies, le pic de température est lissé par le mélange, ce qui réduit encore l'activité chimique. L'influence de la turbulence sur le non-équilibre thermique est plus significative. On a constaté que ce dernier se produit et persiste en raison des fluctuations de la vitesse. Les temps de relaxation vibrationnelle retardent le retour vers l'équilibre du gaz entraîné par le mouvement turbulent dans une région avec température moyenne différente, ce qui à entretenir un écart entre les températures vibrationnelles et translationnelles; dans la majeure partie du domaine l'écoulement est sous-excité, c'est à dire caractérisé par une température vibrationnelle inférieure à la température translationnelle. Les forts effets de compressibilité favorisent encore cet écart, mais d'une façon moins prononcée que dans les configurations de turbulence non confinée. Pour confirmer l'interaction entre la turbulence et les effets à haute température, les termes d'interaction turbulence/chimie et turbulence/relaxation vibrationnelle ont été quantifiés. Les résultats de cette analyse ont montré que ce couplage n'est pas négligeable et qu'il est plus significatif dans le "buffer layer". Par conséquent, il convient d'accorder une attention particulière au développement de modèles de turbulence dans le contexte des écoulements hypersoniques, tant pour la fermeture des termes classiques de transport turbulent que pour les termes non fermés découlant des équations d'énergie des espèces et des vibrations.

Les présentes simulations numériques directes représentent une première contribution à la connaissance de la turbulence confinée en présence d'effets thermo-chimiques. Cependant, un effort scientifique important est encore nécessaire. Par exemple, le comportement de la paroi en termes de participation aux processus chimiques est de la plus haute importance: l'hypothèse d'une surface non catalytique ne doit pas être tenue pour acquise, car les matériaux adoptés pour les systèmes de protection thermique deviennent catalytiques au-delà de certains degrés de dissociation et de certaines valeurs de température. En même temps, l'ablation provoque des défauts à la surface qui pourraient induire différents scénarios de transition de turbulence, ce qui doit être pris en compte en plus de l'effet de la rugosité de la paroi. En outre, les différentes combinaisons de conditions de fonctionnement, telles que le nombre de Mach, l'enthalpie totale et l'altitude, peuvent favoriser un phénomène plus intensément qu'un autre. En effet, les régimes turbulents sont plus susceptibles de se produire à basse altitude, tandis que les phénomènes de relaxation thermique prédomineraient plus haut dans l'atmosphère. En même temps, des densités et une énergie cinétique plus élevées favorisent les collisions moléculaires, ce qui peut entraîner une activité chimique plus intense. En élargissant autant que possible cette gamme de paramètres de contrôle, il serait possible de tirer des conclusions plus générales sur la nature des écoulements hypersoniques à haute enthalpie.

Riassunto esteso

Introduzione

Negli ultimi anni, lo studio di flussi ipersonici ha suscitato grande interesse sia dal punto di vista ingegneristico che accademico. Il campo dell'astronautica è all'origine di questo interesse, ma recentemente concezioni di veicoli ipersonici innovativi stanno spingendo l'uomo verso nuove aree inesplorate, che richiedono una conoscenza e una padronanza sempre maggiori del campo dell'ipersonica. Qualsiasi veicolo che vola a velocità ipersonica genera un'onda d'urto, che causa bruschi cambiamenti nelle proprietà del flusso. L'enorme quantità di energia cinetica del flusso indisturbato viene convertita in energia interna quando il gas attraversa l'onda d'urto e la temperatura aumenta pericolosamente nella regione tra l'urto e la superficie del veicolo, portando alla dissociazione molecolare e all'eccitazione vibrazionale. Una conoscenza accurata delle condizioni del flusso a valle dello shock è fondamentale per progettare accuratamente il sistema di protezione termica e per prevenire un eccessivo riscaldamento aerodinamico. In tale situazione, l'erosione o l'ablazione dello scudo termico potrebbe indurre una transizione del flusso da un regime laminare a un regime turbolento. I carichi termici e meccanici aumentano drasticamente in un flusso completamente turbolento, raggiungendo un picco più o meno forte nella regione di transizione; per questa ragione, valutare a priori la zona di transizione è di fondamentale importanza. Sfortunatamente, sia la turbolenza comprimibile che il regime transizionale in condizioni di alta entalpia sono fenomeni fisici non ancora ben compresi; il legame tra effetti ad alta temperatura e flussi turbolenti è un'area di ricerca ancora più inesplorata. In genere, lo scenario turbolento è di grande preoccupazione sia per i veicoli civili che militari che volano ad altitudini relativamente basse (associate ad alti numeri di Reynolds a causa delle maggiori densità); una migliore conoscenza di tale regime è fondamentale per consentire ai veicoli di volare a velocità sempre più elevate (regime ipersonico) e ad altitudini inferiori (regime turbolento).

Da un punto di vista ingegneristico, un velivolo è fondamentalmente progettato per tollerare determinati carichi. La stima di tali carichi deriva da misurazioni sperimentali o da simulazioni numeriche che forniscono quantità macroscopiche necessarie per la scelta della forma del corpo, del peso e dei materiali. Tuttavia, nel dominio dell'aerotermodinamica, le proprietà macroscopiche sono strettamente legate alla natura microscopica del gas. Questo è uno dei motivi principali per cui i flussi ad alta temperatura richiedono particolare attenzione (Candler, 2019), poiché specifici effetti termochimici si attivano a cause delle alte temperature in gioco: reazioni chimiche e fenomeni di eccitazione vibrazionale possono verificarsi e dare origine a condizioni di non-equilibrio. Tali aspetti sono dettagliati nel seguito. L'energia interna di una generica molecola è composta da diverse forme (o modi) di energia: traslazionale, rotazionale, vibrazionale ed elettronico. In condizioni normali (temperature inferiori a 800 K), i livelli energetici traslazionali e rotazionali sono completamente eccitati e prevalgono su quelli vibrazionali. A temperature più alte, l'energia vibrazionale delle molecole diventa significativa e mod-

ifica le proprietà del gas. Per una miscela di gas, i cui modi vibrazionali delle molecole sono eccitati, l'equazione di stato deve tenere conto del comportamento caloricamente imperfetto. Di conseguenza, l'aria in tali condizioni è una miscela di gas termicamente perfetti e caloricamente imperfetti. Se la temperatura aumenta ulteriormente, oltre 2000 K, si verificano processi chimici: O_2 inizia a dissociare e si esaurisce completamente a 4000 K quando, a sua volta, inizia la dissociazione di N_2 . A temperature ancora più alte (cioè oltre i 9000 K), la maggior parte dell' N_2 si è dissociata e si verificano processi di ionizzazione.

I processi appena descritti avvengono principalmente tramite collisioni molecolari, che hanno bisogno di un certo tempo (finito) per verificarsi. Se il tempo caratteristico di tali fenomeni è paragonabile al tempo caratteristico del flusso (cioè, $\tau/\tau_{\text{flow}} \approx 1$), si dice che il flusso è in uno stato di non-equilibrio chimico e/o termico. Nel caso di non-equilibrio termochimico simultaneo, c'è uno stretto accoppiamento tra i tassi di rilassamento termico e i tassi di reazione chimica. Per esempio, ci si aspetta che le molecole eccitate vibrazionalmente si dissocino più velocemente, poiché richiedono meno scambi di energia durante le collisioni; di conseguenza, i livelli vibrazionali di tali molecole si spopolano facilmente.

Negli ultimi anni sono stati fatti progressi significativi nello studio dei flussi ad alta velocità. La maggior parte degli studi dettagliati si basano su risultati provenienti da simulazioni numeriche, dal momento che la realizzazione di esperimenti nelle condizioni di interesse è generalmente costoso o addirittura impraticabile (Bertin & Cummings, 2006). Le simulazioni numeriche ad alta fedeltà possono essere un potente strumento per integrare i dati sperimentali disponibili, specialmente i risultati riguardanti i flussi turbolenti che sono generalmente scarsi. Una delle configurazioni classiche per studiare i flussi turbolenti confinati comprimibili è lo strato limite, che può essere considerato come una vista ravvicinata di una piccola regione della fusoliera di un veicolo. Il contributo della presente tesi è quindi quello di indagare gli effetti termochimici in strati limite ipersonici per mezzo di simulazioni numeriche dirette, garantendo la risoluzione dell'intera gamma attiva di scale temporali e spaziali. L'obiettivo è quello di fornire una vasta quantità di dati accurati che possono dare accesso a diverse quantità istantanee e statistiche, consentendo analisi approfondite sulla natura della turbolenza, effetti di comprimibilità, topologia del flusso o interazione turbolenza/termochimica e permettendo lo sviluppo di modelli di turbolenza più accurati.

Equazioni di governo e metodo numerico

Nel presente lavoro si analizza una miscela di gas composta da N_2 , O_2 , NO , O e N , la cui natura è descritta dalle equazioni di Navier–Stokes comprimibili tridimensionali per flussi multispecie reagenti e termicamente fuori equilibrio (Gnoffo *et al.*, 1989). Il comportamento del gas è modellato tramite la formulazione “Translational-Rotational-Vibrational” (TRV), che fornisce l'espressione dell'entalpia della singola specie; la legge di Dalton descrive la pressione della miscela e fornisce l'espressione dell'equazione di stato termica. Per chiudere il sistema, occorre specificare l'espressione dei modelli termofisici che descrivono la viscosità, le conduttività termiche e i coefficienti di diffusione di massa. Nelle seguenti simulazioni, la viscosità e le conduttività termiche delle singole specie sono descritte dalle relazioni di Blottner *et al.* (1971) e dalla correzione di Eucken (Hirschfelder & Curtiss, 1969). Le proprietà della miscela sono valutate a partire dalle regole di miscela di Wilke (1950). Per quanto riguarda i coefficienti di diffusione, la legge di Fick è stata utilizzata per descrivere il fenomeno di diffusione di massa; un coefficiente equivalente è stato utilizzato per la diffusione di ogni singola specie nella miscela (Hirschfelder *et al.*, 1954). Per concludere, è necessario fornire un'espressione dei

termini sorgente che appaiono nelle equazioni di conservazione delle singole specie e nell'equazione di conservazione dell'energia vibrazionale media delle tre molecole. Per questo, è stato utilizzato il modello a due temperature di Park (Park, 1988).

Le equazioni di Navier-Stokes sono integrate numericamente utilizzando uno schema alle differenze finite centrato di alto ordine (Sciacovelli *et al.*, 2021). I flussi convettivi sono discretizzati per mezzo uno schema al decimo ordine, mentre i termini viscosi con differenze finite standard al quarto ordine. Uno schema centrato ha una natura puramente dispersiva; per questa ragione, per assicurare robustezza numerica, si adotta una strategia basata su una dissipazione artificiale adattiva. Questa consiste in una combinazione di un termine di dissipazione accurato del nono ordine basato su derivate del decimo ordine delle variabili conservative (utilizzate per smorzare le oscillazioni maglia a maglia) e di un termine di cattura degli shock di basso ordine. Un sensore altamente selettivo è usato per attivare la cattura degli shock nelle immediate vicinanze delle discontinuità del flusso. L'integrazione temporale è effettuata per mezzo di uno schema Runge-Kutta accurato al terzo ordine (Gottlieb & Shu, 1998).

Strato limite turbolento ipersonico su una parete piana adiabatica

In tale sezione si analizza uno strato limite ipersonico che si sviluppa su una parete piana adiabatica in condizioni di non-equilibrio chimico. La seguente analisi è divisa in due parti. Inizialmente, ci concentriamo sulle regioni laminari e di transizione; successivamente, si valuta l'influenza del non-equilibrio chimico sulla regione di turbolenza pienamente sviluppata, grazie anche al confronto con i risultati di una simulazione con l'ipotesi di miscela congelata. Per entrambe le analisi, le condizioni termodinamiche sono simili a quelle adottate in diversi studi di stabilità (Malik & Anderson, 1991; Hudson *et al.*, 1997; Perraud *et al.*, 1999; Franko *et al.*, 2010; Marxen *et al.*, 2014; Miró Miró *et al.*, 2018); in particolare, i valori imposti per il flusso indisturbato sono $M_\infty = 10$, $T_\infty = 350$ K e $p_\infty = 3596$ Pa. I calcoli sono iniziati nella regione laminare, dove l'aria con composizione standard ($Y_{O_2}=0.233$ e $Y_{N_2}=0.767$) entra nel dominio di calcolo.

Un modo di Mack è eccitato con una forte ampiezza, al fine di promuovere una transizione di tipo "second-mode", che risulta essere la più instabile in regime ipersonico. La presente simulazione comprende la regione laminare e di transizione, incorporando la crescita lineare dei disturbi, l'interazione tra i modi secondari e l'esplosione non lineare in turbolenza. Il tipo di scenario di transizione generato prevede, per la prima volta, una transizione di tipo "second-mode" subarmonica. Infatti, nonostante un modo di Mack (bidimensionale e ad alta frequenza) sia eccitato con un'ampiezza significativa rispetto ai modi secondari, il processo di transizione non è governato dal modo fondamentale. I modi subarmonici bidimensionali e obliqui sono naturalmente selezionati e amplificati, drenando energia da quello fondamentale. Verso gli ultimi stadi della transizione i modi stazionari emergono causando una distorsione del campo medio. L'interazione dei modi bidimensionali e obliqui porta alla formazione di vortici di tipo λ . Sia l'analisi modale che la descrizione delle visualizzazioni istantanee confermano che lo scenario di transizione condivide notevoli somiglianze, almeno in termini qualitativi, con la transizione di tipo H per flussi incomprimibili (Herbert, 1988). In uno scenario di tipo H , appaiono strutture a forma di λ e sono organizzate in modo perfettamente sfalsato; inoltre, questo percorso è caratterizzato dall'amplificazione dei modi subarmonici. Ulteriori analisi sono state pianificate per chiarire tale scenario, specialmente negli ultimi stadi della transizione, per investigare come l'instabilità dei vortici di tipo λ insieme alla predominanza dei modi stazionari producano uno scenario completamente turbolento. Inoltre, un confronto con uno scenario senza reazioni chimiche è anche previsto. Nel seguito, ci concentriamo sulla regione turbolenta con lo scopo di capire se e in che misura il

non-equilibrio chimico altera la turbolenza comprimibile confinata. La presente configurazione di una piastra piana quasi-adiabatica, pur essendo un'approssimazione puramente teorica, permette di studiare l'influenza di valori di temperatura estremamente elevati nella regione vicino a parete, che è quella di estrema importanza per la progettazione di un veicolo. L'effetto principale della dissociazione del gas è quello di cambiare la composizione della miscela vicino alla parete, nella regione compresa tra il sottostrato viscoso e il "buffer layer", modificando le proprietà termofisiche del fluido. Inoltre, le reazioni chimiche endotermiche drenano energia dal flusso nella regione di produzione della turbolenza, portando a un'intensità turbolenta leggermente inferiore e a una riduzione delle fluttuazioni di temperatura di circa il 10%. I piccoli valori osservati per i numeri di Damköhler medi delle specie indicano che la dissociazione chimica è molto più lenta della scala temporale caratteristica del flusso, cioè il flusso non è lontano dalle condizioni di flusso congelato. In questa situazione, le principali differenze rispetto a un flusso congelato si osservano per le quantità termodinamiche; al contrario, la presenza di reazioni chimiche non altera sostanzialmente le quantità dinamiche o gli spettri turbolenti. I dati forniti da questa simulazione sono stati utilizzati anche per valutare alcune ipotesi classiche di modellazione derivanti dalla teoria della Strong Reynolds Analogy (SRA). Quest'ultima è dimostrata rimanere generalmente valida. Le ipotesi di un numero di Prandtl turbolento costante e di un numero di Schmidt turbolento costante, classicamente utilizzate per modellare il trasporto turbolento di calore e il trasporto di massa turbolento, forniscono un'approssimazione non del tutto errata e ancora accettabile in certe condizioni.

Strato limite turbolento ipersonico su una parete piana raffreddata

In questa sezione, il legame tra la turbolenza e gli effetti di non-equilibrio sia termico che chimico sono analizzati. La configurazione in esame è uno strato limite che si sviluppa su una parete piana raffreddata. Le proprietà del flusso indisturbato corrispondono alle condizioni di post-shock di un "wedge" di 6° che vola a Mach 20, ad un'altitudine di circa 36 km. In tali condizioni, il flusso è in uno stato di non-equilibrio vibrazionale, mentre l'attività chimica rimane relativamente debole.

Allo scopo di quantificare il non-equilibrio termico, si definisce un numero di Damköhler vibrazionale, basato su diverse scale temporali caratteristiche del flusso. I risultati illustrano che, eccetto la regione vicina alla parete dove il flusso è vibrazionalmente congelato, forti condizioni di non-equilibrio termico persistono fino al bordo dello strato limite. L'azoto molecolare risulta essere il responsabile del non-equilibrio termico, poiché la sua temperatura caratteristica è abbastanza alta da causare tassi di rilassamento lenti. L'eccitazione vibrazionale è in gran parte causata dal mixing turbolento, come osservato dallo stretto accoppiamento con gli eventi di "sweep" e "ejection". Le fluttuazioni di velocità infatti trasportano aria più fredda dalle regioni esterne verso la parete oppure aria più calda lontano dallo strato interno. I modi rot-traslazionali si adattano rapidamente a queste grandi fluttuazioni di temperatura, contrariamente ai modi vibrazionali. A livello macroscopico, la diretta conseguenza è che la temperatura vibrazionale è in ritardo rispetto a quella traslazionale fino alla prima metà della zona logaritmica; da lì in poi, il flusso passa verso uno stato vibrazionalmente sovraeccitato che si mantiene fino al bordo dello strato limite. L'ispezione dei bilanci energetici vibrazionali conferma che il trasporto turbolento gioca un ruolo fondamentale. Seguendo le usuali strategie di modellazione RANS, si può definire un numero di Prandtl vibrazionale turbolento che assume valori vicini all'unità per la maggior parte dello strato limite. Le statistiche del secondo ordine mostrano che le tensioni di Reynolds sono qualitativamente simili a quelle osservate in condizioni di bassa entalpia; inoltre, la condizione di parte isoterma porta ad un profilo di temperatura fluttuante non monotono e caratterizzato da

due picchi. Al contrario, le fluttuazioni di temperatura vibrazionale mostrano profili monotonamente crescenti a causa delle marcate condizioni di non-equilibrio esistenti nel “buffer layer”. Le analisi sugli effetti di comprimibilità hanno mostrato che i forti moti di dilatazione si trovano principalmente vicino alla parete, con forti compressioni leggermente più probabili delle forti espansioni. Nessuna relazione diretta esiste tra compressioni/espansioni e sottoeccitamento/sovraccitamento vibrazionale, contrariamente a quanto osservato per la turbolenza non confinata, ma si può concludere che in generale i forti eventi di comprimibilità aumentano indirettamente il non-equilibrio termico.

Conclusioni

I risultati illustrati in questa tesi rappresentano un contributo alla conoscenza della turbolenza comprimibile confinata di flussi ipersonici e forniscono approfondimenti su alcuni fenomeni fisici che coesistono nella dinamica dei gas ad alta velocità. I flussi turbolenti di gas ad alta entalpia rappresentano un importante campo di ricerca per numerose applicazioni. A questo scopo, è stato condotto uno studio numerico sull’influenza degli effetti di alta temperatura innescati dalle condizioni ipersoniche su flussi di aria turbolenti. Il nostro studio si concentra su flussi attorno a veicoli ipersonici con le seguenti caratteristiche: i) il numero di Mach nel freestream è abbastanza alto da mantenere forti condizioni ipersoniche a valle dell’onda d’urto; ii) di conseguenza, l’energia termica aumenta in modo da innescare effetti chimici e di rilassamento vibrazionale e l’aria è una miscela reagente di azoto, ossigeno e ossido nitrico; iii) il numero di Reynolds è tale che il flusso sia in un regime prevalentemente turbolento. Per avere un’idea dei meccanismi alla base di tali flussi, abbiamo effettuato uno studio numerico di uno strato limite su una lamina piana; sono state studiate la configurazione di lamina adiabatica e raffreddata, dal regime laminare fino a quello completamente turbolento.

La turbolenza comprimibile confinata di gas ad alta temperatura condivide alcune somiglianze con le configurazioni in condizioni criogeniche. Nonostante le alte temperature raggiunte, l’attività chimica è risultata relativamente lenta. Di conseguenza, le grandi scale temporali chimiche hanno causato un leggero disaccoppiamento tra i fenomeni chimici e il moto dinamico, portando a velocità medie e profili di intensità turbolenta simili a quelli incontrati nei flussi ipersonici a bassa entalpia, una volta correttamente scalati con quantità semi-locali. Per la stessa ragione, la transizione verso il regime turbolento è rimasta qualitativamente simile a quella prevista per un gas perfetto non reagente; la redistribuzione dell’energia modale dovuta al cambiamento della composizione della miscela è la differenza più significativa. D’altra parte, la parte di energia drenata per innescare fenomeni di dissociazione ha causato una riduzione globale delle fluttuazioni turbolente e della temperatura. L’altro aspetto che deve essere preso in considerazione è il cambiamento delle proprietà termofisiche dovuto al variare delle frazioni massiche delle specie; le proprietà di trasporto e termodinamiche possono deviare significativamente dai loro valori congelati, modificando l’impatto dei flussi diffusivi rispetto a quelli turbolenti. Globalmente, il mixing turbolento insieme alla diffusione molecolare ridistribuisce il gas e influenza la composizione. Allo stesso tempo, per le configurazioni raffreddate a parete, il picco di temperatura viene smussato dalla miscelazione, riducendo ulteriormente l’attività chimica. Più significativa è l’influenza della dinamica della turbolenza sul non-equilibrio termico. Si è scoperto che quest’ultimo si verifica e persiste a causa delle fluttuazioni di velocità. I tempi di rilassamento vibrazionale causano un ritardo per il flusso nel tendere verso l’equilibrio con il nuovo gas trasportato dal moto turbolento, portando a diverse temperature vibrazionali e traslazionali; la maggior parte del non-equilibrio è sottoeccitato. Forti effetti di comprimibilità promuovono ulteriormente questo divario, ma l’effetto è meno marcato rispetto alle configurazioni di turbolenza non confinata. A conferma dell’interazione tra turbolenza

ed effetti ad alta temperatura, sono stati quantificati i termini di interazione turbolenza/chimica e turbolenza/rilassamento vibrazionale. I risultati di questa analisi hanno evidenziato che questo accoppiamento non è trascurabile ed è più significativo nel “buffer layer”. Di conseguenza, è necessario prestare particolare attenzione allo sviluppo di modelli di turbolenza nel contesto dei flussi ipersonici, sia per la chiusura dei termini classici di trasporto turbolento che per i termini non chiusi derivanti dalle equazioni di specie e di energia vibrazionale.

Le presenti simulazioni numeriche dirette rappresentano un primo contributo alla conoscenza della turbolenza confinata in presenza di effetti termochimici. Tuttavia, uno sforzo scientifico significativo è ancora richiesto. Per esempio, il comportamento della parete in termini di partecipazione ai processi chimici è della massima importanza: l'ipotesi di superficie non catalitica non dovrebbe essere data per scontata, poiché i materiali adottati per i sistemi di protezione termica diventano catalitici oltre certi gradi di dissociazione e valori di temperatura. Allo stesso tempo, l'ablazione provoca difetti sulla superficie che potrebbero indurre diversi scenari di transizione alla turbolenza, da considerare in aggiunta all'effetto della rugosità delle pareti. Inoltre, la diversa combinazione di condizioni operative, come il numero di Mach, l'entalpia totale e l'altitudine, può promuovere un fenomeno più intensamente di un altro. Infatti, i regimi turbolenti hanno maggiori probabilità di verificarsi ad altitudini più basse, mentre i fenomeni di rilassamento termico sarebbero predominanti più in alto nell'atmosfera. Allo stesso tempo, densità e energia cinetica più alti promuovono le collisioni molecolari, che possono risultare in un'attività chimica più intensa. Ampliare il più possibile questa gamma di parametri di controllo consentirebbe ulteriori approfondimenti sui flussi ipersonici ad alta entalpia e permetterebbe di convenire conclusioni più generali sulla natura di questi gas.

Contents

| | |
|---|-----------|
| Acknowledgments | 5 |
| Résumé étendu | 7 |
| Riassunto esteso | 14 |
| List of Tables | 23 |
| List of Figures | 27 |
| 1 Introduction | 28 |
| 1.1 High-temperature and high-speed gas dynamic | 29 |
| 1.2 Thermochemical models | 31 |
| 1.3 State of the art | 32 |
| 1.4 Motivation | 36 |
| 1.5 Outline | 37 |
| 2 Governing equations and numerical methods | 38 |
| 2.1 Governing equations | 38 |
| 2.1.1 Equation of state | 40 |
| 2.1.2 Thermochemical models | 42 |
| 2.1.3 Transport properties | 43 |
| 2.1.3.1 Viscosity and thermal conductivity | 43 |
| 2.1.3.2 Molecular transport | 43 |
| 2.2 Numerical strategy | 48 |
| 2.2.1 Central numerical fluxes | 49 |
| 2.2.2 Numerical stabilization and shock capturing | 49 |
| 2.2.2.1 Adaptive nonlinear artificial dissipation (ANAD) | 49 |
| 2.2.2.2 High-order filtering and Localized Artificial Diffusivity | 51 |
| 2.2.3 Time integration methods | 53 |
| 2.2.4 Numerical schemes used in this study | 53 |
| 2.3 Description of the CFD code | 53 |
| 3 Numerical solver verification and assessment | 58 |
| 3.1 Thermochemical equilibrium | 58 |
| 3.2 0D heath bath in thermal non-equilibrium | 59 |

CONTENTS

| | | |
|----------|--|------------|
| 3.3 | Shock tube problems | 60 |
| 3.4 | Viscous chemically-reacting shock tubes | 61 |
| 3.5 | Laminar 2D boundary layer with high-temperature effects | 64 |
| 3.6 | Perfect-gas turbulent boundary layers | 64 |
| 4 | Adiabatic hypersonic turbulent boundary layers | 71 |
| 4.1 | Second-mode transition in a high-enthalpy boundary layer | 71 |
| 4.1.1 | Simulation setup and definitions | 73 |
| 4.1.2 | Results | 75 |
| 4.1.2.1 | Breakdown to turbulence | 75 |
| 4.1.2.2 | Modal analysis | 80 |
| 4.1.2.3 | Dynamic Mode Decomposition (DMD) | 83 |
| 4.2 | Analysis of fully turbulent regime | 85 |
| 4.2.1 | Simulations setup and definitions | 87 |
| 4.2.2 | Results | 89 |
| 4.2.2.1 | First-order statistics | 89 |
| 4.2.2.2 | Second-order statistics | 96 |
| 4.2.2.3 | Spectral content | 100 |
| 5 | Cold-wall hypersonic turbulent boundary layers | 103 |
| 5.1 | Simulations setup and definitions | 104 |
| 5.2 | Results | 105 |
| 5.2.1 | Global flow properties | 105 |
| 5.2.2 | Velocity statistics | 107 |
| 5.2.3 | Thermal non-equilibrium effects | 108 |
| 5.2.4 | Chemical activity | 120 |
| 5.2.5 | Compressibility effects | 122 |
| 6 | Conclusions and Perspectives | 130 |
| 6.1 | Future work | 131 |
| | Bibliography | 133 |
| A | Analytical computation of mixture composition for air at equilibrium conditions | 141 |
| B | Similarity solutions for chemically-reacting boundary layers | 143 |
| C | DMD methodology | 146 |
| D | Complementary results of adiabatic boundary layers simulations | 148 |

List of Tables

| | | |
|-----|--|-----|
| 2.1 | Properties of the species present in the mixture. | 41 |
| 2.2 | Parameters for the chemical model of Park (1990). | 44 |
| 2.3 | Coefficients to compute the relaxation time τ_m as in equation (2.24), from Park (1993). | 45 |
| 2.4 | Coefficients to compute pure species viscosity of equation (2.25), from Blottner <i>et al.</i> (1971). | 45 |
| 2.5 | Constants for diffusion coefficient curve fits of equation (2.32), from Gupta <i>et al.</i> (1990). Of note, coefficient A_1 is identically zero. | 47 |
| 2.6 | Numerical schemes adopted in this work. | 53 |
| 2.7 | Strong scalability study. The grid size is $4608 \times 240 \times 300$ ($\approx 332 \times 10^6$ grid points). | 54 |
| 2.8 | Weak scalability study. The grid size per core is $72 \times 60 \times 25$ ($\approx 1 \times 10^5$ grid points per core). | 55 |
| 3.1 | List of the computational grids and selected parameters for the supersonic boundary layers at $M = 2.25$ | 66 |
| 4.1 | Parameters of the modes excited by the forcing function in equation 4.2. | 75 |
| 4.2 | Boundary layer properties for the finite-rate chemistry (CN) case at five downstream stations. | 88 |
| 5.1 | Boundary layer properties at five downstream stations for cold-wall boundary layer case. | 106 |

List of Figures

| | | |
|------|--|----|
| 1.1 | Flight trajectories of some hypersonic vehicles, from Urzay & Di Renzo (2021) | 29 |
| 1.2 | Sketch of thermochemical phenomena at increasing temperature, from Anderson (2006) | 31 |
| 1.3 | Direct connect configuration of the interior of HTF (left) and test chamber of SCIROCCO plasma wind tunnel, from Borrelli & Martucci (2011) (right). | 33 |
| 2.1 | Evolution of specific isobaric heat capacities, for a given temperatures range. | 41 |
| 2.2 | Evolution of specific viscosities (left panel) and thermal conductivities (right panel), for a given temperatures range. | 45 |
| 2.3 | Evolution of specific equivalent diffusion coefficients, for a given temperatures range. | 46 |
| 2.4 | Dispersion and dissipation errors as a function of the reduced wavenumber $k\delta x$ up to of the ninth-order scheme. | 51 |
| 2.5 | Strong (left column) and weak (right column) scalability tests. | 56 |
| 3.1 | Mass fractions versus temperature at thermochemical equilibrium | 59 |
| 3.2 | Virational-Translational relaxation towards equilibrium of N_2 heath bath | 60 |
| 3.3 | Reference and numerical solutions for Sod's and Lax's shock tubes. | 60 |
| 3.4 | Reference and numerical solutions for Grossman's shock tube. | 62 |
| 3.5 | Results for the two-dimensional perfect-gas viscous shock tube. | 62 |
| 3.6 | Results for the two-dimensional chemically-reacting viscous shock tube. | 63 |
| 3.7 | Normalized velocity and temperature profiles as a function of the similarity variable, for $T_\infty=278$ K, $Re_u=9.8425 \times 10^6 \text{ m}^{-1}$ at $x=0.4$ m. | 65 |
| 3.8 | Normalized velocity and temperature profiles as a function of the similarity variable, for $T_\infty=350$ K and $Re_u=6.6 \times 10^6 \text{ m}^{-1}$ at $x=0.6$ m. | 65 |
| 3.9 | Resolutions of the computational grids along the streamwise direction in wall units. | 67 |
| 3.10 | Instantaneous snapshots for the $M = 2.25$ supersonic boundary layer: isosurfaces of the Q -criterion coloured by the distance from the wall. | 68 |
| 3.11 | Skin friction coefficient C_f for the $M = 2.25$ supersonic boundary layer. | 69 |
| 3.12 | Wall-normal profiles of the Van-Driest-transformed longitudinal velocity (a), r.m.s. of velocity (b), temperature (c) and density (d), for the $M = 2.25$ supersonic boundary layer. | 69 |
| 4.1 | Paths to turbulence in boundary layer flows, from Morkovin (1994) | 72 |
| 4.2 | Acoustic mode in a high-speed boundary layer, from Fedorov (2011) | 73 |
| 4.3 | Isosurfaces of Q -criterion, colored with the wall-normal distance for the adiabatic boundary layer case. | 74 |

LIST OF FIGURES

| | | |
|------|--|----|
| 4.4 | Streamwise evolution of wall quantities. Skin friction coefficient (a), normalized wall temperature (b) and wall species mass fractions (c). | 76 |
| 4.5 | Instantaneous visualization of a xz -plane, colored with the molecular oxygen mass fraction Y_{O_2} | 77 |
| 4.6 | Mean flow distortion. Isocontours and isolines (solid black lines) of normalized mean streamwise velocity, superposed with isolines (dashed white lines) of normalized streamwise velocity deriving from a steady laminar computation. | 77 |
| 4.7 | Streamwise evolution of skin friction coefficient (solid line) superposed with Renard-Deck decomposition (symbols) (a) and contribution of each terms of equation (4.5) (b). | 78 |
| 4.8 | Instantaneous visualization of normalized streamwise velocity fluctuations in xz -planes. | 79 |
| 4.9 | Instantaneous visualization of x -vorticity in zy -planes. | 79 |
| 4.10 | Isosurfaces of the Q -criterion colored with the distance from the wall. | 80 |
| 4.11 | Streamwise developments of modal total energy (a), modal kinetic energy (b) and maximum u -velocity disturbance amplitude (c). | 82 |
| 4.12 | Streamwise evolution of streaks amplitude. | 83 |
| 4.13 | Eigenvalues spectra obtained from DMD analysis on τ_w | 84 |
| 4.14 | Spatial DMD modes of τ_w in the laminar and transitional zone of the domain. | 84 |
| 4.15 | Comparison between instantaneous flow field of τ_w and reconstructed flow field from DMD modes. | 85 |
| 4.16 | Eigenvalues spectra obtained from DMD analysis on u | 86 |
| 4.17 | Distribution of two-point correlations in the spanwise direction, at $Re_\tau = 185$ | 88 |
| 4.18 | One-dimensional energy spectra in the spanwise direction, at $Re_\tau = 185$ | 89 |
| 4.19 | Isosurfaces of Q -criterion, colored with the local values of O_2 mass fraction for the CN case. | 90 |
| 4.20 | Wall distributions of the skin friction coefficient C_f as a function of Re_x | 90 |
| 4.21 | Instantaneous visualizations of the normalized streamwise velocity in a $x - z$ plane for FR case (top) and CN case (bottom). | 91 |
| 4.22 | Streamwise evolution of averaged dynamic viscosity $\bar{\mu}$ (a) and thermal conductivity $\bar{\lambda}$ (b) at the wall, normalized with respect the constant values of the FR case. | 91 |
| 4.23 | Streamwise evolution of the averaged mass fractions \bar{Y}_n at the wall for species O_2 , NO , O and N | 92 |
| 4.24 | Wall-normal profiles of the van Driest-transformed streamwise velocity (a) and of the normalized mean temperature (b) at $Re_\tau = 185$ | 93 |
| 4.25 | Wall-normal mean profiles of viscosity and thermal conductivity (a), specific heat capacity at constant pressure (b), Prandtl number (c) and specific heat ratio γ (d) at $Re_\tau = 185$ | 94 |
| 4.26 | Wall-normal evolution of mean Lewis number (a) and Schmidt number (b) at $Re_\tau = 185$, for the chemically-reacting simulation, in inner scaling. | 94 |
| 4.27 | Wall-normal profiles of the average Damköhler number (a), species mass fractions (b), and species Damköhler number Da_n^I at $Re_\tau = 185$ | 95 |
| 4.28 | Wall-normal profiles of Reynolds stresses (a) and of the normalized r.m.s. temperature (b), at $Re_\tau = 185$ | 96 |
| 4.29 | Wall-normal profiles of r.m.s. mass fractions at $Re_\tau = 185$ for the CN case. | 97 |

LIST OF FIGURES

| | | |
|------|--|-----|
| 4.30 | Correlation coefficient between u'' and T'' without total temperature correction (a) and with total temperature correction (b), at $Re_\tau = 185$ | 98 |
| 4.31 | Wall-normal profiles of the turbulent Prandtl number for CN case, at $Re_\tau = 185$ | 99 |
| 4.32 | Normalized turbulent transport of species mass fractions in the streamwise (a) and wall-normal (b) directions; normalized turbulent diffusion fluxes in the streamwise (c) and wall-normal (d) directions, at $Re_\tau = 185$ | 99 |
| 4.33 | Wall-normal profiles of the turbulent Schmidt number for CN case, at $Re_\tau = 185$ | 100 |
| 4.34 | Premultiplied spanwise spectra $k_z E_{vv}/u_\infty^2$ (a), $k_z E_{uu}/u_\infty^2$ (b) and $k_z E_{TT}/T_\infty^2$ (c) for the chemical non-equilibrium simulation, at $Re_\tau = 185$ | 101 |
| 5.1 | Sketch of the configuration under investigation. | 105 |
| 5.2 | Evolution of (a) skin friction coefficient C_f and (b) normalized wall heat fluxes C_q and $C_{q,V}$ | 106 |
| 5.3 | Evolution of the skin friction coefficient C_f and Renard-Deck decomposition (symbols) (z) and contribution of each term of equation (4.5) (b). | 107 |
| 5.4 | Wall-normal profiles of the van Driest-transformed streamwise velocity (a), of Trettel & Larsson's transformation (b) and comparison between Trettel & Larsson transformation and total-stress-based transformation of Griffin <i>et al.</i> (2021). | 109 |
| 5.5 | Reynolds stresses in the streamwise direction (a)-(b), wall-normal direction (c)-(d), spanwise direction (e)-(f) and Reynolds shear stresses (g)-(h). | 110 |
| 5.6 | Vibrational Damköhler numbers for N_2 (first row), O_2 (second row) and NO (third row). | 111 |
| 5.7 | Normalized mean translational temperature (a) and vibrational temperature (b) at the selected streamwise stations. | 112 |
| 5.8 | Normalized difference $(\tilde{T} - \tilde{T}_V)/T_w$ at the selected streamwise stations; (a) semi-local units, (b) outer scale. | 112 |
| 5.9 | Instantaneous isocontours of $T - T_V$ in a xy -plane and Q -criterion coloured by $T - T_V$ | 113 |
| 5.10 | Rms of temperature Favre fluctuations normalized by the local Favre average for translational temperature (a) and vibrational temperature (b). | 114 |
| 5.11 | Premultiplied energy spectra $k_z E_{T'T'}/\tilde{T}$ (a) and $k_z E_{T_V T_V}/\tilde{T}_V$ (b), at $Re_\theta = 6200$ | 114 |
| 5.12 | Mean values of \tilde{T} and \tilde{T}_V conditioned on sweep and ejection events, at $Re_\theta = 6200$ at various wall-normal heights. | 115 |
| 5.13 | Conditional p.d.f. of translational and vibrational temperature at $Re_\theta = 6200$ for y^* approximately equal to 10, 100 and 3000, respectively. | 116 |
| 5.14 | Terms of equation 5.6. Turbulent transport in the streamwise (a) and wall-normal (b) directions; molecular diffusion term in the streamwise (c) and (d) wall-normal directions. | 117 |
| 5.15 | Turbulent Prandtl number (a) and turbulent vibrational Prandtl number (b). | 117 |
| 5.16 | Correlation coefficients between Favre fluctuations of vibrational temperature and streamwise velocity (a) and wall-normal velocity (b) and of translational temperature and streamwise velocity (c) and wall-normal velocity (d). | 118 |
| 5.17 | Wall-normal profiles of $\overline{Q_{TV}} J/(\text{m}^3\text{s})$ (a) and Q_{TV}^I , defined in equation (5.8) (b). | 120 |
| 5.18 | Mean mass fractions of molecular nitrogen (a), molecular oxygen (b), nitric oxide (c), atomic oxygen (d) and atomic nitrogen (e). | 121 |
| 5.19 | Normalized source terms for molecular nitrogen (a), molecular oxygen (b), nitric oxide (c), atomic oxygen (d) and atomic nitrogen (e). | 122 |

LIST OF FIGURES

| | | |
|------|---|-----|
| 5.20 | Mass fractions fluctuations for molecular nitrogen (a), molecular oxygen (b), nitric oxide (c) and atomic oxygen (d). | 123 |
| 5.21 | Correlation coefficients between velocity fluctuations and mass fractions fluctuations for molecular nitrogen (a), molecular oxygen (b), nitric oxide (c), atomic oxygen (d) and atomic nitrogen (e). | 124 |
| 5.22 | Wall-normal profiles of the turbulent Schmidt for molecular oxygen (a) and atomic nitrogen (b). The horizontal dashed-dotted lines denote the SRA estimation. | 124 |
| 5.23 | Profiles of turbulent Mach number (a) and rms Mach number (b). | 125 |
| 5.24 | Instantaneous snapshot of the normalized density gradient magnitude along a slice of the computational domain. | 125 |
| 5.25 | Instantaneous snapshot of the normalized divergence along the last portion of the computational domain. | 126 |
| 5.26 | P.d.f. of normalized divergence at $Re_\theta = 6200$ for $y^* \approx 10$ and $y^* \approx 1000$. | 126 |
| 5.27 | Joint p.d.f. of density gradient magnitude and normalized divergence at $Re_\theta = 6200$ for $y^* \approx 10$ (a) and $y^* \approx 1000$ (b). | 126 |
| 5.28 | Profiles of fluctuating quantities of divergence (a) and vorticity (b). | 127 |
| 5.29 | Conditional p.d.f. of normalized translational-vibrational energy exchange at $Re_\theta = 6200$ for $y^* \approx 10$ (first row) and $y^* \approx 1000$ (second row). | 128 |
| 5.30 | Joint p.d.f. of normalized divergence and normalized Q_{TV} at $Re_\theta = 6200$ for $y^* \approx 10$ (a) and $y^* \approx 1000$ (b). | 128 |
| B.1 | Evolution of normalized velocity and temperature (left column) and species mass fractions (right column), at the inflow for adiabatic and wall-cooled test case. | 144 |
| B.2 | Wall-normal profiles of normalized velocity and temperature at $x = 0.05$ m. Comparison between Navier-Stokes solution (line) and locally self-similar solution (symbols). | 145 |
| D.1 | Modified Walz's equation (solid lines) for frozen simulation (a) and chemically-reacting simulation (b), at $Re_\tau = 185$. | 149 |
| D.2 | Turbulent kinetic energy budgets, at $Re_\tau = 185$. | 149 |
| D.3 | Premultiplied spanwise spectra $k_z E_{v'v'}/u_\infty^2$ (a), $k_z E_{u'u'}/u_\infty^2$ (b) and $k_z E_{T'T'}/T_\infty^2$ (c) for frozen simulation. | 150 |
| D.4 | Wall-normal distributions of the turbulent (a) and fluctuating (b) Mach numbers, and fluctuating speed of sound (c) at $Re_\tau = 185$. | 150 |
| D.5 | Distribution of the normal Reynolds stress anisotropies (a) and Reynolds shear stress anisotropy (b) at $Re_\tau = 185$. | 151 |
| D.6 | Anisotropy invariants map for frozen simulation (a) and chemically reacting simulation (b), at $Re_\tau = 185$. | 151 |
| D.7 | Probability density function of normalized density (a) and normalized dilatation (b). | 151 |

Chapter 1

Introduction

Contents

| | |
|--|-----------|
| 1.1 High-temperature and high-speed gas dynamic | 29 |
| 1.2 Thermochemical models | 31 |
| 1.3 State of the art | 32 |
| 1.4 Motivation | 36 |
| 1.5 Outline | 37 |

In recent years, the study of high-speed flows has raised great interest both from an engineering and academic standpoint. Understanding the physics behind such flows is a continuous challenge; keeping up with the extremely demanding technological progress has pushed the man towards new unexplored areas, which require increasing knowledge and mastery. The domain of astronautics is actually at the origin of this interest, fed by the competition to spatial exploration started with the Mercury, Gemini and Apollo programs. Objects entering a planetary atmosphere, such as bluff bodies or even meteorites, are subjected to extremely high thermal and mechanical loads that must be accounted for; Mach numbers up to 36 were reached by the Apollo capsule and the Shuttle Orbiter touched a Mach number equal to 25 in its reentry. Nowadays, new vehicle concepts involving hypersonic flight are being developed. For instance, Virgin Galactic is designing commercial spacecraft and aims at providing suborbital touristic space flights, in addition to suborbital launches for scientific missions. The most famous prototype is the SpaceShipTwo, designed to fly in the lower termosphere after being released by the WhiteKnightTwo vehicle. The Lockheed Martin SR-72 is designed for intelligence and strategic reconnaissance and is expected to conduct a fly-test by 2023. The research scramjet experimental aircraft Boeing X-51 Waverider has completed two successful flight tests flying at Mach 6 and the X-43A was a single-use vehicle that was destroyed after a malfunctioning in 2001. The Synergetic Air Breathing Rocket Engine (SABRE) UK project is being developed for a hypersonic precooled hybrid air-breathing rocket engine, designed to achieve single-stage-to-orbit capabilities. Moreover, the French Experimental Maneuvering Vehicle (V-MaX) project aims at designing a hypersonic glider which travels at more than five times the speed of sound. We also mention the Hypersonic Technology Vehicle 2 (HTV-2), an experimental glide vehicle developed as part of the DARPA Falcon Project. To have an idea of the wide range of Reynolds and Mach numbers spanned by existing hypersonic vehicles, figure 1.1 published in [Urzay & Di Renzo \(2021\)](#) is a good summary of relevant flight trajectories. Of note, atmosphere reentry conditions, typical of Shuttle Orbiter and Apollo vehicles, are characterized

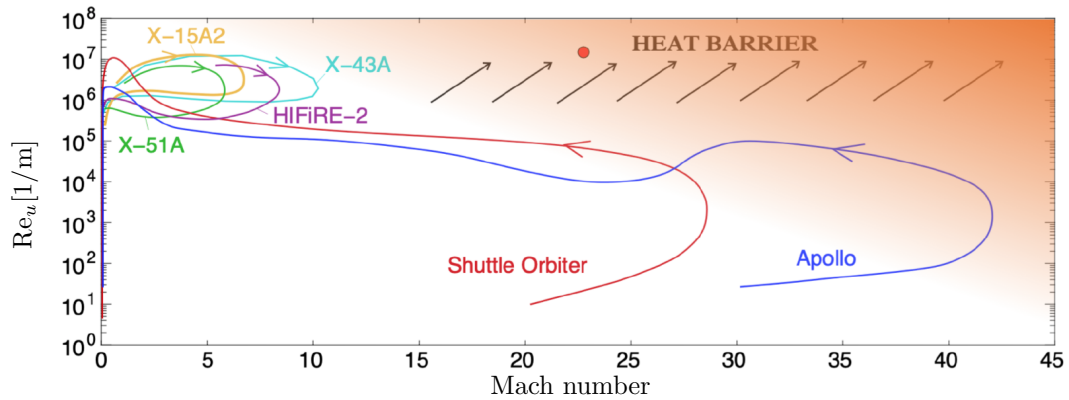


Figure 1.1: Flight trajectories of some hypersonic vehicles, from [Urzay & Di Renzo \(2021\)](#).

by high Mach numbers and low Reynolds numbers, whereas newer experimental hypersonic vehicles fly at lower Mach numbers and higher Reynolds numbers. As a consequence, additional research efforts are required to address the challenges raised in such flow regimes.

A conventional rule defines as “hypersonic” the aerodynamics regime in which the Mach number $M = \frac{u}{c}$ (with u the body velocity and c the speed of sound) is greater than 5. Nevertheless, the flow does not instantly turn from supersonic to hypersonic, but rather it progressively approaches a regime in which some physical aspects become increasingly important. Any vehicle flying at hypersonic speed generates a strong bow shock ahead of its leading edge, which causes abrupt changes in flow properties. The massive amount of flow kinetic energy in a hypersonic freestream is converted into internal energy as the gas crosses the shock wave and the temperature increases dramatically in the region between the bow shock and the vehicle’s surface, leading to molecular dissociation and vibrational nonequilibrium. An accurate knowledge of the flow conditions downstream of the shock is crucial to accurately design the Thermal Protection System (TPS) and to prevent excessive aerodynamic heating. In such a situation, erosion or ablation of the TPS, along with freestream disturbances, could induce a flow transition from a laminar to a turbulent regime, which represents a major concern in the design of flying vehicles. The thermal and mechanical loads increase even more after the breakdown to turbulence, reaching a more or less sharp peak in the transitional region. However, transition to turbulence and compressible turbulence at high-enthalpy conditions are two physical phenomena not well understood yet; the coupling between high-temperature effects and turbulent flows is an even more unexplored research area. The turbulent scenario is of major concern for both civilian and military vehicles flying at relatively low altitudes (associated to high Reynolds numbers because of the higher free-stream densities); an improved knowledge of such regime is of the utmost importance for enabling vehicles flying at increasingly higher velocities (hypersonic regime) and lower altitudes (turbulent regime).

1.1 High-temperature and high-speed gas dynamic

From an engineering point of view, a flying vehicle is fundamentally designed to tolerate certain loads. The prediction of such loads derives from experimental measurements or numerical simulations which provide macroscopic quantities needed for the choice of the body shape, weight or materials. Nonetheless, in the domain of aerothermodynamics, macroscopic properties are tightly related to the

microscopic nature of the gas. This is one of the main reasons why high-temperature flows are treated differently from classical flows (Candler, 2019). High-temperature effects have been often referred-to as real gas effects in the literature, but such a terminology is improper: a “real gas” is a gas in which intermolecular forces are important and must be accounted for. This is the case for high-pressure flows (or, more generally, for fluids operating in thermodynamic conditions close to their liquid/vapor critical point), for which it is necessary to use so-called real-gas equations of state to represent the gas behavior. For high-temperature flows, the intermolecular forces are relatively weak and the assumption of thermally perfect gas still holds. However, complex thermochemical effects are activated by the high temperatures at stake: chemical reactions and vibrational excitation phenomena may occur and give rise to nonequilibrium conditions. Such aspects are detailed in the following.

Let us consider a single molecule, for instance N_2 or O_2 . These molecules have different forms (or modes) of energy; they are free to translate, to rotate, and each of their atom can vibrate with respect to an equilibrium position. Additionally, electrons are in a continuous motion around any atom nucleus. The total energy is composed of the sum of these contributions and each energy mode is composed of a series of fixed (and quantized) energetic levels. Under normal conditions (temperatures lower than 800 K), the translational and rotational energetic levels are fully excited and prevail over the vibrational ones. At higher temperatures, the vibrational energy of the molecules becomes significant and modifies the gas properties. At this stage, all the energetic levels are sparsely populated, since the particles are distributed over all of them. A number of different ways exist for populating the available energetic levels; the most probable distribution is called a Boltzmann distribution (see Chapter 11 of Anderson, 2006). Statistical Mechanics is a powerful tool for connecting microscopic dynamics to macroscopic world, allowing one to retrieve the gas thermodynamic properties on the basis of simple considerations. Let us stress again that we are considering a single molecule for now. For a gas mixture with only translational and rotational modes fully activated (i.e., under 800 K), each species can be faithfully described by the equation of state of calorically perfect gases with a constant specific heat ratio γ . When vibrational energy is no longer negligible, the specific heats are functions of the temperature; in this range, the equation of state must therefore take into account the calorically imperfect behavior. Air in such conditions is a mixture of thermally-perfect and calorically-imperfect gases. If temperature is further increased beyond 2000 K, chemical processes are produced: O_2 starts to dissociate and is completely depleted at 4000 K when, in turn, the dissociation of N_2 begins. At the same time, the occurrence of recombination reactions give rise to nitric oxide production. At even higher temperatures (i.e., beyond 9000 K), most of the N_2 has dissociated and ionization processes occur. These physical processes are schematized in figure 1.2.

The aforementioned vibrational and chemical processes take place mainly by molecular collisions, which need a certain (finite) time to occur. If the characteristic time of such phenomena is comparable to the flow characteristic time (i.e., $\tau/\tau_{\text{flow}} \approx 1$), the flow is said to be in a state of chemical and/or thermal nonequilibrium. For $\tau/\tau_{\text{flow}} \ll 1$, chemical and vibrational rates (proportional to the inverse of the time scales) tend to infinity, which means that chemical and vibrational processes occur instantly with respect to the characteristic time of the fluid motion. The opposite situation occurs when the rates tend to zero and $\tau/\tau_{\text{flow}} \gg 1$, resulting in mixture compositions and vibrational energies that are “frozen” with respect to the fluid motion. Such an idealization is generally not verified in high-speed flows, especially when strong flow discontinuities are involved. Actually, the finite rate of change of vibrational energy of a gas depends on the difference between its equilibrium and nonequilibrium values. As for chemical nonequilibrium, the finite time rate of reactions depend on the local mixture density and temperature. Vibrational (or thermal) and chemical nonequi-

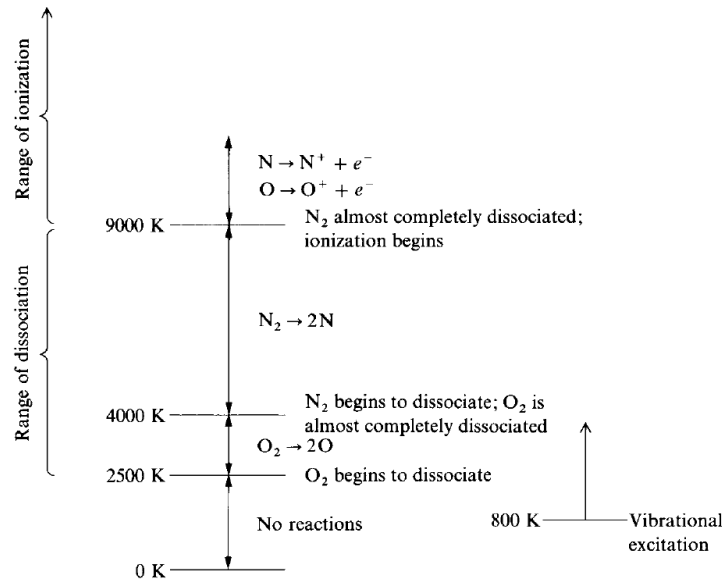


Figure 1.2: Sketch of thermochemical phenomena at increasing temperature, from [Anderson \(2006\)](#).

librium may occur separately: for instance, at lower altitudes (higher densities) molecular collisions become more frequent and vibrational relaxation times decrease consequently; at the same time, the temperature may be high enough to promote finite-rate chemistry. In the case of simultaneous thermochemical nonequilibrium, there is a tight coupling between thermal relaxation rates and chemical reaction rates; vibrationally-excited molecules are expected to dissociate faster, since they require less energy exchanges during the collisions; as a consequence, the vibrational levels of such molecules will depopulate easily.

1.2 Thermochemical models

Various models of vibrational relaxation phenomena exist, with different levels of approximation. The State-to-State (StS) and Multi-Temperature (MT) models represent the two most common strategies. In a StS approach, each vibrational level is modeled much like a separate species subjected to different processes. If we consider a 11-species mixture (five neutral species and the products of the ionization mechanism), the total number of “species” for such a modeling can easily jump to hundreds or even thousands; hence, following this strategy for multi-dimensional unsteady simulations rapidly becomes computationally infeasible. On the other hand, MT models assign a single temperature for translational and rotational modes, whereas the energetic levels of each molecule are supposed to follow a Boltzmann distribution described by its own characteristic temperature; then, the vibrational-translational energy exchange is described by the behavior of an harmonic oscillator. The coupling of relaxation and chemical phenomena is taken into account by the definition of i) an effective temperature which takes part in the reaction rates computation and ii) a source term modeling the vibrational energy variation due to chemical dissociation. Lastly, MT models can be further simplified by assuming that the vibrational levels of all the molecules are described by the same temperature, as in the classical two-temperature (2T) model of [Park \(1988\)](#). The difference between MT and 2T models can be very small in given ranges of thermodynamic conditions. It is the case for the current work: we

will show later that N_2 is essentially the only species promoting thermal nonequilibrium in turbulent flows; since the temperatures reached in the configurations here analyzed are way far from triggering substantial molecular nitrogen dissociation, the choice of a MT model would be unnecessary. Concerning the purely chemical mechanism, Park's 2T model takes into account a reaction mechanism which is nonlinear in species concentrations, composed of heavy-particle (if a neutral mixture is considered) impact dissociations and exchange reactions. The chemical production for a given species is given by the sum of all reaction producing or depleting the species (with positive and negative sign, respectively). There exist more sophisticated models to describe finite-rate chemistry; for instance, [Panesi *et al.* \(2013\)](#) have developed a method to improve the description of energy transfers and nitrogen dissociation. [Venturi *et al.* \(2020\)](#) compiled a database for all the elementary collisional processes in an oxygen mixture, by combining trajectory calculations, master equation and dimensionality reduction. It has been shown that certain deficiencies exist in classical and simpler approaches, which might fail mainly in the characterization of the dissociation processes. Apart from the implementation of suitable thermochemical models, additional considerations must be taken into account in a Computational Fluid Dynamics (CFD) code. It is straightforward to imagine that viscosity and thermal conductivity of the mixture could not be described by classical laws, since they have to include the varying chemical composition and, consequently, mass diffusion phenomena are also present due to species concentration gradients. Additionally, when simulating turbulent flows, the stringent time-step limitations dictated by turbulent flow timescales might become even stricter because of the chemical and thermal characteristic timescales, which could be the bottleneck for correctly capturing the entire flow dynamics.

1.3 State of the art

Significant advances have been made in the last years in the study of high-speed flows. Most detailed studies rely on CFD analyses, since carrying out physical experiments in the working conditions of interest is generally a costly or even infeasible task ([Bertin & Cummings, 2006](#)). To get insights into the hypersonic regime, hypervelocity wind tunnels have been designed to generate high-speed flows in their working section. Unfortunately, the power required to obtain the prescribed flow conditions is directly proportional to the flow density, velocity, stagnation enthalpy and cross-sectional area. Reproducing such severe conditions may cause overheating and result in structural damage; to avoid such problems, the test duration is often short. Moreover, instrumentation working efficiently at such extreme temperatures is also difficult to obtain. For all these reasons, the cost of carrying out experiments can be extremely high. However, there exist high-enthalpy ground-based facilities and in the following we mention some of them. The NASA Hypersonic Tunnel Facility (HTF) (see [figure 1.3 \(left\)](#)), originally designed to test nuclear thermal rocket nozzles, is capable of simulating flows up to Mach 7 at high enthalpy conditions. To simulate the effects of hypersonic conditions on TPS of reentry vehicles, the SCIROCCO and GHIBLI facilities of Plasma Wind Tunnel Complex at CIRA are able to reach Mach 12 and extremely high heat fluxes; the test chamber of SCIROCCO, in which the experimental measurements of pressure and temperatures are carried out, is shown in [figure 1.3 \(right\)](#). In France, the PHEDRA wind tunnel simulates plasma gases of nitrogen, air and methane and provide experimental database of planetary atmospheric conditions of Earth and Mars, and the ONERA F4 wind tunnel provides air flows at high enthalpy and pressure. The Plasmatron at Von Karman Institute is also a high enthalpy facility, which reaches temperatures up to 10000 K; hot gas from the test chamber exits through a 700 kW heat exchanger and a 1050 kW cooling system is

1.3. STATE OF THE ART



Figure 1.3: Direct connect configuration of the interior of HTF (left) and test chamber of SCIROCCO plasma wind tunnel, from Borrelli & Martucci (2011) (right).

used. To overcome the aforementioned problematic, a number of hypersonic wind tunnels work at low enthalpy cryogenic conditions. The Purdue Mach 6 quiet tunnel, built by the end of 90s, is designed to achieve laminar nozzle-wall boundary layers to study natural transition to turbulence in cryogenic conditions. The Sandia Hypersonic wind tunnel accelerates the flow up to Mach 5 for an air mixture, and Mach 14 for a nitrogen mixture and the stagnation temperature is of the order of ≈ 1400 K; this facility reproduces reentry vehicles or rockets flight conditions. A Mach number equal to 14 is reached by the AEDC Hypervelocity Wind Tunnel 9.

High-fidelity numerical simulations may be a powerful tool to supplement the available experimental data, especially results concerning turbulent flows which are generally scarce. One of the classical configurations to study turbulent compressible flows is the flat-plate boundary layer, which may be considered as a close-up view of a small region of a vehicle's fuselage. In the case of hypersonic conditions, boundary layer thickens more rapidly than at lower Mach number exerting a major displacement effect on the inviscid flow outside the layer. Furthermore, the large kinetic energy of the high-speed object, dissipated by friction within the boundary layer, leads to high temperature values in the near-wall region, thus being responsible of the strong aerodynamic heating typical of such flows.

Thermochemical effects caused by hypersonic conditions have been initially investigated in more or less simple configurations. In the 90s, a pronounced interest developed for stagnation-point flows, representative of what happens around bluff bodies reentering the atmosphere. Fay & Riddell (1958) showed the variation of the heat transfer depending on catalysis processes and concluded that a correlation formula is enough to correctly predict the heat transfer, since it is mainly unaffected by nonequilibrium. On the other hand, Armenise *et al.* (1996) found that the behavior of the wall in terms of participation to the chemical processes may influence the results and pointed out that nonequilibrium kinetics is of relevant importance, even when considering simple chemical and fluid dynamic models. Colonna *et al.* (2019) performed a direct comparison of macroscopic experimental data with the results obtained by the StS approach, proving the necessity of using accurate nonequilibrium models with respect to the MT approaches. One of the major drawback of the latter resides in the estimation of the stand-off distance, for which Park's model predicts a shock closer to the body in most of the cases. Bonelli *et al.* (2017a) performed a similar analysis focusing mostly on computational performances; in the study, driven by the impelling need of reducing computational costs (especially for

StS approaches), the authors compared the performances of a classical CPU code against a new GPU approach. These pioneering studies have paved the way for using more detailed and expensive kinetic models and represent a starting point for a suitable calibration of simplified models. For instance, [Liu *et al.* \(2015\)](#) showed that the excessive amount of equations deriving from the StS model can be easily decreased to a few equations through a reduced model which still accurately predicts the energy populations. Other more or less simple laminar configurations have been also investigated over the years, such as nozzles or double cones. [Colonna *et al.* \(1999\)](#) illustrated a non-Arrhenius behavior for nozzles expansion flows, whereas [Bonelli *et al.* \(2017b\)](#) showed a good agreement with experimental nozzles measurements, even with a MT model.

A particular effort has been dedicated to the study of laminar hypersonic boundary layers by means of linear and non-linear stability analyses; a few works have also investigated the initial stages of transition. Starting from the work of [Malik & Anderson \(1991\)](#) and [Perraud *et al.* \(1999\)](#), linear stability analysis of chemically out-of-equilibrium flows are compared with results obtained for equilibrium flows. Globally, the authors illustrate that the presence of chemical reactions tend to destabilize the second mode instability while stabilizing the first mode one, similarly to what happens in the presence of strongly cooled walls. [Hudson *et al.* \(1997\)](#) confirmed that chemical and thermochemical nonequilibrium states are destabilizing, albeit the presence of wall cooling prevented the authors to completely isolate the effect of the model's choice. The analysis of the influence of chemical models on linear stability prediction has been further investigated by [Franko *et al.* \(2010\)](#), who pointed out that more accurate kinetic processes lead to significant differences in the modes growth rate with respect to MT models. The same test case has been also considered by [Miró Miró *et al.* \(2018\)](#) to test the effect of diffusion phenomena; they concluded that the flow is most destabilized when mass diffusion is hundreds of times faster than viscous diffusion. Similar conclusions have been obtained by means of parabolized stability equations ([Johnson & Candler, 2005](#)). More recently, direct simulations have been performed by [Marxen *et al.* \(2013, 2014\)](#), who evaluated the maximum streamwise velocity disturbance caused by large- or weak-amplitude waves. They observed that dissociation reactions do not directly influence the growth of secondary perturbations; weakly nonlinear effects were also evaluated. [Stemmer *et al.* \(2017\)](#) and [Di Giovanni & Stemmer \(2018\)](#), instead, focused their attention on the disturbances development, and eventually induced transition in a hypersonic boundary layer with obstacles or distributed roughness. The nonlinear development of the instabilities and the generation of vortices downstream of the obstacle were shown to be particularly influenced by the assumptions in the chemical model. In the same context, [Lefieux *et al.* \(2021\)](#) studied the roughness-induced transition on a forebody flying at Mach 6, observing that crossflow-like vortices destabilize due to high-frequency secondary instabilities in the wake and promote breakdown to turbulence. Thorough analyses have been conducted by [Mortensen & Zhong \(2016\)](#) and [Miró Miró & Pinna \(2021\)](#) who took into account the effect of ablation on instability for thermochemical nonequilibrium flows. Other recent stability studies have illustrated the effects of nonequilibrium together with a parametric study on wall temperature ([Kline *et al.*, 2019](#); [Knisely & Zhong, 2019b](#)); particular attention was paid to the existence of supersonic modes. None of the preceding works has encompassed the spatial evolution of a boundary layer subject to a complete transition-to-turbulence process.

Wall-bounded turbulence has been carefully investigated over the years in channel flow configurations ([Modesti & Pirozzoli, 2016](#); [Sciacovelli *et al.*, 2017](#)) and flat-plate boundary layers. A handful of computations of turbulent boundary layer configurations have been carried out at low-enthalpy conditions and in the low-Mach regime. [Guarini *et al.* \(2000\)](#), [Gatski & Erlebacher \(2002\)](#) and [Pirozzoli *et al.* \(2004\)](#) performed Direct Numerical Simulations (DNS) of boundary layers subjected to freestream

Mach numbers around 2 and nearly adiabatic walls. The validity of classical relations used to report the variables in an incompressible scaling (Morkovin, 1962) has been highlighted and exhaustive databases up to moderate values of Reynolds numbers have been provided. The work of Pirozzoli & Bernardini (2011) reports a detailed documentation of higher-order statistical quantities and carries out an analysis of the turbulence structures as well. Hypersonic regime has been initially included in boundary layer studies by Duan *et al.* (2010b) and Franko & Lele (2013). The first authors adopted nominal freestream Mach numbers up to 8 and proved the robustness of Morkovin’s hypothesis even in hypersonic regimes, albeit the enhancement of compressibility effects due to the increasing Mach numbers. Franko & Lele performed a DNS of a nearly transitional boundary layer at Mach 6. This study represents a benchmark for all the works where turbulence is induced by means of suction-and-blowing methods, since it exhaustively reports the dynamics of the breakdown to turbulence in case of first-mode oblique, second-mode oblique and second-mode resonance breakdown. Additionally, mean and fluctuating quantities are also investigated in the small portion of turbulent domain. The wide range of Mach numbers spanned by the research group of Duan was extended by Lagha *et al.* (2011), who considered Mach numbers up to 20. Once again, comparison against incompressible data is possible when considering variable-density effect; even probability density functions of velocity divergence, which are significantly affected by the turbulent Mach number, can be scaled when variable density is accounted for. As for now, studies on compressible turbulence have pointed out analogies (and differences) with respect to classical incompressible works (Schlatter & Orlu, 2010). Things start to be trickier when considering the effect of wall-cooling. Duan *et al.* (2010a) performed the simulation of a turbulent boundary layer at Mach 5 and conducted a parametric study on wall temperature. The authors found that compressibility effects are enhanced by wall-cooling and turbulence structures appear being more coherent. The interest in wall-cooling is prominent, since it is closer to practical flight conditions than adiabatic assumption. Recently, Zhang *et al.* (2018) produced a thorough database of spatially-evolving boundary layers with flow conditions similar to the operational ones of hypervelocity wind tunnels. Some basic key points are illustrated: i) the transformation of Trettel & Larsson (2016) for the streamwise velocity provides a better agreement with respect to the one of Van Driest (1956) (albeit not being completely satisfactory in the logarithmic region); ii) Walz’s relation for mean velocity and mean temperature starts to fail at high heat transfer rates; the semilocal scaling still provides a good collapse for most of the fluctuating quantities; iii) the components of Reynolds stresses anisotropies change, as well as dilatational dissipation and pressure dilatation. Finally, Huang *et al.* (2020) produced a DNS database, with flow conditions similar to experimental data, used to conduct a priori and a posteriori studies for comparing the performances of different Reynolds–Averaged Navier–Stokes (RANS) models. Even fewer works focused on hypersonic conditions (with or without the effect of wall cooling) such that chemical reactions are triggered. The work of Martín & Candler (2001) illustrates that the endothermic nature of the reactions (described by a simplified reaction mechanism) drain energy from temperature fluctuations and conceived a model for temperature fluctuations to be used in the context of RANS or Large–Eddy Simulations (LES). Duan & Martín (2009) studied the effect of finite-rate chemistry, as well as turbulence/chemistry interaction, in a temporally-evolving boundary layer; the authors found that dissociation and recombination reactions are differently influenced by turbulent fluctuations, even if they did not address the spatial flow evolution. A comparative study between low- and high-enthalpy, reactive boundary layers can be found in the work of Duan & Martín (2011); they found that the two cases closely resemble, since removing the assumption of calorically perfect-gas is sufficient to extend the validity of incompressible transformations and Reynolds analogies. Once again, these conclusions were obtained for temporally-evolving boundary layers and with a

moderate chemical activity. Concurrently with the production of the present work, [Di Renzo & Urzay \(2021\)](#) have performed a DNS of a transitional hypersonic boundary layer at Mach 10 in suborbital flight conditions, taking into account chemical nonequilibrium and providing a thorough discussion on basic statistical quantities. The mutual influence of thermal nonequilibrium and turbulence behavior has never been investigated for confined turbulence, apart from a priori considerations by [Urzay & Di Renzo \(2021\)](#). On the other hand, it has been recently analyzed for unconfined configurations, such as decaying isotropic turbulence ([Neville *et al.*, 2014](#)) and shear flows configurations ([Neville *et al.*, 2015](#)). The former studied the effect of vibrational relaxation for isotropic turbulence; they concluded that vibrational nonequilibrium does not alter significantly the decay of turbulent kinetic energy but damps thermodynamic fluctuating quantities, whereas relaxation times are affected by the varying turbulent Mach number. The coupling of thermal nonequilibrium and turbulence decay is shown to depend on the initial degree of nonequilibrium and state of turbulence by [Khurshid & Donzis \(2019\)](#). More recently, [Zheng *et al.* \(2020\)](#) performed simulations of forced isotropic turbulence and assessed the influence of vibrational relaxation times and characteristic temperatures. The authors pointed out that there exists a link between energy transfer and compressibility effects; specifically, a transfer from translational to vibrational modes occurs most likely in compression regions and viceversa. Finally, [Fiévet *et al.* \(2019\)](#) investigated the link between vibrational nonequilibrium and turbulent mixing of two nitrogen streams, confirming that compressibility effects alter the modes' distribution of energy.

1.4 Motivation

It can be concluded from the previous section that a knowledge gap exists, concerning the two-way coupling of confined turbulence with both thermal and thermochemical nonequilibrium effects. Studies based on RANS or LES models for hypersonic flows may result inaccurate, since most of the underlying models have been calibrated for conditions far away from those of high-speed flows. Only a few DNS studies cover the coexistence of high-temperature effects within a turbulent regime. The contribution of the present thesis is therefore to investigate thermochemical effects in spatially-evolving, hypersonic boundary layers by means of high-fidelity numerical simulations, ensuring the resolution of the whole active range of temporal and spatial scales. Our aim is to provide a vast amount of accurate data that can give access to several instantaneous and statistical quantities, enabling in-depth analyses of compressibility effects, large-scale unsteadiness, flow topology or turbulence/thermochemistry interaction and allowing for the development of improved RANS or LES models.

To this purpose, we first focus on thermodynamic conditions widely employed in the past for stability studies of adiabatic boundary layers at freestream Mach number equal to 10, in order to investigate the effect of finite-rate chemistry uniquely. This work is viewed as an extension of a fundamental test case, only analyzed in the laminar and nearly transitional regimes so far ([Malik & Anderson, 1991](#); [Franko *et al.*, 2010](#); [Marxen *et al.*, 2014](#)). For such a configuration, we first investigate the transition mechanism including the latest stage of turbulent breakdown, and subsequently the interaction of chemical nonequilibrium phenomena with wall-bounded turbulence. A companion DNS based on frozen-flow chemistry is used to isolate the influence of finite-rate chemical reactions on turbulent flow properties. Afterwards, we perform a DNS of a wall-cooled flat plate boundary layer, subjected to post-shock conditions of a sharp wedge flying at Mach 20, leading to a thermochemical nonequilibrium state. For the first time to the authors' best knowledge, the behavior of turbulent boundary layers in presence of thermal nonequilibrium is investigated. In this more realistic configuration, the temperature peak is shifted away from the wall, matching the peak of turbulence production; the interaction

between high-temperature effects and turbulence is then expected to increase. Additionally, thermal nonequilibrium effects are shown to be significant. The present DNS study is meant to show up the interaction of such effects with turbulent motions.

1.5 Outline

The thesis is organized as follows. Chapter 2 describes the governing equations, the fluid modeling and the thermochemical formulation considered, as well as the numerical strategy adopted. A brief description of the numerical tool is also outlined. Some preliminary verifications of the numerical solver are provided in Chapter 3, starting from simple zero dimensional cases up to complete three-dimensional turbulent configurations. The results of the adiabatic boundary layer simulations are documented in Chapter 4, whereas Chapter 5 is dedicated to the configuration of the wall-cooled boundary layer. Conclusions and future works are drawn in Chapter 6.

Chapter 2

Governing equations and numerical methods

Contents

| | |
|---|-----------|
| 2.1 Governing equations | 38 |
| 2.1.1 Equation of state | 40 |
| 2.1.2 Thermochemical models | 42 |
| 2.1.3 Transport properties | 43 |
| 2.2 Numerical strategy | 48 |
| 2.2.1 Central numerical fluxes | 49 |
| 2.2.2 Numerical stabilization and shock capturing | 49 |
| 2.2.3 Time integration methods | 53 |
| 2.2.4 Numerical schemes used in this study | 53 |
| 2.3 Description of the CFD code | 53 |

In this chapter, the governing equations used to describe multicomponent thermochemical out-of-equilibrium flows are presented. Section 2.1 describes the conservation equations along with the underlying assumptions, whereas subsection 2.1.2 outlines the thermodynamic and the thermochemical models adopted. In 2.1.3, an overview of the transport properties is given, with specific details on mass diffusion phenomenon, present only in mixture of gases. The numerical strategy adopted is described in section 2.2 where the two methods used for stabilizing central approximations are presented; the time integration strategy is also detailed. A summary of the numerical strategies used in this work is reported in section 2.2.4. Finally, a brief description of the in-house CFD code is presented in section 2.3, along with the results of some scalability tests.

2.1 Governing equations

Flows under investigation in this work are governed by the compressible Navier–Stokes equations for multicomponent, chemically reacting and thermally relaxing gases (Gnoffo *et al.*, 1989). Species in a mixture are characterized by their mass fractions Y_n , $n \in [1, \text{NS}]$ with NS the total number of species.

2.1. GOVERNING EQUATIONS

By definition,

$$Y_n = \frac{\rho_n}{\rho}, \quad (2.1)$$

where ρ_n is the partial density of species n and ρ the total density of the gas, $\rho = \sum_{n=1}^{\text{NS}} \rho_n$. It is useful to introduce the concept of molar fraction

$$X_n = \frac{\mathcal{M}}{\mathcal{M}_n} Y_n, \quad (2.2)$$

which is the ratio of the number of moles of species n in a volume V to the total number of moles in the same volume; here, \mathcal{M}_n is the molecular weight of species n and \mathcal{M} is the mean molecular weight of the mixture. Hence, the governing equations, written in differential form, read:

$$\frac{\partial \rho}{\partial t} + \frac{\partial \rho u_j}{\partial x_j} = 0 \quad (2.3)$$

$$\frac{\partial \rho u_i}{\partial t} + \frac{\partial (\rho u_i u_j + p \delta_{ij})}{\partial x_j} = \frac{\partial \tau_{ij}}{\partial x_j} \quad (2.4)$$

$$\frac{\partial \rho E}{\partial t} + \frac{\partial [(\rho E + p) u_j]}{\partial x_j} = \frac{\partial (u_i \tau_{ij} - q_j - q_{Vj})}{\partial x_j} - \frac{\partial}{\partial x_j} \left(\sum_{n=1}^{\text{NS}} \rho_n u_{nj}^D h_n \right) \quad (2.5)$$

$$\frac{\partial \rho_n}{\partial t} + \frac{\partial (\rho_n u_j)}{\partial x_j} = - \frac{\partial \rho_n u_{nj}^D}{\partial x_j} + \dot{\omega}_n \quad (n = 1, \dots, \text{NS} - 1) \quad (2.6)$$

$$\frac{\partial \rho e_V}{\partial t} + \frac{\partial \rho e_V u_j}{\partial x_j} = \frac{\partial}{\partial x_j} \left(-q_{Vj} - \sum_{m=1}^{\text{NM}} \rho_m u_{mj}^D e_{Vm} \right) + \sum_{m=1}^{\text{NM}} (Q_{TVm} + \dot{\omega}_m e_{Vm}). \quad (2.7)$$

In the preceding equations, t is the time and x_j with $j \in [1, 3]$ a Cartesian coordinate system; u_i are the velocity vector components, p the pressure, δ_{ij} the Kronecker symbol and τ_{ij} the viscous stress tensor. In the total energy equation (2.5), $E = e + \frac{1}{2} u_i u_i$ represents the specific total energy (with e the mixture specific internal energy, including the contribution of chemical energy), q_j the heat flux, u_{nj}^D and h_n the n -th species diffusion velocity and specific enthalpy, respectively. The energy equation is formally identical to the one describing the conservation energy of single-species gas, apart from the last term in the right hand side, which is related to diffusion phenomena and will be detailed later. For temperature values lower than 9000 K, ionization and electronic processes can be neglected; air can be then modeled as a five-species mixture of N_2 , O_2 , NO , O and N ($\text{NS} = 5$, [Park, 1990](#)). It should be pointed out that, in order to respect the total mass conservation, one has

$$\sum_{n=1}^{\text{NS}} Y_n u_{nj}^D = 0 \quad \text{and} \quad \sum_{n=1}^{\text{NS}} \dot{\omega}_n = 0. \quad (2.8)$$

To numerically enforce mass conservation, we solve for the mixture density and $\text{NS}-1$ species conservation equations, the NS -th species being computed as $\rho_{\text{NS}} = \rho - \sum_{n=1}^{\text{NS}-1} \rho_n$. This species is chosen to be Nitrogen since it has the largest mass fraction throughout the computational domain. Lastly, equation (2.7) represents the total vibrational energy conservation, where e_V is the vibrational energy per unit of volume defined as

$$e_V = \sum_{m=1}^{\text{NM}} Y_m e_{Vm}, \quad (2.9)$$

2.1. GOVERNING EQUATIONS

with NM the number of molecular species and e_{Vm} the vibrational energy per unit of volume of m -th molecule; finally, q_{Vj} represents the vibrational heat flux.

In the n -th species conservation equation (2.6), we denote with $\dot{\omega}_n$ the mass rate of production of the species, indicating the production or depletion of a specific species in the mixture due to the reaction mechanism, modeled as in Park (1990). The approach adopted in this work for thermal nonequilibrium is Park's 2T model (Park, 1988), as already stated in Chapter 1. Such a model takes into account the energy exchange between the roto-translational and vibrational modes by means of the term $Q_{TV} = \sum_{m=1}^{NM} Q_{TVm}$, present in equation (2.7). The population of vibrational energy levels may also change due to dissociation and recombination processes; this variation is taken into account in the last term of (2.7), $\dot{\omega}_m e_{Vm}$.

The viscous stress tensor is modeled as:

$$\tau_{ij} = \mu \left(\frac{\partial u_i}{\partial x_j} + \frac{\partial u_j}{\partial x_i} \right) + \left(\beta - \frac{2}{3}\mu \right) \frac{\partial u_k}{\partial x_k} \delta_{ij}, \quad (2.10)$$

with μ the mixture dynamic viscosity and β the bulk viscosity, which is neglected according to Stokes' hypothesis; q_j and q_{Vj} are modeled by means of the Fourier law as

$$q_j = -\lambda \frac{\partial T}{\partial x_j} \quad \text{and} \quad q_{Vj} = -\lambda_V \frac{\partial T_V}{\partial x_j}, \quad (2.11)$$

where λ and λ_V are the mixture translational and vibrational thermal conductivities, respectively. The system has to be supplemented with an equation of state as well as constitutive relations for transport properties, diffusion velocity and expressions of the source terms $\dot{\omega}_n$ and Q_{TVm} .

2.1.1 Equation of state

Each species is assumed to behave as a perfect gas; Dalton's pressure mixing law leads then to the thermal equation of state:

$$p = \sum_{n=1}^{NS} p_n = T \sum_{n=1}^{NS} \rho_n R_n, \quad (2.12)$$

$R_n = \mathcal{R}/M_n$ being the gas constant and $\mathcal{R} = 8.314$ J/mol K the universal gas constant. The thermodynamic properties of high- T air species are computed considering the contributions of the translational, rotational and vibrational modes (named TRV formulation, Gnoffo *et al.*, 1989); specifically, the internal energy reads:

$$e = \sum_{n=1}^{NS} Y_n h_n - \frac{p}{\rho}, \quad \text{with} \quad h_n = h_{f,n}^0 + \int_{T_{\text{ref}}}^T (c_{p,n}^{\text{tr}} + c_{p,n}^{\text{rot}}) dT' + e_{Vn}. \quad (2.13)$$

Here, $h_{f,n}^0$ is the n -th species enthalpy of formation at the reference temperature ($T_{\text{ref}} = 298.15$ K), $c_{p,n}^{\text{tr}}$ and $c_{p,n}^{\text{rot}}$ the translational and rotational contributions to the isobaric heat capacity of the n -th species, computed as

$$c_{p,n}^{\text{tr}} = \frac{5}{2} R_n \quad \text{and} \quad c_{p,n}^{\text{rot}} = \begin{cases} R_n & \text{for diatomic species} \\ 0 & \text{for monoatomic species} \end{cases}, \quad (2.14)$$

2.1. GOVERNING EQUATIONS

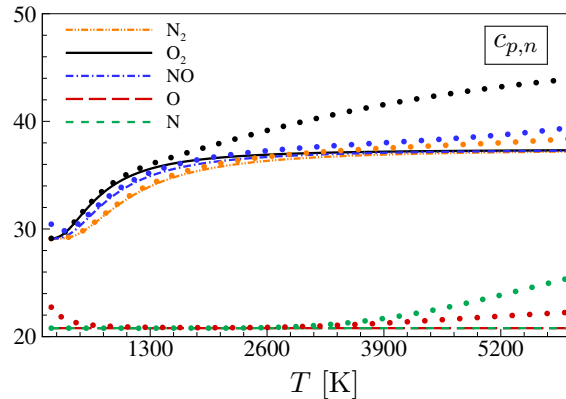


Figure 2.1: Evolution of specific isobaric heat capacities [J/(kgK)], for temperatures in the range [300, 5000] K. TRV formulation (lines) and 9-coefficients NASA polynomials (symbols).

Table 2.1: Properties of the species present in the mixture. Molecular weight \mathcal{M} , characteristic vibrational temperature θ_V , enthalpy of formation h^0 , critical temperature T_c and critical pressure p_c .

| | | N ₂ | O ₂ | NO | O | N |
|---------------|----------|----------------|----------------|-------|-------|-------|
| \mathcal{M} | [g/mol] | 28 | 32 | 30 | 16 | 14 |
| θ_V | [K] | 3393 | 2270 | 2739 | | |
| h^0 | [kJ/mol] | 0 | 0 | 91.27 | 249.2 | 472.7 |
| T_c | [K] | 126.2 | 154.8 | 180 | | |
| p_c | [MPa] | 3.39 | 5.08 | 6.48 | | |

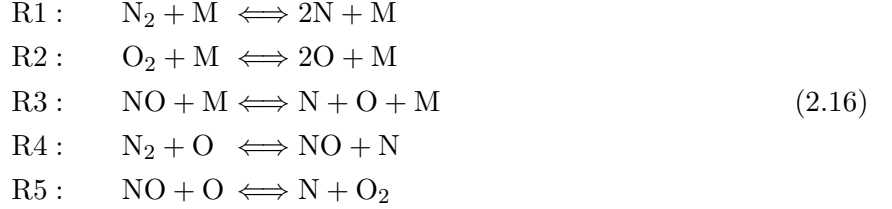
and e_{Vn} the vibrational energy of species n , given by

$$e_{Vn} = \frac{\theta_n R_n}{\exp(\theta_n/T_V) - 1}, \quad (2.15)$$

with θ_n the characteristic vibrational temperature of each molecule. The vibrational energy for atomic species is identically zero. Figure 2.1 shows the evolution of the specific isobaric heat capacities (sum of the three contributions), compared with the ones computed by means of the 9-coefficients NASA polynomials (Burcat *et al.*, 2005). The two models start to diverge significantly at high temperatures. In the following computations, the TRV formulation has been retained for consistency between thermal equilibrium and nonequilibrium cases. After the numerical integration of the conservation equations, the static temperature is computed from the specific internal energy (without the vibrational contribution) directly, whereas the vibrational temperature by means of Newton–Raphson iterations. General properties of the five species present in the mixture are reported in table 2.1.

2.1.2 Thermochemical models

The five species interact with each other through a reaction mechanism consisting of five reversible chemical steps, according to Park's model (Park, 1990):



being M the third body (any of the five species considered). Dissociation and recombination processes are described by reactions R1, R2 and R3; whereas the shuffle reactions R4 and R5 represent rearrangement processes. The mass rate of production of the n -th species is governed by the law of mass action:

$$\dot{\omega}_n = \mathcal{M}_n \sum_{r=1}^{\text{NR}} (\nu''_{nr} - \nu'_{nr}) \times \left[k_{f,r} \prod_{n=1}^{\text{NS}} \left(\frac{\rho Y_n}{\mathcal{M}_n} \right)^{\nu'_{nr}} - k_{b,r} \prod_{n=1}^{\text{NS}} \left(\frac{\rho Y_n}{\mathcal{M}_n} \right)^{\nu''_{nr}} \right], \tag{2.17}$$

where ν'_{nr} and ν''_{nr} are the stoichiometric coefficients for reactants and products in the r -th reaction for the n -th species, respectively, and NR is the total number of reactions. Lastly, $k_{f,r}$ and $k_{b,r}$ denote the forward and backward reaction rates of reaction r , modeled by means of Arrhenius' law:

$$k_{f,r} = C_r T^{a_r} \exp(-T_{\text{act},r}/T_d) \quad \text{and} \quad k_{b,r} = k_{f,r}/K_{eq,r}. \tag{2.18}$$

Here, T_{act} is the activation temperature of the reaction r , whose values are reported in table 2.2, together with the values of the pre-exponential parameter C_r and of the exponent a_r . T_d is an average temperature which is equal to T in thermal equilibrium conditions. In the general case of thermochemical non-equilibrium, Park's 2T model considers a weighted average of the two temperatures (only for the dissociation reactions):

$$T_d = T^q T_V^{1-q}; \tag{2.19}$$

we select $q = 0.7$ according to Park (1993). In equation (2.18), $K_{eq,r}$ is the equilibrium constant of the r -th reaction, modeled by Park with a curve fit of the form

$$K_{eq,r} = \exp(A_{1r}/Z + A_{2r} + A_{3r} \log Z + A_{4r}Z + A_{5r}Z^2), \tag{2.20}$$

with $Z = \frac{10000}{T_d}$, and $A_{\bullet r}$ some constants given in table 2.2. In order to avoid too many operations involving exponential, the computations of the reaction rates are implemented in a logarithmic form. Finally, the vibrational-translational energy exchange is computed as:

$$Q_{\text{TV}} = \sum_{m=1}^{\text{NM}} Q_{\text{TV}m} = \sum_{m=1}^{\text{NM}} \rho_m \frac{e_{Vm}(T) - e_{Vm}(T_V)}{\tau_m}, \tag{2.21}$$

where τ_m is the corresponding relaxation time evaluated with the expression of Millikan & White (1963). Specifically, the relaxation time of the molecule m with respect to the species n reads

$$\tau_{mn}^{\text{MW}} = \frac{p}{p_{\text{atm}}} e^{(a_{mn}(T^{-1/3} - b_{mn}) - 18.42)}, \tag{2.22}$$

2.1. GOVERNING EQUATIONS

where p is the pressure in Pa, $p_{\text{atm}} = 101325$ Pa and a_{mn} and b_{mn} are coefficients reported in table 2.3. Since this expression tends to underestimate the experimental data at temperatures above 5000 K, a high-temperature correction was proposed by Park (1989):

$$\tau_{mn} = \tau_{mn}^{\text{MW}} + \tau_{mn}^c \quad \text{with} \quad \tau_{mn}^c = \sqrt{\frac{\Phi_{mn}}{\mathcal{M}_m \sigma}}. \quad (2.23)$$

Here, $\Phi_{mn} = \frac{\mathcal{M}_m \mathcal{M}_n}{\mathcal{M}_m + \mathcal{M}_n}$ and $\sigma = \sqrt{\frac{8\mathcal{R}}{T\pi} \frac{7.5 \times 10^{-12} \text{NA}}{T}}$, NA being the Avogadro's number. The mean value is then evaluated with a weighted harmonic average:

$$\tau_m = \sum_{n=1}^{\text{NS}} \frac{\rho_n}{\mathcal{M}_n} \sum_{n=1}^{\text{NS}} \frac{\tau_{mn}}{\rho_n / \mathcal{M}_n}. \quad (2.24)$$

2.1.3 Transport properties

2.1.3.1 Viscosity and thermal conductivity

Pure species' viscosity and thermal conductivities are computed using curve-fits by Blottner *et al.* (1971) and Eucken's relations (Hirschfelder & Curtiss, 1969):

$$\mu_n = 0.1 \exp[(A_n \ln T + B_n) \ln T + C_n], \quad \lambda_n = \mu_n \left(\frac{5}{2} c_{v,n}^{\text{tr}} + c_{v,n}^{\text{rot}} \right), \quad \lambda_{Vn} = \mu_n c_{v,n}^{\text{vib}}, \quad (2.25)$$

where A_n , B_n and C_n are fitted parameters reported in table 2.4. The evolution of these quantities in a given temperatures range is shown in figure 2.2. The corresponding mixture properties are evaluated by means of Wilke's mixing rules (Wilke, 1950):

$$\mu = \sum_{n=1}^{\text{NS}} \frac{X_n \mu_n}{\sum_{m=1}^{\text{NS}} X_m \phi_{nm}}, \quad \lambda = \sum_{n=1}^{\text{NS}} \frac{X_n \lambda_n}{\sum_{m=1}^{\text{NS}} X_m \phi_{nm}}, \quad \lambda_V = \sum_{n=1}^{\text{NS}} \frac{X_n \lambda_{Vn}}{\sum_{m=1}^{\text{NS}} X_m \phi_{nm}} \quad (2.26)$$

with

$$\phi_{nm} = \frac{1}{\sqrt{8}} \left(1 + \frac{\mathcal{M}_n}{\mathcal{M}_m} \right)^{-\frac{1}{2}} \left[1 + \left(\frac{\mu_n}{\mu_m} \right)^{-\frac{1}{2}} \left(\frac{\mathcal{M}_m}{\mathcal{M}_n} \right)^{\frac{1}{4}} \right]^2. \quad (2.27)$$

2.1.3.2 Molecular transport

In multicomponent gases, in addition to the physical processes of viscous diffusion and thermal conduction, the phenomenon of mass diffusion must be accounted for. When a system contains two or more components with variable concentrations, there is a natural tendency for mass to be transferred minimizing any concentration difference within the system. The mass diffusion flux of species n in the direction j depends on different driving forces. Specifically, mass can be transferred by the action of a pressure gradient, a temperature gradient, external forces or chemical potential differences. As a result, the species diffusion velocities \mathbf{u}_n^D are obtained by solving

$$\nabla X_n = \sum_{k=1}^{\text{NS}} \frac{X_n X_k}{D_{nk}} (\mathbf{u}_n^D - \mathbf{u}_k^D) + (Y_k - X_n) \frac{\nabla P}{P} + \frac{\rho}{p} \sum_{k=1}^{\text{NS}} Y_n Y_k (\mathbf{f}_n - \mathbf{f}_k), \quad (2.28)$$

2.1. GOVERNING EQUATIONS

Table 2.2: Parameters for the chemical model of Park (1990). Pre-exponential constant C , exponent a , activation temperature T_{act} and coefficients $A_{\bullet r}$ for computing the equilibrium constant K_{eq} .

| Reaction | C | a | T_{act} | A_1 | A_2 | A_3 | A_4 | A_5 |
|--|----------------------|------|------------------|-----------|-----------|-----------|------------|-----------|
| $\text{N}_2 + \text{N}_2 \rightleftharpoons 2\text{N} + \text{N}_2$ | 7.0×10^{21} | -1.6 | 113 200 | 1.476600 | 1.629100 | 1.215300 | -11.457000 | -0.009444 |
| $\text{N}_2 + \text{O}_2 \rightleftharpoons 2\text{N} + \text{O}_2$ | 7.0×10^{21} | -1.6 | 113 200 | 1.476600 | 1.629100 | 1.215300 | -11.457000 | -0.009444 |
| $\text{N}_2 + \text{NO} \rightleftharpoons 2\text{N} + \text{NO}$ | 7.0×10^{21} | -1.6 | 113 200 | 1.476600 | 1.629100 | 1.215300 | -11.457000 | -0.009444 |
| $\text{N}_2 + \text{O} \rightleftharpoons 2\text{N} + \text{O}$ | 3.0×10^{22} | -1.6 | 113 200 | 1.476600 | 1.629100 | 1.215300 | -11.457000 | -0.009444 |
| $\text{N}_2 + \text{N} \rightleftharpoons 2\text{N} + \text{N}$ | 3.0×10^{22} | -1.6 | 113 200 | 1.476600 | 1.629100 | 1.215300 | -11.457000 | -0.009444 |
| $\text{O}_2 + \text{N}_2 \rightleftharpoons 2\text{O} + \text{N}_2$ | 2.0×10^{21} | -1.5 | 59 500 | 0.509890 | 2.477300 | 1.713200 | -6.544100 | 0.029591 |
| $\text{O}_2 + \text{O}_2 \rightleftharpoons 2\text{O} + \text{O}_2$ | 2.0×10^{21} | -1.5 | 59 500 | 0.509890 | 2.477300 | 1.713200 | -6.544100 | 0.029591 |
| $\text{O}_2 + \text{NO} \rightleftharpoons 2\text{O} + \text{NO}$ | 2.0×10^{21} | -1.5 | 59 500 | 0.509890 | 2.477300 | 1.713200 | -6.544100 | 0.029591 |
| $\text{O}_2 + \text{O} \rightleftharpoons 2\text{O} + \text{O}$ | 1.0×10^{22} | -1.5 | 59 500 | 0.509890 | 2.477300 | 1.713200 | -6.544100 | 0.029591 |
| $\text{O}_2 + \text{N} \rightleftharpoons 2\text{O} + \text{N}$ | 1.0×10^{22} | -1.5 | 59 500 | 0.509890 | 2.477300 | 1.713200 | -6.544100 | 0.029591 |
| $\text{NO} + \text{N}_2 \rightleftharpoons \text{N} + \text{O} + \text{N}_2$ | 5.0×10^{15} | 0.0 | 75 500 | 0.507650 | 0.735750 | 0.480420 | -7.497900 | -0.016247 |
| $\text{NO} + \text{O}_2 \rightleftharpoons \text{N} + \text{O} + \text{O}_2$ | 5.0×10^{15} | 0.0 | 75 500 | 0.507650 | 0.735750 | 0.480420 | -7.497900 | -0.016247 |
| $\text{NO} + \text{NO} \rightleftharpoons \text{N} + \text{O} + \text{NO}$ | 5.0×10^{15} | 0.0 | 75 500 | 0.507650 | 0.735750 | 0.480420 | -7.497900 | -0.016247 |
| $\text{NO} + \text{O} \rightleftharpoons \text{N} + \text{O} + \text{O}$ | 1.0×10^{17} | 0.0 | 75 500 | 0.507650 | 0.735750 | 0.480420 | -7.497900 | -0.016247 |
| $\text{NO} + \text{N} \rightleftharpoons \text{N} + \text{O} + \text{N}$ | 1.0×10^{17} | 0.0 | 75 500 | 0.507650 | 0.735750 | 0.480420 | -7.497900 | -0.016247 |
| $\text{N}_2 + \text{O} \rightleftharpoons \text{NO} + \text{N}$ | 6.4×10^{17} | -1.0 | 38 400 | 0.969210 | 0.893290 | 0.735310 | -3.959600 | 0.006818 |
| $\text{NO} + \text{O} \rightleftharpoons \text{N} + \text{O}_2$ | 8.4×10^{12} | 0.0 | 19 400 | -0.002428 | -1.741500 | -1.233100 | -0.953650 | -0.045850 |

2.1. GOVERNING EQUATIONS

Table 2.3: Coefficients to compute the relaxation time τ_m as in equation (2.24), from Park (1993).

| | M | a | b |
|--------------------|----------------|------|--------|
| N ₂ – M | N ₂ | 221 | 0.0290 |
| | O ₂ | 229 | 0.0295 |
| | NO | 225 | 0.0293 |
| | O | 72.4 | 0.0150 |
| | N | 180 | 0.0262 |
| O ₂ – M | N ₂ | 134 | 0.0295 |
| | O ₂ | 138 | 0.0300 |
| | NO | 136 | 0.0298 |
| | O | 47.7 | 0.0590 |
| | N | 72.4 | 0.0150 |
| NO-M | N ₂ | 49.5 | 0.0420 |
| | O ₂ | 49.5 | 0.0420 |
| | NO | 49.5 | 0.0420 |
| | O | 49.5 | 0.0420 |
| | N | 49.5 | 0.0420 |

Table 2.4: Coefficients to compute pure species viscosity of equation (2.25), from Blottner *et al.* (1971).

| | A | B | C |
|----------------|-----------|------------|-------------|
| N ₂ | 0.0268142 | 0.3177838 | -11.3155513 |
| O ₂ | 0.0449290 | -0.0826158 | - 9.2019475 |
| NO | 0.0436378 | -0.0335511 | - 9.5767430 |
| O | 0.0203144 | 0.4294404 | -11.6021403 |
| N | 0.0115572 | 0.6031679 | -12.4327495 |

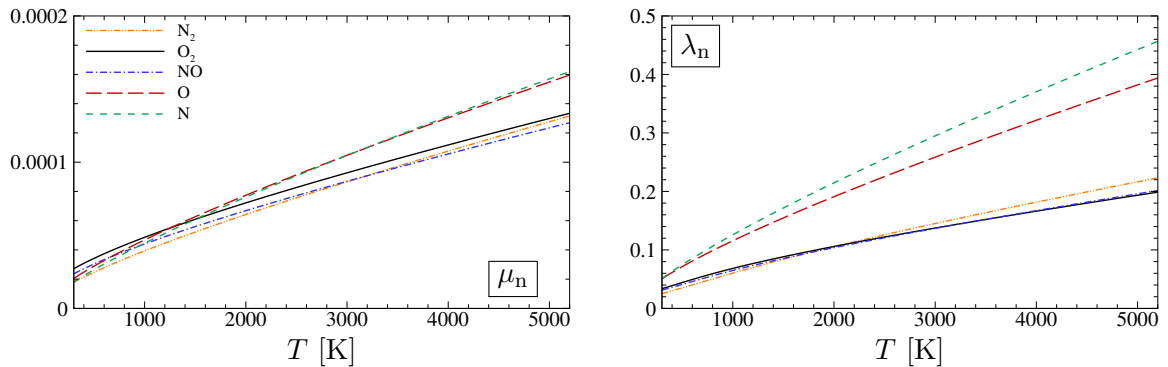


Figure 2.2: Evolution of specific viscosities [Pa s] and thermal conductivities [W/(mK)], for a given temperatures range, computed as in equation (2.25).

2.1. GOVERNING EQUATIONS

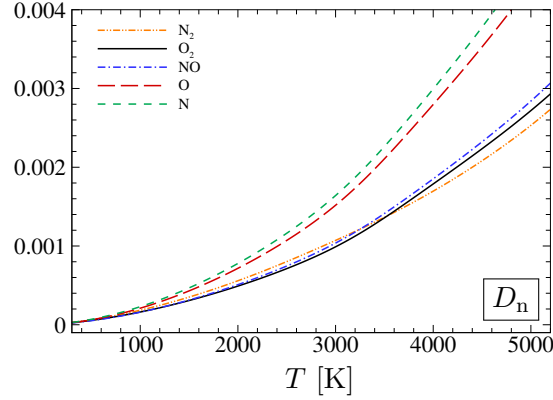


Figure 2.3: Evolution of equivalent diffusion coefficients [m^2/s], for a given temperatures range, computed as in equation (2.32).

where $D_{nk} = D_{kn}$ is the binary diffusion coefficient of species n into species k . Here, the diffusion of mass due to temperature gradients (usually referred-to as Soret effect) is neglected, being often orders of magnitude smaller compared to the effect of other driving forces. System (2.28), of size $\text{NS} \times \text{NS}$, should be solved in each spatial direction for each grid point and, for unsteady configurations, at each temporal instant. By neglecting volume forces and considering small pressure gradients, the diffusion velocities depend only on the species concentration gradients and on the mass diffusion coefficients. For a binary mixture composed of species 1 and 2, equation (2.28) reduces to

$$\nabla X_1 = \frac{X_1 X_2}{D_{12}} (\mathbf{u}_1^D - \mathbf{u}_2^D). \quad (2.29)$$

Knowing that $Y_1 + Y_2 = 0$ and $Y_1 \mathbf{u}_1^D + Y_2 \mathbf{u}_2^D = 0$ for the condition (2.8), equation (2.29) leads to

$$u_1^D Y_1 = -D_{12} \nabla Y_1, \quad (2.30)$$

known as Fick's law. The issue of the costly computation still holds since equation (2.30) is exact only for binary mixtures. To cope with these limitations, the approximation of Hirschfelder *et al.* (1954) is usually adopted, which reads:

$$u_{nj}^D X_n = -D_n \frac{\partial X_n}{\partial x_j} \quad \text{or} \quad u_{nj}^D \rho_n = -\rho D_n \frac{\partial Y_n}{\partial x_j}. \quad (2.31)$$

Specifically, D_n is an equivalent diffusion coefficient of species n into the mixture given by

$$D_n = \frac{1 - Y_n}{\sum_{\substack{m=1 \\ m \neq n}}^{\text{NS}} \frac{X_m}{D_{mn}}}, \quad \text{with} \quad D_{mn} = \frac{1}{p} \exp(A_{4,mn}) T^{[A_{1,mn}(\ln T)^2 + A_{2,mn} \ln T + A_{3,mn}]}. \quad (2.32)$$

Here, D_{mn} is the binary diffusion coefficient of species m into species n , and $A_{1,mn}, \dots, A_{4,mn}$ are curve-fitted coefficients computed as in Gupta *et al.* (1990); their values are reported in table 2.5. The evolution of the equivalent coefficients for a chemically-equilibrated mixture is shown in figure 2.3. In our calculations, the mass diffusion phenomenon is expressed by the sum of two terms, namely

$$\rho_n u_{nj}^D = -\rho D_n \frac{\partial Y_n}{\partial x_j} + \rho_n \sum_{n=1}^{\text{NS}} D_n \frac{\partial Y_n}{\partial x_j}, \quad (2.33)$$

2.1. GOVERNING EQUATIONS

Table 2.5: Constants for diffusion coefficient curve fits of equation (2.32), from Gupta *et al.* (1990). Of note, coefficient A_1 is identically zero.

| | A_2 | A_3 | A_4 |
|-------------|---------|--------|-----------|
| $N_2 - N_2$ | 0.0112 | 1.6182 | -11.30910 |
| $N_2 - O_2$ | 0.0465 | 0.9271 | - 8.11370 |
| $N_2 - NO$ | 0.0291 | 1.2676 | - 9.68780 |
| $N_2 - O$ | 0.0140 | 1.5824 | -10.88910 |
| $N_2 - N$ | 0.0195 | 1.4880 | -10.36540 |
| $O_2 - O_2$ | 0.0410 | 1.0023 | - 8.35970 |
| $O_2 - NO$ | 0.0438 | 0.9647 | - 8.23800 |
| $O_2 - O$ | 0.0226 | 1.3700 | - 9.66310 |
| $O_2 - N$ | 0.0169 | 1.4848 | -10.28100 |
| $NO - NO$ | 0.0364 | 1.1176 | - 8.96950 |
| $NO - O$ | 0.0179 | 1.4848 | -10.31550 |
| $NO - N$ | 0.0185 | 1.4882 | -10.33010 |
| $N - N$ | 0.0033 | 1.5572 | -11.16160 |
| $N - O$ | -0.0048 | 1.9195 | -11.92610 |
| $O - O$ | 0.0034 | 1.5572 | -11.17290 |

where the first term on the r.h.s. represents the effective diffusion velocity, and the second one is a mass correction term that should be taken into account in order to satisfy the continuity equation when dealing with non-constant species diffusion coefficients (Poinot & Veynante, 2005; Giovangigli, 1999). The coefficients D_n could also be related to the Lewis or Schmidt numbers

$$Le_n = \frac{\lambda}{\rho c_p D_n} \quad \text{and} \quad Sc_n = \frac{\mu}{\rho D_n}, \quad (2.34)$$

which represent the ratios of thermal diffusivity to mass diffusivity and of momentum diffusivity to mass diffusivity, respectively. These dimensionless numbers are also linked to the Prandtl number $Pr = (\mu c_p)/\lambda$, as $Le_n = \frac{Sc_n}{Pr_n}$. A stronger approximation can be made by considering a constant Sc or Le number for the mixture, which is equivalent to having a single diffusion coefficient D for all the species (i.e., $Le = \frac{\lambda}{\rho D}$). Unless otherwise specified, Hirschfelder's hypothesis will be adopted in this work.

To verify the numerical solver, single-species configurations of calorically-perfect gases will also be considered. In these cases, a constant specific heat ratio is considered ($\gamma = 1.4$), such that $c_p = \gamma R/(\gamma - 1)$. Since $NS = 1$ and there is no chemical activity, equation (2.6) is not solved and the diffusion velocity is identically zero. Furthermore, viscosity is computed by means of Sutherland's Law, $\mu(T) = CT^{3/2}/(T + S)$, with $C = 1.457933 \times 10^{-6} \text{ kg/m s K}^{1/2}$ and $S = 110.4 \text{ K}$, whereas the thermal conductivity follows a constant-Prandtl assumption ($Pr=0.72$), for which $\lambda = Pr/(\mu c_p)$.

2.2 Numerical strategy

The Navier-Stokes equations in system (2.3) can be cast in flux form:

$$\frac{\partial \mathbf{U}}{\partial t} + \frac{\partial(\mathbf{F} - \mathbf{F}_v)}{\partial x} + \frac{\partial(\mathbf{G} - \mathbf{G}_v)}{\partial y} + \frac{\partial(\mathbf{H} - \mathbf{H}_v)}{\partial z} = \mathbf{W}, \quad (2.35)$$

where $\mathbf{U} = [\rho, \rho u, \rho v, \rho w, \rho E, \rho_1, \rho_2, \dots, \rho e_V]^T$ is the state vector containing the conservative variables; \mathbf{F} , \mathbf{G} and \mathbf{H} are the inviscid fluxes along x , y and z directions, respectively, and \mathbf{F}_v , \mathbf{G}_v and \mathbf{H}_v are the viscous ones. The inviscid fluxes read:

$$\begin{aligned} \mathbf{F} &= [\rho u, \rho u^2 + p, \rho uv, \rho uw, (\rho E + p)u, \rho_1 u, \rho_2 u, \dots, \rho e_V u]^T, \\ \mathbf{G} &= [\rho v, \rho uv, \rho v^2 + p, \rho vw, (\rho E + p)v, \rho_1 v, \rho_2 v, \dots, \rho e_V v]^T, \\ \mathbf{H} &= [\rho w, \rho uw, \rho vw, \rho w^2 + p, (\rho E + p)w, \rho_1 w, \rho_2 w, \dots, \rho e_V w]^T, \end{aligned}$$

and the viscous ones:

$$\begin{aligned} \mathbf{F}_v &= \left[0, \tau_{xx}, \tau_{xy}, \tau_{xz}, u\tau_{xx} + v\tau_{xy} + w\tau_{xz} - q_x - \sum_n \rho_n u_n^D h_n, \rho_1 u_1^D, \rho_2 u_2^D, \dots, -q_{V,x} - \sum_m \rho_m u_m^D e_{Vm} \right]^T, \\ \mathbf{G}_v &= \left[0, \tau_{xy}, \tau_{yy}, \tau_{yz}, u\tau_{xy} + v\tau_{yy} + w\tau_{yz} - q_y - \sum_n \rho_n v_n^D h_n, \rho_1 v_1^D, \rho_2 v_2^D, \dots, -q_{V,y} - \sum_m \rho_m v_m^D e_{Vm} \right]^T, \\ \mathbf{H}_v &= \left[0, \tau_{xz}, \tau_{yz}, \tau_{zz}, u\tau_{xz} + v\tau_{yz} + w\tau_{zz} - q_z - \sum_n \rho_n w_n^D h_n, \rho_1 w_1^D, \rho_2 w_2^D, \dots, -q_{V,z} - \sum_m \rho_m w_m^D e_{Vm} \right]^T, \end{aligned}$$

with $n \in [1, \text{NS} - 1]$ and $m \in [1, \text{NM}]$. Finally, \mathbf{W} is the vector of the source terms:

$$\mathbf{W} = \left[0, 0, 0, 0, 0, \dot{\omega}_1, \dot{\omega}_2, \dots, \sum_m (Q_{\text{TV}m} + \dot{\omega}_m e_{Vm}) \right]^T.$$

For the sake of simplicity, we describe the numerical strategy for a 1D system; extension to multidimensional cases is straightforwardly carried out by applying the scheme in each direction. We consider the following 1D system of hyperbolic conservation laws:

$$\frac{\partial w}{\partial t} + \frac{\partial f(w)}{\partial x} = 0 \quad (2.36)$$

where w is the vector of conservative variables and $f(w)$ the flux function, such that $A = \partial f / \partial w$ is a diagonalizable matrix with real eigenvalues. Introducing the classical difference and cell-average operators over one cell:

$$(\delta \bullet)_j := (\bullet)_{j+\frac{1}{2}} - (\bullet)_{j-\frac{1}{2}}, \quad (\mu \bullet)_{j+\frac{1}{2}} := \frac{1}{2} [(\bullet)_{j+1} + (\bullet)_j] \quad (2.37)$$

and considering a regular Cartesian grid with constant mesh spacing δx (so that $x_j = j \delta x$), a conservative semi-discrete approximation of the spatial derivative writes:

$$\left(\frac{\partial w}{\partial t} \right)_j + \frac{(\delta \mathcal{F})_j}{\delta x} = 0 \quad (2.38)$$

2.2. NUMERICAL STRATEGY

The numerical flux at cell interface $j+\frac{1}{2}$, $\mathcal{F}_{j+\frac{1}{2}}$, is discretized by means of a centered scheme, written hereafter as \mathcal{H} :

$$\mathcal{F}_{j+\frac{1}{2}} = \mathcal{H}_{j+\frac{1}{2}} \quad (2.39)$$

For the discretization of the centered term \mathcal{H} , we will use high-order finite-difference numerical schemes, described in the following. Dissipation and dispersion errors of the discretization strategy may alter modes representation and may interact with not-well resolved scales. High-order schemes palliate these deficiencies, since they ensure low discretization errors. At the same time, the non-dissipative nature of centered numerical schemes lead to numerical instabilities due to the accumulation of aliasing errors resulting from the discretization process. As a result, numerical dissipation terms must be added to damp grid-to-grid oscillations. Finally, supersonic and hypersonic flows may exhibit flow discontinuities such as shocks, which cannot be handled by linear schemes. A suitable shock capturing term is then added. All the elements are described in the following.

2.2.1 Central numerical fluxes

The fluxes are approximated by means of centered finite difference schemes. For a scheme of order $2P + 3$ with a stencil of $2(P + 2) + 1$ points, the numerical flux is of the form:

$$\mathcal{H}_{j+\frac{1}{2}} = \left[\left(I - \sum_{p=0}^P a_p \delta^{2+2p} \right) \mu f \right]_{j+\frac{1}{2}}, \quad (2.40)$$

which gives a centered approximation of order $2N$ using $2N+1$ points in each direction. The coefficients a_p have alternate negative and positive signs as P increases. For the sake of clarity, we give hereafter the expressions of the schemes of order 3 to 9 (i.e. $P = 0, 1, 2$ and 3) of the preceding family:

$$\mathcal{H}_{j+\frac{1}{2}} = \left[\left(I - \frac{1}{6} \delta^2 \right) \mu f \right]_{j+\frac{1}{2}} \quad (\text{order 4}) \quad (2.41)$$

$$\mathcal{H}_{j+\frac{1}{2}} = \left[\left(I - \frac{1}{6} \delta^2 + \frac{1}{30} \delta^4 \right) \mu f \right]_{j+\frac{1}{2}} \quad (\text{order 6}) \quad (2.42)$$

$$\mathcal{H}_{j+\frac{1}{2}} = \left[\left(I - \frac{1}{6} \delta^2 + \frac{1}{30} \delta^4 - \frac{1}{140} \delta^6 \right) \mu f \right]_{j+\frac{1}{2}} \quad (\text{order 8}) \quad (2.43)$$

$$\mathcal{H}_{j+\frac{1}{2}} = \left[\left(I - \frac{1}{6} \delta^2 + \frac{1}{30} \delta^4 - \frac{1}{140} \delta^6 + \frac{1}{630} \delta^8 \right) \mu f \right]_{j+\frac{1}{2}} \quad (\text{order 10}) \quad (2.44)$$

In the following calculations, the tenth-order central schemes is used for inviscid fluxes.

2.2.2 Numerical stabilization and shock capturing

2.2.2.1 Adaptive nonlinear artificial dissipation (ANAD)

The purely centered numerical flux $\mathcal{H}_{j+\frac{1}{2}}$ is supplemented with a nonlinear adaptive artificial term (Kim & Lee, 2001). In this work, we choose to combine a ninth-order accurate dissipation of the form:

$$\mathcal{D}_{j+\frac{1}{2}} = \left[\frac{a_P}{2} |Q| \delta^{2P+3} w \right]_{j+\frac{1}{2}} \quad (2.45)$$

2.2. NUMERICAL STRATEGY

with a lower-order shock capturing term controlled by a highly selective shock sensor; here, Q is a dissipation matrix. Specifically, our ANAD numerical dissipation read:

$$\mathcal{D}_{j+\frac{1}{2}} = \rho(A)_{j+\frac{1}{2}} \left[\varepsilon_2 \delta w + (-1)^{(P+1)} \varepsilon_{2(P+2)} \delta^{(2P+3)} w \right]_{j+\frac{1}{2}} \quad (2.46)$$

with

$$\varepsilon_{2j+\frac{1}{2}} = k_2 \max(\varphi_j, \varphi_{j+1}), \quad \varepsilon_{2(P+2)j+\frac{1}{2}} = \max(0, k_{2(P+2)} - k_\varepsilon \varepsilon_{2j+\frac{1}{2}}), \quad (2.47)$$

where $\rho(A)$ is the spectral radius of the flux Jacobian matrix A , whereas k_2 and $k_{2(P+2)}$ are adjustable dissipation coefficients and k_ε is a constant equal to a_0/a_P , determining the threshold below which the higher-order dissipation is switched off. The dissipative flux in equation (2.46) is $(2P+1)^{\text{th}}$ -order accurate in smooth flow region and becomes 1st-order accurate close to flow discontinuities.

For schemes of order 3 to 9, this gives the following expressions:

$$\mathcal{D}_{j+\frac{1}{2}} = \rho(A)_{j+\frac{1}{2}} \left[\varepsilon_2 \delta w - \varepsilon_4 \delta^3 w \right]_{j+\frac{1}{2}} \quad \varepsilon_{4j+\frac{1}{2}} = \max(0, k_4 - \varepsilon_{2j+\frac{1}{2}}) \quad (2.48)$$

$$\mathcal{D}_{j+\frac{1}{2}} = \rho(A)_{j+\frac{1}{2}} \left[\varepsilon_2 \delta w + \varepsilon_6 \delta^5 w \right]_{j+\frac{1}{2}} \quad \varepsilon_{6j+\frac{1}{2}} = \max(0, k_6 - \frac{1}{5} \varepsilon_{2j+\frac{1}{2}}) \quad (2.49)$$

$$\mathcal{D}_{j+\frac{1}{2}} = \rho(A)_{j+\frac{1}{2}} \left[\varepsilon_2 \delta w - \varepsilon_8 \delta^7 w \right]_{j+\frac{1}{2}} \quad \varepsilon_{8j+\frac{1}{2}} = \max(0, k_8 - \frac{3}{70} \varepsilon_{2j+\frac{1}{2}}) \quad (2.50)$$

$$\mathcal{D}_{j+\frac{1}{2}} = \rho(A)_{j+\frac{1}{2}} \left[\varepsilon_2 \delta w + \varepsilon_{10} \delta^9 w \right]_{j+\frac{1}{2}} \quad \varepsilon_{10j+\frac{1}{2}} = \max(0, k_{10} - \frac{1}{105} \varepsilon_{2j+\frac{1}{2}}) \quad (2.51)$$

The activation of the low-order dissipation component rests on the value of the shock-capturing sensor φ_j , which consists in a combination of different terms. More precisely, the terms read:

$$\varphi_j = \underbrace{\frac{1}{2} \left[1 - \tanh \left(2.5 + 10 \frac{\delta x}{c} \nabla \cdot \mathbf{u} \right) \right]}_{\text{I}} \times \underbrace{\frac{(\nabla \cdot \mathbf{u})^2}{(\nabla \cdot \mathbf{u})^2 + |\nabla \times \mathbf{u}|^2 + \epsilon}}_{\text{II}} \times \underbrace{\left| \frac{p_{j+1} - 2p_j + p_{j-1}}{p_{j+1} + 2p_j + p_{j-1}} \right|}_{\text{III}} \quad (2.52)$$

The second and third terms denote the classical Ducros' (Ducros *et al.*, 1999) and Jameson's pressure-based (Jameson *et al.*, 1981) shock sensors, respectively, ϵ being a small positive value ($\epsilon = 10^{-16}$) to avoid division by zero. Their combination palliates to some of the deficiencies related to the stand-alone application of the Ducros' sensor, which takes into account only the relative magnitudes of dilation and vorticity and may result in unwanted activations of the shock-capturing term in regions where both of these two quantities are small (e.g., in the irrotational flow outside boundary layers or mixing layers). To correct this deficiency, the constant ϵ can be parametrized by introducing suitable characteristic velocity and length scales depending on the flow under investigation (Pirozzoli, 2011). The main drawback of this method resides in the loss of generality, ϵ being transformed in a configuration-dependent parameter. The introduction of the pressure-based sensor allows one to bypass the activation of Ducros' sensor, strongly reducing the amount of low-order dissipation injected and leaving the acoustic perturbations crossing the domain much less affected. The first term of equation (2.52) takes into account the Ducros' sensor modification of Bhagatwala & Lele (2009), initially proposed to enhance the selectivity of the artificial bulk viscosity in the Localized Artificial Diffusivity (LAD) technique. In regions of positive dilation φ_j is switched off, whereas its value increases slowly with the magnitude of the negative dilation. Moreover, the scaling factor $10\delta x/c$ has the twofold role of i) normalize the grid-dependent numerical dilation and ii) make it invariant with

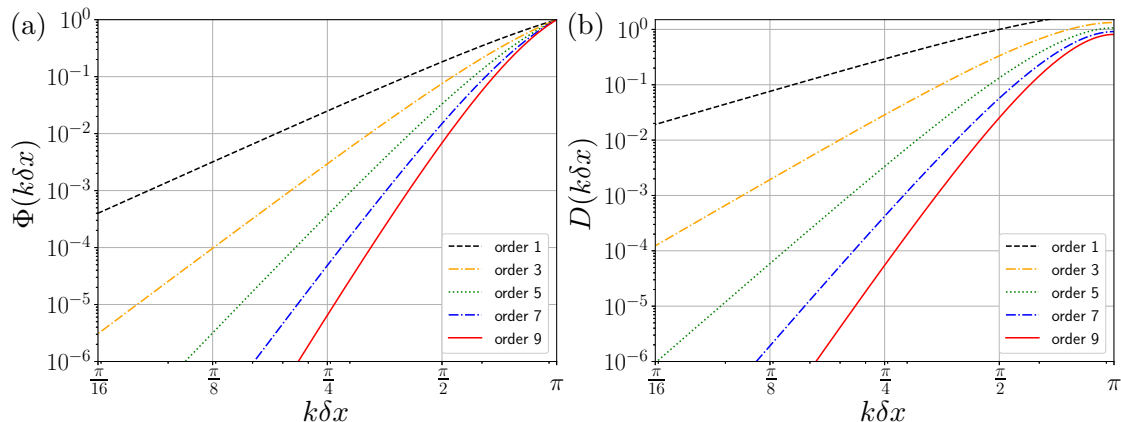


Figure 2.4: Dispersion and dissipation errors as a function of the reduced wavenumber $k\delta x$ up to of the ninth-order scheme. (a) dispersion error Φ , (b) dissipation error D .

the mesh-size. The sensor is $\mathcal{O}(1)$ in high-divergence regions and tends to zero in vortex-dominated regions, allowing the capture of flow discontinuities with minimal damping of the vortical structures inside the flow. In figure 2.4 we report the dissipation and phase errors of the ninth-order scheme for the approximation of a linear advection problem, as a function of the reduced wavenumber $k\delta x$. Lower-order schemes of the same family are also reported to illustrate the effect of increasing accuracy. For all schemes, the dispersion errors is exactly the same as for the standard central scheme of order $2(P+2)$. Thanks to its selectiveness in the wavenumber space, the ninth-order dissipation constitutes a suitable implicit subgrid regularization term for LES simulations (Gloerfelt & Cinnella, 2019), with the capability of seamlessly converging to DNS in smooth flow regions as the grid is refined. Further details of this numerical approach are reported in Sciacovelli *et al.* (2021). Note that, for the vibrational energy equation (2.7), the use of a pressure-based shock sensor could not damp spurious oscillations due to strong vibrational energy variations, since p and T_V are not directly linked through the equation of state. Consequently, an *ad hoc* sensor is built for equation (2.7), in which the pressure-based term is replaced by an analogous term built by means of the vibrational temperature (i.e., p is replaced by T_V).

2.2.2.2 High-order filtering and Localized Artificial Diffusivity

For two DNSs reported in section 4.2, an alternative strategy is used to avoid high-frequency oscillations. A selective centered (non-dispersive) filter is used to damp the grid-to-grid oscillations without altering low wavenumbers. More specifically, we use a tenth-order standard filter of the form:

$$f^{\text{filt}}(x_0) = f(x_0) - \sigma_d D_f(x_0) \quad \text{with} \quad D_f(x_0) = d_0 f(x_0) + \sum_{j=1}^N d_j [f(x_0 + j\Delta x) + f(x_0 - j\Delta x)] \quad (2.53)$$

where $0 < \sigma_d < 1$ is a coefficient used to adjust the filter strength. Furthermore, the scheme is supplemented with Localized Artificial Diffusivity (LAD), initially introduced by Cook & Cabot (2004). The method consists in adding artificial transport properties to smooth out discontinuities. The advantages of this method are its simple formulation, low computational cost with respect to an upwind scheme and ease of implementation. In the context of turbulent flows involving discontinuities,

2.2. NUMERICAL STRATEGY

this approach has been already adopted (Franko & Lele, 2013), even for multicomponent flows (Kawai *et al.*, 2010; Kawai & Terashima, 2010; Marxen *et al.*, 2014). Therefore, the transport coefficients read:

$$\mu = \mu_f + \mu^*, \quad \lambda = \lambda_f + \lambda^*, \quad \beta = \beta_f + \beta^*, \quad D_k = D_{f,k} + D_k^*,$$

where the subscript f and asterisks denote fluid and artificial transport coefficients, respectively. In the general form, the LAD coefficients can be written as:

$$\mu^* = C_{\mu\rho} \overline{\left| \sum_{l=1}^3 \frac{\partial^r S}{\partial \xi_l^r} \Delta_{l,\mu}^2 \right|}, \quad (2.54)$$

$$\lambda^* = C_{\lambda} \frac{\rho c}{T} \overline{\left| \sum_{l=1}^3 \frac{\partial^r e}{\partial \xi_l^r} \Delta_{l,\lambda}^2 \right|}, \quad (2.55)$$

$$\beta^* = C_{\beta\rho} f_{sw} \overline{\left| \sum_{l=1}^3 \frac{\partial^r \nabla \cdot \mathbf{u}}{\partial \xi_l^r} \Delta_{l,\beta}^2 \right|}, \quad (2.56)$$

$$D_k^* = C_{D,k} c \overline{\left| \sum_{l=1}^3 \frac{\partial^r Y_k}{\partial \xi_l^r} \Delta_{l,D_k}^2 \right|} + C_{Y_k} c \overline{(Y_k - 1)H(Y_k - 1) - Y_k(1 - H(Y_k))\Delta_{Y_k}}, \quad (2.57)$$

where C_{μ} , C_{λ} , C_{β} , $C_{D,k}$ and C_{Y_k} are dimensionless user-specified constants, c is the speed of sound and H is the Heaviside function. Here, S is the strain-rate tensor magnitude and f_{sw} a switching function, or shock sensor, designed to remove unnecessary artificial bulk viscosity in the region without shocks:

$$f_{sw} = \frac{H(-\nabla \cdot \mathbf{u})(\nabla \cdot \mathbf{u})^2}{(\nabla \cdot \mathbf{u})^2 + (\nabla \times \mathbf{u})^2 + \epsilon}, \quad (2.58)$$

where ϵ is a cutoff needed to prevent divisions by zero. In the present work, the integer r has been set equal to 4, resulting in computing the fourth-derivative of each function; the derivative has been evaluated by a fourth-order explicit scheme at interior points and a second-order scheme near boundary points. $\Delta_{l,\bullet}$ is the grid spacing, properly scaled:

$$\Delta_{l,\mu} = |\Delta_{xl}|, \quad \Delta_{l,\beta} = \left| \Delta_{xl} \frac{\nabla \rho}{|\nabla \rho|} \right|, \quad \Delta_{l,D_k} = \left| \Delta_{xl} \frac{\nabla Y_k}{|\nabla Y_k|} \right| \quad (2.59)$$

where Δ_{xl} is the local displacement vector along the grid line in the ξ_l direction. Finally, Δ_{Y_k} in equation 2.57 is defined by

$$\Delta_{Y_k} = \frac{\sum_{l=1}^3 \left| \frac{\partial^r Y_k}{\partial \xi_l^r} \right| \Delta_{l,D_k}}{\sqrt{\sum_{l=1}^3 \left(\frac{\partial^r Y_k}{\partial x_l^r} \right)^2 + \epsilon}}. \quad (2.60)$$

The over-bar in equations (2.54), (2.55), (2.56) and (2.57) denotes an approximated truncated Gaussian filter (Cook & Cabot, 2004), applied to remove the cusps introduced by the high-order derivative operators. In our calculations, only artificial bulk viscosity and thermal conductivity are introduced, whereas the artificial shear viscosity and mass diffusion coefficients were found not to be necessary.

2.3. DESCRIPTION OF THE CFD CODE

Table 2.6: Numerical schemes adopted in this work.

| | Flux discretization | Stabilization strategy |
|-----------|---|---|
| FD10ANAD9 | 10 th -order finite difference | 9 th -order adaptive non-linear artificial dissipation |
| FD10LAD | 10 th -order finite difference | 10 th -order standard filter + LAD |

2.2.3 Time integration methods

Time advancement is carried out by means of an explicit third-order TVD Runge–Kutta scheme (Gottlieb & Shu, 1998). Given the equation $\partial U/\partial t = F(U, t)$, the general form of a Runge–Kutta method with p sub-iterations reads:

$$U^{n+1} = U^n + \Delta t \sum_{i=1}^p b_i K^i \quad \text{with} \quad K^i = F \left(U^n + \sum_{j=1}^{i-1} a_{ij} K^j, t^n + c_i \Delta t \right) \quad (2.61)$$

where $c_i = \sum_{j=1}^{i-1} a_{ij}$ ($i \in \{1, \dots, p\}$). At the step $n + 1$, the solution is obtained as:

$$\begin{aligned} U^1 &= u^n + \Delta t F(U^n) \\ U^2 &= \frac{3}{4}U^n + \frac{1}{4}U^1 + \frac{1}{4}\Delta t F(U^1) \\ U^{n+1} &= \frac{1}{3}U^n + \frac{2}{3}U^2 + \frac{2}{3}\Delta t F(U^2). \end{aligned}$$

2.2.4 Numerical schemes used in this study

To summarize, as spatial discretization strategy, we will use two approaches in this work:

- Tenth-order accurate finite difference schemes supplemented with the adaptive non-linear artificial dissipation, ninth-order accurate; we will refer to this scheme as FD10ANAD9.
- Tenth-order accurate finite difference scheme with a selective tenth-order explicit standard filter and LAD technique used as shock-capturing; we will name this scheme FD10LAD.

The details of the schemes are reported in table 2.6; in all cases, the viscous fluxes are discretized with a fourth-order central scheme. As time integration method, a third-order Runge Kutta (RK3) scheme is adopted for all the calculations.

2.3 Description of the CFD code

The simulations have been carried out by means of an in-house code which solves the compressible, multicomponent Navier–Stokes equations under thermal and chemical non-equilibrium condition. It is entirely written in Fortran 2003 and makes extensive use of pre-processing flags and procedure pointers, to ensure a high modularity of the kernel while enabling fast computations at the same time. An important part of the work of this thesis was dedicated to the implementation of high-temperature models in our code, which was initially suited for multicomponent inert flows of real gases. Other numerical ingredients have also been added, as well as modifications and improvements for scope of optimization. The code can thus be considered as a collection of independent libraries containing

2.3. DESCRIPTION OF THE CFD CODE

Table 2.7: Strong scalability study. The grid size is $4608 \times 240 \times 300$ ($\approx 332 \times 10^6$ grid points). The absolute timing is given per iteration, averaging over 100 iterations. The points/core repartition highlighted in bold corresponds to the one selected for the weak scalability study.

| # cores | points / core | Absolute timing (s) | Speedup | Efficiency (%) |
|---------|--|---------------------|---------|----------------|
| 192 | $576 \times 60 \times 50$ | 21.295 | 1 | 100 |
| 384 | $288 \times 60 \times 50$ | 10.591 | 2.011 | 100.55 |
| 768 | $144 \times 60 \times 50$ | 5.2609 | 4.018 | 100.45 |
| 1536 | $72 \times 60 \times 50$ | 2.6813 | 7.946 | 99.33 |
| 3072 | $72 \times 60 \times 25$ | 1.3901 | 15.32 | 95.75 |
| 6144 | $72 \times 30 \times 25$ | 0.7193 | 29.60 | 92.52 |
| 12288 | $36 \times 30 \times 25$ | 0.3726 | 57.15 | 89.3 |

a number of procedures and variables related to its scope; these libraries are then used and glued together by the “kernel” at the beginning of the simulation. Each module is equipped with unit tests designed to check the results of the contained procedures; whereas the `kernel` integrates a series of non-regression tests to verify the backward compatibility of new code developments. All tests are performed by using “CTest”, a testing tool distributed as a part of “CMake” package.

The code is parallelized by using MPI libraries; since Cartesian domains are considered, efficient partitioning is obtained through domain decomposition by means of `MPI_CART`. Nonblocking directives are implemented in order to perform efficient halo communications, involving 3D slices of variable thickness (according to the stencil of the schemes chosen for derivative and filter). Lastly, `MPI_IO` routines are used for dumping parallel outputs of large datafiles, required for restart and advanced post-processing.

Scalability tests have been performed on French supercomputers thanks to the allocations granted by GENCI (Grand Equipement National de Calcul Intensif). The selected machine is Irene SKL partition of the French TGCC center. The SKL partition consists of 1 656 bi-processor nodes equipped with Intel Skylake 8168 @ 2.7 Ghz processors and 192 GB RAM DDR4/node, for a total of 79 488 cores (6.86 Pflop/s Peak Power). First, a strong scalability test is carried out on a configuration representative of the runs to be performed (namely, a turbulent boundary layer in chemical non-equilibrium) in terms of number of points, numerical strategy and boundary conditions. The study is performed by keeping constant the total grid size and continuously increasing the number of tasks. Due to the increasing communication cost with respect to the workload distributed per each task, a performance saturation must eventually occur. The grid size considered is $4608 \times 240 \times 300$ ($\approx 332 \times 10^6$ grid points); table 2.7 and figure 2.5 (left column) show the strong scalability results. It should be noted that the number of points in the streamwise direction (first index, which is memory-contiguous in Fortran) is usually larger with respect to the wall-normal and spanwise directions, in order not to interfere with the efficient loop vectorization. Very good performances are obtained, the loss of efficiency with respect to the ideal behaviour being very limited ($\approx 90\%$ efficiency for 12 288 cores). The baseline run uses 192 cores (4 nodes) for a total memory allocation of 2.5 GB RAM/core. A further halving of the cores would have exceeded the maximum available RAM memory per core. Note that it would have been possible to carry out a run with 96 cores by requesting a double amount of compute nodes together with 1 proc./node; nevertheless, the test was not performed as the available cache memory per task would be

2.3. DESCRIPTION OF THE CFD CODE

Table 2.8: Weak scalability study. The grid size per core is $72 \times 60 \times 25$ ($\approx 1 \times 10^5$ grid points per core). The absolute timing is given per iteration, averaging over 100 iterations.

| # cores | Total grid points | Absolute timing (s) | Efficiency (%) w.r.t. 1 node |
|---------|-------------------------------|---------------------|------------------------------|
| 1 | $72 \times 60 \times 25$ | 0.60566 | 217.42 |
| 2 | $144 \times 60 \times 25$ | 0.68038 | 193.54 |
| 6 | $144 \times 60 \times 75$ | 0.67539 | 194.97 |
| 12 | $288 \times 60 \times 75$ | 0.82822 | 158.99 |
| 24 | $288 \times 120 \times 75$ | 1.2884 | 102.20 |
| 48 | $576 \times 120 \times 75$ | 1.3168 | 100 |
| 96 | $576 \times 120 \times 150$ | 1.3579 | 96.973 |
| 192 | $576 \times 240 \times 150$ | 1.3657 | 96.419 |
| 384 | $1152 \times 240 \times 150$ | 1.3732 | 95.893 |
| 768 | $2304 \times 240 \times 150$ | 1.3737 | 95.858 |
| 1536 | $4608 \times 240 \times 150$ | 1.3843 | 95.124 |
| 3072 | $4608 \times 240 \times 300$ | 1.4012 | 94.057 |
| 6144 | $9216 \times 240 \times 300$ | 1.3929 | 94.537 |
| 12288 | $18432 \times 240 \times 300$ | 1.4098 | 93.390 |

doubled with respect to the general cases (48 tasks per node); hence it would not be representative of the actual performances achievable on the targeted architecture. A slightly super-linear scalability is shown for 384 and 768 cores, which can be explained by the different relative weight of the boundary conditions in longitudinal and vertical directions, which are non homogeneous (different equations are solved on a number of rows/lines corresponding to half of the molecule stencil). The spanwise direction remains homogeneous with periodic conditions. Next, a weak scalability test is carried out on the same system. The test consists in keeping constant the workload unit per core (i.e., the number of points) while increasing the number of cores (and the total grid size consequently). In order to select the minimal working unit per core, a minimal acceptable efficiency of 95 % for the strong scalability study was considered. According to this criterion, a $72 \times 60 \times 25$ points/core workload was chosen. Note that a larger minimal working unit would result in even better performances. Table 2.8 and figure 2.5 (right column) show the weak scalability results. Good performances are observed up to 12 288 cores, with efficiencies larger than 90%. Efficiency is normalized with respect to single-node performance (48 cores) in order to avoid cache-related effects: it is indeed worth noticing that much better performances are obtained when considering a number of tasks smaller than 48.

2.3. DESCRIPTION OF THE CFD CODE

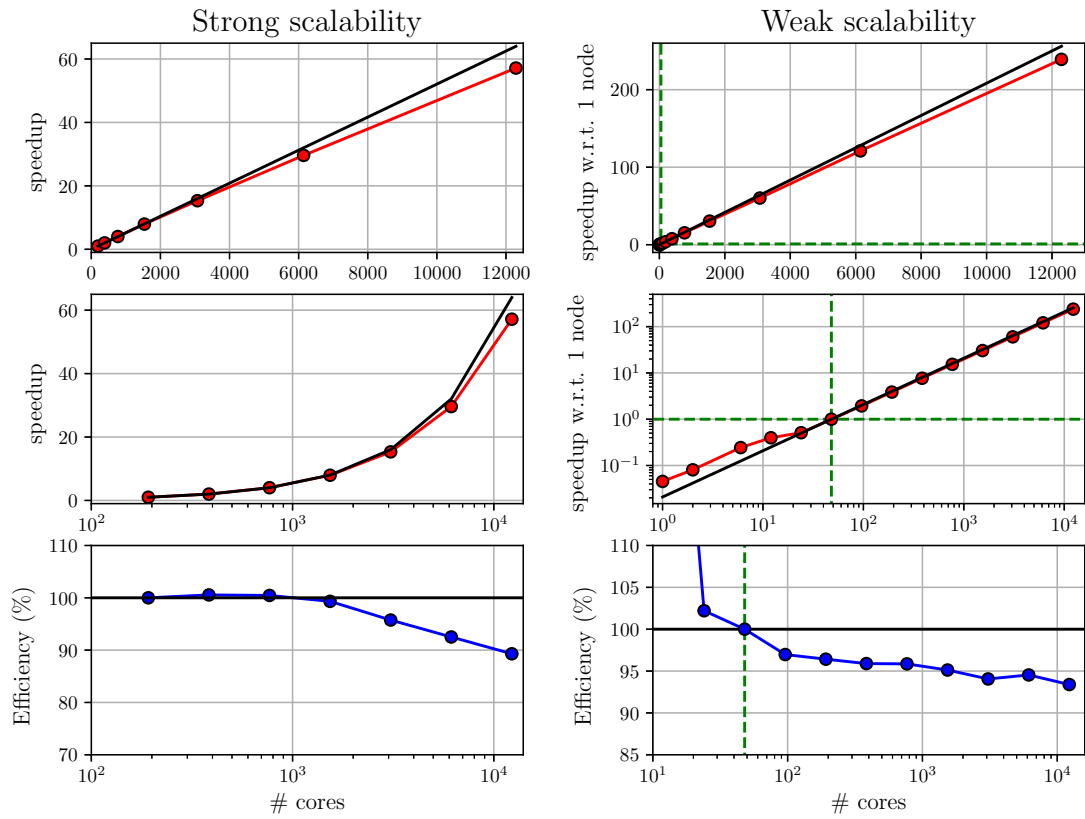


Figure 2.5: Strong (left column) and weak (right column) scalability tests. The x -axis represent the number of cores, in linear (first row) and logarithmic (second and third row) scales. The black lines denote the ideal behaviour. The dashed green lines in the right column refer to the baseline performance (1 node, 48 cores).

SUMMARY

The governing equations, the numerical strategy and the CFD code used in this work have been presented.

- Governing equations:
 - The considered flow is air modeled as a five-species mixture of thermally-perfect gases: N_2 , O_2 , NO , O and N .
 - Transport properties are modeled by means of Blottner, Ecken's correction and Hirschfelder's approximation.
 - Park's 2T approach is used as thermochemical non-equilibrium model.
- Numerical methods:
 - Centered fluxes approximated by means of high-order schemes.
 - Numerical stabilization performed by means of standard filtering + LAD technique or adaptive nonlinear dissipation.
 - RK3 as time integration method.
- CFD code:
 - Flexible and modular code.
 - Dedicated solver for compressible multicomponent and turbulent flows.
 - Implementation of high- T routines and analysis of MPI scalability.

Chapter 3

Numerical solver verification and assessment

Contents

| | |
|--|-----------|
| 3.1 Thermochemical equilibrium | 58 |
| 3.2 0D heath bath in thermal non-equilibrium | 59 |
| 3.3 Shock tube problems | 60 |
| 3.4 Viscous chemically-reacting shock tubes | 61 |
| 3.5 Laminar 2D boundary layer with high-temperature effects | 64 |
| 3.6 Perfect-gas turbulent boundary layers | 64 |

In this chapter, the different numerical ingredients of the solver are verified. The implementation of the thermochemical model is first assessed in sections 3.1 and 3.2. Well-known 1D shock tube configurations are analyzed in section 3.3 and a 2D viscous chemically-reacting shock tube is investigated in section 3.4. Lastly, the flat-plate boundary layer configuration is considered, starting from a laminar 2D setup under high-enthalpy conditions, up to a fully 3D supersonic perfect gas boundary layer in section 3.5 and 3.6, respectively. In the following test cases, both FD10ANAD9 and FD10LAD are used and compared. Part of the tests presented here are published in Sciacovelli *et al.* (2021). We have found that both schemes are accurate and provide a good agreement of the results, even if FD10ANAD9 is shown to be more robust; for certain test cases FD10LAD was not able to handle strong events such as the interplay of shock waves and wall. Moreover, a major drawback of FD10LAD is the introduction of the artificial bulk viscosity which causes additional time-step limitations; also, the computation of the transport artificial coefficients is computationally non-negligible. For these reasons, FD10ANAD9 has been sometimes preferred in main simulations of this work.

3.1 Thermochemical equilibrium

The validity of Park’s chemical model is first assessed by means of computations of air composition at chemical equilibrium. Specifically, we seek the steady-state solution of

$$\frac{dY_n}{dt} = \dot{\omega}_n. \tag{3.1}$$

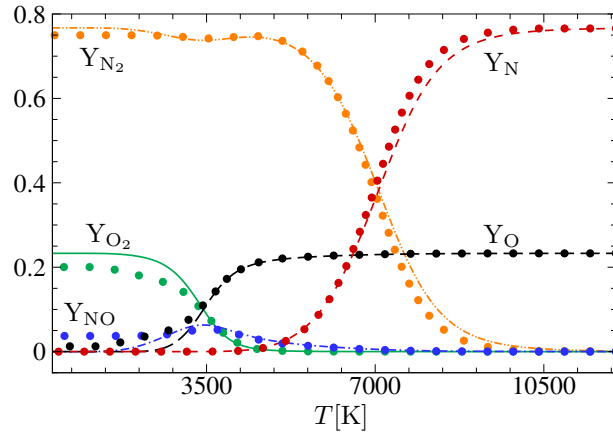


Figure 3.1: Mass fractions versus temperature at thermochemical equilibrium. Analytical method of Iannelli (2003) (lines) and Park's method (symbols), at $p = 101325$ Pa.

Time integration is executed by means of a fourth-order Runge–Kutta method and time advancement is performed until an equilibrium state is reached. The source terms $\dot{\omega}_n$ have been computed for a fixed pressure and for temperatures in the range $300 \text{ K} < T < 12000 \text{ K}$. At the same time, the method described by Iannelli (2003) has been considered, which consists in a two-equation procedure allowing to calculate exactly the thermodynamic properties for five-species chemically-reacting equilibrium air (see Appendix A for details). Figure 3.1 compares the results obtained with this analytical procedure and with Park's model. The two approaches match quite well for medium and high temperature values, whereas for low temperatures (below $\approx 2000 \text{ K}$), Park's model does not perfectly converge to the equilibrium composition. Indeed, chemical activity starts approximately at these temperatures at which the values of the equilibrium constants become stiff, giving rise to algorithm convergence problems. For this reason, the molecular oxygen mass fraction is slightly underestimated in this range. Nevertheless, in case of finite-rate chemistry considered in this work, such problematic is not encountered, since no steady solution must be reached. Lastly, for $T < 2000 \text{ K}$ chemical activity is essentially negligible.

3.2 0D heath bath in thermal non-equilibrium

The 2T model of Park (1988) is now validated by means of a zero-dimensional (0D) heath bath. Starting from an out-of-equilibrium system of a single-species mixture, the gas tends to an equilibrium point through the Vibrational-Translational (V-T) energy exchange. The validation is supported by comparison against literature (Casseau *et al.*, 2016). Figure 3.2 shows the timewise temperature distributions in a case of vibrational heating (left panel) and vibrational cooling (right panel) for a N_2 molecule. The initial pressure is equal to 1 atm for both cases; in the vibrational heating, the initial temperatures are $T^0 = 10000 \text{ K}$ and $T_V^0 = 1000 \text{ K}$ and the system reaches an equilibrium temperature of roughly 7625 K , whereas in the cooling configuration, with $T^0 = 3000 \text{ K}$ and $T_V^0 = 10000 \text{ K}$, the equilibrium temperature reached is $\approx 4972 \text{ K}$. The profiles, in excellent agreement with reference results, underline that return to equilibrium is achieved in physical times between 10^{-5} and 10^{-4} seconds.

3.3. SHOCK TUBE PROBLEMS

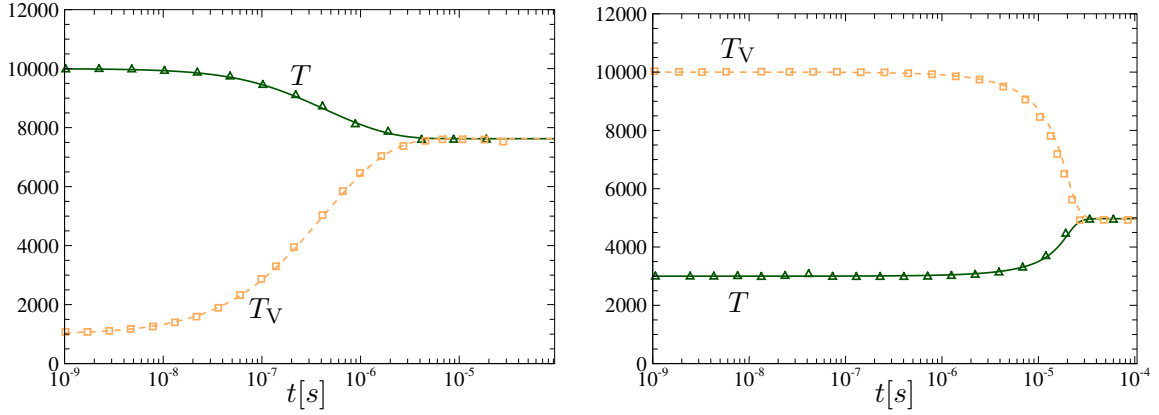


Figure 3.2: Virational-Translational relaxation towards equilibrium of N_2 heat bath. Left: vibrational heating: $T^0 = 10000$ K and $T_V^0 = 1000$ K. Right: vibrational cooling: $T^0 = 3000$ K and $T_V^0 = 10000$ K. Symbols from Casseau *et al.* (2016).

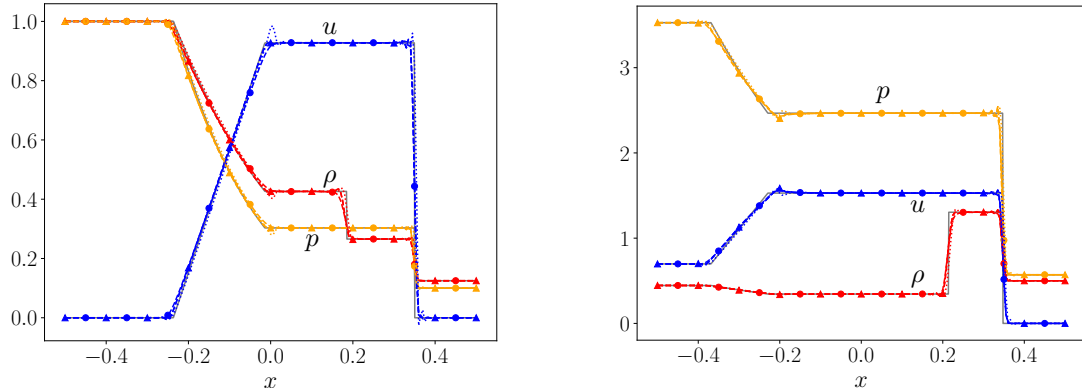


Figure 3.3: Reference and numerical solutions for Sod's (left) and Lax's (right) shock tubes. Dashed lines: FD10ANAD9, dotted lines: FD10LAD. Triangles: single species, circles: N_2 - O_2 mixture. The gray solid line denotes the reference solution.

3.3 Shock tube problems

This test case is a classical benchmark for the assessment of shock-capturing capabilities. Specifically, we consider the well-known Sod (1978) and Lax (1954) 1D shock tube problems, corresponding to the following Riemann problems:

$$(\rho, u, p)_{\text{SOD}} = \begin{cases} (1, 0, 1) & x < 0 \\ (0.125, 0, 0.1) & x \geq 0 \end{cases}; \quad (\rho, u, p)_{\text{LAX}} = \begin{cases} (0.445, 0.698, 3.528) & x < 0 \\ (0.5, 0, 0.571) & x \geq 0 \end{cases} \quad (3.2)$$

Numerical results are compared to the exact solutions at the nondimensional time $t^* = 0.2$ ($\Delta t^* = 5 \times 10^{-4}$) and $t^* = 0.13$ ($\Delta t^* = 10^{-3}$), respectively. The numerical domain is discretized with 200 evenly-spaced grid points; air is considered either as a single-species, calorically-perfect gas ($\gamma = 1.4$)

3.4. VISCOUS CHEMICALLY-REACTING SHOCK TUBES

or as a two-species mixture of Nitrogen ($Y_{\text{N}_2} = 79\%$) and Oxygen ($Y_{\text{O}_2} = 21\%$). Figure 3.3 shows the results for density, velocity and pressure, whose profiles are compared to the corresponding exact solutions. The scheme FD10ANAD9 is in good agreement for both cases; the single- and multi-species numerical solutions are perfectly superposed. The slight smearing of the numerical solution across the contact discontinuity can be attributed to the high-order dissipation term, the shock-capturing component being switched off in that region due to the constant value of the pressure. Note that a similar behavior is observed for other high-order schemes (Fu *et al.*, 2017). FD10LAD, plotted with dotted lines, exhibits some differences for Sod’s tube; small oscillations are visible in correspondence of the shock and at the beginning at the expansion fan, maybe due to a non-optimal calibration of tuning parameters.

Another inviscid 1D test case consists of a multi-species, high-temperature shock tube designed to study thermochemical effects (Grossman & Cinnella, 1990). At $t = 0$, the left (L) and right (R) initial conditions are the following:

$$P_L = 1.95256 \times 10^5 \text{ Pa}, \quad u_L = 0 \text{ m/s}, \quad T_L = 9000 \text{ K} \quad (3.3)$$

$$P_R = 10^4 \text{ Pa}, \quad u_R = 0 \text{ m/s}, \quad T_R = 300 \text{ K}, \quad (3.4)$$

and the initial values for the species mass fractions correspond to the mixture equilibrium composition at the given pressure and temperature for the right and left states, respectively. Due to the stiffness of the chemical source terms, the solution is advanced in time using a CFL number of 0.02 as suggested in Grossman & Cinnella (1990) for explicit Runge–Kutta time integrations; 800 grid points are for spatial discretization. The simulation is stopped when the shock-wave reaches the location $x = 0.110 \text{ m}$. Given the severe flow conditions developed in the present problem, the Bhagatwala & Lele’s modification of the shock sensor was turned off when using FD10ANAD9 for better numerical robustness. Results at the final time are shown in figure 3.4. The numerical schemes are able to capture correctly the rarefaction wave, the contact discontinuity and the shock; moreover, the distributions of the species mass fractions agree very well with data from Grossman & Cinnella (1990). Some oscillations are visible for FD10LAD in all the thermodynamic quantities in the vicinity of the shock.

3.4 Viscous chemically-reacting shock tubes

In order to prove the scheme’s ability to deal with strong unsteady discontinuities under reactive conditions, we also considered a two-dimensional chemically-reacting viscous shock tube. In such a configuration, a complex unsteady interaction is generated between the incident boundary layer and the shock wave reflected at the end wall. This case was first studied by Daru & Tenaud (2009), who performed numerical simulations for a perfect gas at different Reynolds numbers by means of a high-resolution monotonicity-preserving scheme. In the following, we only show results for FD10ANAD9 since FD10LAD was not able to handle such strong shock waves and their interaction with the wall. For the perfect-gas test case, the computational domain is a square shock tube with a unit side length and adiabatic walls at each boundary. The initial conditions for the perfect gas case read:

$$(\rho, u, v, p)_{\text{DARU}} = \begin{cases} \left(120, 0, 0, \frac{120}{\gamma} \right) & x < 0.5 \\ \left(1.2, 0, 0, \frac{1.2}{\gamma} \right) & x \geq 0.5 \end{cases} \quad (3.5)$$

with $\gamma = 1.4$. Three different resolutions are analysed, using respectively 2000, 4000 and 6000 grid points per direction. Reference data are given for $N = 4000$. Figure 3.5 shows the density distribution

3.4. VISCOUS CHEMICALLY-REACTING SHOCK TUBES

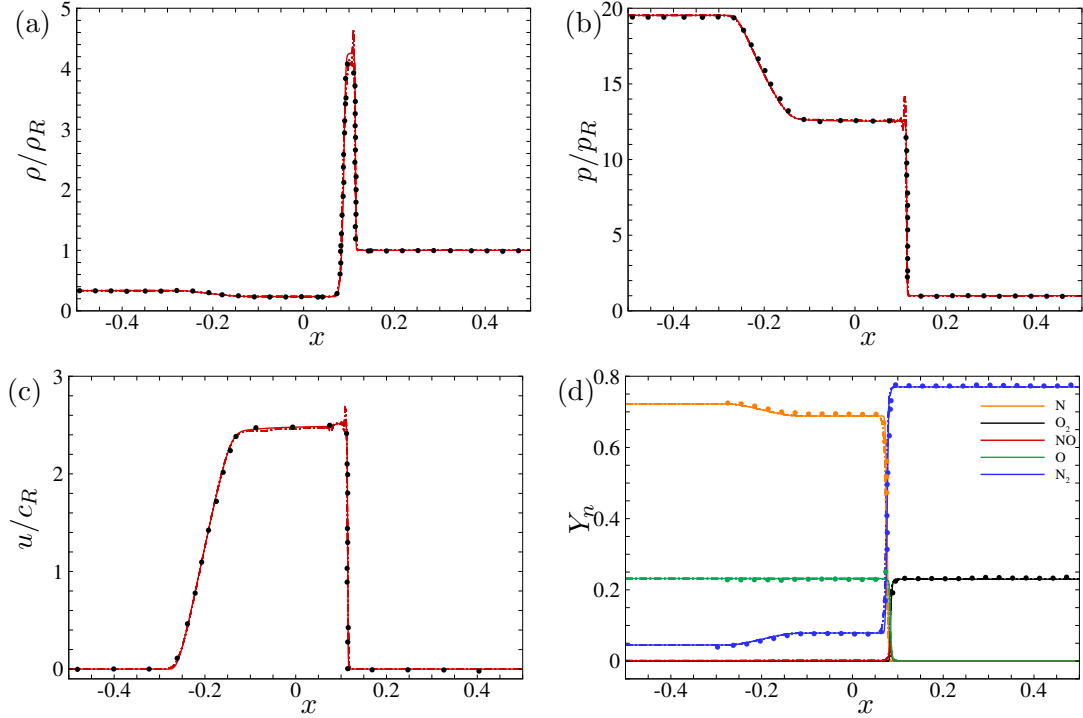


Figure 3.4: Profiles of density, pressure, velocity and mass fractions for the reacting shock tube case. Solid lines: FD10ANAD9; dash dot lines: FD10LAD; symbols: reference solution of Grossman & Cinnella (1990).

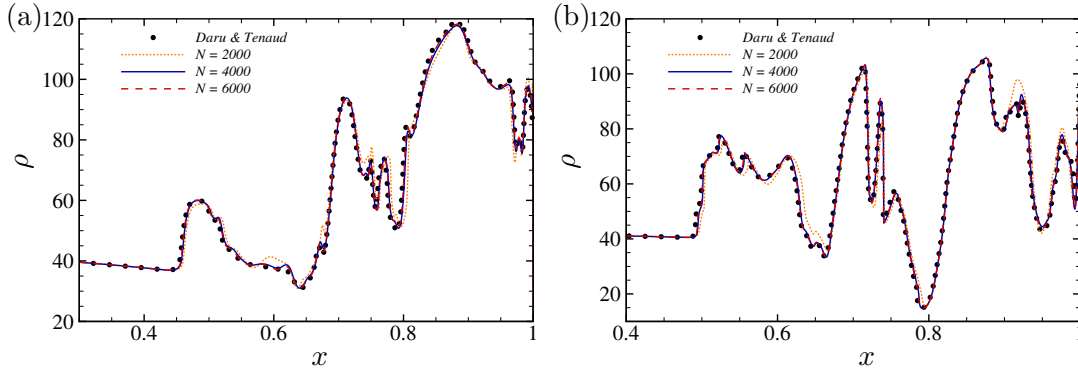


Figure 3.5: Results for the two-dimensional perfect-gas viscous shock tube, for $Re = 1000$ at $t = 1$. (a): density distribution along the bottom adiabatic wall ($y = 0$); (b): density distribution at $y = 0.05$.

along the bottom wall and at $y = 0.05$ for the case $Re = 1000$ at the final time ($t = 1$). Results are in excellent agreement with reference data and grid convergence is already obtained at $N = 4000$. Such a configuration was recently extended to chemical non-equilibrium conditions by Chen *et al.* (2019), who considered a relatively low initial temperature ($T_{\text{ref}} = 800$ K) in order to trigger only oxygen dissociation-recombination reactions and therefore simulate a simplified $\text{O}_2/\text{O}/\text{N}_2$ mixture. Here, we select $T_{\text{ref}} = 2000$ K such that NO production is enabled by means of the Zeldovich mechanism. The

3.4. VISCOUS CHEMICALLY-REACTING SHOCK TUBES

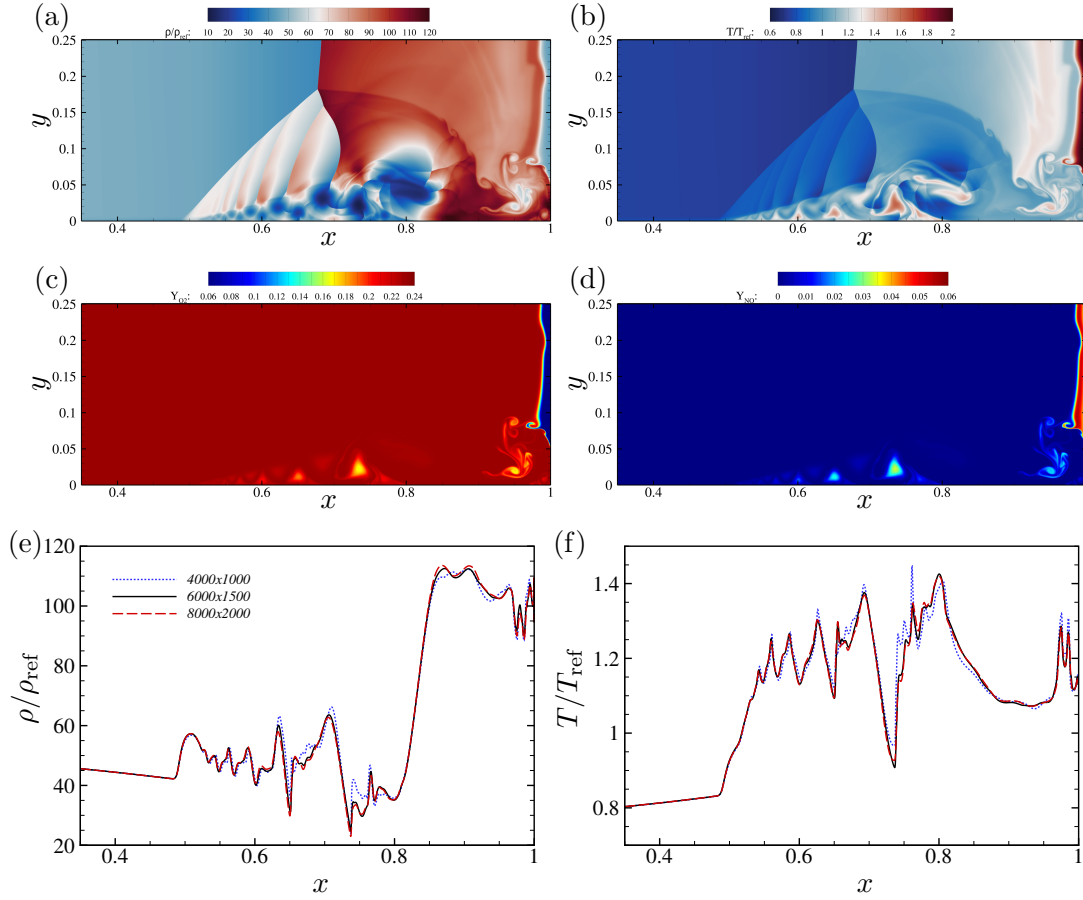


Figure 3.6: Results for the two-dimensional chemically-reacting viscous shock tube at $t = 1$ ms. Instantaneous visualizations of (a) normalized density, (b) normalized temperature, (c) O₂ mass fraction and (d) NO mass fraction. Panels (e) and (f) show the normalized density and temperature distributions, respectively, along the bottom adiabatic wall for the different computational grids considered.

left and right pressure values are 12 kPa and 0.12 kPa, respectively, and the initial mass fractions are $Y_{\text{N}_2} = 0.767$, $Y_{\text{O}_2} = 0.233$. The computational domain lengths are $L_x = 1$ m and $L_y = 0.25$ m; non-catalytic adiabatic walls are considered at the left, bottom and right boundaries, whereas purely non-reflective conditions are applied at the top end. Three computational grids are considered (4000×1000 , 6000×1250 and 8000×2000 , respectively). Results at the final time $t = 1$ ms are shown in figure 3.6. After the shock reflection on the end wall, a lambda-shock pattern is generated and extends into the bottom boundary layer, where a separation bubble entraining hot gases develops. Kelvin-Helmholtz instabilities are also observed along the slip line originating at the triple point; for a detailed description of the influence of high-temperature effects one might refer to the reference of [Chen *et al.* \(2019\)](#). The large temperature values ($T > 4000$ K) and small flow velocity near the end wall promote a strong chemical activity; almost all molecular oxygen dissociates and the nitric oxide amount is close to the equilibrium composition at the same p and T values. Figures 3.6(e)-(f) show density and temperature profiles along the bottom wall, where the footprints of the vortical structures contained inside the separation bubble are observed; grid-converged results are obtained starting from the 6000×1500

grid.

3.5 Laminar 2D boundary layer with high-temperature effects

The first step towards the simulation of a 3D turbulent boundary layer is generating a 2D laminar base flow. This allows to verify the correctness of the setup, boundary and initial conditions and to draw preliminary estimations on grid resolution and computational cost. Thus, the classical setup of a laminar two-dimensional boundary layer over a flat plate is presented. The domain is rectangular with even spacing in the streamwise (x) direction and with grid stretching in the direction normal to the wall (y). The initial condition is generated using the compressible similarity boundary layer solution for a frozen flow; at the inflow, the same profiles are imposed. As we will show later in chapter 4, we derived the solution of the similarity theory in presence of finite-rate chemistry, but we chose not to use it in this section to allow direct comparison with literature. The wall boundary conditions are no slip, adiabatic and non-catalytic. At the top and right boundaries the Local one-Dimensional Inviscid (LODI) relations are used (Poinsot & Lele, 1992). Both FD10ANAD9 and FD10LAD have been used; however, results are identical for such laminar flows without discontinuities and therefore we report only results obtained with FD10ANAD9.

The setup follow a well-known benchmark case used in the past for stability studies in chemical non-equilibrium conditions (Hudson *et al.*, 1997; Franko *et al.*, 2010; Miró Miró *et al.*, 2018); namely $M_\infty = 10$, a free-stream temperature of $T_\infty = 278$ K and a unit Reynolds number of $Re_u = 9.8425 \times 10^6$ m^{-1} . The free-stream composition is assumed to be $Y_{O_2} = 0.232918$ and $Y_{N_2} = 0.767082$. The computation has been performed with a constant Schmidt number equal to 0.5, in order to match the reference setup, and the results are compared at $x = 0.4$ m. Figure 3.7 shows the thermodynamic profiles for a frozen computation (left panel) and for a chemically out-of-equilibrium one (right panel). The agreement with Miró Miró *et al.* (2018) is quite satisfactory. On the other hand, slight differences are reported with respect to the results of Marxen *et al.* (2013) for the finite-rate chemistry case. Such deviations are mainly caused by the different set of transport properties and chemistry models provided by the MUTATION++ library (Magin & Degrez, 2004): the higher viscosity and thermal conductivity estimated by MUTATION++ lead to a thicker boundary layer, as explained by Franko *et al.* (2010) and also confirmed by our results. A second verification case has been considered, at the same free-stream Mach number and species composition, but at a larger temperature ($T_\infty = 350$ K). Such conditions can lead to temperatures of about 4500 K at the wall, triggering a much stronger chemical activity. Here, the unity Reynolds number is $Re_u = 6.6 \times 10^6$ m^{-1} as in Miró Miró *et al.* (2018). The results presented in figure 3.8 show the base-flow profiles at $x = 0.6$ m, for both frozen and chemically-reacting cases. Once again, the profiles match perfectly with the reference. The present base-flow has been selected as starting point for the full three-dimensional turbulent simulation, investigated in chapter 4.

3.6 Perfect-gas turbulent boundary layers

One of the most important aspects of turbulent flows simulations is injecting the correct (low) amount of dissipation while preserving the robustness of the scheme, especially near the boundaries. A compromise between the accurate representation of the wide range of temporal and spatial active scales and numerical stabilization has to be found, especially when considering the smallest flow scales for under-resolved configurations, in the context of Implicit Large Eddy Simulations (ILESs). For the latter, no subgrid-scale (SGS) model is directly added in the governing equations and the modeling

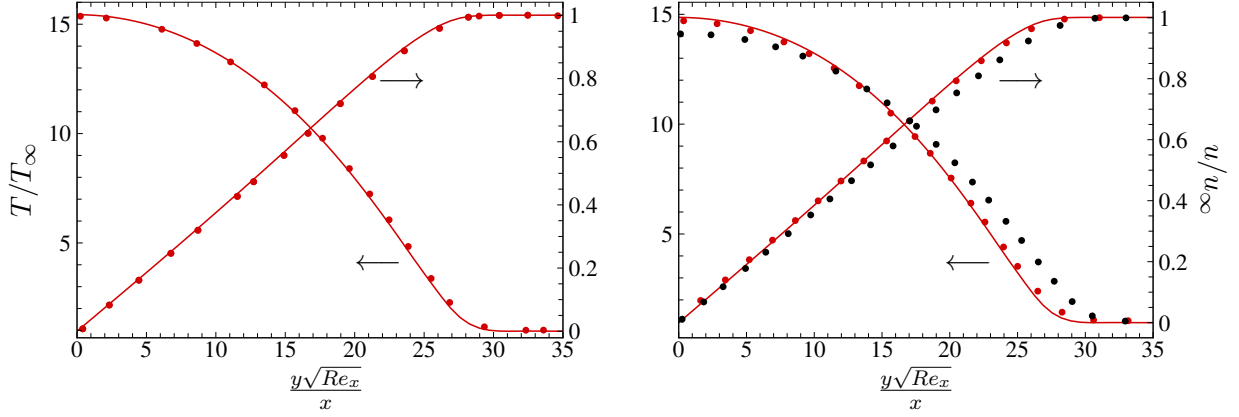


Figure 3.7: Normalized velocity and temperature profiles as a function of the similarity variable, for $T_\infty=278$ K, $Re_u=9.8425 \times 10^6$ m $^{-1}$ at $x=0.4$ m for frozen case (left panel) and chemically-reacting case (right panel). Reference solutions: Miró Miró *et al.* (2018) (●) and Marxen *et al.* (2013) (●).

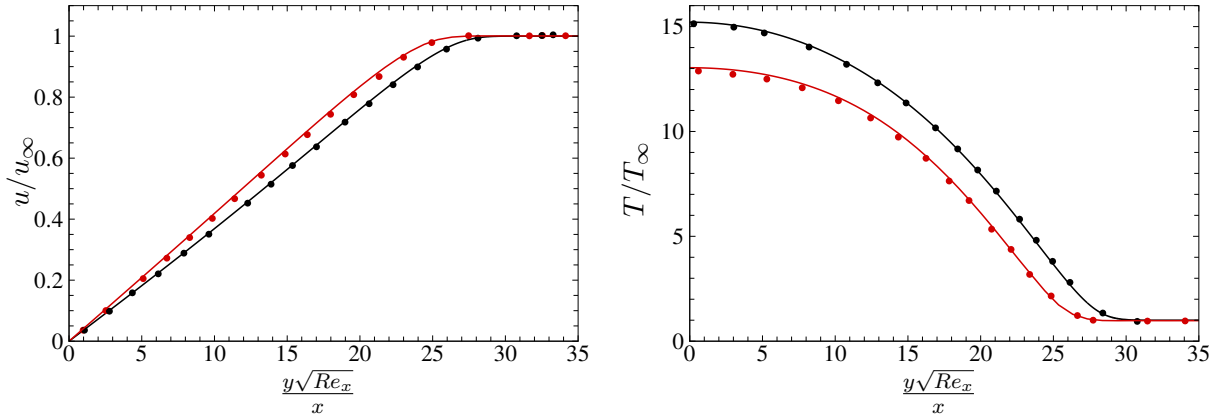


Figure 3.8: Normalized velocity (a) and temperature (b) profiles as a function of the similarity variable, for $T_\infty=350$ K and $Re_u=6.6 \times 10^6$ m $^{-1}$ at $x=0.6$ m for frozen case (black) and chemically-reacting case (red). Symbols from Miró Miró *et al.* (2018).

of small scales is left entirely to the property of the scheme. Consequently, this section investigates a compressible, calorically-perfect turbulent boundary layer, carrying out a grid-sensitivity analysis to compare results obtained by means of wall-resolved ILES-like grids with respect to reference DNS data. The sensitivity study has been performed with FD10ANAD9, since FD10LAD requires a higher computational cost due to time step limitations. Nevertheless, one numerical simulation has run with FD10LAD, in order to verify the validity of both schemes in the configuration of interest.

The flow conditions for such a configuration are similar to those investigated by several authors (Guarini *et al.*, 2000; Pirozzoli *et al.*, 2004, 2008; Pirozzoli & Bernardini, 2011; Wenzel *et al.*, 2018); specifically, a nominal Mach number equal to 2.25, a free-stream temperature of 65 K and a free-stream density of 0.13 kg/m 3 . The rectangular computational domain is discretized with even spacing in the streamwise (x) and spanwise (z) direction and grid stretching in the wall-normal (y) direction,

3.6. PERFECT-GAS TURBULENT BOUNDARY LAYERS

Table 3.1: List of the computational grids (and associated legend) selected for the supersonic boundary layer, along with the total number of grid points and resolutions in inner units. Δy_w^+ and Δy_δ^+ refer to the wall-normal resolutions at the wall and at the boundary layer edge, respectively. ILES-Ab corresponds to the simulation performed with FD10LAD.

| | Legend | N_{tot} | N_x | N_y | N_z | Δx^+ | Δy_w^+ | Δy_δ^+ | Δz^+ |
|---------|--------|--------------------|-------|-------|-------|--------------|----------------|---------------------|--------------|
| DNS | ○ | 1.23×10^9 | 8000 | 300 | 512 | 5.78 | 0.77 | 5.23 | 3.55 |
| ILES-A | --- | 3.07×10^8 | 4000 | 300 | 256 | 11.69 | 0.78 | 5.38 | 7.17 |
| ILES-B | --- | 1.54×10^8 | 4000 | 300 | 128 | 11.58 | 0.77 | 4.94 | 14.17 |
| ILES-C | --- | 7.68×10^7 | 2000 | 300 | 128 | 22.58 | 0.76 | 4.66 | 13.85 |
| ILES-D | --- | 1.92×10^7 | 1000 | 300 | 64 | 43.00 | 0.71 | 5.44 | 26.36 |
| ILES-Ab | --- | 3.07×10^8 | 4000 | 300 | 256 | 11.35 | 0.80 | 5.88 | 6.98 |

following the profile:

$$\frac{y(j)}{L_y} = (1 - \alpha) \left(\frac{j - 1}{N_y - 1} \right)^3 + \alpha \frac{j - 1}{N_y - 1} \quad (3.6)$$

where L_y and N_y denote the domain length and the number of grid points along y -direction, respectively; $j \in [1, N_y]$ and $\alpha=0.08$. The total extent of the domain is $L_x \times L_y \times L_z = 1600\delta_{in}^* \times 100\delta_{in}^* \times 20\pi\delta_{in}^*$, the initial boundary layer thickness δ_{in}^* being used as length scale. No-slip and isothermal boundary conditions at a temperature close to the laminar adiabatic value ($T_w = 120.18$ K) are applied at the wall, whereas characteristic-based conditions are used for the top and right boundaries and periodic conditions in the spanwise direction. A similarity profile is imposed as inlet condition at a distance x_0 from the leading edge, corresponding to $Re_{\delta^*} = 1700$. Transition to turbulence is triggered by means of a suction-and-blowing forcing method; this excitation technique consists in applying a time-and-space-dependent wall normal velocity disturbance of the form:

$$\frac{v_w}{u_\infty} = Af(x)g(z) [\cos(\omega t + \beta z) + \cos(\omega t - \beta z)] \quad (3.7)$$

where A , $\omega = \tilde{\omega}\delta_{in}^*/c_\infty$ and $\beta = \tilde{\beta}\delta_{in}^*$ represent the amplitude, non-dimensional pulsation and spanwise wave number, respectively. Here, the symbol $(\tilde{\bullet})$ denotes dimensional values and c_∞ is the free-stream speed of sound; $f(x)$ and $g(z)$ are two perturbation-modulation functions defined as in [Franko & Lele \(2013\)](#). The forcing strip is located near the inlet, at $Re_{\delta^*} = 2000$; the parameters prescribed for the current set of simulations are $A = 0.025$, $\omega = 0.12$ and $\beta = 0.2$. Of note, the spanwise extent of the domain has been selected in order to contain exactly two oblique waves. Statistics are computed by averaging both in time and in the periodic direction; their collection spans approximately two turnover times and starts after that the initial transient has been evacuated and a statistically-steady state is reached. The sampling time interval is constant and equal to $\Delta t = \Delta \tilde{t}c_\infty/\delta_{in}^* \approx 3.93 \times 10^{-3}$.

Five different computational grids have been considered for FD10ANAD9 and are listed in table 3.1; the last computation in the table uses the same grid as ILES-A, but the FD10LAD scheme has been used. A reference solution is generated by means of a well-resolved DNS and is compared to data obtained on coarser, ILES-like grids, built by progressively halving the total number of points in the streamwise and spanwise directions. On the contrary, the wall-normal grid point distribution is kept unaltered such that discrepancies with respect to DNS data can directly be attributed to excessively

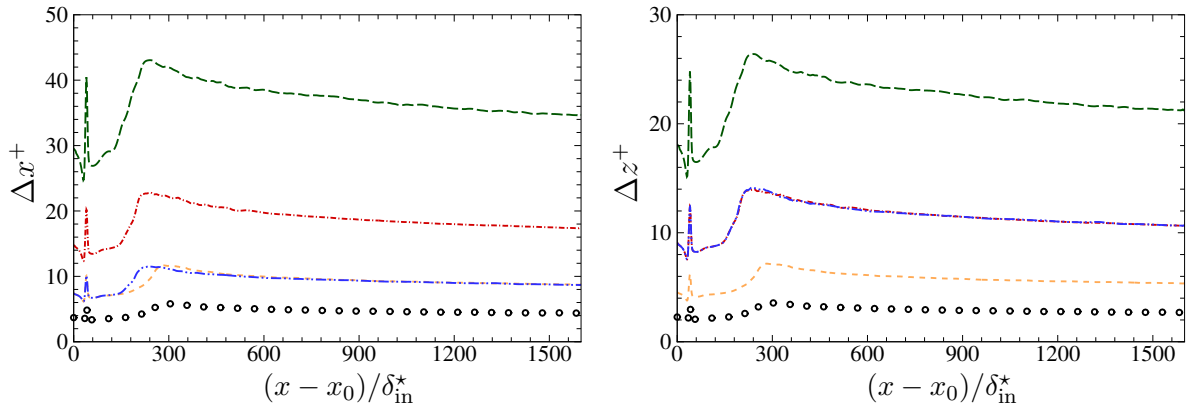


Figure 3.9: Resolutions of the computational grids along the streamwise direction in wall units for FD10ANAD9. Line legend as in table 3.1.

coarse discretizations in the other two directions. The least-refined grid has less than 20 million grid points; that is, it is 64 times coarser than the grid used for DNS, which counts more than 1.2 billion grid points. Note that the $(\bullet)^+$ quantities listed in table 3.1 have been evaluated at the point where the skin friction coefficient peaks, corresponding to the most stringent requirements in terms of resolution. The overall streamwise evolutions of Δx^+ and Δz^+ for the five computational meshes, reported in figure 3.9, clearly show that their values rapidly grow during transition and become approximately constant in the fully turbulent region. The influence of resolution can be appreciated from the lateral and frontal instantaneous views of the Q -criterion shown in figure 3.10 for all cases but ILES-C (not shown), which bears a strong resemblance with case ILES-B. DNS (panels a and e) and ILES-A (panels b and f) are almost indistinguishable; fine-scale structures are properly resolved and the streamwise development of the boundary layers is alike in terms of integral thicknesses. Some visual discrepancies start to appear for case ILES-B, in which both the transition region and the smallest features of the flow are shown to be more grainy. Lastly, the coarser grid of case ILES-D (panels d and h) results in excessive damping of the turbulent motions: hairpin-like structures are smeared out and the occurrence of coherent structures becomes much more sporadic.

The streamwise profile of the skin friction coefficient C_f is displayed in figure 3.11, along with a close-up in the fully-turbulent region of the same quantity as a function of the momentum-thickness-based Reynolds number Re_θ . DNS and ILES-A results are almost superposed both in the laminar-to-turbulent transition and fully-developed turbulent regions, confirming that grid resolutions of $\Delta x^+ < 15$ and $\Delta z^+ < 10$ are fine enough to capture the main flow features; slight deviations are found for ILES-Ab maybe due to a sudden increase of artificial properties at the skin friction peak. On the contrary, ILES-B and ILES-C cases present some discrepancies in the breakdown to turbulence, the C_f peak being slightly smaller and moved towards the domain inlet. A comparison with ILES-A underlines the importance of keeping $\Delta z^+ < 10$ for the spanwise resolution, whereas the influence of doubling the streamwise mesh size (from $\Delta x^+ \approx 11.5$ to $\Delta x^+ \approx 22.5$) is shown to be much less pronounced. Lastly, the ILES-D grid results in wrong predictions of both transitional and fully turbulent regions. Despite the much coarser resolutions with respect to the DNS, the fully-turbulent regions tend to match DNS predictions as Re_θ increases, mainly due to boundary-layer thickening. The C_f evolution is indeed in good agreement with values extracted from numerical simulations of similar configurations available in literature (Pirozzoli *et al.*, 2008; Pirozzoli & Bernardini, 2011; Wenzel

3.6. PERFECT-GAS TURBULENT BOUNDARY LAYERS

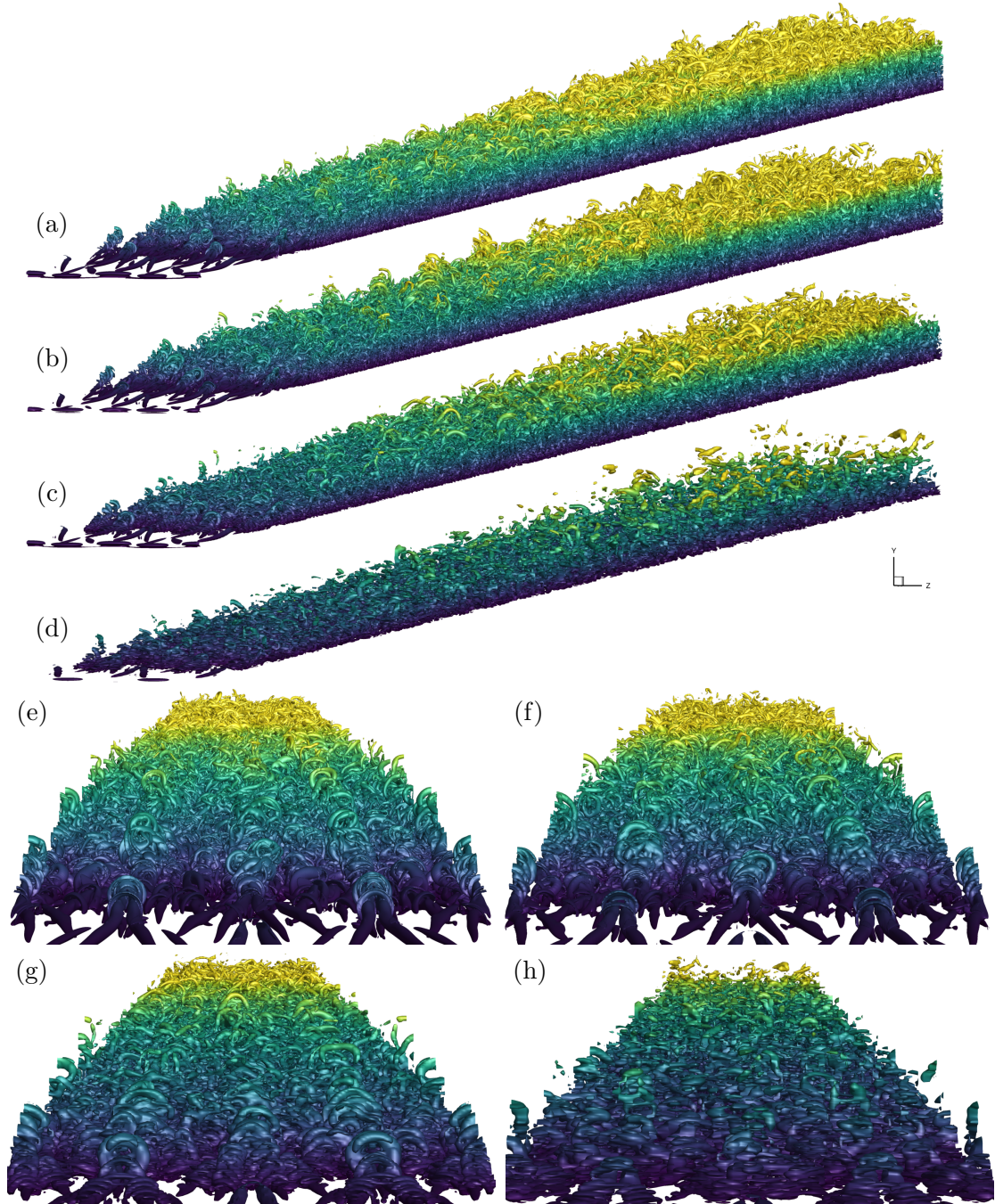


Figure 3.10: Lateral and frontal views of instantaneous snapshots for the $M = 2.25$ supersonic boundary layer. Isosurfaces of the Q -criterion coloured by the distance from the wall. (a, e): DNS; (b, f): ILES-A; (c, g): ILES-B; (d, h): ILES-D.

et al., 2018), the slight discrepancies being related to different free-stream Mach numbers and forcing locations. In figure 3.12(a), the Van-Driest-transformed velocity profiles collapse reasonably well for all the computational meshes (and for the two different schemes) except for ILES-D, in which the log-region values are shown to be largely overestimated (in accordance with observations of previous studies about the resolution limits for turbulent boundary layers Sayadi & Moin (2012); Poggie *et al.* (2015)).

3.6. PERFECT-GAS TURBULENT BOUNDARY LAYERS

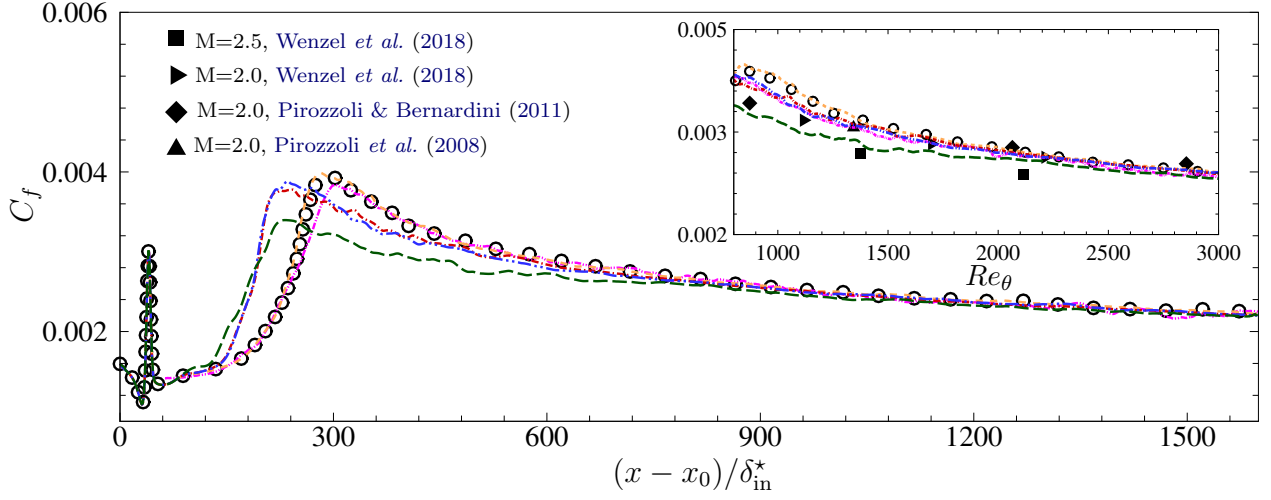


Figure 3.11: Skin friction coefficient C_f as a function of $(x - x_0)/\delta_{in}^*$. Sub-figure: C_f as a function of Re_θ in the fully turbulent zone. Line legend as in table 3.1.

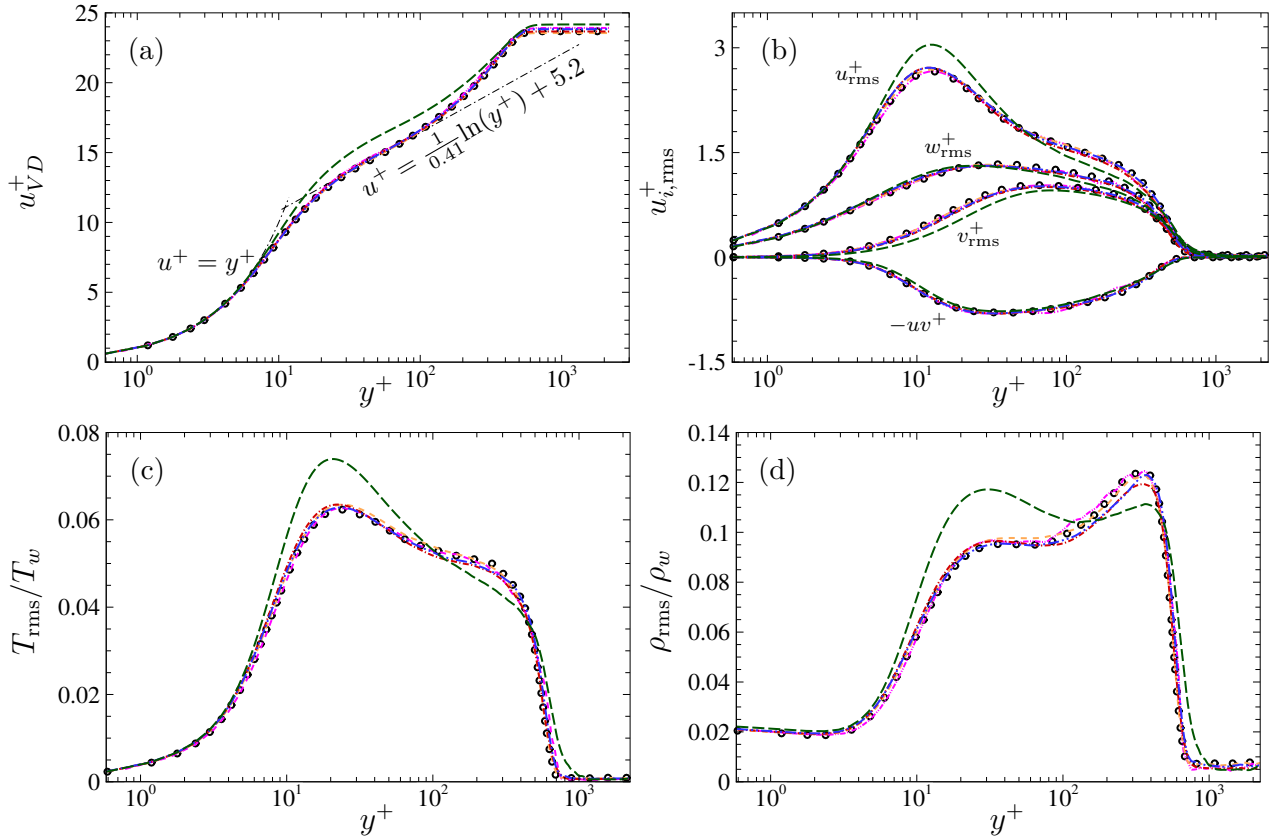


Figure 3.12: Wall-normal profiles of the Van-Driest-transformed longitudinal velocity (a), r.m.s. of velocity (b), temperature (c) and density (d), extracted at $Re_\theta = 3500$. Line legend as in table 3.1.

Root-mean-square values for each component of velocity, temperature and density are displayed in figures 3.12(b)-(c) and (d), respectively; here, the same conclusions hold: all the computational grids predict wall-normal profiles very close (or superposed) to the DNS solution, the only exception being ILES-D case which registers large mismatches in proximity of the inner peak. Slight discrepancies between ILES-A and ILES-Ab are visible in the fluctuating values of density, but they are mainly due to a non-perfect convergence of flow statistics for ILES-Ab. The current grid resolution study confirms the reliability of the numerical strategy in a wall-resolved ILES framework, pointing out that i) $\Delta x^+ < 15$ and $\Delta z^+ < 10$ should be used to obtain DNS-like results, and ii) slightly coarser resolutions may be considered when focusing the analysis only on fully-turbulent regions.

SUMMARY

The correctness of the models implemented in the CFD solver and the performances of the numerical strategy are tested:

- Thermochemical equilibrium and 0D heath bath in thermal non-equilibrium:
 - Park’s model fits for configurations considered in this work.
 - The results of relaxation towards equilibrium conditions perfectly match reference data.
- Shock tube problems:
 - FD10ANAD9 handles strong shocks and contact discontinuities, even in presence of non-equilibrium.
 - FD10LAD fails in reproducing viscous 2D cases with strong discontinuities.
- Laminar 2D boundary layers:
 - Base-flow for the simulation of 3D turbulent boundary layer with high- T .
 - Testing the correctness of the setup, boundary and initial conditions and drawing preliminary estimations on grid resolution and computational cost.
 - Matching with reference data.
- Turbulent 3D perfect-gas boundary layers:
 - Robustness and reliability of the schemes in case of wall-bounded turbulence.
 - Testing FD10ANAD9 on coarse ILES-like grids; computations are stable also for severely under-resolved simulations.
- Comparison between FD10ANAD9 and FD10LAD:
 - Both schemes provide the same results and accuracy, with some difficulties in handling strong events by FD10LAD.
 - FD10ANAD9 is more robust and less computationally expensive.

Chapter 4

Adiabatic hypersonic turbulent boundary layers

Contents

| | |
|---|-----------|
| 4.1 Second-mode transition in a high-enthalpy boundary layer | 71 |
| 4.1.1 Simulation setup and definitions | 73 |
| 4.1.2 Results | 75 |
| 4.2 Analysis of fully turbulent regime | 85 |
| 4.2.1 Simulations setup and definitions | 87 |
| 4.2.2 Results | 89 |

In this chapter we investigate a hypersonic boundary layer developing over an adiabatic wall under chemical nonequilibrium conditions. We focus first on the laminar and transitional regions (section 4.1); then, section 4.2 presents the influence of finite-rate chemistry on the turbulent region, along with the results of a companion simulation with frozen-chemistry assumption. Part of these results have been published in [Passiatore *et al.* \(2021\)](#) and presented at the 55th Edition of the 3AF International Conference on Applied Aerodynamics.

For both the analyses, the prescribed thermodynamic conditions are similar to those adopted in several stability studies (see, for instance, [Malik & Anderson, 1991](#); [Hudson *et al.*, 1997](#); [Perraud *et al.*, 1999](#); [Franko *et al.*, 2010](#); [Marxen *et al.*, 2014](#); [Miró Miró *et al.*, 2018](#)); specifically, the imposed free-stream values are $M_\infty = 10$, $T_\infty = 350$ K and $p_\infty = 3596$ Pa. The calculations are initiated in the laminar region, where air with standard composition ($Y_{\text{O}_2}=0.233$ and $Y_{\text{N}_2}=0.767$) enters the computational domain.

4.1 Second-mode transition in a high-enthalpy boundary layer

The flow regime of the boundary layer on a vehicle can have a significant impact on aerodynamics, heating and skin friction, since transitional thermal and mechanical loads may become more than thrice the laminar ones. These effects are more pronounced as the Mach number increases. Unfortunately, the process by which a laminar boundary layer transitions to turbulence is complicated and not fully understood. With very small perturbations, the transition process is initiated by linear instabilities

4.1. SECOND-MODE TRANSITION IN A HIGH-ENTHALPY BOUNDARY LAYER

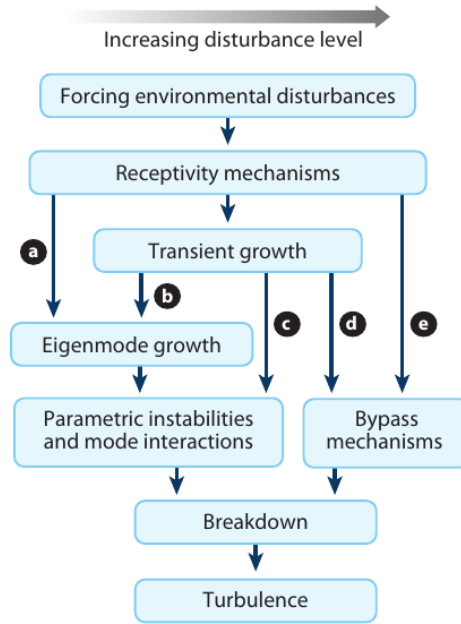


Figure 4.1: Paths to turbulence in boundary layer flows, from Morkovin (1994).

of the laminar boundary layer, including streamwise instabilities in the form of first and second (or Mack) mode instabilities (Mack, 1969); hence, the waves initially grow with a small amplitude and behave linearly before exhibiting nonlinear behavior (path (a) of figure 4.1).

For hypersonic flow fields, the instability that often dominates transition is the second mode instability, characterized by higher frequencies with respect to first-mode. The second Mack mode is an inviscid instability that arises when a region of the mean flow becomes supersonic relative to the phase speed of the instability. As a consequence, acoustic waves are trapped and reflected by the wall and near the sonic line, the boundary layer acting as a sort of waveguide, shown in the sketch in figure 4.2. Both linear and weakly nonlinear stability studies have pointed out that wall cooling tend to stabilize first-mode instability while destabilizing the second-mode, which may become the most unstable at even lower Mach numbers. Of note, even if first-mode instability is weakened for high Mach numbers, it can be still present, depending on the configuration and thermodynamic conditions. Additionally, it is more unstable in 3D (oblique instability waves). Particular effort has been made to investigate Mack modes and understand the influence of different parameters on second-mode instability (Stetson & Kimmel, 1992; Fedorov, 2011; Sivasubramanian & Fasel, 2014) and, more recently, different research groups are focusing their attention on the existence of supersonic Mack modes (Knisely & Zhong, 2019a; Kline *et al.*, 2019; Gloerfelt *et al.*, 2020). Most of results have been obtained for cryogenic conditions, allowing direct comparisons with ground test facilities; information about the hot hypersonic regime are much more scarce. Globally, once the two dimensional Mack wave has grown enough, oblique harmonic and subharmonic waves start to gain energy, giving rise to fundamental or subharmonic transition, respectively. Nevertheless, most studies focused on the linear mechanism leading to the growth of secondary instabilities, without including the nonlinear interaction or the full breakdown, due to the computational cost and the large extent of the transitional zone; as a result, the way the second-mode instability breaks down into turbulence at the late stage of transition is partially

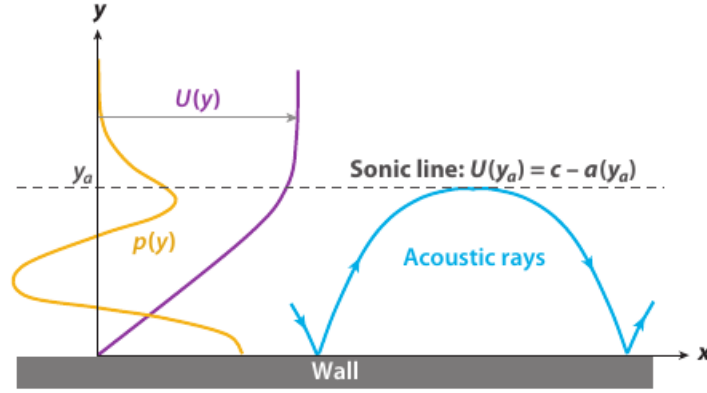


Figure 4.2: Acoustic mode in a high-speed boundary layer, where $U(y)$ is the mean-flow profile, and $p(y)$ is the pressure disturbance profile, from Fedorov (2011).

unknown.

This work explores a controlled transition, as opposed to transition due to wind tunnel large spectrum noise (usually referred-to as natural transition), of a flat-plate adiabatic boundary layer. A Mack mode is excited with a strong amplitude, in order to promote a second-mode transition. This DNS encompasses the laminar and transitional region, embedding linear growth of the disturbances and nonlinear breakdown to turbulence. A spectral analysis and modal decomposition will be used to understand the mechanism and clarify the transition path.

4.1.1 Simulation setup and definitions

The current setup considers a boundary layer developing over a semi-infinite plate. A sketch of the computational domain and boundary conditions is shown in figure 4.3. The domain is rectangular with even spacing in the streamwise (x) and spanwise (z) directions; in the wall-normal (y) direction the stretching function described in equation (3.6) is adopted, with $\alpha = 0.13$. The extent of the computational domain is $L_x \times L_y \times L_z = 8000\delta_{in}^* \times 320\delta_{in}^* \times 100\pi\delta_{in}^*$ discretized with $N_x \times N_y \times N_z = 5520 \times 256 \times 240$ points, for a total of ≈ 340 million grid points. The spanwise length has been chosen in order to contain integer multiples of the spanwise wave numbers of the forcing function (see later table 4.1). Characteristic-based boundary conditions are applied at the top and right edges of the domain, and periodic conditions in the spanwise direction. At the inflow, locally self-similar profiles are prescribed, corresponding to a displacement-thickness-based Reynolds number $Re_{\delta^*} = 6375$. The strategy adopted to obtain the locally self-similar solution is described in Appendix B. Based on the initial displacement thickness δ_{in}^* , we define a dimensionless streamwise coordinate as

$$\hat{x} = \frac{x - x_0}{\delta_{in}^*} \quad (4.1)$$

that will be used in the following. Here, x_0 is the distance from the virtual leading edge, equal to $x_0 = 1 \times 10^{-2}$ m given the inlet Re_{δ^*} . A sponge layer is applied at the inflow from $\hat{x} = 0$ to $\hat{x} = 35$ to prevent abrupt flow distortions. At the wall, no-slip and adiabatic wall conditions are applied, along with non-catalytic boundary conditions for species equations (i.e., $\partial Y_{\bullet} / \partial y = 0$). This hypothesis implies that the surface does not participate to chemical processes. However, in practical

4.1. SECOND-MODE TRANSITION IN A HIGH-ENTHALPY BOUNDARY LAYER

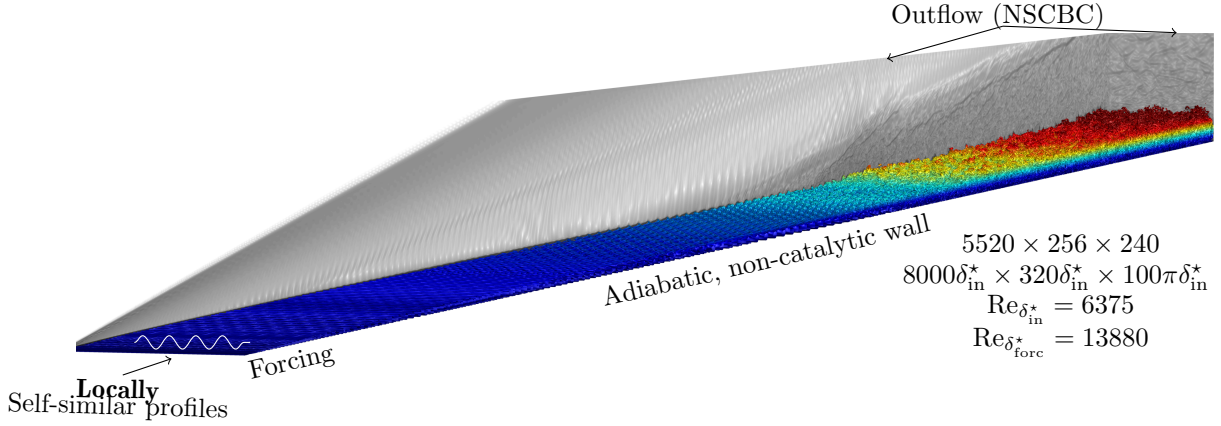


Figure 4.3: Isosurfaces of Q -criterion, colored with the wall-normal distance for the adiabatic boundary layer case.

flight conditions, the materials constituting the TPS of flight vehicles may be catalytic, promoting recombination of the atoms in the mixture in the near wall region. The investigation of finite-rate catalysis is beyond the scope of the present discussion; the reader may refer to [Bonelli *et al.* \(2021\)](#) for a discussion on the subject.

In order to trigger transition to turbulence, a blowing and suction forcing method is used. Second-mode transition is achieved with a technique similar to [Franko & Lele \(2013\)](#); the forcing strip is located at $\text{Re}_{\delta^*} = 13\,880$ (corresponding to $\hat{x} \approx 40$) and the suction-and-blowing function reads:

$$\frac{v_w}{u_\infty} = f(x)g(z) \left[\sum_{m=1}^{N_{\text{mode}}} A_m \sin(\omega_m t + \beta_m z) \right], \quad (4.2)$$

with

$$f(x) = \exp\left(-\frac{(x - x_f)^2}{2\sigma^2}\right) \quad (4.3)$$

$$g(z) = 1.0 + 0.1 \left\{ \exp\left[-\left(\frac{z - z_c}{z_w} - 1\right)^2\right] - \exp\left[-\left(\frac{z - z_c}{z_w} + 1\right)^2\right] \right\}. \quad (4.4)$$

Here, x_f is the centre of the Gaussian-like function (corresponding to the forcing Reynolds number) with variance $2\sigma^2 = 0.425 \frac{2\pi}{\omega}$, $z_c = L_z/2$ and $z_w = 2\pi\delta_{\text{in}}^*$ which results in a slight dissymmetry from the sinus function. In equation 4.2, $\omega = \tilde{\omega}\delta_{\text{in}}^*/c_\infty$ is the non-dimensional pulsation corresponding to a dimensional frequency $\tilde{f} = \tilde{\omega}/2\pi = 100$ kHz, in order to approximately match the one used by [Marxen *et al.* \(2014\)](#) for the same freestream conditions; finally A is the forcing function amplitude. The complete set of forcing parameters for each mode is listed in table 4.1. To induce a second-mode instability, the primary wave is a 2D Mack mode forced with a strong amplitude, together with lower-amplitude waves. An additional 2D disturbance is excited at the subharmonic frequency and different oblique modes of opposite orientation at both the harmonic and subharmonic frequency are added. This allows to assess whether the fundamental or the subharmonic instability prevails. Finally, stationary waves are also injected to induce three-dimensionality. The selection of the lower-amplitude

4.1. SECOND-MODE TRANSITION IN A HIGH-ENTHALPY BOUNDARY LAYER

Table 4.1: Parameters of the modes excited by the forcing function in equation 4.2: non-dimensional frequency, amplitude and spanwise wave number.

| #mode | 1 | 2 | 3 | 4 | 5 | 6 | 7 | 8 | 9 |
|-----------------------|------|-------|------|------|------|-----------|-----------|-----------|-----------|
| ω_m | 1.71 | 0.855 | 0 | 0 | 0 | 1.71 | 0.855 | 1.71 | 1.71 |
| $A_m(\times 10^{-3})$ | 50 | 2.50 | 2.50 | 2.50 | 2.50 | 2.50 | 2.50 | 2.50 | 2.50 |
| β_m | 0 | 0 | 0.2 | 0.4 | 0.6 | ± 0.2 | ± 0.2 | ± 0.4 | ± 0.6 |

disturbances is based on the strategy adopted by Franko & Lele (2013).

The calculations are run with the FD10ANAD9 scheme. Given the severe conditions, the Bhagatwala & Lele’s modification of the shock sensor was turned off. The artificial viscosity parameters are: $k_2 = 2.5$ and $k_{10} = 2.5/1260$.

In the results presented in the following (and in Chapter 5), flow statistics are computed by averaging in time and in the spanwise homogeneous direction, after that the initial transient is evacuated. For a given variable f , we denote with $\bar{f} = f - f'$ the standard time- and spanwise average, being f' the corresponding fluctuation, whereas $\tilde{f} = f - f''$ represents the density-weighted Favre averaging, with f'' the Favre fluctuation and $\tilde{f} = \overline{\rho f} / \bar{\rho}$. After having reached a statistically steady state, statistics are collected for approximately two turnover times with a sampling time interval of $\Delta t_s c_\infty / \delta_{in}^* = 3.45 \times 10^{-2}$. In view of spectral analysis, snapshots are extracted at a sampling interval of $\Delta t_s c_\infty / \delta_{in}^* = 2.30 \times 10^{-1}$, corresponding exactly to sixteen samples per each period of the fundamental forcing harmonic.

4.1.2 Results

4.1.2.1 Breakdown to turbulence

The evolution of selected wall quantities along the plate is shown in figure 4.4. The computed average skin friction coefficient $C_f = \bar{\tau}_w / (0.5 \rho_\infty u_\infty^2)$ is compared with the compressible extension of Blasius’ laminar correlation, $C_f^{lam} = \frac{0.664}{\sqrt{Re_x}} \sqrt{\frac{\bar{\rho}_w \bar{\mu}_w}{\rho_\infty \mu_\infty}}$ (with $Re_x = \frac{\rho_\infty u_\infty x}{\mu_\infty}$), and with the results predicted by the locally self-similar theory; $\bar{\mu}_w$ and $\bar{\rho}_w$ denote the time- and spanwise-averaged wall values of viscosity and density. After the forcing strip (not visible in the figure) and despite the presence of chemical reactions, the evolution of C_f follows the laminar correlation up to $\hat{x} \approx 3300$, where transition to turbulence starts. On the other hand, the similarity solution, which does not take into account the external pressure gradient created by the viscous/inviscid interaction (see Appendix B), tends to overestimate the skin friction coefficient. The averaged distribution of normalized temperature and species mass fractions along the wall are displayed in figure 4.4(b)-(c), respectively. The extremely high temperature triggers the dissociation of O_2 and, to a lesser extent, of N_2 , as well as the formation of NO. As a result, the amount of O_2 decreases (and contrariwise, O and NO increase) as the flow evolves in the laminar region. This behavior agrees with the results of the locally self-similar theory. After the transition point, the average temperature tends to a constant value and the mass fractions \bar{Y}_n vary at a lower rate. It is worth noting the inversion of species mass fractions trend in the fully turbulent region with respect to the laminar evolution, which is due to the enhanced mixing with the colder, external layers. At the domain outflow, the mixture composition remains far from the equilibrium one. The streamwise evolution of Y_{O_2} close to the wall is also shown in the xz -plane of

4.1. SECOND-MODE TRANSITION IN A HIGH-ENTHALPY BOUNDARY LAYER

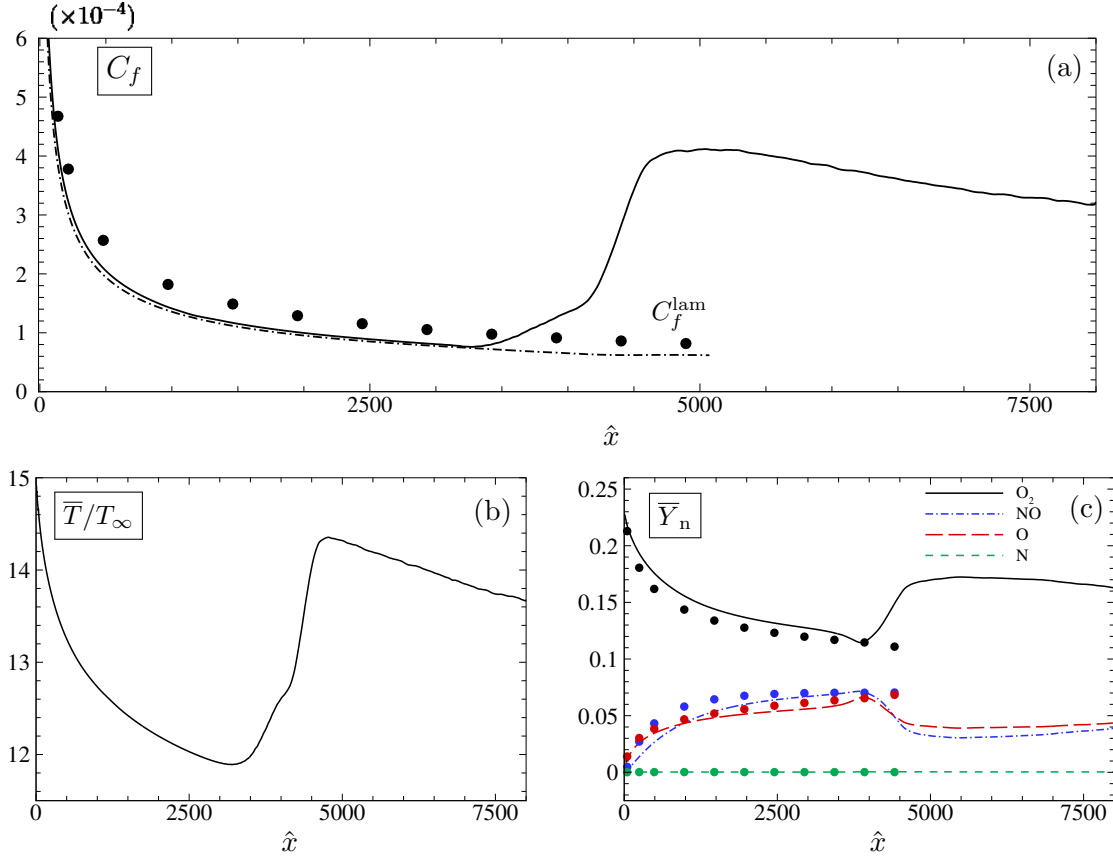


Figure 4.4: Streamwise evolution of wall quantities. Skin friction coefficient (solid line) together with laminar Blasius' correlation (dashed-dotted line) (a), normalized wall temperature (b) and wall species mass fractions (c). Bullets represent the results of the locally self-similar theory at selected stations.

figure 4.5, extracted at $y/\delta_{in}^* = 12$.

The evolution of C_f does not exhibit a clear overshoot at the transition location, but rather it is characterized by a smooth ramp in the transitional zone and by an asymptotic decay in the fully turbulent region. At the same time, both in the wall temperature and skin friction trend, a small kink is present at $\hat{x} \approx 3800$. This is related to the occurrence of Mean Flow Distortion (MFD), corresponding to the deviation of the laminar mean flow from the steady self-similar solution, i.e., to the occurrence of non-linear development of flow disturbances. This phenomenon can be clearly observed in figure 4.6, where the mean velocity distribution starts to deviate from the dashed white isolines after $\hat{x} = 3500$. In order to get some insights on the physical phenomena at play, we consider the Renard and Deck (RD) decomposition of the skin friction coefficient (Renard & Deck, 2016). The RD identity was generalized for compressible channel flows by Li *et al.* (2019) and extended to compressible boundary layers by Fan *et al.* (2019). The present identity is constructed by means of the kinetic energy transport equation in an absolute reference frame and assumes i) no-slip at wall, ii)

4.1. SECOND-MODE TRANSITION IN A HIGH-ENTHALPY BOUNDARY LAYER

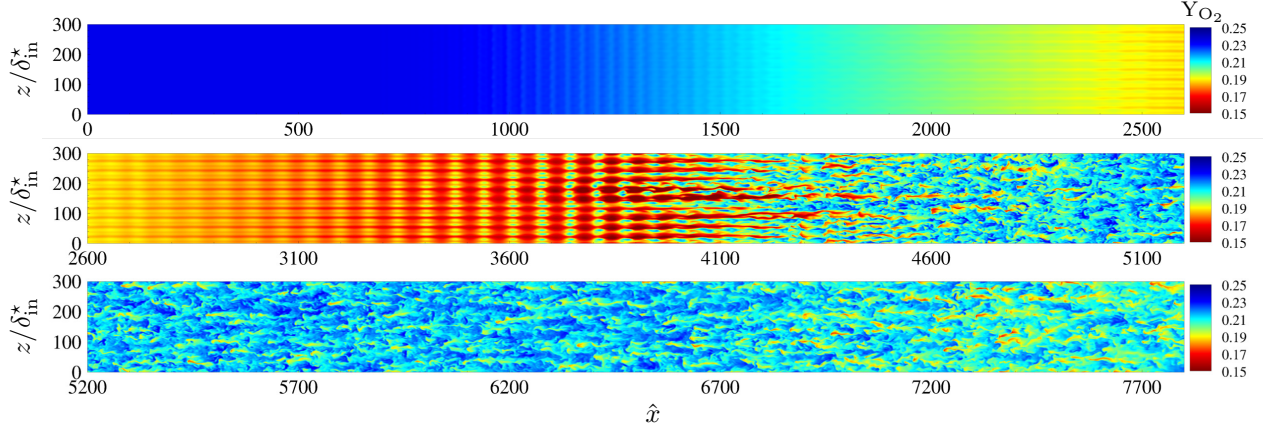


Figure 4.5: Instantaneous visualization of a xz -plane extracted at $y/\delta_{\text{in}}^* = 12$, colored with the molecular oxygen mass fraction Y_{O_2} .

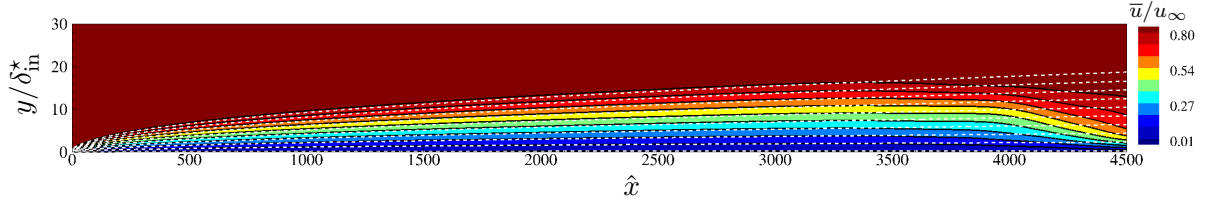


Figure 4.6: Mean flow distortion. Isocontours and isolines (solid black lines) of normalized mean streamwise velocity, superposed with isolines (dashed red lines) of normalized streamwise velocity deriving from a steady laminar computation.

homogeneity in the spanwise direction and iii) no body force:

$$\begin{aligned}
 C_f = & \underbrace{\frac{2}{\rho_\infty u_\infty^3} \int_0^\delta \bar{\tau}_{xy} \frac{\partial \tilde{u}}{\partial y} dy}_{C_{f,1}} + \underbrace{\frac{2}{\rho_\infty u_\infty^3} \int_0^\delta -\overline{\rho u'' v''} \frac{\partial \tilde{u}}{\partial y} dy}_{C_{f,2}} \\
 & + \underbrace{\frac{2}{\rho_\infty u_\infty^3} \int_0^\delta (\tilde{u} - u_\infty) \left[\bar{\rho} \left(\tilde{u} \frac{\partial \tilde{u}}{\partial x} + \tilde{v} \frac{\partial \tilde{u}}{\partial y} \right) - \frac{\partial}{\partial x} \left(\bar{\tau}_{xx} - \overline{\rho u'' u''} - \bar{p} \right) \right] dy}_{C_{f,3}}. \quad (4.5)
 \end{aligned}$$

Three terms can be distinguished: $C_{f,1}$ and $C_{f,2}$ represent the contributions of the mean-field dissipation and the dissipation due to the Reynolds stresses, respectively; $C_{f,3}$ accounts for the boundary layer spatial growth and includes the effects of streamwise heterogeneity. It is shown in figure 4.7(a) that the identity captures well the DNS solution, despite the presence of chemical reactions and strong aerodynamic heating. Of major interest is figure 4.7(b), which reports the magnitude of the different contributions. Up to $\hat{x} \approx 3500$, the viscous dissipation is predominant with respect to the other two contributions, the flow being still in a laminar regime. In correspondence of the kink in the skin friction's evolution, there is a sudden increase of the fluctuating kinetic energy production which is compensated by a local reduction of the boundary layer thickness; this mechanism was found to be the cause for MFD. Finally, in the fully turbulent region, $C_{f,3}$ slowly increases whereas the other two

4.1. SECOND-MODE TRANSITION IN A HIGH-ENTHALPY BOUNDARY LAYER

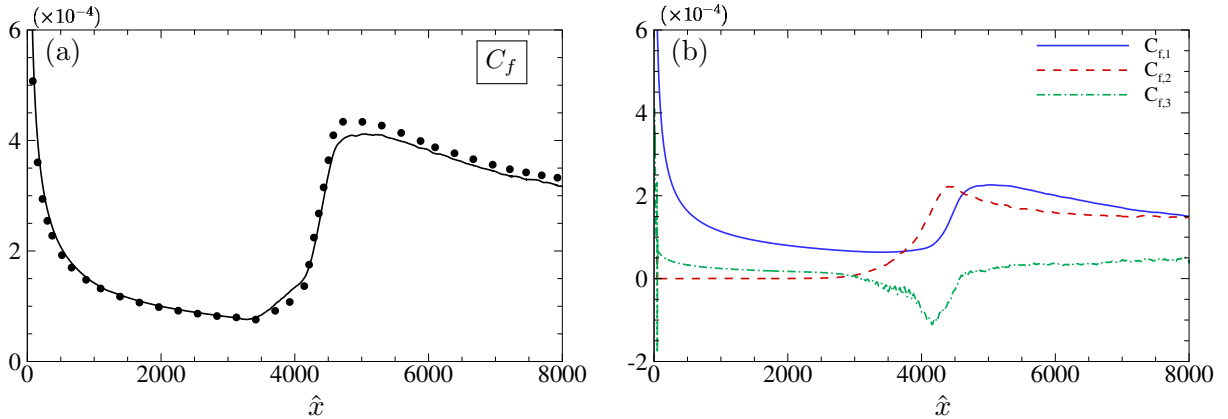


Figure 4.7: Streamwise evolution of skin friction coefficient (solid line) superposed with Renard-Deck decomposition (symbols) (a) and contribution of each terms of equation (4.5) (b).

terms start to asymptotically decrease.

After the MFD, nonlinear effects emerge and transition to turbulence occurs. In the view of analyzing the mechanism responsible for the breakdown, a series of instantaneous snapshots of xz -planes at different wall-normal locations are presented in figure 4.8. The normalized fluctuations of the streamwise velocity are displayed along horizontal planes at various heights. Specifically, we focus on the region comprised between $\hat{x} = 2000$ and the end of the transitional zone. At $y/\delta_{in}^* = 1$, $y/\delta_{in}^* = 5$ and $y/\delta_{in}^* = 10$, the footprint of the fundamental harmonic, given by the thinnest structures with a roll-like shape is observed for $2000 < \hat{x} < 2600$. Further downstream, the fundamental 2D mode tends to fade and a subharmonic emerges and becomes more and more significant by moving towards the edge of the boundary layer. Besides, the qualitative evolution of the disturbances shows also a modulation in the spanwise direction, mainly due to the emerging stationary modes, initially injected at low amplitude. Nonlinear effects lead to the growth of stationary waves and cause the development of streaky structures at $4000 < \hat{x} < 4500$ which, in this specific configuration, rapidly destabilize the flow and promote the breakdown to turbulence. On the other hand, at $y/\delta_{in}^* = 20.0$, oblique structures are visible with a strong intensity starting from $\hat{x} \approx 2500$. As shown later in three-dimensional flow field visualizations, these structures are the top view of λ -vortices. The positions marked with C, D and E correspond to the emergence of specific modes, further illustrated in figure 4.11. Specifically, at station C the first streak mode is predominant, whereas the 2D subharmonic mode is gaining energy until it reaches a maximum at station D. Finally, at location E the second streak mode has gained enough energy to promote breakdown. It is worth noting that the breakdown occurs thanks to a localized spot almost in the middle of the spanwise domain, which is actually responsible for the destabilization of the entire flow. This behavior is also observable in the x vorticity component ($\omega_x = \frac{\partial w}{\partial y} - \frac{\partial v}{\partial z}$) plotted along zy -planes in figure 4.9. At the two first selected stations, relatively regular vortical structures are present; at $\hat{x} = 4000$, the flow is not completely turbulent since it still exhibits coherent structures, but in the region $150 < z/\delta_{in}^* < 200$ an unstable packet appears, promoting a fully turbulent state visible at $\hat{x} = 4500$. Coherent structures generated in the transition process can be observed in figure 4.10, which reports an isosurface of the Q -criterion, colored with the distance from the wall. Figure 4.10(a) shows the portion of the domain $1500 < \hat{x} < 4500$; along this entire region the structures are regular and distinguishable, meaning that no breakdown has occurred yet. Roll-like vortices

4.1. SECOND-MODE TRANSITION IN A HIGH-ENTHALPY BOUNDARY LAYER

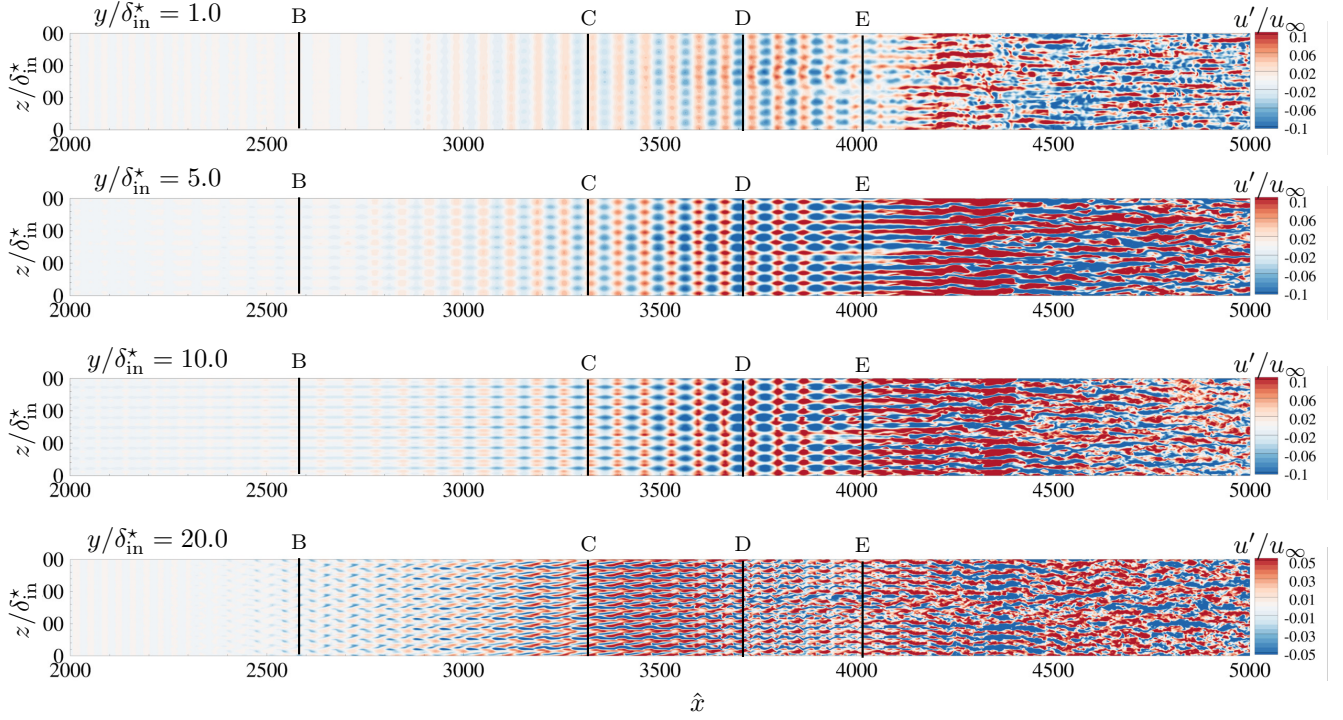


Figure 4.8: Instantaneous visualization of normalized streamwise velocity fluctuations in xz -planes, extracted at different y/δ_{in}^* positions.

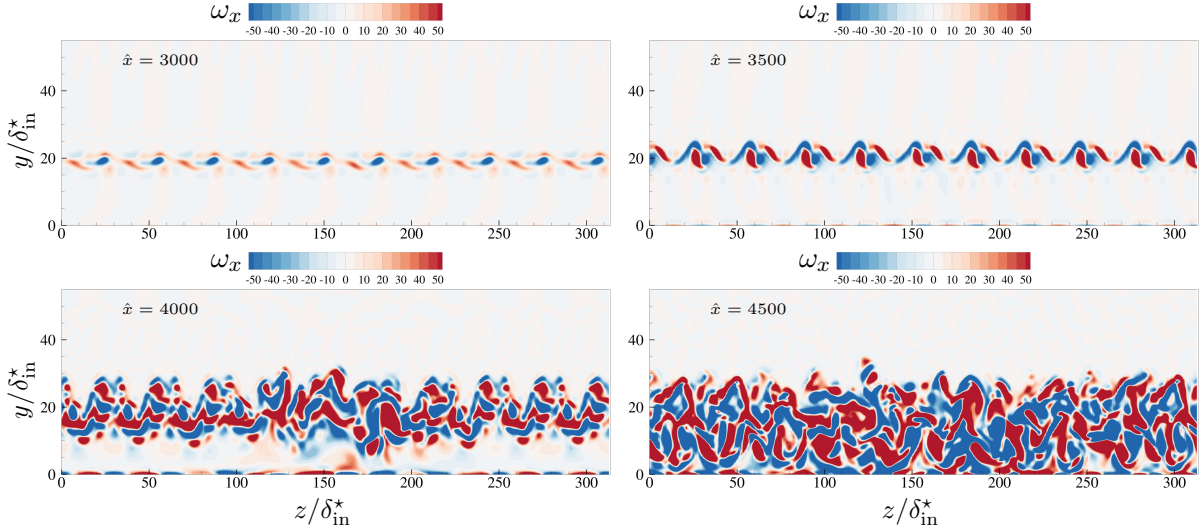


Figure 4.9: Instantaneous visualization of x -vorticity ($\omega_x = \frac{\partial w}{\partial y} - \frac{\partial v}{\partial z}$) in zy -planes, extracted at different streamwise locations.

are observed in the near-wall layer, with a characteristic size that increases progressively when moving downstream. On top of these vortices, λ -shaped structures are clearly observed. The head of the

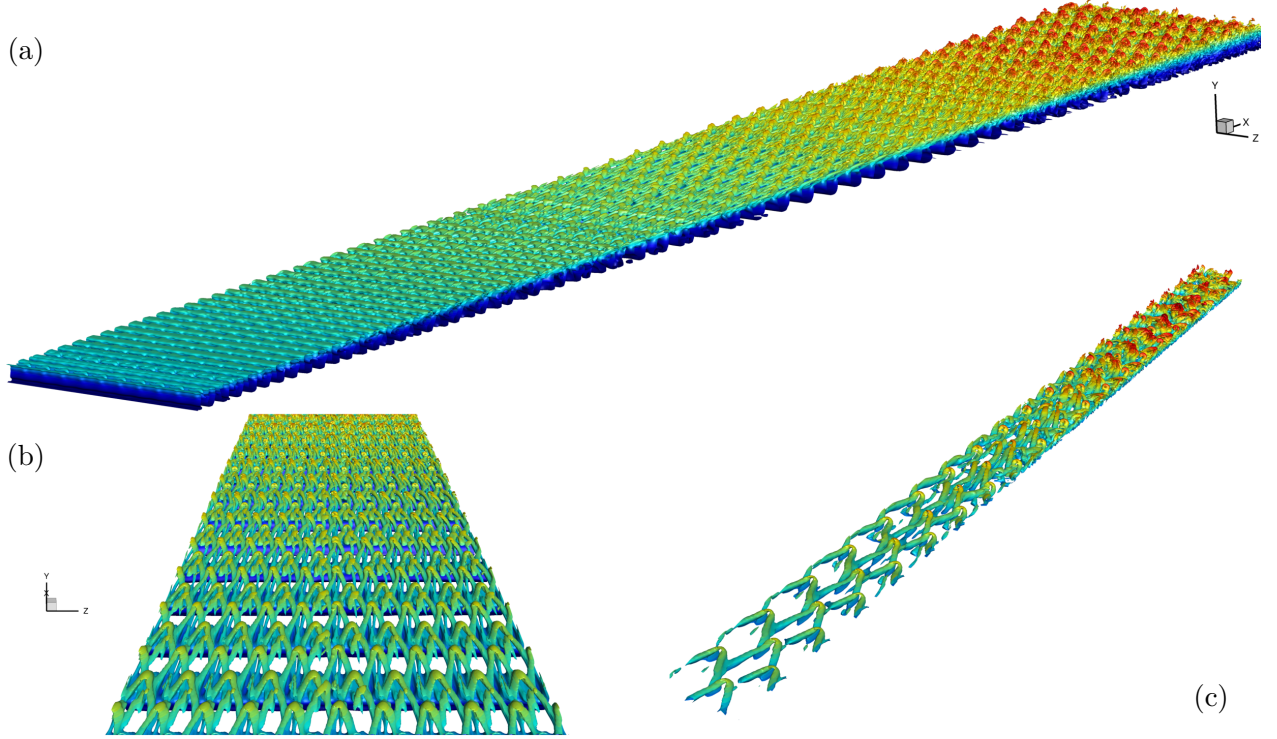


Figure 4.10: Isosurfaces of the Q -criterion colored with the distance from the wall. (a) Computational domain from $\hat{x} = 1500$ up to $\hat{x} = 4500$; (b) top view starting from $\hat{x} \approx 3000$; (c) detail of λ -vortices which become hairpins moving further downstream.

λ -vortices undergo the classical lift-up phenomenon and their heads create spikes. From the two top views (figure 4.10(b)-(c)) one can observe an almost staggered organization of the λ -vortices, modulated by the underlying 2D vortices and by very thin longitudinal vortices. Figure 4.10(c) highlights the evolution of the λ -vortices into hairpins, and the formation of spikes at the hairpin heads.

4.1.2.2 Modal analysis

The laminar-to-turbulent transition has only been analyzed by a qualitative description of the flow structures so far. In the following, the role of each mode is quantified by means of spectral analysis, which consists in evaluating the amplitude of excited modes through a spatio-temporal Fourier transform. Of note, a similar approach was adopted in the works of Franko & Lele (2013) and Gloerfelt & Robinet (2017). The Fourier components are denoted as (ω, β) , where ω is the angular frequency and β the spanwise wavenumber. These quantities are normalized by $\omega_f = 1.71$ and $\beta_f = 0.2$, respectively, corresponding to the frequency of the fundamental harmonic and to the smallest spanwise wave number listed in table 4.1. In the aforementioned works, the amplitude of each mode is evaluated by computing the modal energy, which takes into account the kinetic and internal energy contributions, as

$$E_m = \frac{1}{\delta \rho_\infty u_\infty^2} \int_0^\delta \left[\frac{1}{2} \bar{\rho} (\widehat{u}' \widehat{u}'^* + \widehat{v}' \widehat{v}'^* + \widehat{w}' \widehat{w}'^*) + \bar{\rho} \sqrt{e' e'^*} \right] dy.$$

4.1. SECOND-MODE TRANSITION IN A HIGH-ENTHALPY BOUNDARY LAYER

Here, $\widehat{(\bullet)}$ stands for the Fourier component and $(\bullet)^*$ denotes the complex conjugate; δ is the local boundary layer thickness. In single-species flows of calorically-perfect gases, the internal energy may be expressed as a function of a primitive variable, such as pressure or temperature. In the present study instead, the specific internal energy is a function of both temperature and species mass fractions ($e = e(T, Y_n)$); the Fourier analysis has therefore been performed directly by considering the variable e . This formulation takes directly into account the contribution of chemical activity, since both density and internal energy vary species production or depletion. As an alternative, one can isolate only the kinetic contribution and analyze the growth rate by means of modal kinetic energy

$$K_m = \frac{1}{\delta \rho_\infty u_\infty^2} \int_0^\delta \frac{1}{2} \bar{\rho} \left(\widehat{u}' \widehat{u}'^* + \widehat{v}' \widehat{v}'^* + \widehat{w}' \widehat{w}'^* \right) dy.$$

Other references make use of the maximum amplitude of the streamwise velocity fluctuation solely, as $|u'|_{\max}^2 = |\widehat{u}' \widehat{u}'^*| / u_\infty^2$, which is the quantity actually measured in experiments allowing a direct comparison (see, e.g., Marxen *et al.*, 2014). In the following, we test and compare these three methods. To this aim, the instantaneous flow field is stored in a portion of the domain comprised between $\hat{x} = 0$ and $\hat{x} \approx 4300$; a total number of 800 time samples is considered, corresponding to a sampling rate equal to sixteen times the fundamental forcing harmonic.

In order to investigate the role of different waves in the transition process, figure 4.11 shows the streamwise development of modal total energy, modal kinetic energy and maximum u -velocity disturbance of the selected modes explicitly excited by the forcing function. First, the mild differences between K_m and E_m plots (panels a and b, respectively) indicate that the kinetic contribution overwhelms the internal energy one. Furthermore, chemical activity is shown to contribute to the variation of the internal energy term, but without significant alteration of the waves modal growth. The fundamental harmonic (1, 0), excited with the strongest amplitude at the station A, predominates over all the excited modes in the early stages, but soon after it rapidly decays and then saturates. At the same time, the harmonic and subharmonic oblique waves, (1, 1) and (1/2, 1), after an initial drop of several orders of magnitude, start to grow; however, only the subharmonic oblique wave recovers enough energy and eventually becomes one of the predominant modes at position B, corresponding to $\hat{x} \approx 2000$. This behavior is better seen in the evolution of the integral kinetic energy rather than the u -velocity disturbance, since in figure 4.11(c) the wave (1/2, 1) seems to decay again right after $\hat{x} = 2000$. This discrepancy could be related to the non-negligible transversal and wall-normal velocity components, which may significantly contribute to the modal growth of an oblique wave. Moreover, this result is consistent with the qualitative evolution of the velocity fluctuations in figure 4.8 at $y/\delta_{\text{in}}^* = 20$, where the three-dimensional structures start to be visible at $\hat{x} > 2500$. Downstream of this station, the streak modes (0,1) and (0,2) start to emerge. The higher streak mode (0,2) initially dominates becoming the most energetic at station C, but at later transition stages (position E) the principal stationary mode (0,1) overwhelms the former, leading to the breakdown and to the final saturation stage (not shown in the figure). Of note, the subharmonic 2D mode (1/2, 0) exhibits an exponential growth downstream of the forcing strip, becoming one of the most energetic modes in the region $3000 < \hat{x} < 4000$ (station D). Such a growth is likely favored by the quick thickening of the hypersonic boundary layer, leading to an increased local Reynolds number and to the amplification of lower frequency disturbances.

At this point, one may wonder if λ -vortices (i.e., oblique modes) or streak (i.e., stationary modes) instability is ultimately responsible for breakdown to turbulence. In the attempt to answer this question, the streaks amplitude has been estimated as (Andersson *et al.*, 2001):

$$A_s = \frac{1}{2u_\infty} \left[\max_{y,z} (\bar{u} - u_{\text{BF}}) - \min_{y,z} (\bar{u} - u_{\text{BF}}) \right], \quad (4.6)$$

4.1. SECOND-MODE TRANSITION IN A HIGH-ENTHALPY BOUNDARY LAYER

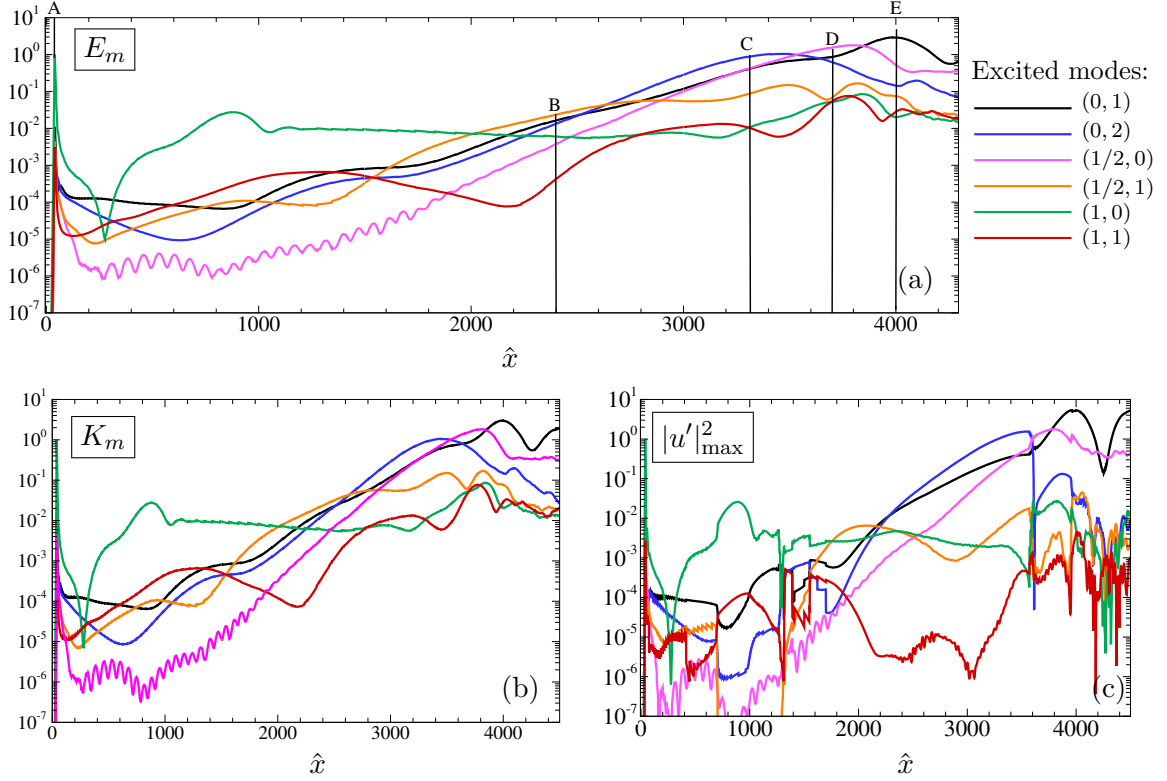


Figure 4.11: Streamwise developments of modal total energy (a), modal kinetic energy (b) and maximum u -velocity disturbance amplitude (c), for the couples $(\omega/\omega_f, \beta/\beta_f)$ marked in the legend (explicitly excited in the suction-and-blowing forcing).

where u_{BF} stays for the velocity of the base flow. The results are shown in figure 4.12. In the region up to $\hat{x} < 2000$, the amplitude is nearly zero, consistently with the slow growth of waves (0, 1) and (0, 2) observed in figure 4.11. Right after this station, the amplitude of the stationary modes starts to increase, even if its maximum value remains below under the threshold of 25% (generally considered as the critical value beyond which the streaks burst in, see e.g. Andersson *et al.*, 2001) up to $\hat{x} \approx 4000$. Only further downstream, a prompt growth is observed and the streaks break down into turbulence. The transition scenario seems then initially dominated by hairpin spikes, but ultimately governed by the streaks burst at the latest stages.

To summarize, despite an unstable 2D Mack mode is excited at high amplitude, the transition process is not ruled by the fundamental mode. Instead, subharmonic 2D and oblique modes, along with streaky modes are naturally selected and amplified, draining energy from the fundamental one. The location where such modes become predominant also correspond to MFD. The interaction of 2D and oblique modes lead to the formation of λ -vortices, as shown previously. Both the modal analysis and the instantaneous visualizations description confirm that the transition scenario shares remarkable similarities, at least in qualitative terms, with H -type transition in incompressible boundary layers (Herbert, 1988) despite the hypersonic and chemically-reacting flow environment. In a H -type scenario, λ -shaped structures appear and they are organized in a perfectly staggered manner; moreover, this path is characterized by the amplification of subharmonic modes and the transition is delayed. Another

4.1. SECOND-MODE TRANSITION IN A HIGH-ENTHALPY BOUNDARY LAYER

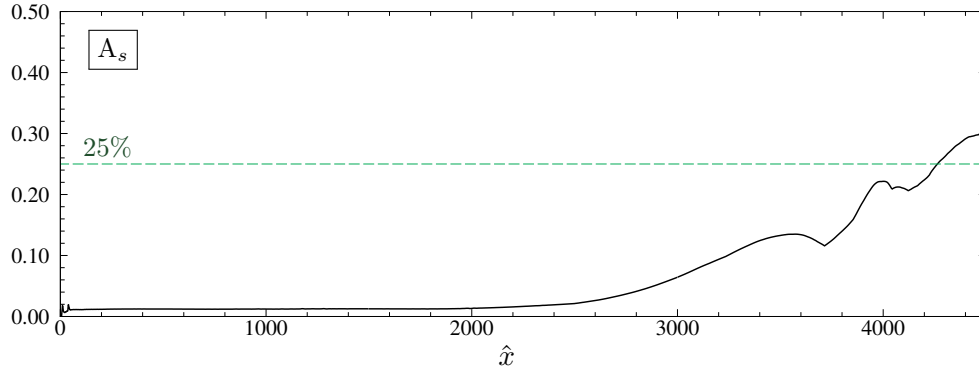


Figure 4.12: Streamwise evolution of streaks amplitude, defined as in equation (4.6).

common path in incompressible boundary layers transition is the K -type scenario (Klebanoff *et al.*, 1962), in which the λ -vortices generated are completely aligned and an early fundamental transition leads to the breakdown. Since the structures are not perfectly staggered, it is difficult to identify to which scenario the present transition resemble most. Besides, due to the rapid thickening of the boundary layer in the present hypersonic conditions, it cannot be stated for sure that the transition is of the “subharmonic” type, since the original mean flow has changed and the fundamental mode could have changed as well. Moreover, the λ -structures stand above roll-like-shaped ones induced by 2D modes, and this is a peculiarity of this transition mechanism only. Further analyses have been planned to elucidate such a scenario, including cross spectra and in-depth inspections of coherent structures. Moreover, previous stability studies showed that dissociation reactions tend to destabilize the second-mode instability and stabilize the first-mode one (albeit most of these results have been obtained by means of linear stability analyses). Here, no particular conjectures can be drawn regarding the role of chemical activity, since a direct comparison with a non-reacting configuration was not feasible because of its computational cost. The role of the temperature, which is directly related to chemical activity, is currently being assessed to understand whether or not such high values have a significant impact on the transition dynamics.

4.1.2.3 Dynamic Mode Decomposition (DMD)

After having analyzed the evolution of all the modes explicitly injected by the wall forcing, we now evaluate if, among these modes, there exists a subset including only the most significant ones. To this aim, Dynamic Mode Decomposition (DMD) is used. DMD is a modal decomposition technique initially introduced by Schmid (2010) which has been proven to be extremely useful for the analysis of the dynamics of nonlinear systems. In the specific case of fluid mechanics, this tool is helpful for finding coherent structures in turbulent flows, identifying the most significant modes (i.e., the most energetic ones) sufficient to describe the behavior of the flow field. Details on the methodology are reported in Appendix C. The decomposition has first been applied to a sequence of snapshots corresponding to the wall plane and the quantity τ_w . The same sampling interval and number of snapshots used for the spectral analysis has been selected. Figures 4.13(a)-(b) display the spectrum and the growth rate, respectively, whereas figure 4.13(c) reports the amplitude of each mode as a function of the frequency. The DMD modes have been sorted from the most energetic to the less energetic ones. The results show that the most energetic modes are at 2 kHz, 50 kHz and 100 kHz, respectively. These modes are

4.1. SECOND-MODE TRANSITION IN A HIGH-ENTHALPY BOUNDARY LAYER

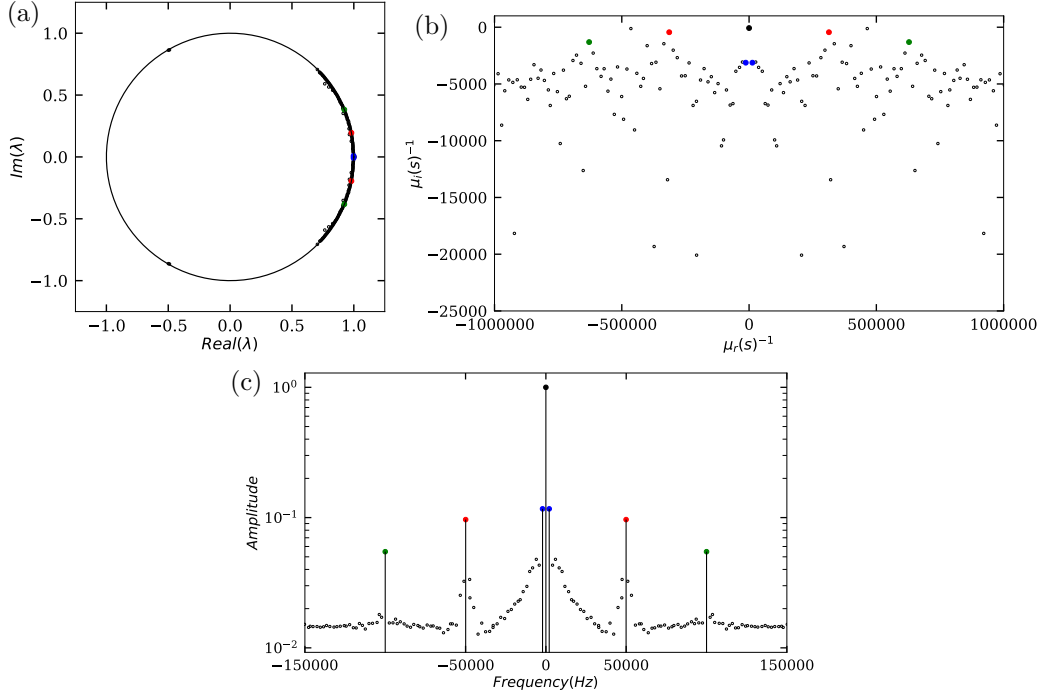


Figure 4.13: Eigenvalues spectra obtained from DMD analysis on τ_w . (a) Spectrum and unit circle; (b) growth rate; (c) amplitude vs frequency. The filled circles correspond to the mean flow (black) and to the three first energetic modes at 2 kHz (blue), 50 kHz (red) and 100 kHz (green).

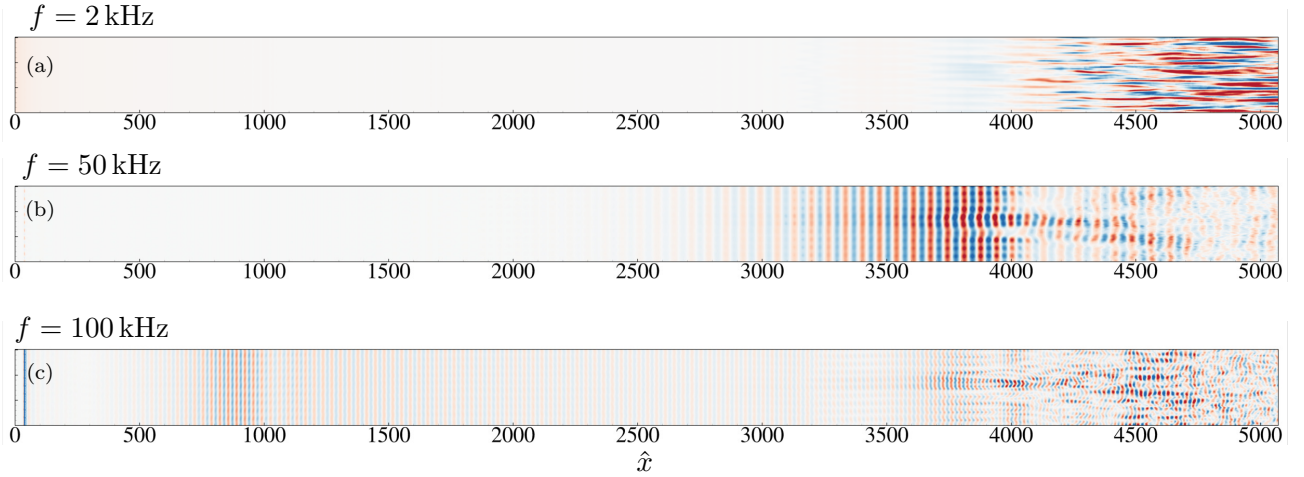


Figure 4.14: Spatial modes of τ_w in the laminar and transitional zone of the domain for the DMD modes corresponding to $f = 2$ kHz (a), $f = 50$ kHz (b) and $f = 100$ kHz (c).

highlighted in figure 4.13 with colored filled circles, whereas the black filled circles stand for the mean (zero frequency) flow. Several considerations are in order. The frequency of the first energetic mode is close to zero, i.e., it corresponds to a nearly stationary mode, consistently with the energy gained by streaks before the final saturation stage. The subsequent significant frequencies are 50 kHz and

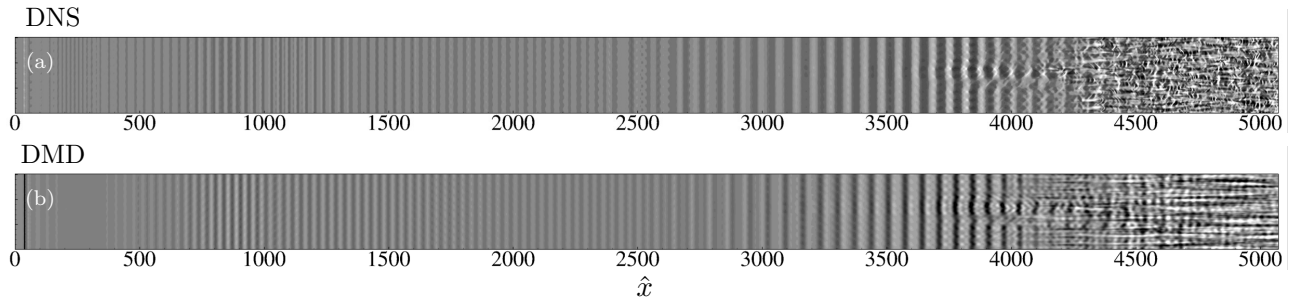


Figure 4.15: Comparison between instantaneous flow field of τ_w (a) and reconstructed flow field (b) with the superposition of the modes at $f = 2$ kHz, 50 kHz and 100 kHz.

100 kHz; of note, the subharmonic frequency prevails on the principal harmonic in the flow region at hand, as previously shown in the modal analysis. To corroborate the previous statements, the spatial structures of each DMD mode ϕ_r (see equation C.5) are shown in figure 4.14. The mode with the smallest frequency presents elongated structures similar to streaky modes which emerge uniquely by the end of the transitional zone. The harmonic and subharmonic modes are associated with roll-like structures in the near-wall region; additionally, in figure 4.14(c), corresponding to the fundamental frequency, the amplitude exhibits a peak at $\hat{x} \approx 1000$, i.e. the point at which the mode begins to saturate. The results of this decomposition are in accordance with the previous qualitative observations and spectral analysis. The superposition of the three most energetic modes is shown in figure 4.15: the reconstructed field is very similar to the DNS solution, meaning that these modes are reasonably responsible for most of the flow dynamics in the transitional region and, specifically, are enough to describe the evolution of the wall shear stress (i.e., skin friction).

The DMD has also been applied to the streamwise velocity in a three dimensional sub-domain in the range $1500 < \hat{x} < 4500$. The spectrum and the amplitude (figure 4.16(a)-(b)) are similar to those reported for τ_w . The mode corresponding to 100 kHz does not appear among the most energetic ones since the portion of the domain upstream of $\hat{x} \approx 1500$ has been excluded from the analysis. On the other hand, the DMD modes at 2 kHz and 50 kHz emerge again as the most significant ones. The modal growth rate shown in figure 4.16(a) reveals the existence of a mode (marked with an arrow in the figure) having a frequency extremely similar to the subharmonic one, whose growth rate is larger than zero, meaning that it is unstable. This is the confirmation of the actual unstable mode, which has a frequency of ≈ 50 kHz. Both the 2D and the oblique mode at this frequency can be considered unstable and responsible for the transition to turbulence. Figure 4.16(c), reporting the spatial structures of the mode at 50 kHz colored with the distance from the wall, confirms the coexistence of multiple structures at different heights, and specifically rolls and λ -vortices (as also previously shown in figure 4.3).

4.2 Analysis of fully turbulent regime

As for now, the laminar and transitional regimes have been investigated. In the following of this chapter, we focus on the turbulent region with the aim of understanding whether and to which extent chemical non-equilibrium alters boundary-layer turbulence. Due to the significant transition length previously observed for modal transition, a new setup is considered where streaky modes are directly excited at high amplitude at the strip location. Such a configuration allows to simulate a shorter

4.2. ANALYSIS OF FULLY TURBULENT REGIME

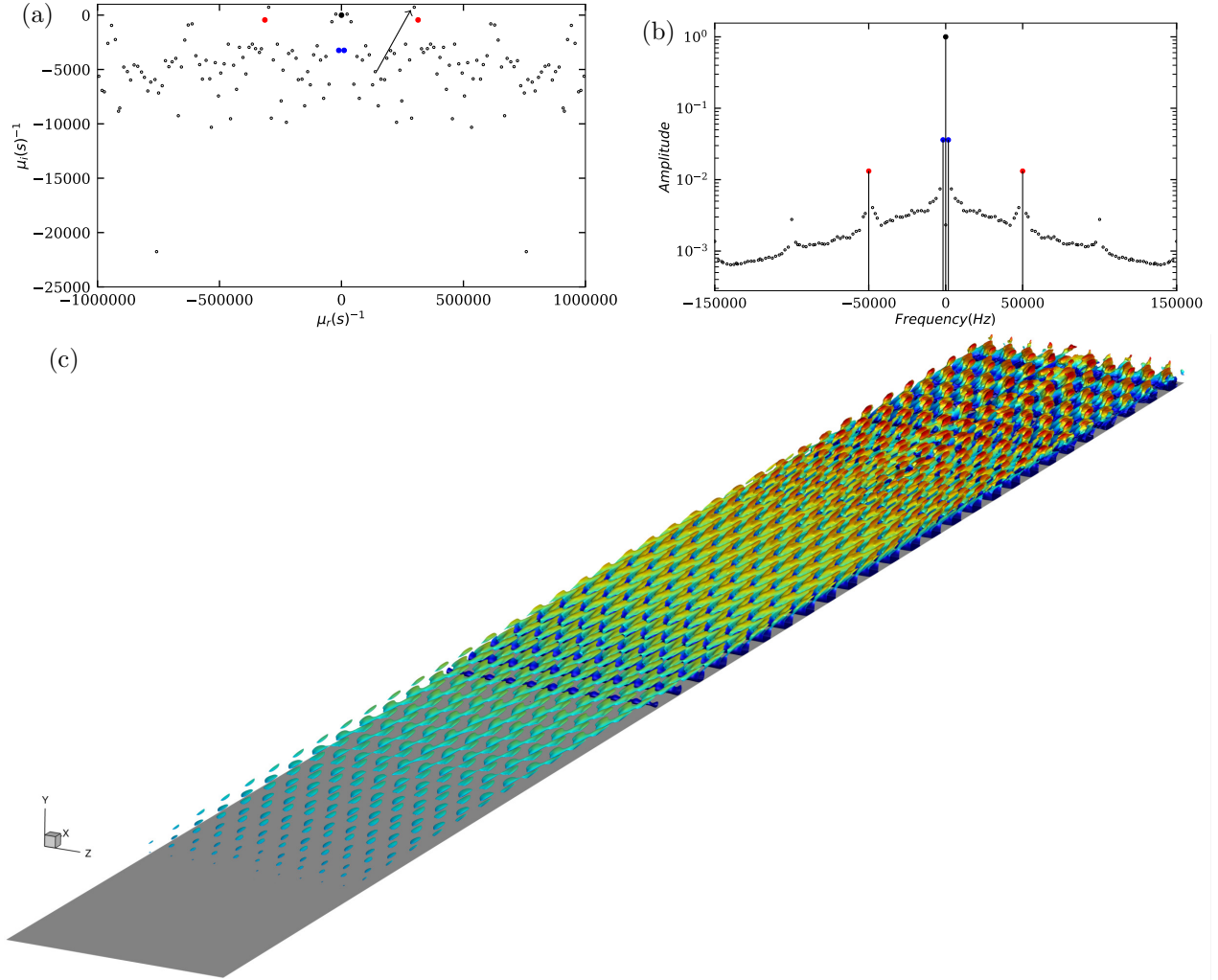


Figure 4.16: Eigenvalues spectra obtained from DMD analysis on u . (a) Growth rate; (b) amplitude vs frequency and (c) spatial structures of the DMD mode at 50 kHz. The filled circles correspond to the mean flow (black) and to the two first energetic modes at 2 kHz (blue) and 50 kHz (red).

computational domain, the breakdown to turbulence occurring much earlier in the streamwise direction. Moreover, using a computational grid similar to the one in section 4.1 on a smaller domain allows to obtain the DNS-like resolution required for the investigation of turbulence dynamics. The chemically-reacting case is also compared to a companion simulation carried out under the frozen-chemistry hypothesis; in such conditions, the species mass fractions do not vary in the computational domain and are equal to those imposed at the inflow boundary.

The present configuration of a quasi-adiabatic flat-plate, despite being a crude and purely theoretical approximation, enables the study of the influence of extremely high temperature values in the near-wall region. Moreover, the results might prove to be useful for the purpose of comparison with existing and upcoming DNSs of strongly-cooled boundary layers. As mentioned in section 4.1, such a configuration has been adopted as reference test case over the years for stability studies, but the

turbulent regime has never been characterized. A collection of complementary results can be found in Appendix D.

4.2.1 Simulations setup and definitions

For the analysis of the fully turbulent regime, we simulate two hypersonic, zero-pressure-gradient, spatially-evolving boundary layers over a flat plate, in chemical non-equilibrium (“CN” case) and under a frozen-chemistry assumption (“FR” case), respectively. The free-stream conditions are the same adopted in section 4.1. Self-similar profiles of the flow properties, corresponding to a compressible Blasius boundary layer solution under frozen-chemistry assumptions, are prescribed at the computational domain inlet which is located to a distance $x_0 = 6.13 \times 10^{-3}$ m from the plate leading edge (not included in the domain). The choice of using the assumption of frozen-chemistry as inlet boundary condition has been made in order to preserve the same setup for CN and FR cases. At the inflow the δ_{in}^* -based Reynolds number is set to $\text{Re}_{\delta^*} = 5000$; a sponge layer is applied from $\hat{x} = 0$ to $\hat{x} = 100$ to prevent distortions of the boundary layer similarity profiles. At the plate wall, the adiabatic wall temperature resulting from the similarity solution, $T_w = 5323$ K, is prescribed along with no-slip, non-catalytic conditions. Characteristics-based boundary conditions used at the outflow and free-stream boundaries, whereas periodicity is imposed in the spanwise direction. The dimensions of the computational domain are $L_x \times L_y \times L_z = 5200\delta_{\text{in}}^* \times 240\delta_{\text{in}}^* \times 50\pi\delta_{\text{in}}^*$ in the streamwise (x), wall-normal (y) and spanwise (z) directions, respectively; the domain is discretized with $N_x \times N_y \times N_z = 5236 \times 256 \times 240$ points, corresponding to a total of approximately 3.2×10^8 grid points. The grid spacing is uniform in the streamwise and spanwise directions, whereas the stretching function shown in equation (3.6) is used in the wall-normal direction, with $\alpha = 0.25$. The same computational grid is used for both FR and CN cases; table 4.2 reports the resolutions for the CN case at several downstream locations in wall viscous units, the viscous length scale being $l_v = \bar{\mu}_w / (\bar{\rho}_w u_\tau)$. Here, $u_\tau = \sqrt{\bar{\tau}_w / \bar{\rho}_w}$ is the friction velocity based on the averaged wall shear stress $\bar{\tau}_w$. Poggie *et al.* (2015) indicate that using $\Delta x^+ < 10$, $\Delta y^+ < 1$ and $\Delta z^+ < 5$ is sufficient to obtain well-converged first- and second-order statistics. The grid resolutions obtained (with $\Delta x^+ < 2.6$, $\Delta y_w^+ < 0.6$ and $\Delta z^+ < 1.8$ everywhere) are well below the suggested limits and ensure very accurate representation of the small details of the flow; note that similar values were obtained for the frozen-chemistry DNS. According to the same authors, the spanwise extent of the computational domain should be at least twice the local boundary layer thickness δ , in order to ensure proper decorrelation in the spanwise direction. By considering its value at the end of the flat plate, δ_{end} , we obtain for the present simulations $(L_x \times L_y \times L_z) / \delta_{\text{end}} \approx 65 \times 3 \times 2$, which meets the suggested recommendation. Direct confirmation is obtained by inspection of the two-points spanwise correlations, shown in figure 4.17 for density and streamwise velocity at two different wall-normal locations, respectively in the buffer and logarithmic regions. Another important check consists in verifying the absence of energy pileup at high wavenumbers; to this aim, we report the one-dimensional kinetic energy spectra in figure 4.18, at the same two wall positions. The energy distribution cascades down smoothly for approximately nine orders of magnitude, with an inertial range extending for more than a decade in the logarithmic region. The cutoff wavenumber indicates again a good grid resolution and no energy accumulation is observed at the smallest scales.

Transition to turbulence is induced by means of a suction-and-blowing forcing applied at the wall along a spanwise strip located close to the inflow. In this region, a time-and-space-varying vertical velocity is prescribed, corresponding to two-dimensional waves with different amplitudes and phase angles. Additionally, a cosine modulation in the z direction, at the same amplitude of the principal harmonic, is used to speed-up flow tridimensionalisation and reduce the transition length, since the

4.2. ANALYSIS OF FULLY TURBULENT REGIME

Table 4.2: Boundary layer properties for finite-rate chemistry (CN) case at five downstream stations. In the following, $\text{Re}_x = \frac{\rho_\infty u_\infty x}{\mu_\infty}$ is the Reynolds number based on the distance from the leading edge x ; $\text{Re}_\theta = \frac{\rho_\infty u_\infty \theta}{\mu_\infty}$ is the Reynolds number based on the local momentum thickness; $\text{Re}_\theta^{\text{inc}} = \frac{\mu_\infty}{\mu_w} \text{Re}_\theta$ is the momentum-thickness-based Reynolds number in the incompressible scaling and $\text{Re}_\tau = \frac{\rho_w u_\tau \delta}{\mu_w}$ the friction Reynolds number. Δx^+ , Δy_w^+ , Δy_δ^+ and Δz^+ denote the grid size in inner variables in the x -direction, y -direction at the wall and at the boundary layer edge, and in the z -direction, respectively. Finally, $M_\tau = \frac{u_\tau}{c_w}$ stands for the friction Mach number and $H = \frac{\delta^*}{\theta}$ is the boundary layer shape factor. The last station, $\hat{x}=5100$, will be considered in the following for data analysis.

| \hat{x} | 1000 | 2000 | 3000 | 4000 | 5100 |
|---------------------------------|--------------------|---------------------|---------------------|---------------------|---------------------|
| Re_x | 5.04×10^6 | 10.03×10^6 | 15.04×10^6 | 20.04×10^6 | 25.54×10^6 |
| Re_θ | 1741 | 3141 | 4494 | 5784 | 7149 |
| $\text{Re}_\theta^{\text{inc}}$ | 272 | 494 | 705 | 907 | 1120 |
| Re_τ | 35 | 89 | 120 | 154 | 185 |
| Δx^+ | 2.04 | 2.78 | 2.58 | 2.50 | 2.45 |
| Δy_w^+ | 0.48 | 0.66 | 0.61 | 0.59 | 0.58 |
| Δy_δ^+ | 0.73 | 1.47 | 1.80 | 2.15 | 2.42 |
| Δz^+ | 1.35 | 1.83 | 1.70 | 1.65 | 1.61 |
| M_τ | 0.14 | 0.17 | 0.16 | 0.16 | 0.15 |
| H | 35.6 | 33.8 | 34.6 | 34.9 | 34.4 |

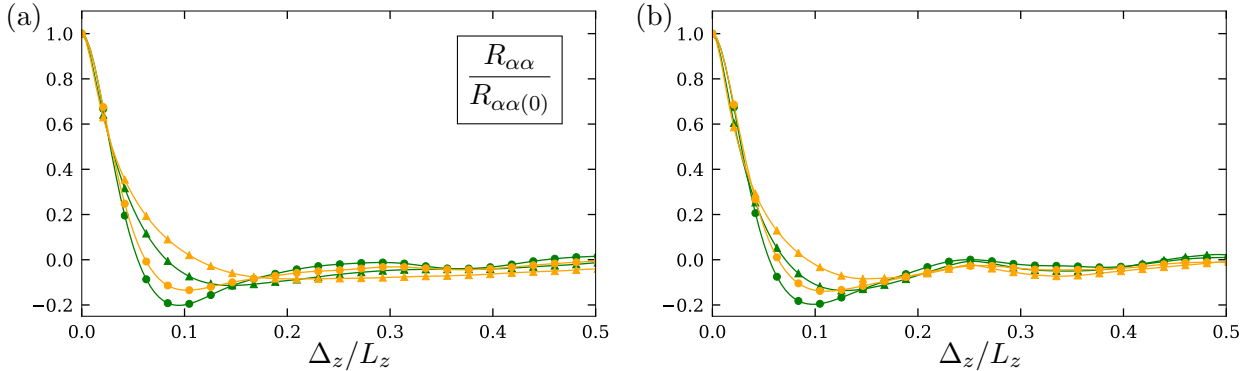


Figure 4.17: Distribution of two-point correlations in the spanwise direction, at $\text{Re}_\tau = 185$: $\alpha = u$, at $y^+ = 10$ ($\text{---}\bullet\text{---}$) and $y^+ = 150$ ($\text{---}\blacktriangle\text{---}$); $\alpha = \rho$, at $y^+ = 10$ ($\text{---}\bullet\text{---}$) and $y^+ = 150$ ($\text{---}\blacktriangle\text{---}$). Panel (a), CN case; panel (b), FR case.

investigation of breakdown to turbulence has already been carried out in section 4.1. The entire forcing function reads:

$$\frac{v_{\text{wall}}}{u_\infty} = e^{-0.4g(x)^2} A \left\{ \sin(2\pi g(x) - \omega t) + \cos(4\beta z) \left[0.008 \sin(2\pi g(x) - \omega t + \frac{\pi}{4}) + 1 \right] \right\}, \quad (4.7)$$

where $g(x) = (x - x_{\text{forc}})/L_{\text{forc}}$ and x_{forc} and L_{forc} denote the centerline of the forcing strip and its streamwise extent. The excitation frequencies and wavelengths are derived from the stability study of Marxen *et al.* (2014); specifically, we set $\omega = 1.70c_\infty/\delta_{\text{in}}^*$, $\beta = 0.04/\delta_{\text{in}}^*$ and $A = 0.025$. Lastly, the forcing strip is located at $\hat{x} = 300$ and it extends over $L_{\text{forc}} = 30\delta_{\text{in}}^*$.

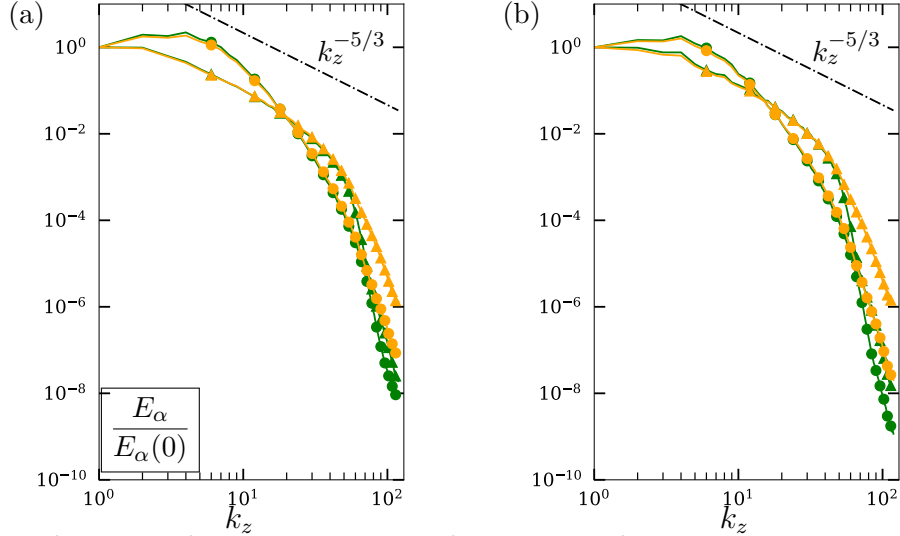


Figure 4.18: One-dimensional energy spectra in the spanwise direction, at $Re_\tau = 185$: $\alpha = \rho u^2$, at $y^+ = 10$ (\bullet) and $y^+ = 150$ (\blacktriangle); $\alpha = T$, at $y^+ = 10$ (\circ) and $y^+ = 150$ (\blacktriangleright). Panel (a), CN case; panel (b), FR case.

A fully turbulent state is achieved at streamwise locations corresponding to momentum Reynolds numbers approximately equal to 2300 and 2600 for the FR and CN simulations, respectively. In both cases, the fully turbulent region extends over approximately the last third of the computational domain. A global view of the computational domain is given in figure 4.19 showing the boundary conditions, the location of the forcing strip and the fully turbulent domain. A close-up view of the transitional zone is presented in the inset.

In such simulations the FD10LAD numerical scheme is used, with a filter amplitude of 0.1 and LAD coefficients equal to $C_\lambda = 0.01$ and $C_\beta = 1.75$. First- and second-order moments of various flow quantities are collected for more than three turnover times, after that the initial transient is evacuated and the flow has reached a statistically steady state. The sampling time interval is constant and equal to $\Delta t_{\text{stats}}^+ = \Delta t_{\text{stats}} \frac{u_\tau}{l_v} = 5.4 \times 10^{-2}$, for a total of ≈ 70000 samples.

4.2.2 Results

4.2.2.1 First-order statistics

Figure 4.20 reports the distribution of the skin friction coefficient together with Blasius' laminar correlation rescaled for compressible boundary layers, which is shown to be in excellent agreement with C_f up to the suction-and-blowing forcing location. The large temperatures close to the wall lead to a strong friction heating of the boundary layer, and consequently to rather small values of the scaled momentum-thickness Reynolds number $Re_\theta^{\text{inc}} = \frac{\mu_\infty}{\mu_w} Re_\theta$, in the range $270 \div 950$ for the fully turbulent region. Accordingly, the friction Reynolds number is $Re_\tau \approx 200$ at the rear end of the plate, as shown in table 4.2. Despite the very high wall temperature, finite-rate chemistry little affects the skin friction distribution in the laminar and fully turbulent regions, where the chemical non-equilibrium and frozen flow models give very similar results. Significant quantitative discrepancies are observed only in the transition region, albeit the qualitative trends are close-by. Figure 4.21

4.2. ANALYSIS OF FULLY TURBULENT REGIME

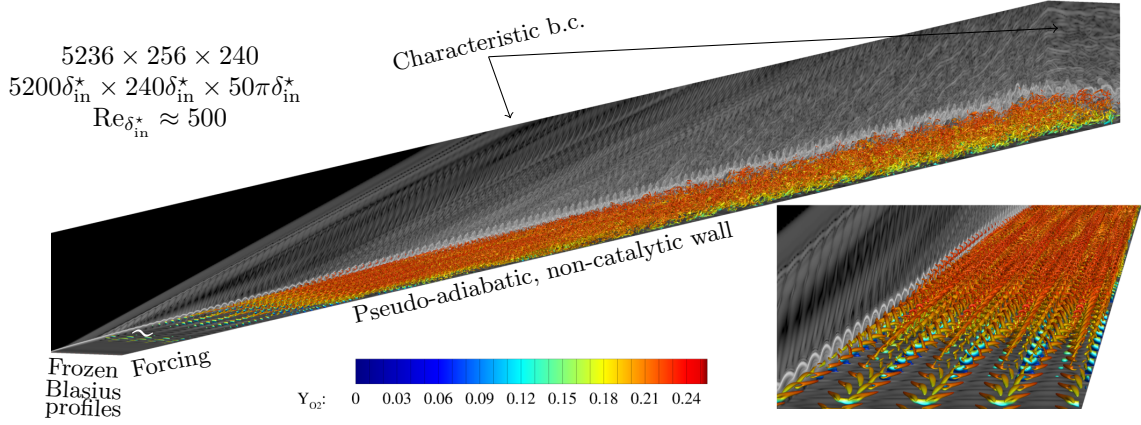


Figure 4.19: Isosurfaces of Q -criterion, colored with the local values of O_2 mass fraction for the CN case. The entire computational domain is displayed, along with a zoom on the laminar-to-turbulent transition region.

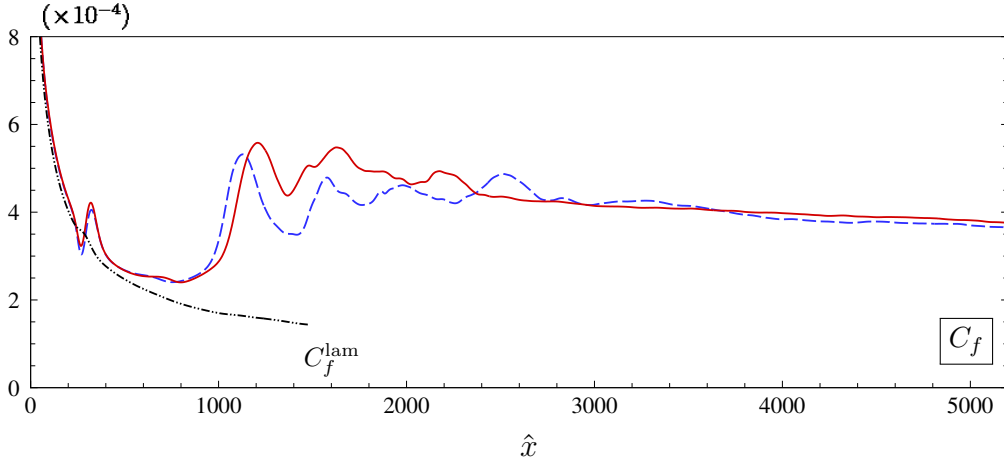


Figure 4.20: Wall distributions of the skin friction coefficient C_f as a function of Re_x . (—), CN case; (---), FR case. The black dash-dotted lines denote the laminar correlation C_f^{lam} .

shows instantaneous visualizations of the streamwise velocity in a plane parallel to wall extracted at $y \approx 4.5\delta_{\text{in}}^*$. Due to the significant spanwise distortion introduced at the forcing point, streamwise vortical structures and streaks are generated immediately downstream, leading to a sudden increase of C_f which deviates from the laminar correlation. Their complex interaction produces a sharp increase of the skin friction and leads to instabilities growth in the region ranging from $\hat{x} \approx 1000$ to $\hat{x} \approx 2000$, characterized by sinuous streak motions and interactions and by an oscillatory behavior of the skin friction, differently from the case in section 4.1. The flow finally bursts into turbulence at $\hat{x} \approx 3000$ and relaxes subsequently toward a fully turbulent state. We observe that the initial overshoot is slightly delayed in the CN flow, and fine details of the transitional region are different, both in the instantaneous field and in the average quantities. Finite-rate chemistry effects alter the mixture composition as the flow evolves along the plate and modify its thermo-physical properties, as shown in figure 4.22(a)-(b)

4.2. ANALYSIS OF FULLY TURBULENT REGIME

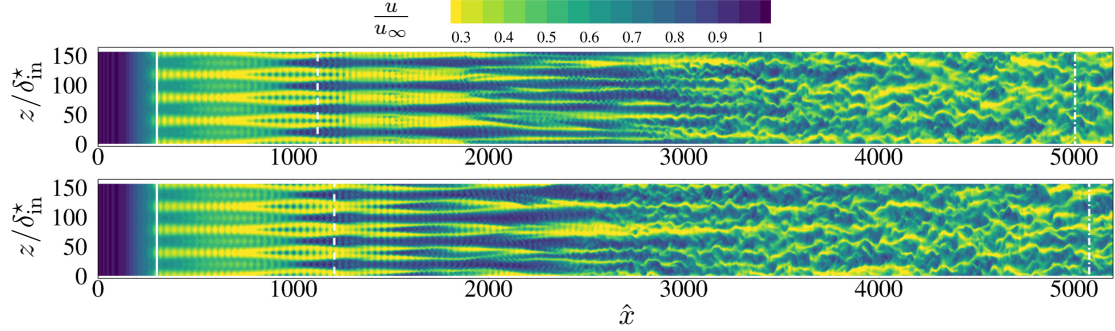


Figure 4.21: Instantaneous visualizations of the normalized streamwise velocity in a $x-z$ plane for FR case (top) and CN case (bottom) at $y \approx 4.5\delta_{in}^*$ (corresponding to $y^+ \approx 30$ at $\hat{x} = 5100$). The spanwise white solid lines denote the blowing-and-suction forcing location; the dashed lines mark the position of the first peak of C_f and the dash-dot lines indicate the streamwise position at which $Re_\tau = 185$. The spanwise direction is stretched for better visualization.

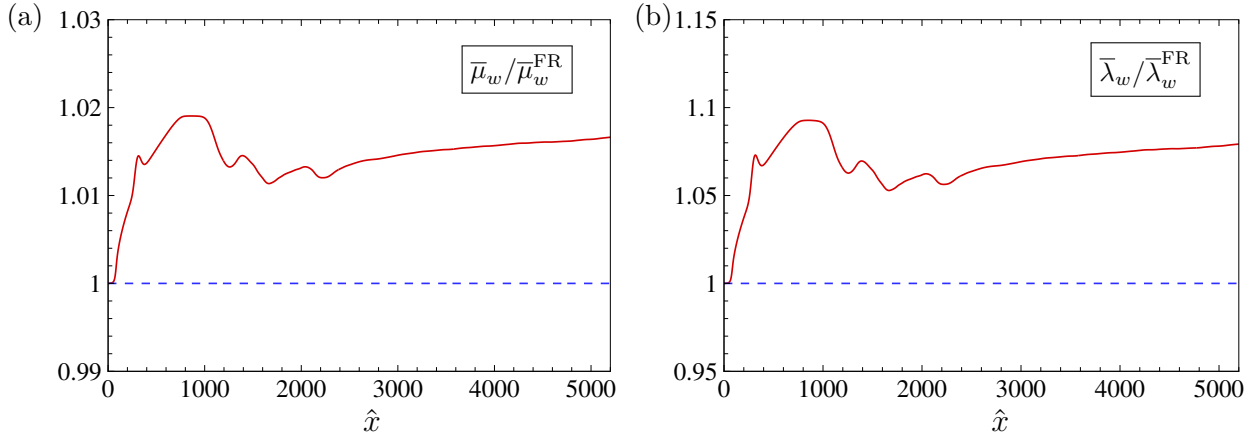


Figure 4.22: Streamwise evolution of averaged dynamic viscosity $\bar{\mu}$ (a) and thermal conductivity $\bar{\lambda}$ (b) at the wall, normalized with respect to the constant values of the FR case. (—), CN case; (---), FR case.

displaying the streamwise evolution of the averaged molecular viscosity and thermal conductivity along the wall. Unlike the FR case, where the transport properties are univocally fixed through the imposed wall temperature, for CN these vary according to the evolving local composition, with deviations of the order of 1.5% for the viscosity and 7% for the thermal conductivity. This leads in turn to slightly lower local Reynolds numbers for the chemically-reacting case. Both quantities rapidly depart from their inlet values, reaching a peak approximately at the same location where C_f overshoots. The variation of the transport coefficients becomes more smooth in the fully turbulent region, where they gradually increase as a consequence of O_2 dissociation and atomic oxygen formation (the latter being characterized by larger diffusion coefficients).

Wall distributions of the averaged species mass fractions for O_2 , NO , O and N are shown in Figure 4.23. At the selected flow conditions, dissociation of O_2 (and, to a much smaller extent, of N_2) is quickly activated downstream of the inlet boundary, leading to sudden formation of atomic oxygen and nitric

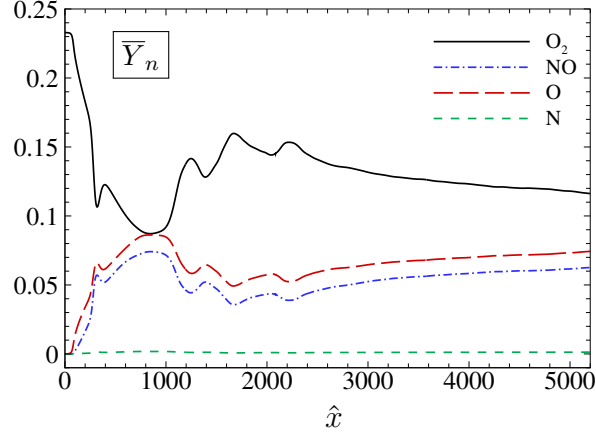


Figure 4.23: Streamwise evolution of the averaged mass fractions \bar{Y}_n at the wall for species O_2 , NO , O and N . \bar{Y}_{N_2} is not shown being outside the y -axis bounds.

oxide. The amounts of molecular oxygen and nitrogen decrease (and, conversely, increase for the other species) until the location of maximum C_f is reached. The trend is reverted from this point on, due to increased mixing with the external layers. The subsequent series of secondary peaks in the range $\hat{x} \in [1000, 2300]$ are registered roughly in correspondence of those observed in the C_f distribution. For $\hat{x} > 2300$, the mass fractions tend to their chemical equilibrium composition values at the given T_w and \bar{p}_w , albeit their slow variation indicates that the characteristic chemical time scales are much smaller than the local residence flow time. This is confirmed by the increasing downstream amounts of NO , an intermediate product generated by the Zel'dovich mechanism that would be subsequently consumed to produce atomic nitrogen, and by streamwise values of Y_N , which are almost negligible across the entire flat plate. The different trend with respect to figure 4.4(c) is uniquely due to the different forcing strategy and the higher wall temperature of the present case; the latter promotes a more significant chemical activity. In the following, the analysis will focus on a selected streamwise station in the fully turbulent region. Due to the relatively small range of Reynolds numbers covered in the turbulent portion of the computational domain, the nondimensional flow profiles do not vary substantially along the flat plate; therefore, a single location will be considered for data analysis. Specifically, we examine the station at which $Re_\tau = 185$ (see table 4.2), corresponding to $\hat{x} = 5100$ for the CN case and $\hat{x} = 5045$ for the FR case. Unless specified otherwise, wall-normal profiles are plotted in inner scaling, i.e. against the wall coordinate y^+ . Figure 4.24(a) displays the longitudinal velocity profiles rescaled according to the classical Van Driest transformation

$$u_{VD}^+ = \frac{1}{u_\tau} \int_0^{\bar{u}} \sqrt{\frac{\bar{\rho}}{\bar{\rho}_w}} du, \quad (4.8)$$

as a function of the inner wall coordinate. The van Driest scaling collapses well velocity profiles for both CN and FR cases in the linear and logarithmic zone; in the outer region the profiles are not perfectly superposed due to the different behavior of $\bar{\tau}_w$ and $\bar{\rho}_w$ which results in slightly different values of u_τ . Of note, the value of the von Karman constant used in the log law is slightly smaller than the classical one, that is $\kappa \approx 0.38$ as suggested by Nagib & Chauhan (2008) and Monkewitz (2017), resulting in a more accurate prediction of the slope of the velocity profile in the logarithmic region. The wall-normal mean temperature profiles reported in figure 4.24(b) show that values for the

4.2. ANALYSIS OF FULLY TURBULENT REGIME

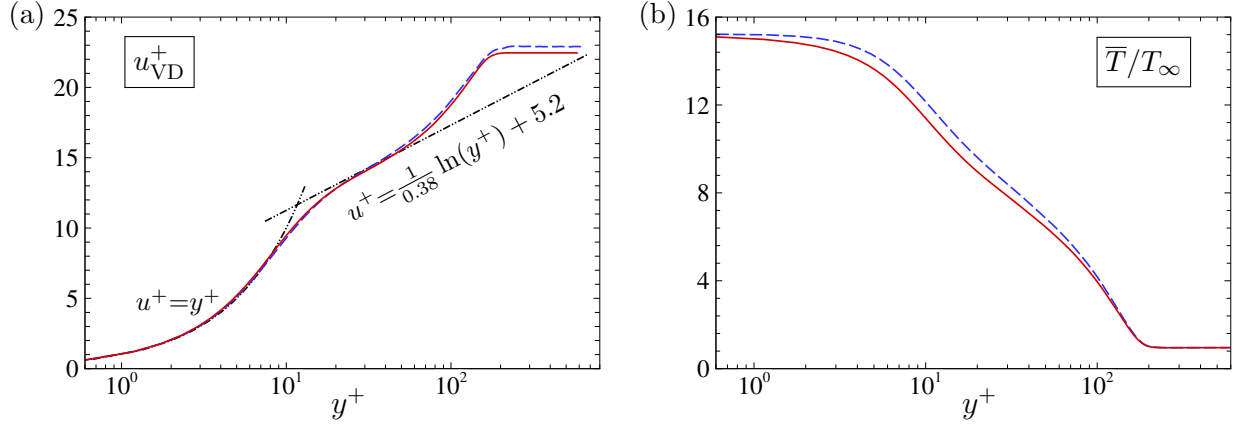


Figure 4.24: Wall-normal profiles of the van Driest-transformed streamwise velocity (a) and of the normalized mean temperature (b) at $Re_\tau = 185$. (—), CN case; (---), FR case.

CN boundary layer are below the FR ones by approximately 5% in the buffer region, as an expected consequence of the preponderant endothermic behavior of chemical processes. On the contrary, the mean density profiles (not shown) are not particularly affected by chemical activity, which redistributes the changing mixture composition, but does not directly alter the mean mixture density. For the sake of clarity, the two curves in figure 4.24(b) do not exactly reach the value one at the freestream since a little compression, starting from the inlet, is present (even if the leading-edge is not considered).

Wall-normal average distributions of transport properties, Prandtl number $\overline{Pr} = \overline{\mu c_p / \lambda}$, specific heat capacity $\overline{c_p}$ and specific heat ratio $\overline{\gamma} = \overline{c_p / c_v}$ are shown in figure 4.25. While chemical activity weakly affects the viscosity profile (as discussed before), larger thermal conductivity and isobaric specific heat values (by approximately 6% and 15%, respectively) are observed in the near wall region for the chemically reacting flow compared to the frozen one. These deviations alter the wall-normal profile of \overline{Pr} (albeit the absolute values never differ by more than 10%), which exhibits a non-monotonic behavior, with a minimum at the wall and a peak in the logarithmic region. No major differences are observed by comparing \overline{Pr} and $\overline{\mu c_p / \lambda}$, indicating that that the peculiar behavior of \overline{Pr} is an effect of the modified mean-flow flow properties and not of the turbulent activity. Finally, changes in chemical composition also lead to minor modifications of the mean specific heat ratio $\overline{\gamma}$ in the inner region of the boundary layer. The latter varies with the temperature in both simulations, deviating from the classical value of 1.4. A larger near-wall value is observed in the reacting flow, also leading to a slightly higher average speed of sound $\overline{c} = \sqrt{\overline{\gamma R T}}$ (not shown).

The next series of figures focuses on the behavior of the chemically reacting mixture. Figure 4.26 shows the wall-normal evolution of the average Lewis and Schmidt numbers for each species, $\overline{Le}_n = \overline{\lambda / \rho c_p D_n}$ and $\overline{Sc}_n = \overline{\mu / \rho D_n}$. Larger Lewis numbers indicate that thermal diffusivity effects tend to dominate mass diffusivity; similarly, for higher Schmidt numbers diffusion of momentum dominates mass diffusion. N and O, characterized by higher diffusion coefficients than other species, also exhibit smaller \overline{Le} and \overline{Sc} numbers in the reacting near-wall layer, meaning that the two atoms diffuse faster into the rest of the mixture. Moving towards the edge of the boundary layer, both non-dimensional coefficients decrease for N_2 and O_2 , and increase for the atoms. Overall, variations of \overline{Le} and \overline{Sc} across the boundary layer are of the order of 20% for all species except NO, for which the profiles are

4.2. ANALYSIS OF FULLY TURBULENT REGIME

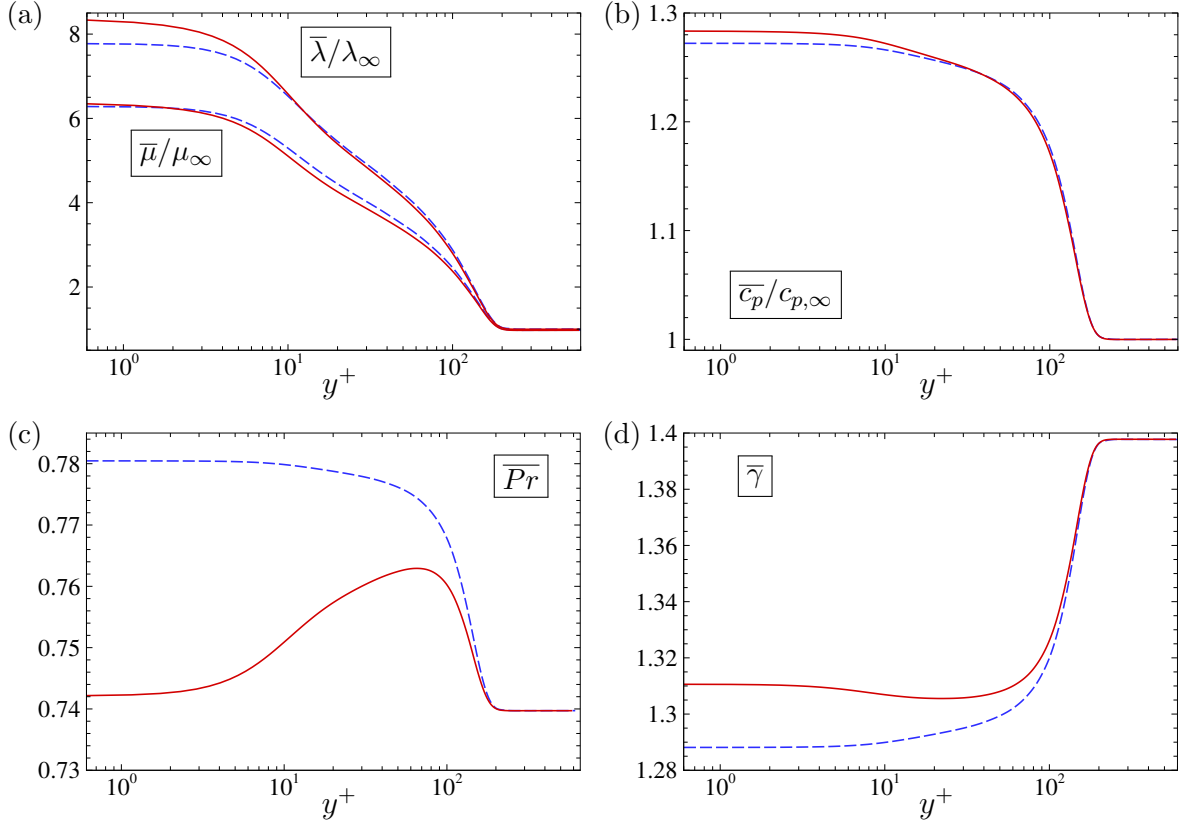


Figure 4.25: Wall-normal mean profiles of viscosity and thermal conductivity (a), specific heat capacity at constant pressure (b), Prandtl number (c) and specific heat ratio γ (d) at $Re_\tau = 185$. (—), CN case; (- - -), FR case.

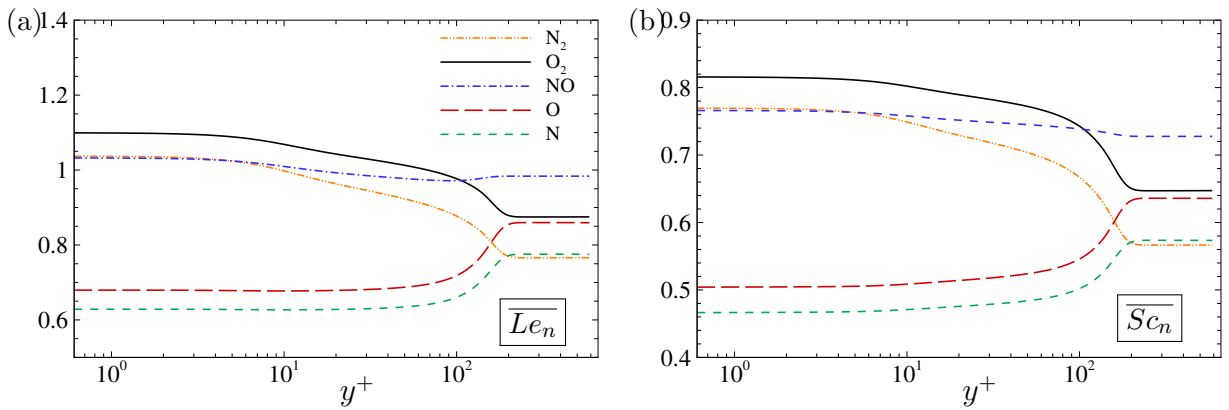


Figure 4.26: Wall-normal evolution of mean Lewis number (a) and Schmidt number (b) at $Re_\tau = 185$, for the chemically-reacting simulation, in inner scaling.

almost constant; moreover, the local fluctuations amount to less than 1% of the corresponding mean values. We conclude therefore that the use of simplified transport models based on the assumption of

4.2. ANALYSIS OF FULLY TURBULENT REGIME

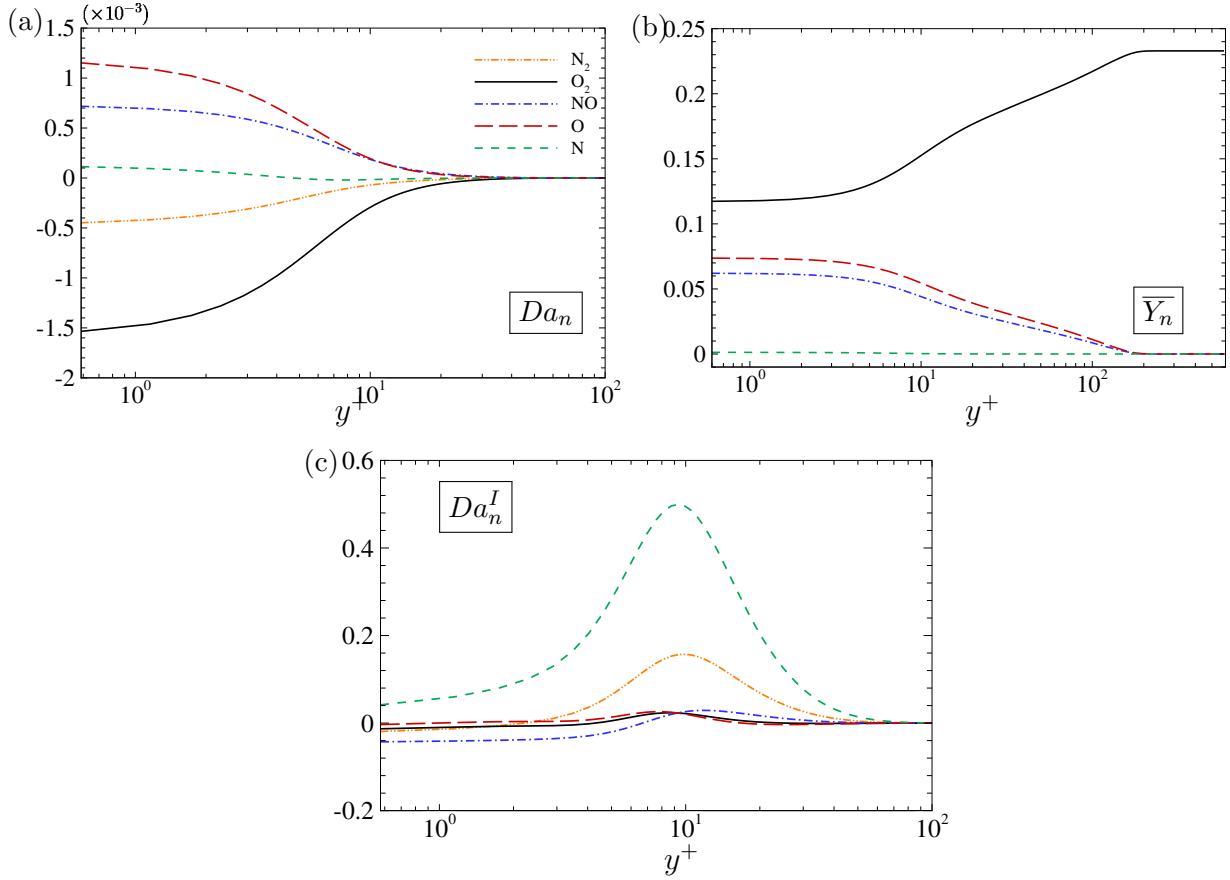


Figure 4.27: Wall-normal profiles of the average Damköhler number (a), species mass fractions (b), and species Damköhler number Da_n^I at $Re_\tau = 185$. In panel (b), N_2 is not shown, being $Y_{N_2} > 0.25$.

constant Le and Sc numbers constitute an acceptable first approximation, at least for thermodynamic conditions similar to those currently under investigation. The average profiles of the n -th species Damköhler number $Da_n = \dot{\omega}_n / \rho \bar{\mu}_w / \bar{\tau}_w$ and mass fraction \bar{Y}_n are reported in figure 4.27(a) and 4.27(b), respectively. The magnitude of Da_n represents the ratio of the flow characteristic time scale to the chemical time scale, while its positive or negative sign indicates production or depletion of a species, respectively. Note that the present definition of Da_n is based on the characteristic time scale of the inner boundary layer region. The small values observed in figure 4.27(a) imply that chemical reactions are characterized by much longer time scales than the residence time of the flow structures; in other terms, the flow is never too far from frozen-chemistry conditions, even in the near-wall region, justifying the relatively small differences registered between the FR and CN cases. Mass fraction profiles confirm that most of the chemical activity is localized in the viscous sublayer, where O_2 dissociates at a high rate. To quantify the strength of turbulence/chemistry interactions, i.e. the influence of temperature and species mass fractions fluctuations on species production rates, profiles of the species interaction Damköhler number are reported in figure 4.27(c). This quantity, defined as

$$Da_n^I = \frac{\overline{\omega_n(T, \rho_n)} - \omega_n(\bar{T}, \bar{\rho}_n)}{\overline{\omega_n(T, \rho_n)}_w}, \quad (4.9)$$

4.2. ANALYSIS OF FULLY TURBULENT REGIME

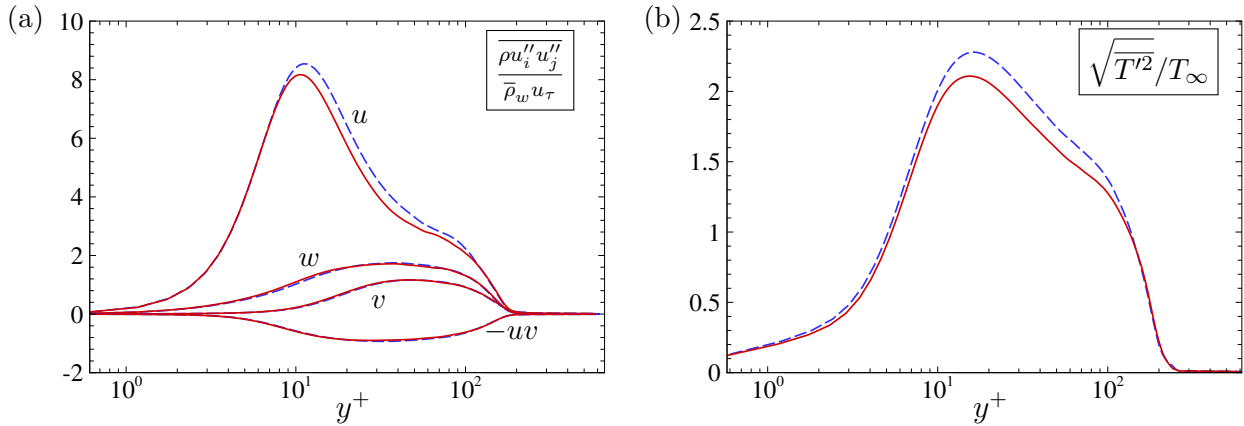


Figure 4.28: Wall-normal profiles of Reynolds stresses (a) and of the normalized r.m.s. temperature (b), at $Re_\tau = 185$. (—), CN case; (---), FR case.

represents a measure of chemical production due to the turbulent fluctuations in Arrhenius' law, i.e. of the difference $\overline{\omega_n(T, \rho_n)} - \omega_n(\bar{T}, \bar{\rho}_n) \neq 0$ due to the nonlinearity of ω_n . Da_n^I takes rather small values across most of the boundary layer, except in the buffer region, where turbulent fluctuations are large enough to generate a significant contribution. Coherently with figure 4.27(a), the species most affected are the ones with the smaller Da_n (i.e., N and N_2), because of their larger sensitivity to temperature and density fluctuations deriving from turbulent motions. Conversely, the most chemically-active species are characterized by small values of Da_n^I , indicating that turbulence/chemistry interactions are somewhat contained in the flow under investigation. A direct consequence is that the evolution of the dynamic quantities is mostly decoupled from that of the chemical species, as discussed in the following by examination of turbulence intensities and energy spectra.

4.2.2.2 Second-order statistics

To further analyze the effect of finite-rate chemistry on turbulent quantities, the wall-normal profiles of Favre-average-based Reynolds stresses are reported in figure 4.28(a). The frozen-flow solution is also reported for reference on the same figure. We observe that finite-rate chemical reactions in the near-wall region partly drain energy from the turbulent fluctuations, which reach a slightly lower peak value of $\overline{\rho u_i'' u_j''} / \bar{\rho}_w u_\tau^2$ in the region of maximum turbulent production. No significant effects are observed for the other Reynolds stress components; a similar behavior has been also registered by [Duan & Martín \(2011\)](#). Contrary-wise, chemical activity does have an effect on the root mean square (r.m.s.) temperature fluctuations $\sqrt{T'^2}/T_\infty$ (reported in figure 4.28b), which exhibit a peak value reduced by approximately 10% with respect to the non-reacting case. Interestingly, the location of the largest temperature fluctuations corresponds to a peak in the species fluctuating mass fractions, also located in the buffer layer (figure 4.29), although the near-wall region is hotter. The most significant fluctuations are obtained for molecular oxygen, which is the most active species in the reaction mechanism; on the contrary, the fluctuating quantities of atomic nitrogen mass fraction are negligible with respect to the other species in the mixture. We will draw further considerations in Chapter 5 which, despite the lower chemical activity, will result being more interesting in terms of turbulent mixing.

Averages of unclosed convective and diffusive fluxes arising from Favre-averaging of the governing

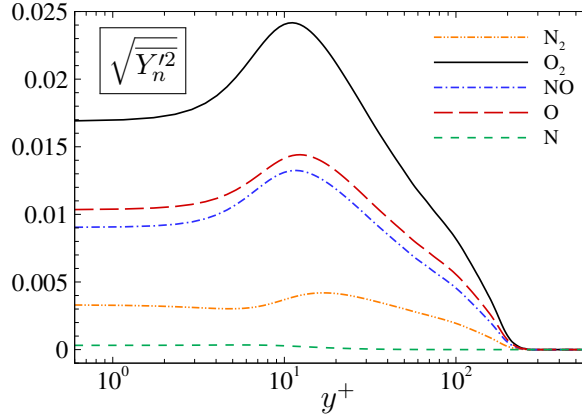


Figure 4.29: Wall-normal profiles of r.m.s. mass fractions at $\text{Re}_\tau = 185$ for the CN case.

equations were also collected to verify the validity of some common modeling assumptions adopted in lower-fidelity simulations relying on the Reynolds-Averaged Navier-Stokes (RANS) equations. Special focus is put into closures of the turbulent heat transport terms arising in the averaged total energy and species transport equations. By applying a Favre averaging to the total energy equation (2.5) one obtains:

$$\begin{aligned} \frac{\partial \bar{\rho} \tilde{E}}{\partial t} + \frac{\partial}{\partial x_j} \left[\bar{\rho} \tilde{u}_j \left(\tilde{h} + \frac{\tilde{u}_i \tilde{u}_i}{2} \right) + \tilde{u}_j \frac{\overline{\rho u_i'' u_j''}}{2} \right] = \\ \frac{\partial}{\partial x_j} \left[-\bar{q}_j - \overline{\rho u_j'' h''} + \overline{\tau_{ij} u_i''} - \overline{\rho u_j'' \frac{1}{2} u_i'' u_i''} \right] + \frac{\partial}{\partial x_j} \left[\tilde{u}_i \left(\tilde{\tau}_{ij} - \overline{\rho u_i'' u_j''} \right) \right]. \end{aligned} \quad (4.10)$$

It is common practice to model the turbulent transport of a flow property f as a linear function of its average gradient, e.g.:

$$-\overline{\rho u'' f''} = \frac{\mu_t}{C_t} \frac{\partial \tilde{f}}{\partial x}, \quad -\overline{\rho v'' f''} = \frac{\mu_t}{C_t} \frac{\partial \tilde{f}}{\partial y}, \quad -\overline{\rho w'' f''} = \frac{\mu_t}{C_t} \frac{\partial \tilde{f}}{\partial z}, \quad (4.11)$$

the last term being zero for the present statistically 2D flow. Here, μ_t denotes the turbulent viscosity and C_t an *ad hoc* coefficient. The turbulent heat transport terms are usually modeled by introducing a “turbulent” Prandtl number defined as

$$\text{Pr}_t = \frac{\overline{\rho u'' v''} \partial \tilde{T} / \partial y}{\overline{\rho v'' T''} \partial \tilde{u} / \partial y}, \quad (4.12)$$

which is expected to be approximately equal to 1 throughout the flow, according to the classical so-called Strong Reynolds Analogy (SRA) first discussed by Morkovin & Favre (1962). The latter holds under the hypothesis of adiabatic wall, nearly constant total temperature and fully anticorrelated velocity and temperature fluctuations, that is

$$-R_{u'' T''} = -\frac{\overline{u'' T''}}{\sqrt{\overline{u''^2}} \sqrt{\overline{T''^2}}} \approx 1. \quad (4.13)$$

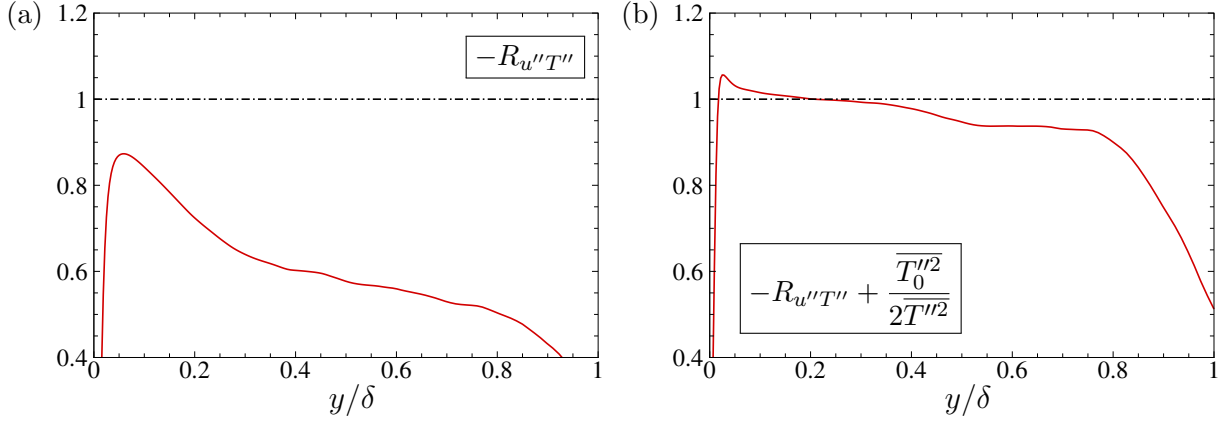


Figure 4.30: Correlation coefficient between u'' and T'' without total temperature correction (a) and with total temperature correction (b), at $\text{Re}_\tau = 185$. (—), CN case; (---), SRA estimation.

For flows with large total temperature fluctuations (such as in the current case), equation (4.13) is corrected to account for them (Guarini *et al.*, 2000):

$$-R_{u''T''} + \frac{\overline{T_0''^2}}{2\overline{T''^2}} \approx 1. \quad (4.14)$$

Figure 4.30 presents the uncorrected (4.13) and corrected (4.14) correlation distributions across the boundary layer, in outer scaling. Clearly, only the corrected correlation approaches reasonably well unity for the present high-enthalpy and high Mach number flow. The assumption is however never satisfied in the outer part of the boundary layer, as also found in the work of Duan & Martín (2011). The turbulent Prandtl number is presented in figure 4.31. For air out of chemical equilibrium, Pr_t follows essentially the trend registered by numerous authors in the literature (Huang *et al.*, 1995; Duan *et al.*, 2010a, 2011; Zhang *et al.*, 2018) and is not constant throughout the flow, in contrast with the SRA assumption which predicts $Pr_t \approx 1$. In the logarithmic and outer layers, Pr_t approaches the value of 0.9, commonly used in turbulence models. A local maximum at about $y^+ = 30$ is observed; in the near-wall region, Pr_t exceeds 1 and becomes singular at the wall due to the quasi-adiabatic boundary condition.

Similarly to the procedure followed for the total energy equation, the Favre averaging of the species transport equation (2.6) leads to

$$\frac{\partial \bar{\rho} \tilde{Y}_n}{\partial t} + \frac{\partial (\bar{\rho} \tilde{Y}_n \tilde{u}_j)}{\partial x_j} = \frac{\partial}{\partial x_j} \left(\bar{\rho} \tilde{D}_n \frac{\partial \tilde{Y}_n}{\partial x_j} \right) + \bar{\rho} \tilde{\omega}_n + \frac{\partial}{\partial x_j} \overline{\rho u_j'' Y_n''} + \frac{\partial}{\partial x_j} \overline{\rho D_n'' \frac{\partial Y_n''}{\partial x_j}} + \bar{\rho} V_c, \quad (4.15)$$

where the unclosed terms are the turbulent transport of chemical species, $\frac{\partial}{\partial x_j} \overline{\rho u_j'' Y_n''}$, and the turbulent species diffusion, $\frac{\partial}{\partial x_j} \overline{\rho D_n'' \frac{\partial Y_n''}{\partial x_j}}$. The last term on the r.h.s., $\bar{\rho} V_c$, resulting from Favre-averaging of the mass diffusion term in equation (2.33), was found to be negligibly small throughout the flow and is not discussed further. The exact turbulent transport and diffusion terms computed from the DNS data are reported in figure 4.32. The turbulent transport of species in the streamwise and wall-normal directions

4.2. ANALYSIS OF FULLY TURBULENT REGIME

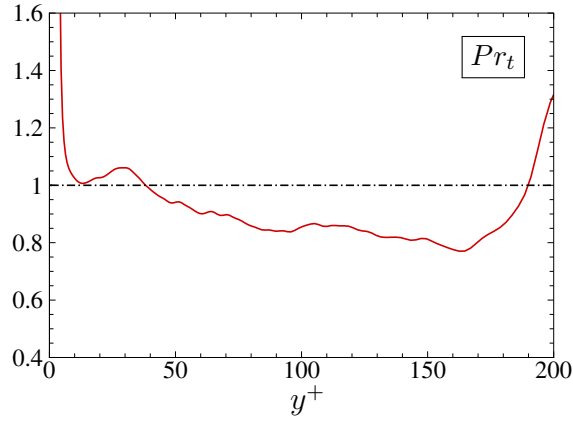


Figure 4.31: Wall-normal profiles of the turbulent Prandtl number for CN case, at $Re_\tau = 185$. The horizontal dashed-dotted lines denote the SRA estimation.

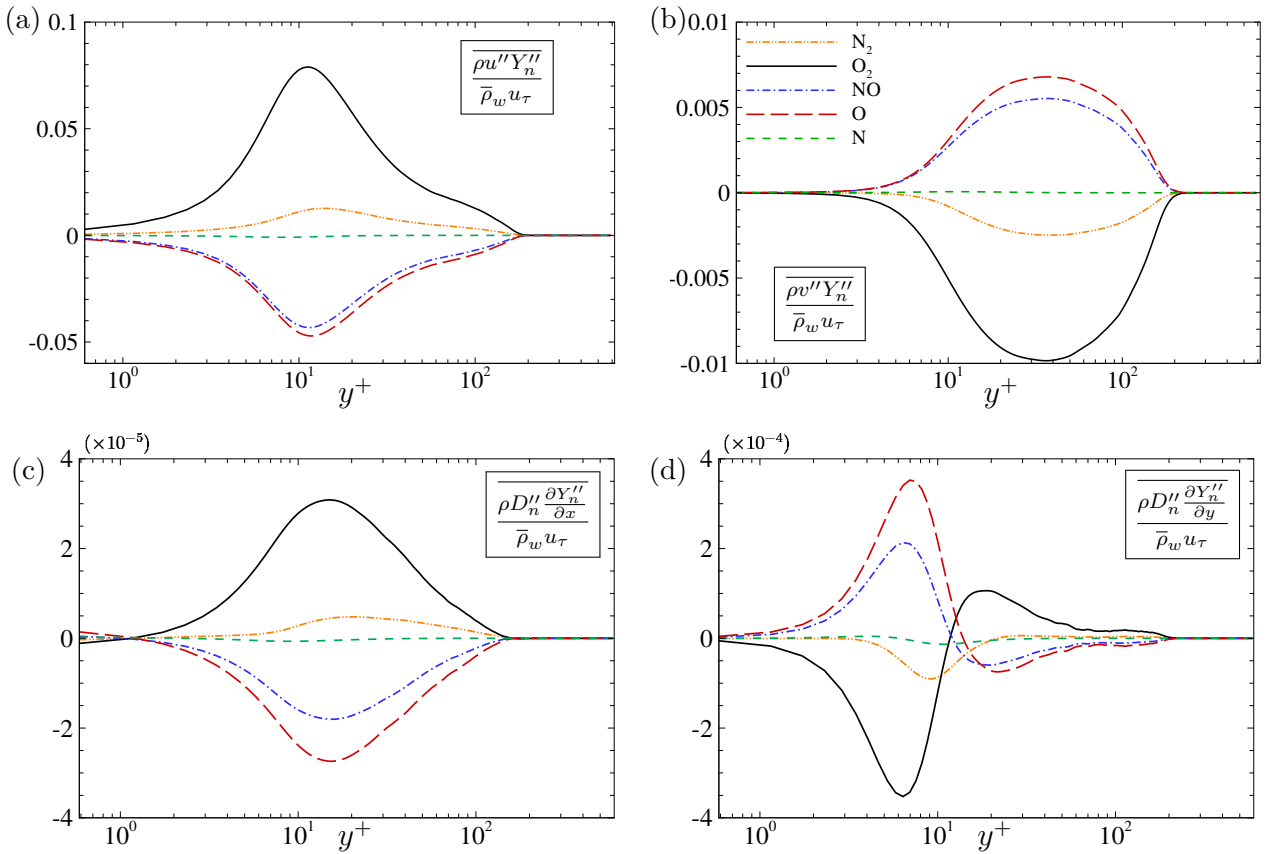


Figure 4.32: Normalized turbulent transport of species mass fractions in the streamwise (a) and wall-normal (b) directions; normalized turbulent diffusion fluxes in the streamwise (c) and wall-normal (d) directions, at $Re_\tau = 185$.

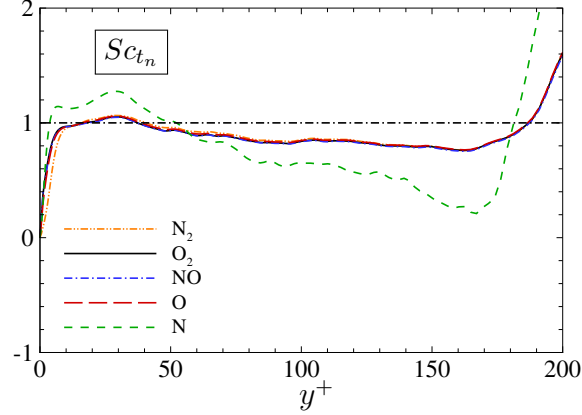


Figure 4.33: Wall-normal profiles of the turbulent Schmidt number for CN case, at $Re_{\tau} = 185$. The horizontal dashed-dotted lines denote the SRA estimation.

(panels a and b) are preponderant in the buffer and logarithmic zone. The turbulent diffusion terms along x and y directions (panels c and d) are 1 or 2 orders of magnitude smaller; in particular, $\overline{\rho D_n'' \frac{\partial Y_n''}{\partial x}}$ is active in the region where $\overline{\rho u'' Y_n''}$ peaks, and its contribution can certainly be neglected. However, $\overline{\rho D_n'' \frac{\partial Y_n''}{\partial y}}$ is not completely negligible compared to the other terms in the viscous sublayer and the buffer region, even though, in the RANS approach, the turbulent fluxes deriving from the diffusive terms are not accounted for explicitly. Likewise the turbulent heat transport fluxes, the species transport fluxes are modeled by introducing a turbulent Schmidt number, e.g.:

$$Sc_{tn} = \frac{\overline{\rho u'' v'' \partial \tilde{Y}_n / \partial y}}{\overline{\rho v'' Y_n'' \partial \tilde{u} / \partial y}}, \quad (4.16)$$

such that

$$-\overline{v'' Y_n''} = \frac{\mu_t}{Sc_{tn}} \frac{\partial \tilde{Y}_n}{\partial y} \quad (4.17)$$

in the wall normal direction, and similarly for the other directions. Figure 4.33 reports the Sc_{tn} profiles for the five species. In all cases, a value reasonably close to unity (corresponding to the common modeling practice) is observed in the logarithmic and outer regions of the boundary layer for all species except N, which is characterized by a very low species mass flux and by some peculiarities that we will see in Chapter 5. Such approximation fails in the near-wall region, where $\partial \tilde{Y}_n / \partial y \approx 0$ due to the non-catalytic boundary condition.

4.2.2.3 Spectral content

To characterize the near-wall turbulent structures, premultiplied spectra of the fluctuating wall-normal and streamwise velocities, as well as of the temperature, are reported in fig. 4.34 as a function of the normalized spanwise wavenumber λ^+ . The well developed spectra indicate that a fully turbulent state has been reached at this position and no memory of the forcing strategy is present. The spectral content is not significantly altered by chemical effects, and the overall trend is similar to perfect-gas simulations (Sciacovelli *et al.*, 2020). All of the spectra exhibit a peak in the buffer layer, at the same

4.2. ANALYSIS OF FULLY TURBULENT REGIME

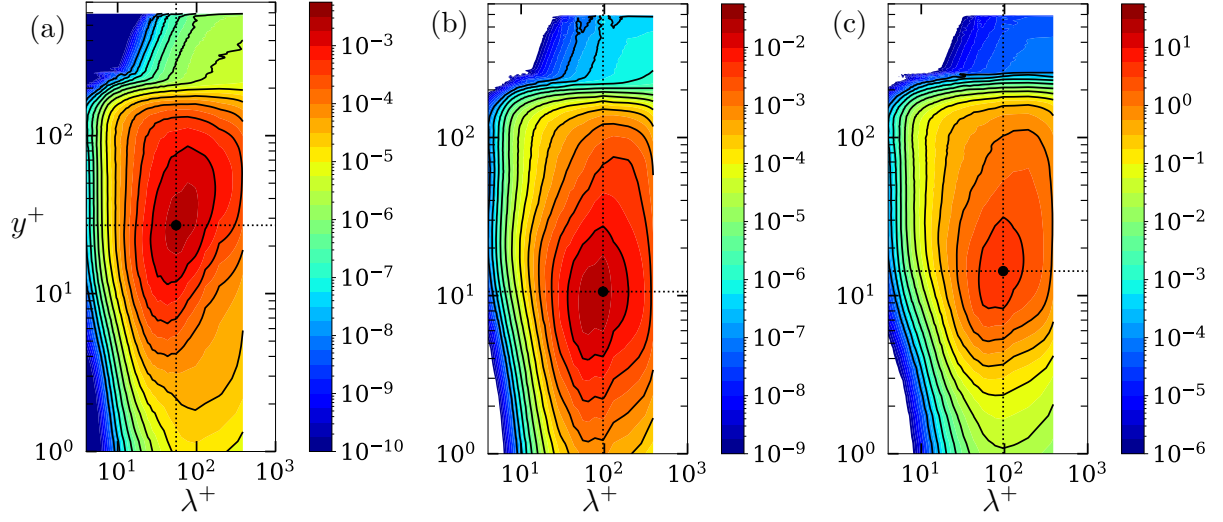


Figure 4.34: Premultiplied spanwise spectra $k_z E_{vv}/u_\infty^2$ (a), $k_z E_{uu}/u_\infty^2$ (b) and $k_z E_{TT}/T_\infty^2$ (c) for the chemical non-equilibrium simulation, at $\text{Re}_\tau = 185$.

location were the Reynolds stresses and the temperature fluctuations peak (see figure 4.28). The same spectra have been computed for the FR case (see Appendix D) and they exhibit the same trend.

SUMMARY

DNSs of hypersonic spatially-developing turbulent adiabatic boundary layers have been performed, taking into account the effect of finite-rate chemistry. The breakdown to turbulence is first investigated and the analysis of the fully turbulent regime is then illustrated.

- Second-mode transition scenario and full breakdown:
 - The suction-and-blowing method excite a Mack mode, along with lower-amplitude disturbances, both harmonic and subharmonic.
 - The laminar evolution matches the solution of the locally self-similar theory also after the forcing strip.
 - Second-mode transition dominated by the growth of subharmonic modes: fundamental mode saturates quickly and transfers energy to 2D and oblique subharmonic modes whose interaction lead to the formation of λ -vortices
 - Further downstream streaks cause breakdown to turbulence.
 - DMD analysis shows that the DNS field up to the transition region is faithfully represented by a subharmonic mode, streaks appearing at the last stages of transition.
 - Chemical activity does not affect the subharmonic transition scenario.
- Analysis of the fully turbulent regime and comparison against frozen-chemistry assumption:
 - The highest temperature is reached at the wall due to the adiabatic condition. The mixture composition and transport properties vary in the region comprised between the wall and buffer layer; these remain constant in a frozen-flow boundary layer.
 - Mean dynamic quantities are weakly altered by chemical activity.
 - Low Damköhler numbers are obtained: chemical dissociation is much slower than the flow characteristic time scales, i.e. the flow is not far from frozen-flow conditions. No significant Turbulence-Chemistry Interactions due to the quasi-frozen composition.
 - The endothermic nature of chemical reactions drain (a small amount of) energy from the flow, leading to smaller streamwise turbulent intensities, mean and r.m.s. temperature values.
 - The peak of species mass fractions fluctuations is registered in correspondence of the maximum turbulent activity.
 - Atomic species diffuse faster than molecular ones inside the boundary layer.
 - The Strong Reynolds Analogy still holds, despite the presence of chemical activity. In order to close the turbulent transport term in the species conservation equations, a turbulent Schmidt number value close to unity is acceptable, albeit species-dependent coefficients should preferably be adopted.

Chapter 5

Cold-wall hypersonic turbulent boundary layers

Contents

| | |
|--|------------|
| 5.1 Simulations setup and definitions | 104 |
| 5.2 Results | 105 |
| 5.2.1 Global flow properties | 105 |
| 5.2.2 Velocity statistics | 107 |
| 5.2.3 Thermal non-equilibrium effects | 108 |
| 5.2.4 Chemical activity | 120 |
| 5.2.5 Compressibility effects | 122 |

In this chapter, the coupling between turbulence and both thermal and chemical non-equilibrium effects is discussed. The configuration under investigation is a cooled flat-plate boundary layer, subjected to post-shock conditions of a 6° sharp wedge moving at Mach 20, at an altitude of approximately 36 km. Currently, no manned vehicle is capable of flying at such low altitudes and high velocities simultaneously. As for now, hypersonic spacecrafts exist in an experimental phase and do not exceed Mach numbers of 10; ballistic missiles instead could operate at such high Mach numbers, albeit in a short part of their trajectories. Nevertheless, technological progress is pushing towards new hypersonic vehicle concepts capable of sustaining trans-atmospheric or endo-atmospheric flights, engendering at the same time complex thermochemical effects due to the high temperatures, turbulent regime because of the higher Reynolds numbers, and high heat transfer rates due to strong wall cooling; whence the interest for the investigation of these severe thermodynamic conditions. The selected edge thermodynamic state is such that a vibrational non-equilibrium layer occurs, sustained by the turbulent mixing, whereas chemical activity stays relatively weak. The results of the present DNS will further elucidate the validity of certain scalings and correlations, coupled with the presence of thermochemical non-equilibrium.

In the following, section 5.1 describes the setup and the numerical method adopted for the simulation, whereas results are analyzed and discussed in section 5.2.

5.1 Simulations setup and definitions

The configuration under investigation is a spatially-evolving, zero-pressure-gradient flat plate boundary layer, sketched in figure 5.1. The prescribed edge conditions of $M_\infty = 12.48$, $T_\infty = 594.3$ K and $p_\infty = 4656$ Pa are representative of those downstream of the shock wave, leading to a stagnation enthalpy of $H_\infty = h_\infty + u_\infty^2/2 = 18.66$ MJ kg⁻¹. Such a value, much larger than the characteristic vibrational energies of the molecules in the mixture, ensures the presence of vibrational excitation as well as dissociation of molecular oxygen. Air in thermochemical equilibrium ($X_{\text{N}_2} = 0.79$, $X_{\text{O}_2} = 0.21$) has been considered at the free-stream; note that similar free-stream conditions have been used by [Kline *et al.* \(2019\)](#) for stability studies. The computational domain is a rectangular box enclosed within the shock layer (highlighted in red in figure 5.1), with an extent of $L_x \times L_y \times L_z = 3000\delta_{\text{in}}^* \times 120\delta_{\text{in}}^* \times 30\pi\delta_{\text{in}}^*$. The computational grid is $N_x \times N_y \times N_z = 9660 \times 480 \times 512$, for a total of ≈ 2.4 billions grid points. The grid spacing is uniform in the streamwise and spanwise directions, whereas a constant grid stretching of 0.7% is applied in the wall-normal direction. The calculation is initiated in the laminar region at a distance $x_0 = 2.7 \times 10^{-2}$ m from the plate leading edge. The profiles of the conservative variables prescribed at the inflow are generated by solving the locally self-similar theory for a two-dimensional chemically out-of-equilibrium and vibrationally-equilibrated boundary layer; the inflow Reynolds number based on the inlet displacement thickness is $Re_{\delta_{\text{in}}^*} = 6054$. A sponge layer is applied downstream of the inlet boundary, up to $\hat{x} = 20$. Characteristic-based boundary conditions are imposed at the top and right boundaries and periodic conditions are set in the spanwise direction. The wall is considered to be non-catalytic and isothermal with $T = T_V = 1800$ K. The hypothesis of wall thermal equilibrium is mainly dictated by a lack of knowledge about the most appropriate conditions to be used for vibrational temperature: in preceding studies of laminar flows around hollow cylinder flares ([Kianvashrad & Knight, 2017, 2019](#)), both adiabatic and isothermal boundary conditions were utilized for the vibrational energy, leading to similar results in terms of heat transfer; furthermore, past boundary layer stability studies accounting for thermal non-equilibrium assumed thermal equilibrium at the wall ([Bitter & Shepherd, 2015](#)). Unfortunately, no information is available for turbulent flows. Nevertheless, the contribution of the vibrational heat transfer to the total wall heat flux will be shown to be small with respect to the roto-translational counterpart, justifying the choice of a Dirichlet condition as a first approximation.

Transition to turbulence is induced by means of a suction and blowing strategy, similar to section 4.2. Specifically, the following wall-normal velocity is imposed along a wall strip close to the inflow:

$$\frac{v_{\text{wall}}}{u_\infty} = e^{-0.4g(x)^2} A \left[\sin(2\pi g(x) - \omega t) + \cos(\beta z) + 0.05 \sin\left(2\pi g(x) - \omega t + \frac{\pi}{4}\right) \cos(\beta z) \right], \quad (5.1)$$

where $g(x) = (x - x_{\text{forc}})/(\delta_{\text{in}}^* \sqrt{2}\sigma)$, with $\sqrt{2}\sigma = 0.85 \frac{2\pi}{\omega}$ and x_{forc} is the centre of the Gaussian-like distribution which modulates the forcing function. The corresponding Reynolds number at the forcing location is $Re_{\delta_{\text{forc}}^*} = 10^4$. In equation (5.1), the non-dimensional pulsation $\omega = \tilde{\omega}\delta_{\text{in}}^*/c_\infty$ corresponds to a dimensional frequency of $\tilde{f} = \tilde{\omega}/2\pi = 75$ kHz and $\beta = 0.4/\delta_{\text{in}}^*$ is the spanwise wave number. Lastly, A is the forcing amplitude, which has been set equal to 5%. Once again, the presence of stationary modes at a strong amplitude in the suction-and-blowing injection strip mimics the effects of a roughness strip and is used to speed-up breakdown to turbulence within the prescribed computational domain.

The Navier–Stokes equations are integrated numerically by means of the scheme FD10ANAD9. Even in this test case, the [Bhagatwala & Lele's](#) modification of the shock sensor was turned off. The tuning parameters are: $k_2 = 2.0$ and $k_{10} = 1/840$. For the vibrational energy equation a shock sensor based

5.2. RESULTS

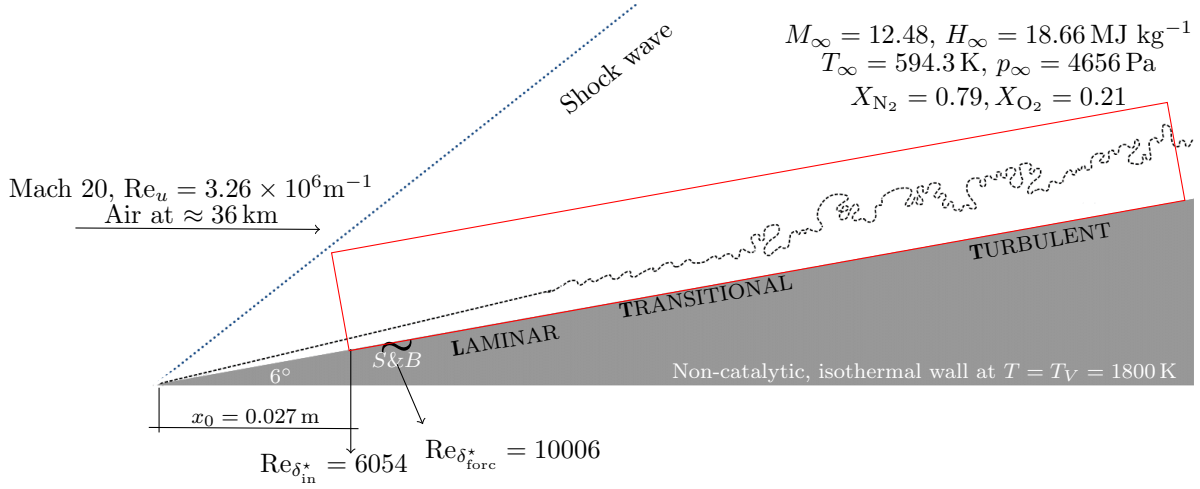


Figure 5.1: Sketch of the configuration under investigation.

on second-order derivatives of the vibrational temperature was preferred to ensure the appropriate damping of spurious oscillations with an *ad hoc* k_2 coefficient equal to 0.5.

In the results presented below, flow statistics are computed by averaging in time and in the spanwise homogeneous direction, after that the initial transient is evacuated. The sampling time interval is constant and corresponds exactly to 300 samples per each period of the forcing harmonic; specifically, $\Delta t_{\text{stats}}^+ = \Delta t_{\text{stats}} \frac{u_\tau^2 \bar{\rho}_w}{\bar{\mu}_w} = 0.16$. Data are collected for more than three turnover times, corresponding to $T_{\text{stats}} \frac{u_\tau^2}{\bar{\mu}_w / \bar{\rho}_w} \approx 6700$ for a total of ≈ 40000 temporal snapshots. In addition to flow statistics, instantaneous planes and specific meshlines are extracted with a frequency twenty and forty times higher with respect to the fundamental mode in the forcing function, respectively, for a total of 3200 and 6400 samples, respectively. The analysis will mainly focus on three selected streamwise stations in the turbulent region; sometimes, some inspections on a laminar and a transitional profiles will be also provided. Table 5.1 reports some boundary layer properties at the selected stations. Of note, the grid spacings ensure a DNS-like spatial resolution everywhere. Unless otherwise specified, the wall-normal evolution of statistics is displayed in inner semi-local units $y^* = \bar{\rho} u_\tau^* y / \bar{\mu}$, with $u_\tau^* = \sqrt{\bar{\tau}_w / \bar{\rho}}$.

5.2 Results

A detailed investigation of integral and statistical variables, as well as insights on instantaneous flow fields and spectral data are provided. A specific discussion on the influence of thermochemical non-equilibrium on turbulent quantities is provided. Finally, compressibility effects are analyzed.

5.2.1 Global flow properties

The streamwise evolution of selected quantities at the wall is first discussed. Figures 5.2(a) and (b) report the distributions of the skin friction coefficient C_f and the normalized wall heat fluxes C_q and $C_{q,V}$, defined as:

$$C_q = \frac{q_w}{\rho_\infty u_\infty^3}, \quad C_{q,V} = \frac{q_{w,V}}{\rho_\infty u_\infty^3}, \quad (5.2)$$

5.2. RESULTS

Table 5.1: Boundary layer properties at five selected downstream stations. In the table, $Re_x = \rho_\infty u_\infty x / \mu_\infty$ and $Re_{\delta^*} = \rho_\infty u_\infty \delta^* / \mu_\infty$ are the Reynolds numbers based on the distance from the leading edge x and the local displacement thickness δ^* , respectively; $Re_\theta = \rho_\infty u_\infty \theta / \mu_\infty$ is the Reynolds number based on the local momentum thickness $\theta = \int_0^{\delta} \rho u / \rho_\infty u_\infty (1 - \rho u / \rho_\infty u_\infty) dy$ and $Re_\theta^{\text{inc}} = \mu_\infty / \bar{\mu}_w Re_\theta$ the incompressible-scaled counterpart. $H = \delta^* / \theta$ is the shape factor, $Re_\tau = \rho_w u_\tau \delta / \bar{\mu}_w$ the friction Reynolds number and $M_\tau = u_\tau / \bar{c}_w$ the friction Mach number; $B_q = q_w / (\bar{\rho}_w u_\tau \bar{h}_w)$ and $B_{q,V} = q_{w,V} / (\bar{\rho}_w u_\tau \bar{h}_w)$ are the roto-translational and vibrational dimensionless heat fluxes. Lastly, Δx^+ , Δy_w^+ , Δy_δ^+ and Δz^+ denote the grid sizes in inner variables in the x -direction, y -direction at the wall and at the boundary layer edge, and in the z -direction, respectively.

| | | | | | |
|------------------------------------|-----------|-----------|-----------|-----------|-----------|
| \hat{x} | 744 | 1396 | 1757 | 2329 | 2900 |
| $Re_x \times 10^{-6}$ | 4.51 | 8.45 | 10.6 | 14.1 | 17.6 |
| $Re_{\delta^*} \times 10^{-4}$ | 6.80 | 9.91 | 13.25 | 13.27 | 16.16 |
| Re_θ | 1600 | 2960 | 3560 | 5030 | 6200 |
| Re_θ^{inc} | 774 | 1426 | 1716 | 2423 | 2994 |
| H | 28.3 | 23.0 | 28.0 | 26.3 | 26.0 |
| Re_τ | 134 | 670 | 845 | 983 | 1128 |
| M_τ | 0.14 | 0.27 | 0.23 | 0.22 | 0.21 |
| B_q^{TR} | 0.14 | 0.38 | 0.30 | 0.26 | 0.24 |
| B_q^{V} | 0.016 | 0.01 | 0.01 | 0.016 | 0.017 |
| Δx^+ | 4.38 | 10.54 | 8.80 | 7.77 | 7.26 |
| Δz^+ | 2.60 | 6.25 | 5.21 | 4.60 | 4.30 |
| $\Delta y_w^+ - \Delta y_\delta^+$ | 0.39-1.36 | 0.93-5.80 | 0.78-6.90 | 0.70-7.82 | 0.64-8.83 |

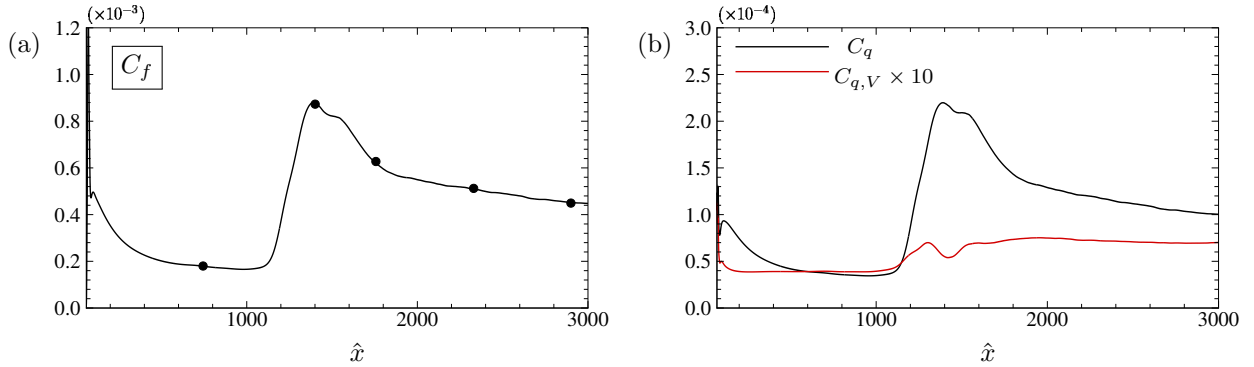


Figure 5.2: Evolution of (a) skin friction coefficient C_f and (b) normalized wall heat fluxes C_q and $C_{q,V}$. The filled symbols in panel (a) denote the position of the stations selected in Table 5.1.

the net total heat flux being given by the sum of the two contributions. A ramp-up starting at $\hat{x} \approx 1100$ leads to a sharp overshoot in the C_f profile, with a peak of the wall shear stress almost five times larger than its corresponding laminar value. The flow achieves a fully-turbulent regime starting from $\hat{x} \approx 1800$, with a smoothly decreasing C_f up to the end of the computational domain. The roto-translational contribution of the wall heat flux C_q is shown to be largely predominant with respect to the vibrational counterpart $C_{q,V}$ (which is multiplied by ten to match the range of figure 5.2(b)), mainly

5.2. RESULTS

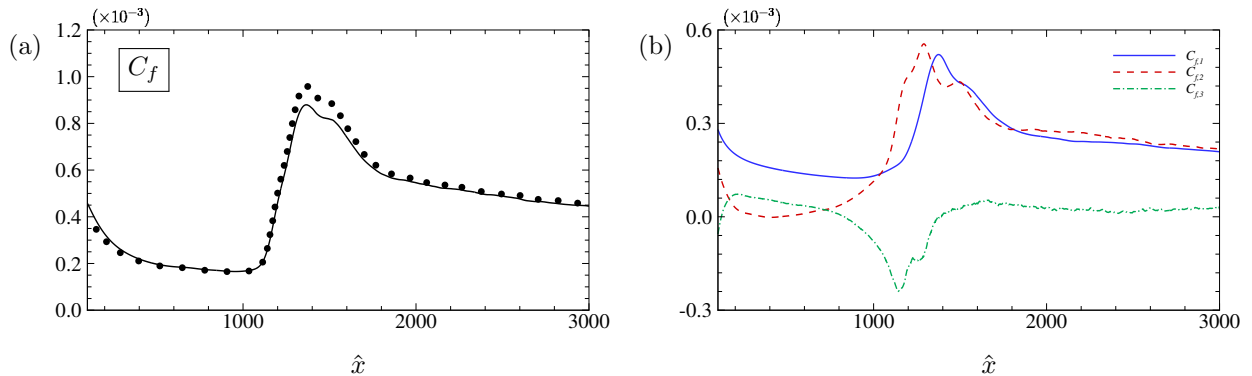


Figure 5.3: Evolution of the skin friction coefficient C_f and Renard-Deck decomposition (symbols) (z) and contribution of each term of equation (4.5) (b).

because of the vibrational thermal conductivity $\overline{\lambda_V}$ whose values are about one order of magnitude smaller than $\overline{\lambda_{TR}}$. While C_q closely follows the skin friction coefficient profile, $C_{q,V}$ exhibits a different evolution. It rapidly decreases after the forcing strip and stays approximately constant up to the breakdown to turbulence; afterwards, the value in the turbulent region almost doubles the one in the laminar regime and keeps a constant value up to the end of the domain. The different trend of the heat fluxes is related to the evolution of vibrational temperature gradients across the boundary layer, as discussed later in section 5.2.3. Even in this case, we show the results of the Renard-Deck decomposition for the skin friction coefficient, in order to highlight the differences or analogies with respect to the adiabatic thermally equilibrated case of Chapter 4. The sum of the three terms and their separate contribution (see equation (4.5)) are displayed in figure 5.3. An excellent agreement with respect to the direct C_f computation is in the pseudo-laminar and fully-turbulent regions, with only minor deviations in the transition region. The $C_{f,3}$ contribution is negligible everywhere but at the breakdown-to-turbulence location, where it takes negative values due to the abrupt thickening of the boundary layer. The decrease of $C_{f,3}$ is counterbalanced by a large increase of the Reynolds stress-related term, whereas the growth of the mean-field contribution, $C_{f,1}$, is slightly delayed with respect to the other two. In the turbulent region, $C_{f,1}$ and $C_{f,2}$ are almost superposed, differently from what observed in section 4.1, where the former was shown to be predominant. Such a discrepancy can be ascribed to the much larger friction Reynolds numbers reached in the current configuration, leading to the an increased importance of the turbulent contribution (Fan *et al.*, 2019).

5.2.2 Velocity statistics

Different scalings for the profiles of the averaged streamwise velocity have been tested. First, the transformations of Van Driest (1956) and Trettel & Larsson (2016) are shown for the three turbulent stations in figures 5.4(a) and (b), respectively. The latter reads:

$$u_{TL} = \int_0^{\bar{u}} \left(\frac{\bar{\rho}}{\rho_w} \right) \left[1 + \frac{1}{2} \frac{1}{\bar{\rho}} \frac{d\bar{\rho}}{dy} y - \frac{1}{\bar{\mu}} \frac{d\bar{\mu}}{dy} y \right] du. \quad (5.3)$$

Van Driest scaling has been shown to work reasonably well for adiabatic boundary layers, even at high speeds and in presence of chemical reactions. On the other hand, it may become inaccurate when high wall-cooled configurations are considered, whether they be boundary layers (Zhang *et al.*, 2018; Huang

5.2. RESULTS

et al., 2020), pipe flows (Ghosh *et al.*, 2010) or channel flows (Modesti & Pirozzoli, 2016; Sciacovelli *et al.*, 2017). Figure 5.4(a) confirms such a trend, both the linear and logarithmic regions being offset with respect to the analytical laws. The semi-local scaling of Trettel & Larsson, as expected, improves the near-wall prediction since it is explicitly built for satisfying the stress-balance condition within the entire inner layer. A large scatter is however observed in the logarithmic region which shows a Re-dependence similar to the Van Driest scaling. Although such a scaling works reasonably well for internal flows, it is not as good for external configurations, most likely because of an interaction with the wake region which is shown to be over-stretched in figure 5.4(b). Recently, Griffin *et al.* (2021) proposed a new total-stress-based transformation (called hereafter Griffin-Fu-Moin scaling, u_{GFM}) with a constant-stress-layer assumption, which reads

$$u_{\text{GFM}} = \int_0^\delta \frac{\frac{1}{\mu^+} \frac{\partial u^+}{\partial y^*}}{1 + \frac{1}{\mu^+} \frac{\partial u^+}{\partial y^*} - \mu^+ \frac{\partial u^+}{\partial y^*}} dy^* \quad (5.4)$$

where μ^+ denotes normalization of the mean viscosity with respect to its wall value. Such a scaling has been shown to successfully collapse channels, pipe flows and boundary layer configurations, even at large Mach numbers. A comparison between u_{TL} and u_{GFM} as a function of y^* is shown in figure 5.4(c) for a velocity profile extracted at $Re_\theta = 6200$. In the inner layer, viscous stresses are predominant and roughly correspond to the total shear stress resulting in a perfect collapse of the two scalings. On the contrary, turbulent shear stresses largely dominate in the logarithmic region and this is correctly taken into account by the total-stress-based scaling, ensuring an excellent collapse onto the universal logarithmic profile. Of note, neither chemical activity nor thermal relaxation process substantially alter the validity of the transformation since a certain degree of decoupling is observed between the thermochemical and turbulent activities.

Figure 5.5 shows the Reynolds stress profiles at the three turbulent stations (first column). The streamwise turbulent intensity exhibits a peak value of $\approx 14.5\bar{\tau}_w$ at $y^* \approx 12$ whereas the other components are of the same order of magnitude of the wall shear stress. The profiles are reasonably self-similar, although some differences are observed for the shear and crossflow components, which conserve the imprint of the transition scenario over a longer streamwise distance. Consistently with previous observations (Duan *et al.*, 2011; Lagha *et al.*, 2011; Zhang *et al.*, 2018), the larger streamwise component and the smaller crossflow one may indicate the presence of strong compressibility effects, as discussed later in section 5.2.5. In the second column, we also report the rms values of the velocity components at $Re_\theta = 6200$, compared to low-enthalpy cases extracted from Zhang *et al.* (2018) (M14Tw018 and M8Tw048) and Xu *et al.* (2021) (M8T1). All the profiles are normalized with respect to the semi-local friction velocity $u_\tau^* = \sqrt{\tau_w/\bar{\rho}}$. Despite the important differences in the values of the free-stream Mach numbers, friction Reynolds numbers, absolute wall temperatures and wall-cooling rates, the turbulent intensity profiles are comparable and do not exhibit any marked influence imputable to TCNE effects.

5.2.3 Thermal non-equilibrium effects

The presence of thermal non-equilibrium is analyzed by comparing the vibrational relaxation time with characteristic time scales of the dynamic field. For that purpose, the following vibrational Damköhler numbers are considered:

$$\text{Da}_v^{\text{VS}} = \frac{\bar{\mu}_w/\bar{\tau}_w}{\tau_m}, \quad \text{Da}_v^{\text{LE}} = \frac{\delta^*/u_\tau}{\tau_m}, \quad \text{Da}_v^{\text{RT}} = \frac{x/u_\infty}{\tau_m}, \quad (5.5)$$

5.2. RESULTS

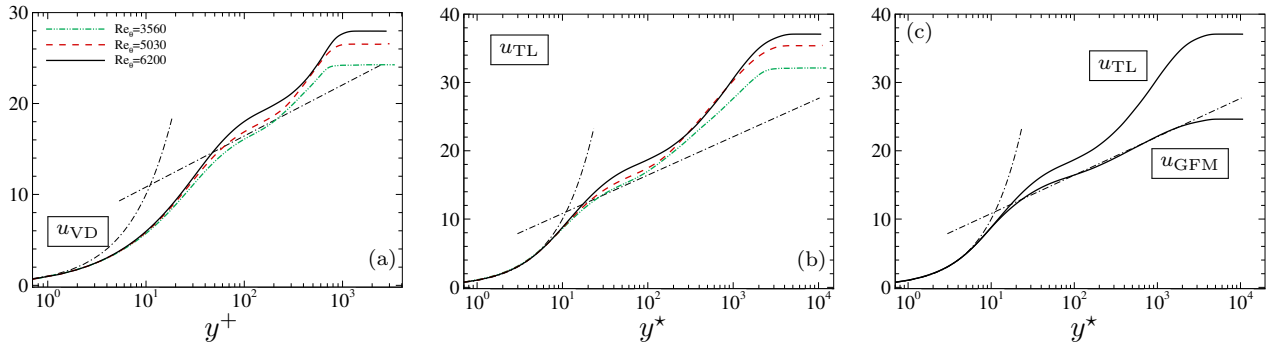


Figure 5.4: Wall-normal profiles of the van Driest-transformed streamwise velocity (a), of Trettel & Larsson’s transformation (b) and comparison between Trettel & Larsson transformation and total-stress-based transformation of Griffin *et al.* (2021).

$Da_v^{(\bullet)} = \mathcal{O}(1)$ denoting the regime in which non-equilibrium effects are relevant. The evolution of these dimensionless numbers is displayed in figure 5.6, for the five stations reported in table 5.1. The first ratio in (5.5) relates the characteristic time of fluid motion in the viscous sublayer (VS) with the vibrational relaxation time of a generic molecule m . Panels (a), (d) and (g) of figure 5.6 show the evolution of this quantity for the three molecules present in the mixture. It is shown that $Da_v^{VS} \ll 1$ everywhere for N_2 and O_2 whereas it is of the order of unity only for NO , whose concentration is however almost negligible (see section 5.2.4). The decoupling of the two timescales indicates that there exists a layer of thickness l_v in the inner (colder) region of the boundary layer in which the molecules are vibrationally frozen. The higher values of $Da_v^{VS} \ll 1$ observed at the laminar position are due to the prevalence of viscous stresses. Of major interest is Da_v^{LE} , representing the ratio between the large-eddies (LE) turnover time and the relaxation time, constructed by means of the displacement thickness δ^* and u_τ . The orders of magnitude of the two timescales are comparable for molecular nitrogen (figure 5.6(b)), for which the peak of Da_v^{LE} ranges from 0.4 to 0.7 at $y^* \approx 10$ as the flow evolves in the turbulent region. On the other hand, figures 5.6(e) and (h) show that $Da_v^{LE} \gg 1$ for O_2 and NO , implying that the two molecules reach a vibrational equilibrium with respect to the characteristic time of the large-scale turbulent motions much faster. Similar considerations hold for Da_v^{RT} , which compares the vibrational relaxation time to the local flow residence time (RT). As the flow evolves along the plate, there is enough time for O_2 and NO to achieve thermal equilibrium, whereas N_2 remains significantly out of equilibrium at all stations. This result should not be surprising since molecular nitrogen relaxation rate is the slowest given its high characteristic vibrational temperature. Of note, both Da_v^{LE} and Da_v^{RT} exhibit much higher values at the last station with respect to laminar and transitional profiles due to the turbulent mixing increase.

Wall-normal profiles of the normalized mean translational and vibrational temperatures are reported in figures 5.7(a) and (b), respectively. The translational temperature reaches a peak value of approximately $[2.3 - 2.5]T_w$, at a wall-normal location $y^* \approx 10$, corresponding to the peak of turbulent intensity. The vibrational temperature \hat{T}_V is 20% to 30% smaller than \hat{T} across the boundary layer, proving the existence of a vibrational-relaxation layer for the thermodynamic conditions under investigation, and also exhibits a peak located between the buffer layer and the lower logarithmic region. The major gap is visible at $Re_\theta = 2960$, which corresponds to the C_f ’s peak, meaning that a step increment of wall stress leads to stronger non-equilibrium conditions. Additionally, the wall gradient

5.2. RESULTS

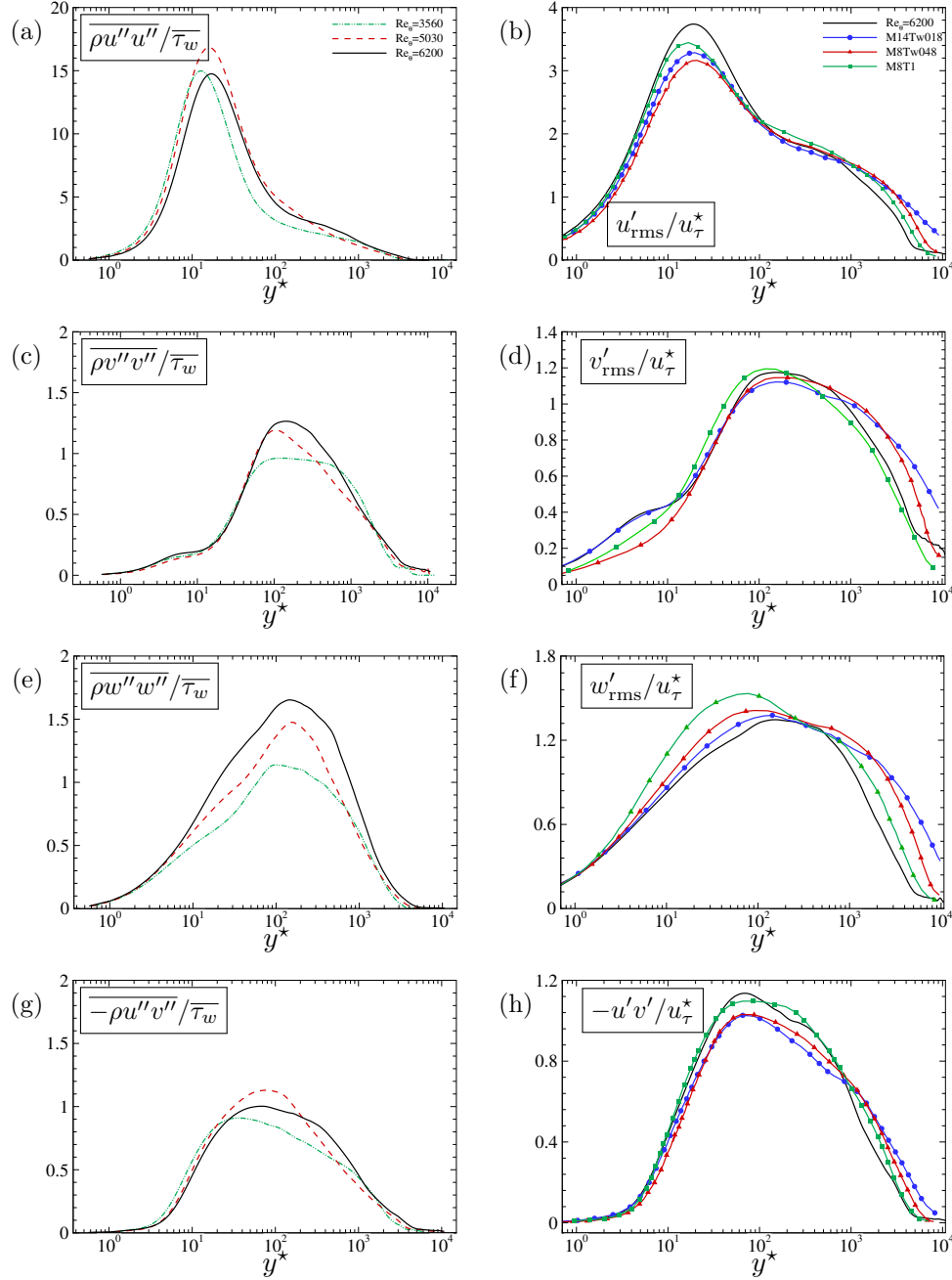


Figure 5.5: Reynolds stresses in the streamwise direction (a)-(b), wall-normal direction (c)-(d), spanwise direction (e)-(f) and Reynolds shear stresses (g)-(h). Favre-averaged (first column) and Reynolds averaged (second column) variables. The M14Tw018 and M8Tw048 profiles are extracted from [Zhang *et al.* \(2018\)](#), whereas M8T1 from [Xu *et al.* \(2021\)](#).

$\partial \widetilde{T}_V / \partial y^*$ is little sensitive to the peak's magnitude and location, explaining the nearly constant trend of $C_{q,V}$ previously observed in figure 5.2(b). To better visualize the gap between the two temperatures,

5.2. RESULTS

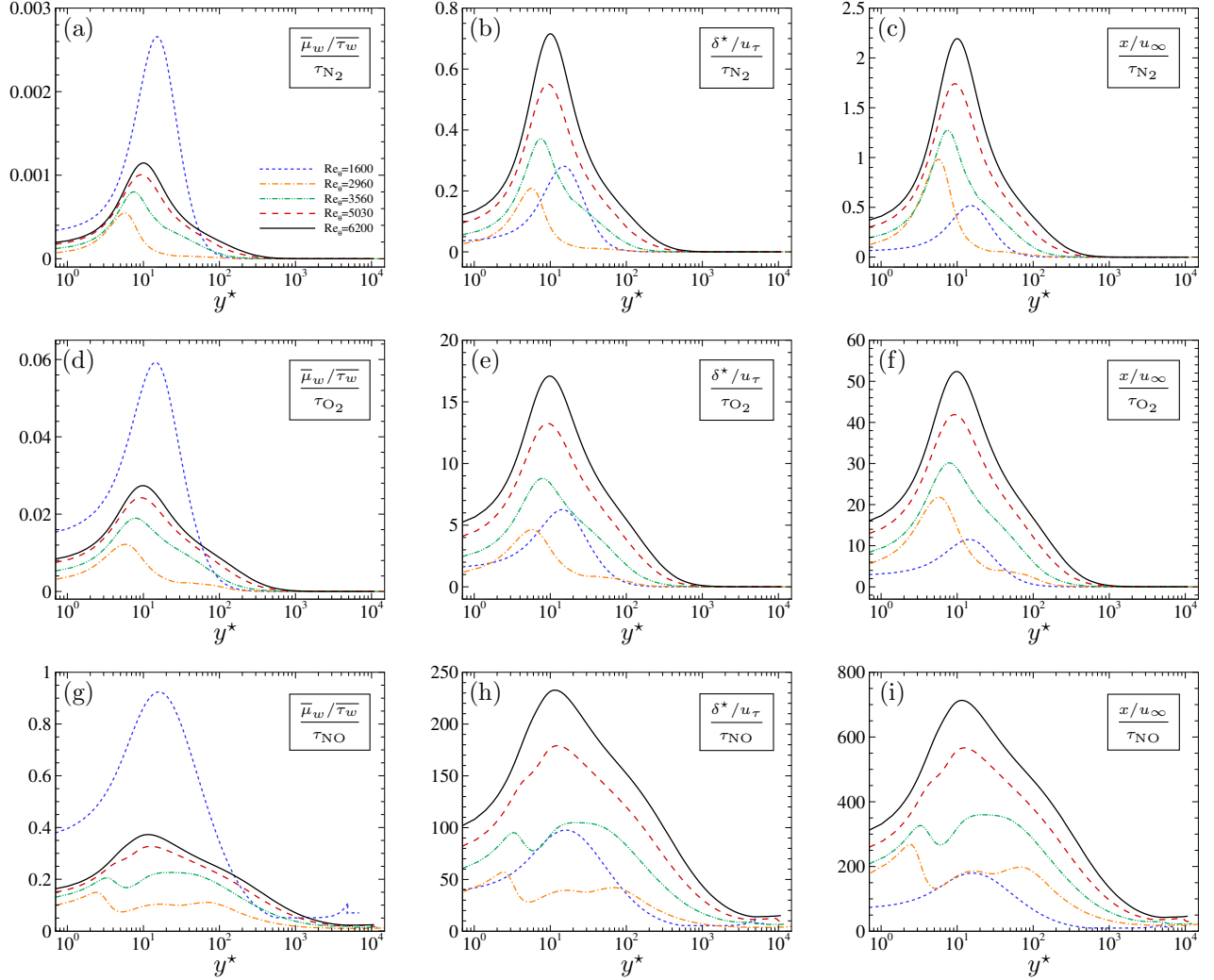


Figure 5.6: Vibrational Damköhler numbers for N_2 (first row), O_2 (second row) and NO (third row). Damköhler number based on inner units (a)-(d)-(g), large-eddies turnover times (b)-(e)-(h) and flow residence time (c)-(f)-(i).

the normalized temperature difference $(\tilde{T} - \tilde{T}_V)/T_w$ (figure 5.8(a) and (b)) increases from the laminar to the transitional region reaching a maximum of the order of ≈ 2000 K where the $\text{Re}_\theta = 29600$, and then tends to decrease moving toward the turbulent region. The wall-normal maximum value moves from the outer part of the boundary layer ($y/\delta \approx 0.6$) to the buffer layer, where it stabilizes at $y^* \approx 8$. Thermodynamic non-equilibrium conditions are kept until the end of the computational domain, as already stated by inspecting the values of the vibrational Damköhler numbers. Positive $\tilde{T} - \tilde{T}_V$ values are observed from the viscous sublayer (we recall that $T = T_V = 1800$ K at the wall) up to the first portion of the logarithmic region. However, as the flow evolves along the flat plate, a region characterized by $\tilde{T} - \tilde{T}_V < 0$ appears, meaning that the flow becomes vibrationally over-excited. The height at which the sign changes smoothly moves from the edge of the boundary layer up to $y/\delta \approx 0.45$, due to the boundary layer thickening. This is clearly visible in figure 5.9 (top),

5.2. RESULTS

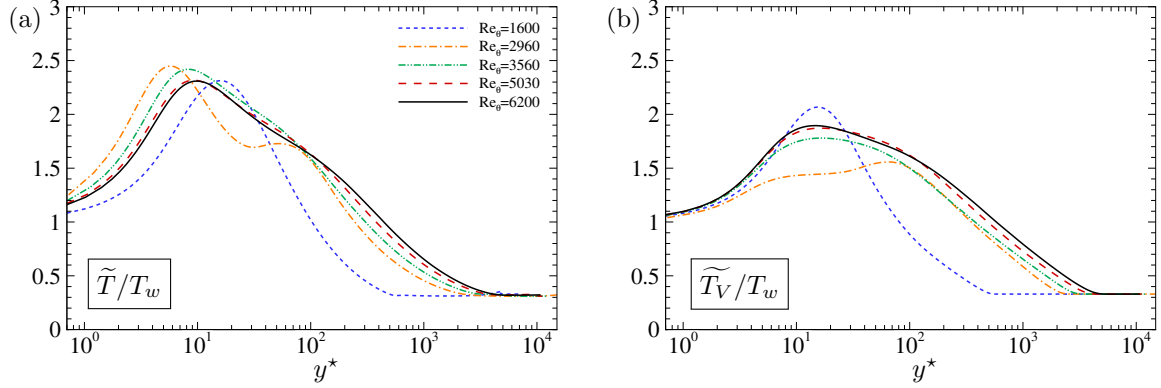


Figure 5.7: Normalized mean translational temperature (a) and vibrational temperature (b) at the selected streamwise stations.

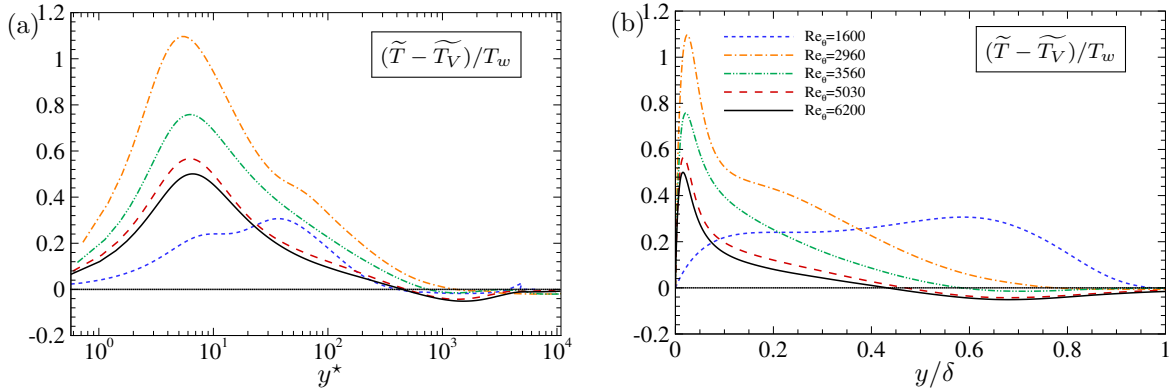


Figure 5.8: Normalized difference $(\tilde{T} - \tilde{T}_V)/T_w$ at the selected streamwise stations; (a) semi-local units, (b) outer scale. Dotted line corresponds to the zero value.

where a snapshot of the temperature difference is reported along a longitudinal cut plane. We also show in figure 5.9 (bottom) an instantaneous snapshot of the Q -criterion on the second half of the computational domain, coloured by the local values of $T - T_V$. As already verified in section 5.2.3, most of the vibrational over-excited states occur in proximity of the boundary layer edge; moreover, their number and magnitude increase moving towards the end of the computational domain. [Fiévet *et al.* \(2019\)](#), who conducted analysis on the coupling between vibrational non-equilibrium and turbulent mixing, observed that the majority of non-equilibrium is under-excited. The rare regions in which there exist an over-excited non-equilibrium are dictated by the link between roto-translational energy and mechanical energy. The static temperature is coupled with the other variables through the equation of state; hence, a decrease of turbulent intensity (moving towards the edge of the boundary layer) produces a decrease of the translational temperature. At the same time, the vibrational energy remains nearly constant because it relaxes slowly, leading to an over-excitation in the outer layer, until the freestream equilibrium conditions are reached by both temperatures.

Normalized root-mean-square of the Favre fluctuations of translational and vibrational temperatures across the boundary layer are displayed in figure 5.10. In figure 5.10(a), a peak emerges on each side

5.2. RESULTS

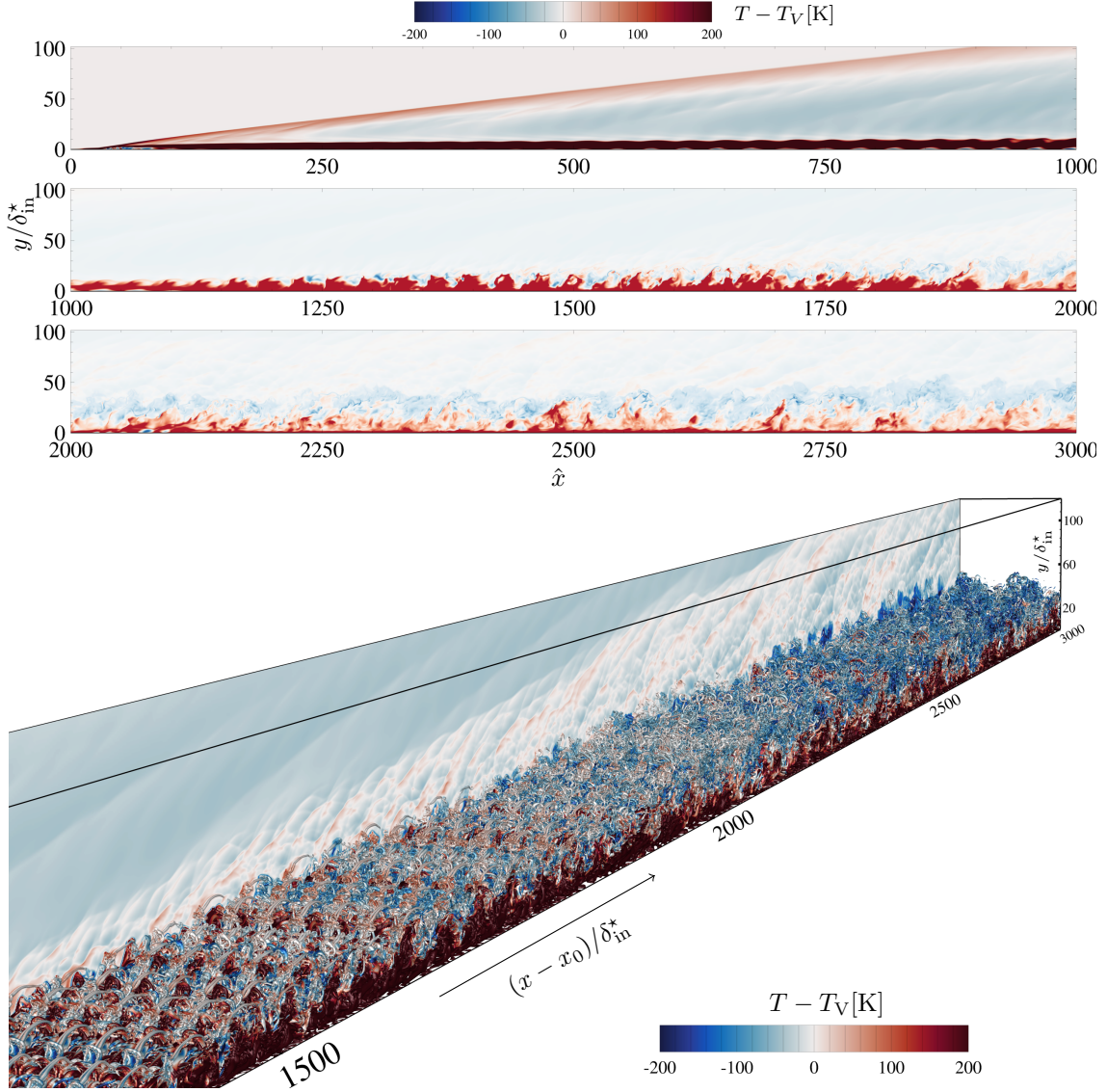


Figure 5.9: Instantaneous isocontours of $T - T_V$ in a xy -plane and Q -criterion coloured by $T - T_V$.

of the \tilde{T}_{\max} location ($y^* \approx 10$), as classically observed for wall-cooled turbulent boundary layers (Duan *et al.*, 2010a; Zhang *et al.*, 2018; Di Renzo & Urzay, 2021). The predominance of the outer rms peak in the turbulent region is mainly caused by the decrease of \tilde{T} toward the outer boundary, the absolute temperature fluctuations being comparable in both the inner and outer regions. In contrast, the vibrational temperature fluctuations exhibit no local minimum (figure 5.10(b)), and increase monotonically up to the boundary layer edge, where they drop abruptly. This is in contrast with profiles typically observed in the laminar region (see the profile at $Re_\theta = 1600$ reported in the figure for comparison), and can be ascribed to thermal non-equilibrium: the vibrational relaxation times being slower than the translational ones and comparable to the turbulence timescales, wall-normal turbulent motions efficiently redistribute vibrational temperature across the boundary layer, smoothing out the local minimum. The premultiplied energy spectra of the fluctuating temperatures, reported in figure 5.11

5.2. RESULTS

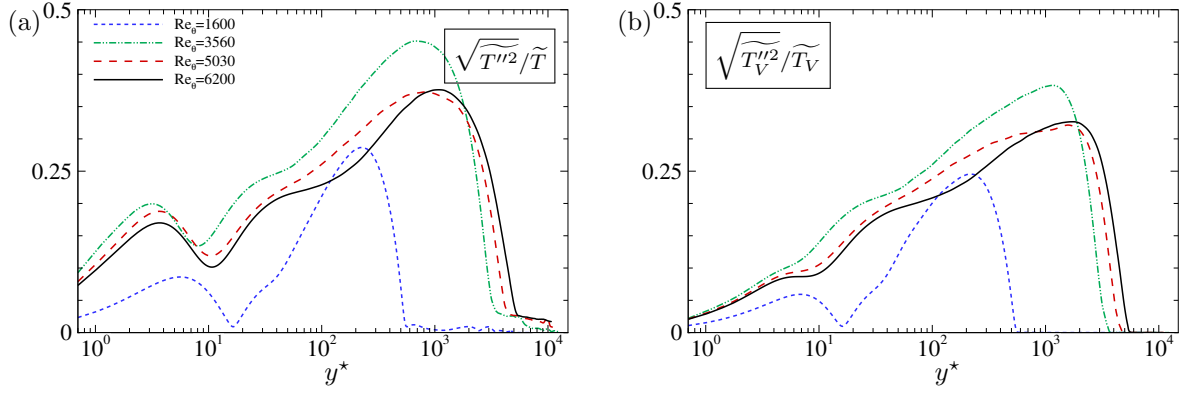


Figure 5.10: Rms of temperature Favre fluctuations normalized by the local Favre average for translational temperature (a) and vibrational temperature (b).

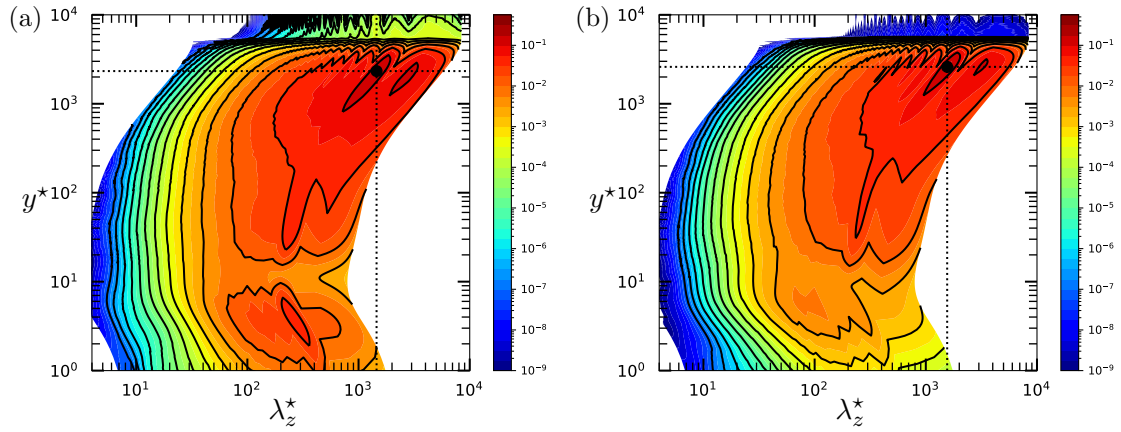


Figure 5.11: Premultiplied energy spectra $k_z E_{T'T'} / \overline{T}$ (a) and $k_z E_{T_V'T_V'} / \overline{T_V}$ (b), at $Re_\theta = 6200$.

as a function of the normalized spanwise wavenumber λ^* , provide a further confirmation of this trend. For both temperatures, a large scale peak is visible at $\lambda_z^* \approx 1500$ and $y^* \approx 2500$, whereas an inner (slightly weaker) peak is observed only for the roto-translational temperature spectrum, coherently with the rms temperature fluctuations. Additionally, the well developed spectra indicate that a fully turbulent state has been reached and the footprint of the forcing strategy has been completely lost.

The persistence of thermal non-equilibrium conditions across the boundary layer is tightly related to the flow turbulent state. Preliminary numerical experiments on the same configuration without boundary layer tripping have shown that, for a laminar flow regime, the difference between the roto-translational and vibrational temperatures is almost negligible (of the order of 50 K) at the end of the plate. Indeed, the evolution of Da_v^{RT} in figure 5.6 (third column) shows that by moving further downstream (i.e., at increasing Reynolds number) the molecules tend to relax faster and the flow exiting the computational domain is closer to vibrational equilibrium than the flow at the inlet. The thermal non-equilibrium observed in the turbulent case is strongly related to sweep and ejection turbulent motions, resulting in enhanced mixing as anticipated by Urzay & Di Renzo (2021) with *a priori* considerations. In figure 5.12 we report the mean values of the two temperatures conditioned

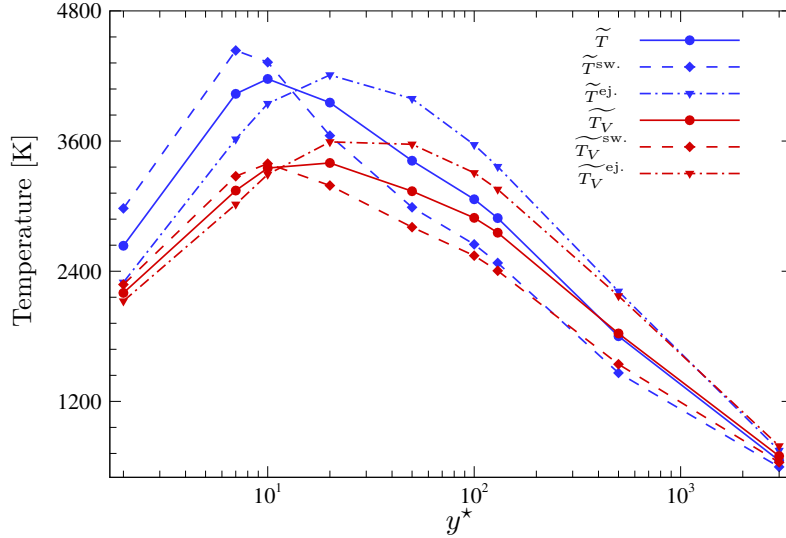


Figure 5.12: Mean values of \widetilde{T} and \widetilde{T}_V conditioned on sweep and ejection events, at $Re_\theta = 6200$ at various wall-normal heights. Blue lines: roto-translational modes; red lines: vibrational modes. (dashed lines, diamonds) average over sweep events; (dashed-dotted lines, triangles) average over ejection events; (solid lines, circles) global average.

on sweep events (characterized by $u'' > 0$ and $v'' < 0$) and ejection events ($u'' < 0$ and $v'' > 0$) at $Re_\theta = 6200$ and for several wall-normal locations. Within the viscous sublayer, sweeps entrain hot fluid from the overlying regions. Consequently, they are characterized by higher mean temperatures with respect to the total average in the inner region. The opposite is true for ejection events. The largest differences between sweeps and ejections conditionally averaged temperatures are registered for the roto-translational modes due to the sharper peak observed for \widetilde{T} . An opposite trend is observed at normal locations beyond the temperature peak ($y^* \approx 10$). In this case, sweeps bring colder air from the outer layers towards the hotter, inner region; here, the translational modes rapidly reach equilibrium, whereas a longer relaxation time is needed for the vibrational ones. As a result, \widetilde{T}_V is always smaller than \widetilde{T} . On the other hand, ejection motions bring hotter, thermally out-of-equilibrium mixture towards the outer region of the boundary layer, where vibrational relaxation times rapidly increase because of the colder environment; therefore, in this region $\widetilde{T}_V > \widetilde{T}$. The largest temperature difference between sweeps and ejections events occurs in the first portion of the logarithmic region (up to $y^* \approx 100$), with values as large as 800 K for vibrational modes and 1000 K for the roto-translational ones. Further evidence of this phenomenon is provided by the conditional probability density functions (p.d.f.s) of the two temperatures, shown in figure 5.13. Three wall-normal stations are considered: the location where the maximum temperature difference is registered (panels a and b, $y^* \approx 10$), the logarithmic region (panels c and d, $y^* \approx 100$) and the boundary layer edge (panels e and f, $y^* \approx 3000$). Close to the boundary layer edge, a heavy right tail is observed for the p.d.f.s of both events, with T_V values slightly larger than T ones. Moving inside the boundary layer, at $y^* \approx 100$, both p.d.f.s tend to become symmetric. The most remarkable differences are observed in the buffer layer with left-skewed distributions for T and symmetric ones for T_V , their shape being related to the presence of a local minimum for \widetilde{T}''^2 and a small plateau for $\widetilde{T}_V''^2$ as shown in figure 5.10.

5.2. RESULTS

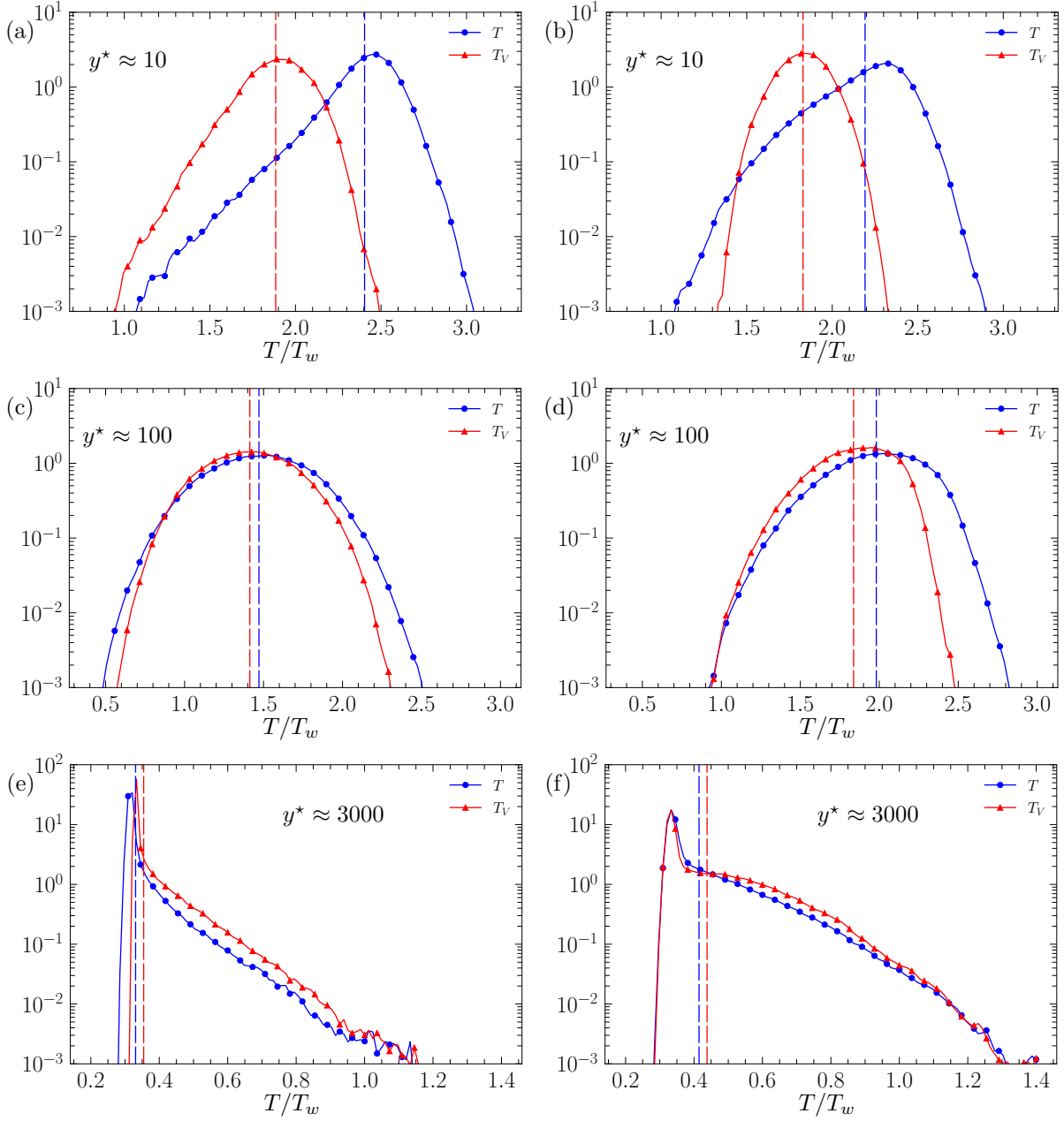


Figure 5.13: Conditional p.d.f. of translational and vibrational temperature at $\text{Re}_\theta = 6200$ for y^* approximately equal to 10, 100 and 3000, respectively; sweeps events (left panels) and ejections events (right panels).

A more quantitative analysis of the interplay between turbulent transport and thermal non-equilibrium is carried out by considering the averaged vibrational energy equation, derived from (2.7).

5.2. RESULTS

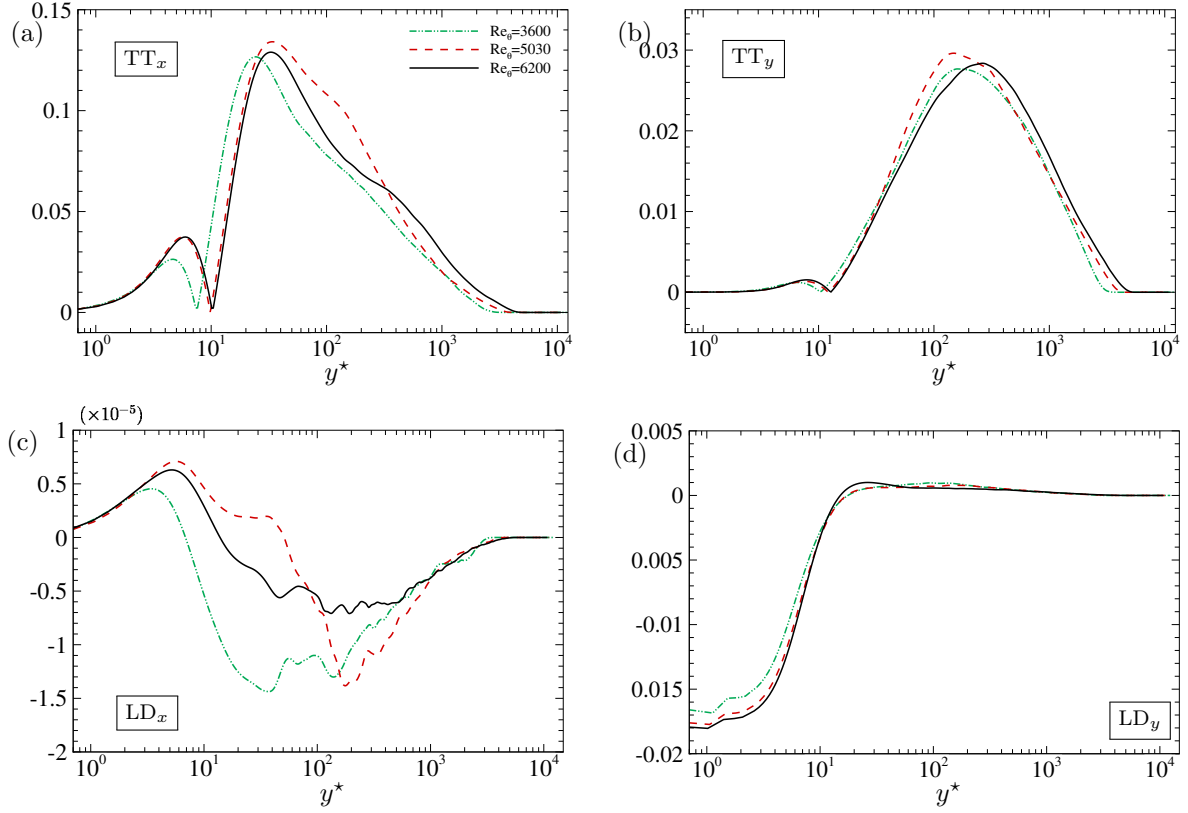


Figure 5.14: Terms of equation 5.6. Turbulent transport in the streamwise (a) and wall-normal (b) directions; molecular diffusion term in the streamwise (c) and (d) wall-normal directions.

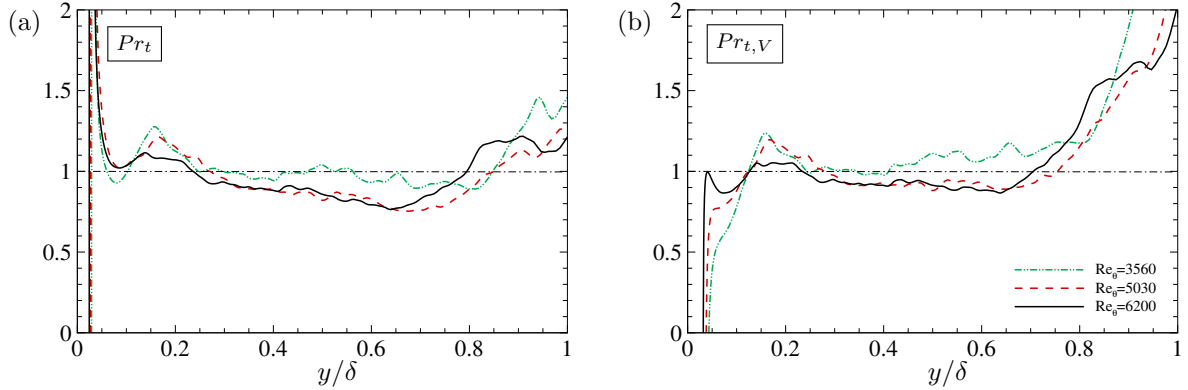


Figure 5.15: Turbulent Prandtl number (a) and turbulent vibrational Prandtl number (b).

The equation reads:

$$\frac{\partial \bar{\rho} \tilde{e}_V}{\partial t} + \underbrace{\frac{\partial}{\partial x_j} (\bar{\rho} \tilde{e}_V \tilde{u}_j)}_{\text{LC}} + \underbrace{\frac{\partial}{\partial x_j} (\overline{\rho u_j'' e_V''})}_{\text{TT}} = \underbrace{\frac{\partial}{\partial x_j} \left(-\overline{q v_j} + \sum_{m=1}^{\text{NM}} \overline{\rho D_m \frac{\partial Y_m}{\partial x_j} e_{V_m}} \right)}_{\text{LD}} + \text{ST} \quad (5.6)$$

5.2. RESULTS

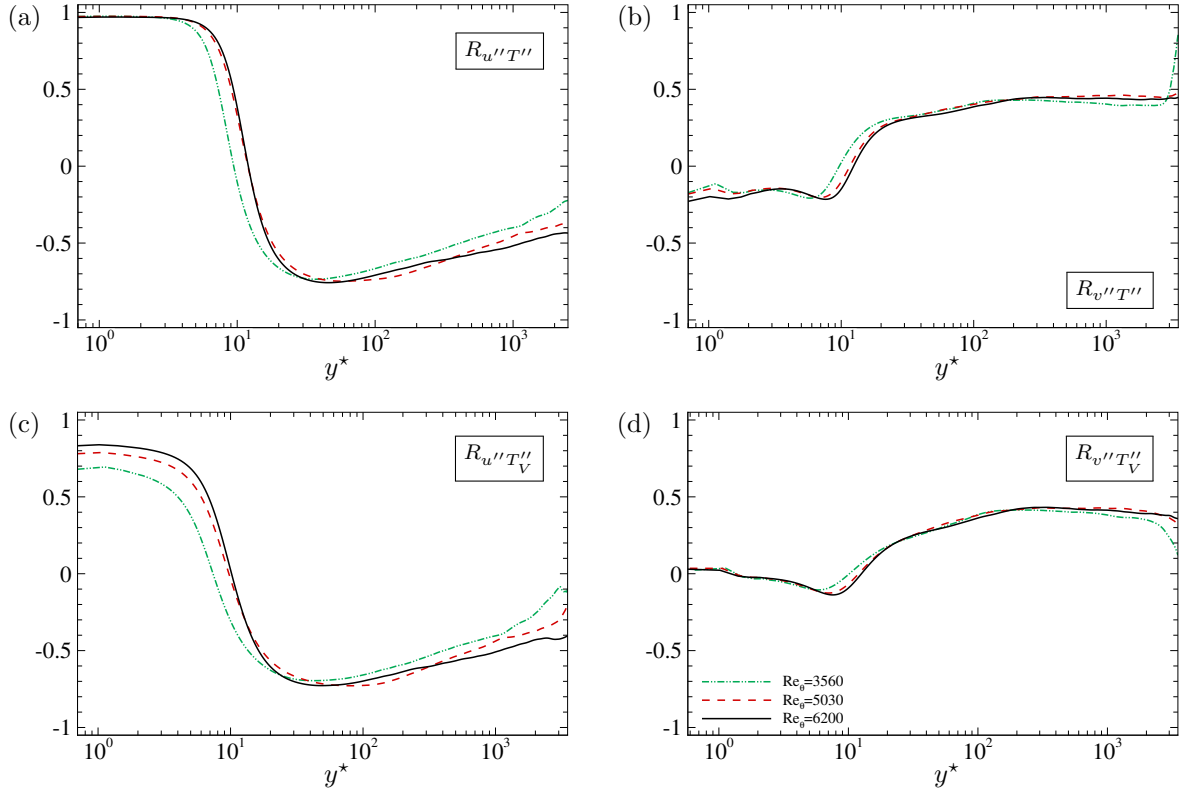


Figure 5.16: Correlation coefficients between Favre fluctuations of vibrational temperature and streamwise velocity (a) and wall-normal velocity (b) and of translational temperature and streamwise velocity (c) and wall-normal velocity (d).

where LC, TT and LD stand for laminar convection, turbulent transport and laminar (molecular) diffusion, respectively. The last term of equation (5.6) incorporates the source terms, whereas mean turbulent diffusion fluxes are found to be extremely small and are therefore neglected in the current analysis. We focus hereafter on the TT and LD terms, plotted in figure 5.14 against y^* and normalized with $\rho_w h_w u_\tau$. The turbulent transport in the streamwise direction (panel a) exhibits a double-peaked trend as already observed for temperature fluctuations and is larger than laminar diffusion (panel c) by approximately four orders of magnitude. On the other hand, TT and LD wall-normal components (panels b and d) have similar magnitudes, with LD_y being predominant in the linear region, as expected, and TT_y taking over in the logarithmic layer. In all cases, turbulent transport terms play a major role in the vibrational energy budget. We recall that the turbulent heat transport term in the total energy equation is usually modeled by means of a turbulent Prandtl number Pr_t . According to the classical Strong Reynolds Analogy (SRA) (Morkovin & Favre, 1962) and as already discussed in section 4.2, the latter is expected to take values close to one throughout the flow (see figure 4.31(a), displayed in external units for better clarity). In wall-cooled configurations, the estimation fails at the peak of \tilde{T} , which corresponds to $y/\delta \approx 0.03$, since the coexistence of null temperature gradient and turbulent heat flux causes an overshoot, as previously observed by Duan & Martín (2011). Similarly, the turbulent transport of vibrational energy can be modeled by introducing a vibrational turbulent

Prandtl number:

$$Pr_{t,V} = \frac{\overline{\rho u'' v'' \partial \widetilde{T}_V / \partial y}}{\overline{\rho v'' T_V'' \partial \widetilde{u} / \partial y}} \quad (5.7)$$

whose trend is plotted in figure 4.31(b). $Pr_{t,V}$ is close to unity in the relatively large region $0.2 \lesssim y/\delta \lesssim 0.7$ where turbulent transport dominates, whereas it diverges at the boundary layer edge (where $\partial \widetilde{u} / \partial y$ tends to vanish) and close to the wall, similarly to Pr_t . We complete the present analysis by reporting, in figure 5.16, correlations of u'' and v'' fluctuations with T'' and T_V'' , respectively. As observed in both low- and high-enthalpy boundary layers (Zhang *et al.*, 2018; Di Renzo & Urzay, 2021), the logarithmic and outer regions are characterized by a negative correlation between u'' and T'' (panel a) and positive correlation for v'' and T'' (panel b). This results from i) sweeps ($u'' > 0$, $v'' < 0$) entraining colder ($T'' < 0$) fluid towards the buffer layer, and ii) ejections ($u'' < 0$, $v'' > 0$) entraining hotter ($T'' > 0$) fluid towards the edge, resulting in $R_{u''T''} < 0$ and $R_{v''T''} > 0$. Below the buffer layer, both correlations change their sign for the same reason, consistently with the trend previously discussed in figure 5.12. Similar considerations hold for $R_{u''T_V''}$ and $R_{v''T_V''}$. However, while streamwise velocity fluctuations close to the wall are perfectly correlated with the translational temperature ones ($R_{u''T''} \approx 1$), the correlation coefficient with the vibrational temperature (panel c) is weaker ($R_{u''T_V''}$ comprised between 0.7 and 0.85). This effect is attributed once again to the larger relaxation time of vibrational modes, T_V needing more time than T for adapting to the surrounding temperature.

To complete the analysis of vibrational non-equilibrium, we investigate the source terms in equation (2.7), which indicate that vibrational energy production/depletion is associated to translational-vibrational energy exchanges (Q_{TV}) or chemical dissociation/recombination processes, the latter having only a marginal influence due to the small chemical rates. Hence, an alternative measure to $(\widetilde{T} - \widetilde{T}_V)$ for characterizing thermal non-equilibrium may be given by the magnitude of $\overline{Q_{TV}}$; positive values indicate vibrational under-excitation since $T > T_V$ (and the opposite for negative values). The wall-normal profiles of $\overline{Q_{TV}}$, shown in figure 5.17(a) as a function of y^* and y/δ , closely follow those shown for $(\widetilde{T} - \widetilde{T}_V)$ in figures 5.8(a) and (b), albeit the negative values visible in the zoomed view of the outer region are much less pronounced (two orders of magnitude lower) than those registered in the inner zone. Such a large difference is due to the concurrent effects of lower absolute temperature values and (to a lesser extent) smaller $(\widetilde{T} - \widetilde{T}_V)$ differences, causing the denominator to increase and the numerator to decrease in equation (2.21), respectively. Following the technique used in section 4.2 for assessing turbulence/chemistry interactions and with the aim of quantifying the coupling between turbulence and thermal relaxation, we built an indicator defined as

$$Q_{TV}^I = \frac{\overline{Q_{TV}(T, T_V, \rho, p, Y_n)} - Q_{TV}(\widetilde{T}, \widetilde{T}_V, \bar{\rho}, \bar{p}, \widetilde{Y}_n)}{\overline{Q_{TV, \max}}}, \quad (5.8)$$

where $\overline{Q_{TV, \max}}$ denotes the maximum wall-normal value of $\overline{Q_{TV}}$ at the selected station. Deviations from null values represent a measure of vibrational energy variations associated to turbulent fluctuations. Figure 5.8(b) shows that computing Q_{TV} from averaged quantities would underestimate its value across the whole boundary layer, with discrepancies larger than 15% of $\overline{Q_{TV, \max}}$ in the inner layer. These data further confirm the tight coupling between thermal non-equilibrium and turbulence discussed in the current section and underline that attention must be paid to the development of suitable turbulence closures, especially in the context of RANS modeling.

5.2. RESULTS

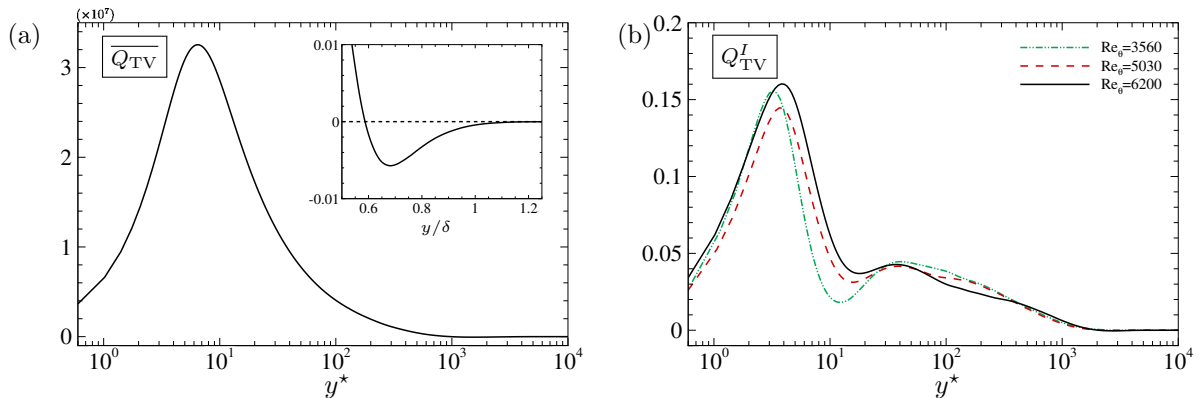


Figure 5.17: Wall-normal profiles of $\overline{Q_{TV}}$ [J/(m³s)] (a) and Q_{TV}^I , defined in equation (5.8) (b). In the subset of panel (a), a zoom of the profile is shown in outer scale; the dashed line denotes the null value.

5.2.4 Chemical activity

In this section we investigate the chemical activity triggered in the high-enthalpy boundary layer by friction heating. The profiles of Favre-averaged mass fractions of species present in the mixture are reported in Figure 5.18. At flow conditions under investigation, molecular oxygen is the species which dissociates most, leading to the formation of atomic oxygen. However, the maximum mass fraction of atomic oxygen in the mixture is approximately 1%, differently from the adiabatic case in which the strong wall temperature triggered a more significant dissociation. The maximum temperatures in the boundary layer are too low to dissociate nitrogen to any significant amount, therefore the atomic nitrogen mass fraction is negligible compared to the other species. This is sufficient however to lead to the formation of a small amount of nitric oxide (approximately 0.7%). The rather low chemical activity is partly due to the strong wall cooling, limiting the maximum temperature to values just above the threshold for oxygen dissociation. Thermal non-equilibrium further limits chemical reactions. Highly vibrationally-excited molecules are meant to dissociate more rapidly, since they require less energy exchange during the collisions. On the contrary, for under-excitation conditions, dissociation is less likely to occur. This mechanism is analytically taken into account in the computation of the reaction rate coefficients, which turn out to be smaller when strong non-equilibrium effects are present. On the other hand, the endothermic chemical reactions tend to drain roto-translational energy, but this is partly compensated by the relaxation of vibrational modes, which supply energy and partly counteract temperature reduction. All species except atomic nitrogen exhibit a plateau in their wall-normal profiles which extends from the wall up to $y^* \approx 10$; they decrease monotonically afterwards and do not follow the mean temperature as shown for the adiabatic case in figure 4.27(b). This is linked to the molecular diffusion of reaction products in the viscous sublayer: with a mean temperature of ≈ 2000 K, recombination processes should be active and the atomic species should be under depletion, but a small percentage of reaction products is visible. The reaction products diffuse from the peak of temperature towards the wall faster than the recombination reactions. Conversely, atomic nitrogen does exhibit a non-monotonic trend, but its concentration is extremely small. In such thermodynamic conditions and given the moderate values of chemical products in figure 5.18, one does not expect considerable turbulence/chemistry interaction, the relaxation phenomena being the most

5.2. RESULTS

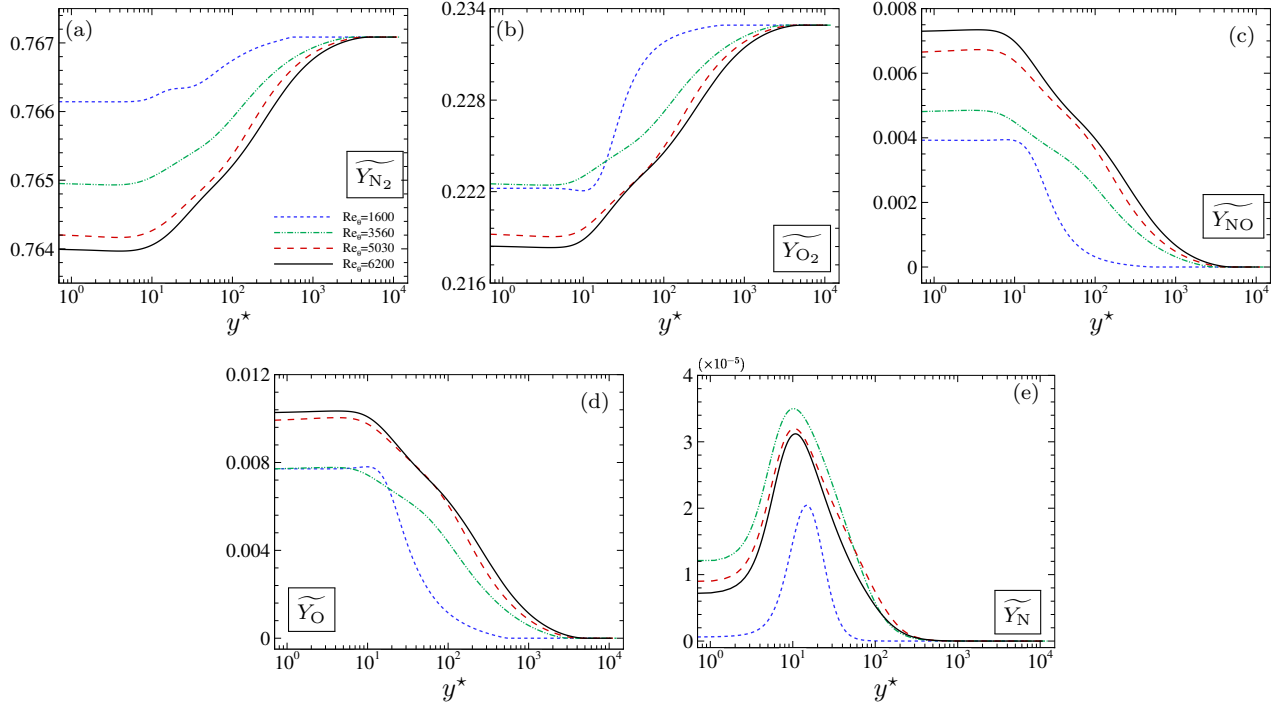


Figure 5.18: Mean mass fractions of molecular nitrogen (a), molecular oxygen (b), nitric oxide (c), atomic oxygen (d) and atomic nitrogen (e).

predominant in such conditions. Hence, the chemical Damköhler number based on the large-eddies turnover time $(\delta^*/u_\tau)/(\overline{\rho/\dot{\omega}_n})$ is at most of the order of 10^{-2} for all species, denoting little interaction between chemical reactions and turbulent motions and an almost frozen-chemistry behavior.

Figure 5.19 shows the evolution of the normalized chemical reaction rates, at the three turbulent locations and at the laminar station. At first, N_2 and NO present a chemical depletion and production, respectively, which is one order of magnitude smaller than O_2 ; production of N is basically negligible. Despite mean species mass fractions exhibit a monotonic trend, the reaction rates follow the evolution of mean temperature closely, with a peak at $y^* \approx 10$. This is not the case of figure 4.27(a), in which the normalized source terms present a maximum at the wall. Of note, the turbulent profiles attain self-similarity, whereas the evolution at $Re_\theta \approx 1600$ (laminar profile) displays the higher reaction rates for all the species active in the process. Mass fractions fluctuations in figure 5.20 display a relatively smooth peak which extends from $y^* \approx 10$ to $y^* \approx 100$, due to the high turbulent mixing. Differently from the adiabatic case, the maximum of species fluctuations does not match the maximum of temperature fluctuations, since in this case T''_{\max} is located by the end of the logarithmic region, where the mean temperature has substantially decreased and species concentrations are almost constant. Of course, an increase in turbulent intensities is encountered at the end of the transitional zone (station not shown) and they stabilize towards smaller values thereafter.

We have already observed that, despite the strong hypersonic conditions, correlations between velocities and temperature show a Morkovian behavior. Accordingly, correlations between velocity fluctuations and species mass fraction fluctuations can be inspected. Chemical reactants, such as N_2 and O_2 , are found to be anticorrelated with the fluctuation of the wall-normal velocity, whereas the

5.2. RESULTS

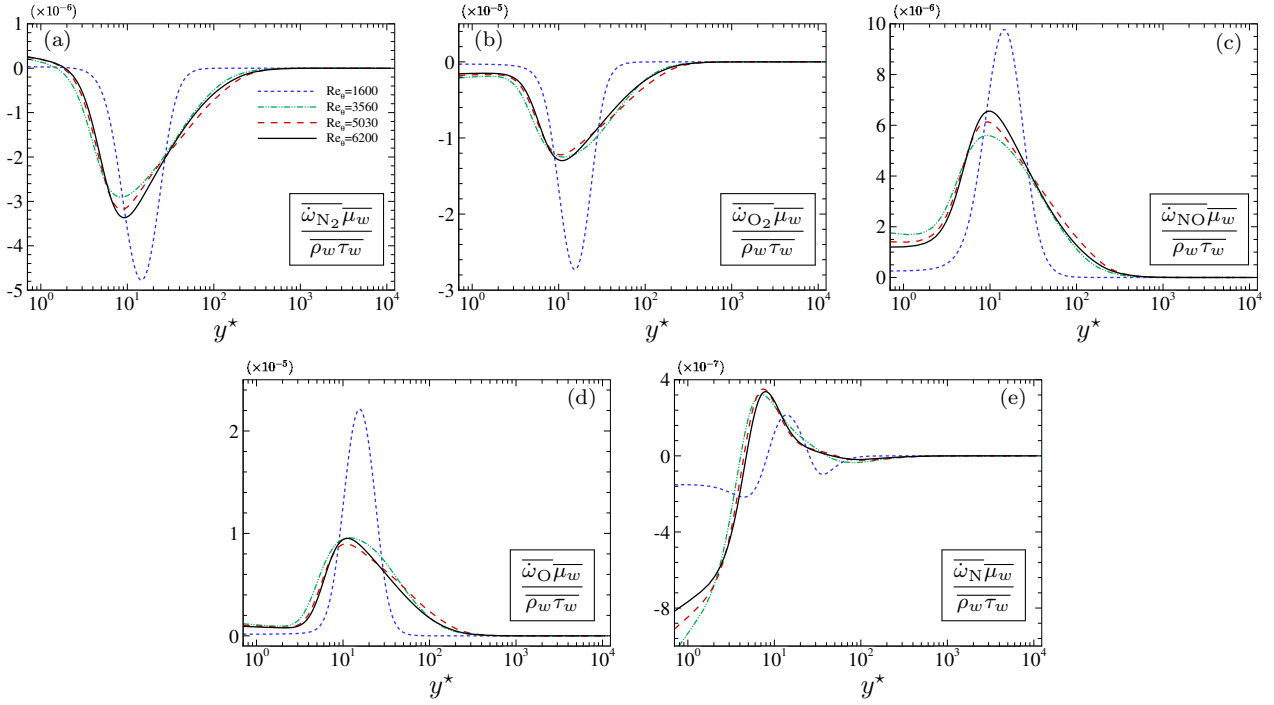


Figure 5.19: Normalized source terms for molecular nitrogen (a), molecular oxygen (b), nitric oxide (c), atomic oxygen (d) and atomic nitrogen (e).

opposite holds for the streamwise velocity fluctuations (see figure 5.21(a)-(b)). Indeed, sweep events bring colder, undissociated air from the outer layer and induce a positive correlation of Y_{N_2}'' and Y_{O_2}'' with u'' . The most significant products of dissociation (O and NO) display the opposite behavior (see 5.21(c)-(d)), with an anticorrelation with the streamwise velocity fluctuations, similarly to the correlation of T'' and u'' towards the edge of the boundary layer. In contrast, Y_N is almost constant, hence the correlation with the streamwise velocity closely follows the one with temperature; a scarce correlation is found with wall-normal velocity fluctuations. Accordingly, the evolution of the turbulent Schmidt number defined in equation (4.16) and reported in figure 5.22(a) for molecular oxygen, shows values close to unity even in wall-cooled configurations, hence the same considerations previously illustrated for the turbulent Prandtl numbers hold. Profiles of $Sc_{t,n}$ are equal for all species but atomic nitrogen (see figure 5.22(b)), which exhibits a singularity close to the wall deriving from given the change of sign of the correlation coefficient between its fluctuations and v'' . Configurations triggering a significant amount of N_2 dissociation should be investigated to find out whether or not a constant $Sc_{t,n}$ assumption may be completely inappropriate as closure for RANS models.

5.2.5 Compressibility effects

The present analysis is completed by discussing the role of compressibility effects and their interaction with thermal non-equilibrium conditions. In figure 5.23 we report the evolutions of the turbulent and fluctuating Mach numbers, defined as $M_t = u_{\text{rms}}/\bar{c}$ and $M_{\text{rms}} = (u/c)_{\text{rms}}$, respectively. Despite the high external Mach number, M_t is shown to be smaller than one everywhere, with maximum values of about 0.8-0.9 registered at the location where the turbulent kinetic energy production peaks. Such values

5.2. RESULTS

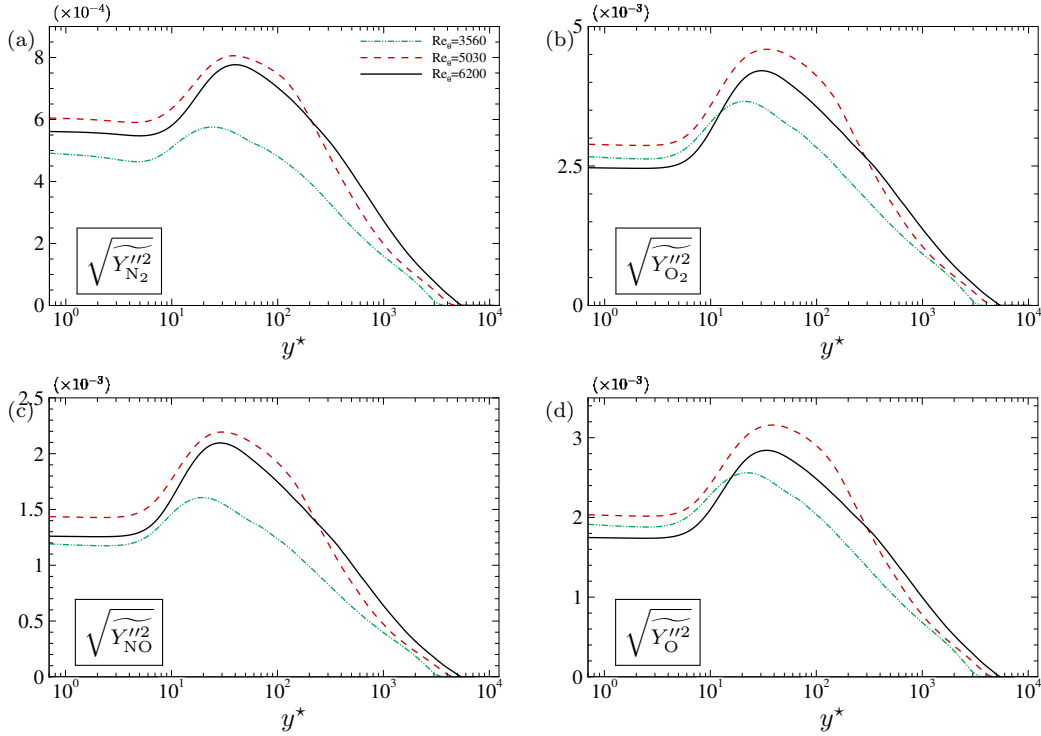


Figure 5.20: Mass fractions fluctuations for molecular nitrogen (a), molecular oxygen (b), nitric oxide (c) and atomic oxygen (d).

are however large enough to enable the formation of eddy shocklets, as also proven by the location of the sonic line (identified by the three vertical lines in figure 5.23(a)) within the viscous sublayer. Accordingly, the fluctuating Mach number is consistently larger than one starting from $y^* \gtrsim 10$. The outer M_{rms} peaks at $y^* \in [1000, 2000]$ (whose values are compatible with those obtained by Zhang *et al.* (2018) for high-speed boundary layers of calorically-perfect gases) are linked to the large fluctuations of thermodynamic properties resulting from the presence of turbulent/non turbulent interfaces along the boundary layer edge. These structures are clearly visible in figure 5.24, displaying the normalized density gradient magnitude on a streamwise slice of the computational domain. Such large fluctuations of the thermodynamic variables are not accompanied by an intense activity of the dynamic field, as testified by the values of the semi-locally-scaled fluctuating velocity divergence $\vartheta''\bar{\mu}/\tau_w$ (with $\vartheta = \partial u_k/\partial x_k$) shown in figure 5.25 in the last portion of the domain. Figure 5.26 displays two p.d.f.s of $\vartheta''\bar{\mu}/\tau_w$ computed at wall-normal positions corresponding to $y^* \approx 10$ and 1000, respectively. Both the profiles are slightly skewed toward negative values, highlighting a mild predominance of the occurrence of strong compressions over strong expansions, although such events are much stronger in the inner region. However, joint p.d.f.s of $(\vartheta''\bar{\mu}/\tau_w, |\nabla\rho|/\rho_\infty/\delta_{99,\text{end}})$, shown in figure 5.27 for the same wall-normal stations, do not exhibit any preferential correlations. At $y^* \approx 10$ the density gradient is only slightly correlated with expansion events, whereas at $y^* \approx 1000$, the density gradients are not correlated neither to expansions or compression events. This amounts to say that even if shocklets might exist inside the boundary layer, their number and/or intensity is not large enough to engender any remarkable effect on thermodynamic and dynamic quantities. Figure 5.28 shows the fluctuating

5.2. RESULTS

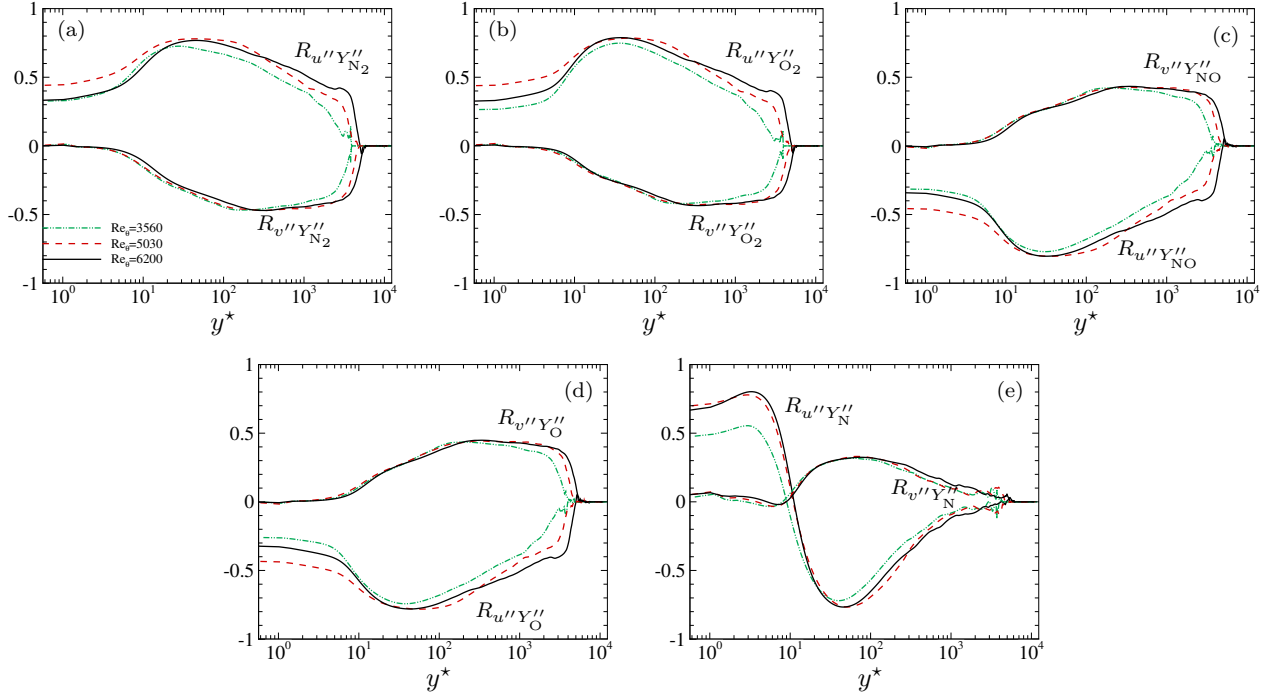


Figure 5.21: Correlation coefficients between velocity fluctuations and mass fractions fluctuations for molecular nitrogen (a), molecular oxygen (b), nitric oxide (c), atomic oxygen (d) and atomic nitrogen (e).

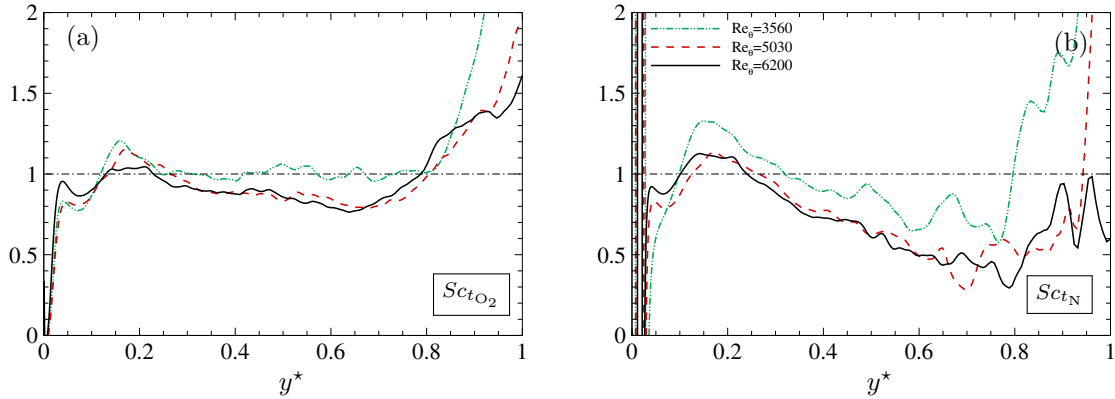


Figure 5.22: Wall-normal profiles of the turbulent Schmidt for molecular oxygen (a) and atomic oxygen (b). The horizontal dashed-dotted lines denote the SRA estimation.

values of divergence and vorticity. As a confirmation, the stronger dilatation events are registered close to the wall and their magnitude monotonically decreases with the wall distance, as shown in figure 5.28(a) where results from Xu *et al.* (2021) are reported for comparison. The evolution of the vorticity fluctuations instead shows that the spanwise and streamwise components follow the same trend of the divergence, that is maximum in the near-wall region.

5.2. RESULTS

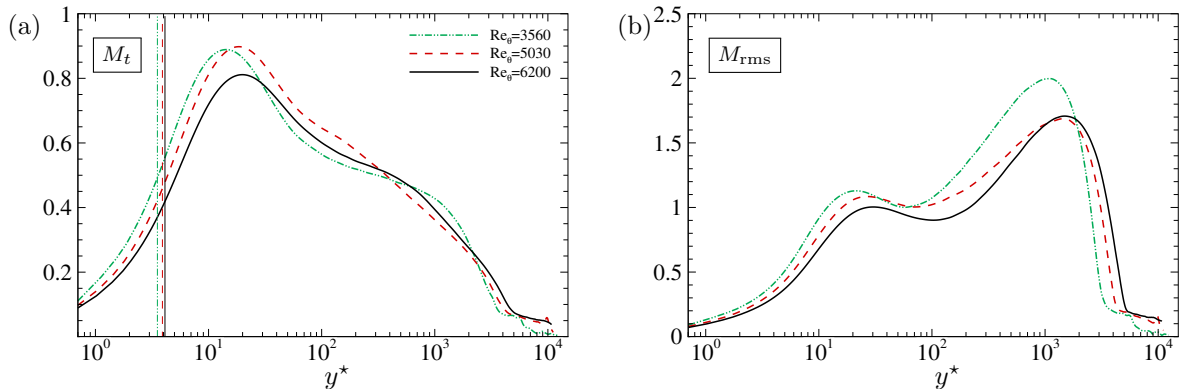


Figure 5.23: Profiles of turbulent Mach number (a) and rms Mach number (b).

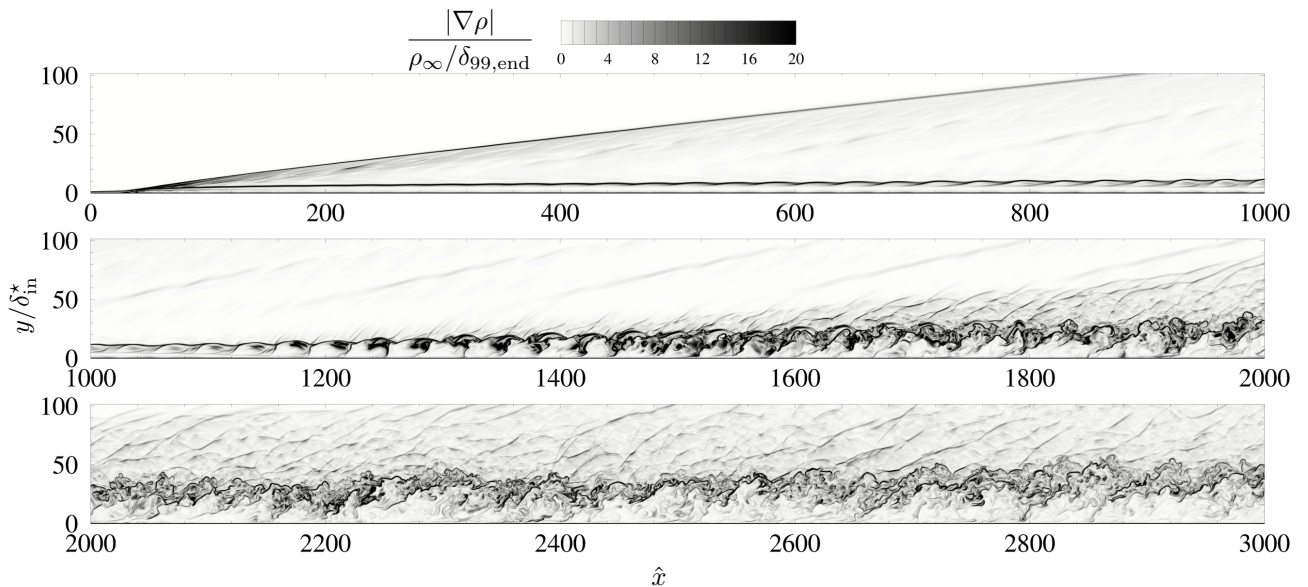


Figure 5.24: Instantaneous snapshot of the normalized density gradient magnitude along a slice of the computational domain.

The interplay between compressibility and thermal nonequilibrium effects has been previously investigated on mixing layers (Fiévet *et al.*, 2019) and homogeneous isotropic turbulence (Zheng *et al.*, 2020) configurations, in which it was observed that vibrational nonequilibrium is somehow enhanced by strong dilatation motions (whether they be expansions or compressions). Impulsive changes of thermodynamic quantities, as in the case of strong density gradients, can increase the difference between the two temperatures because of their different relaxation times. Here, high density gradient regions are mainly found near the boundary layer edge where the average temperature values are relatively low; as a consequence, the interaction between compressibility and vibrational nonequilibrium is expected to be less marked for boundary layer configurations. To clarify this aspect, we show in figure 5.29 the p.d.f.s of $Q_{\text{TV}}/Q_{\text{TV,rms}}$ at the last turbulent station for the same wall-normal positions shown in figure 5.26. The p.d.f.s are conditioned on strong and weak events, defined as

5.2. RESULTS

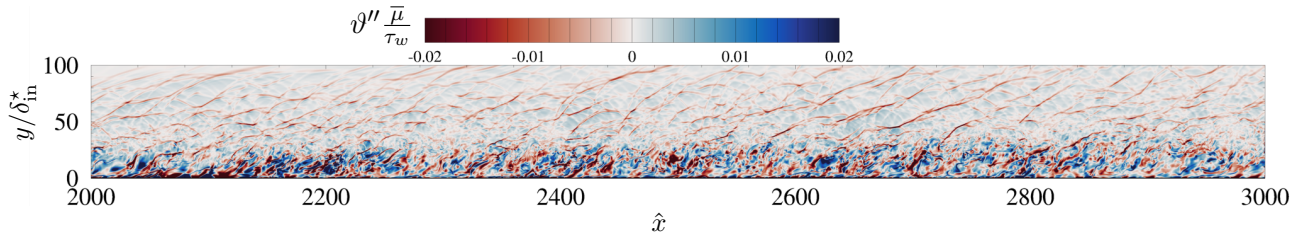


Figure 5.25: Instantaneous snapshot of the normalized divergence along the last portion of the computational domain.

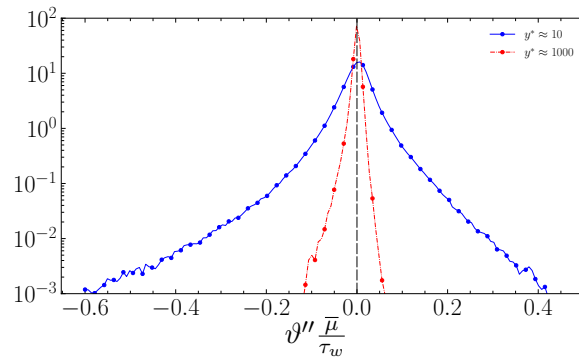


Figure 5.26: P.d.f. of normalized divergence at $\text{Re}_\vartheta = 6200$ for $y^* \approx 10$ and $y^* \approx 1000$.

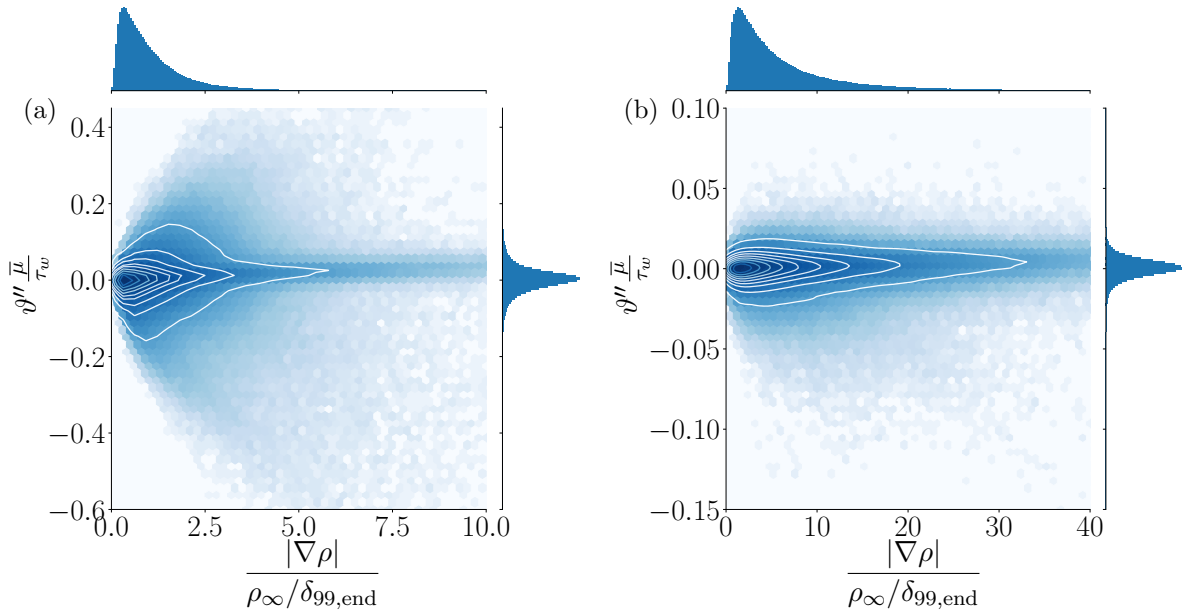


Figure 5.27: Joint p.d.f. of density gradient magnitude and normalized divergence at $\text{Re}_\vartheta = 6200$ for $y^* \approx 10$ (a) and $y^* \approx 1000$ (b).

5.2. RESULTS

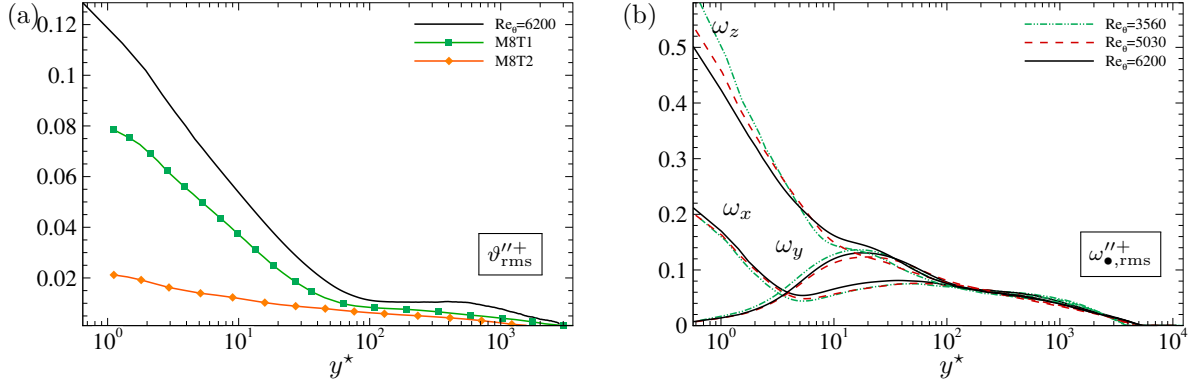


Figure 5.28: Profiles of fluctuating quantities of divergence (a) and vorticity (b). The M8T1 and M8T2 are extracted from Xu *et al.* (2021).

$|\vartheta/\vartheta_{\text{rms}}| \geq 2$ and $0 < |\vartheta/\vartheta_{\text{rms}}| < 2$, respectively. Globally, all the profiles are strongly right-skewed because of the predominance (in magnitude and number) of under-excited states. At both locations, strong compressions are associated to slightly higher values of $Q_{\text{TV}}/Q_{\text{TV,rms}}$ than strong expansions. For $y^* \approx 10$, strong events (figure 5.29(a)) are characterized by wider distributions, thus confirming that higher values of translational-vibrational energy exchange are more probable in case of strong events. At $y^* \approx 1000$, the distributions are steeper and a wider range in the negative axis is covered with respect to $y^* \approx 10$; surprisingly, even in this case, all the distributions are skewed towards positive values. The explanation of such trend may be attributed to the small negative values of $\overline{Q_{\text{TV}}}$ (see figure 5.17(a)). At this wall normal station, the peak of vibrational over-excitation is reached, corresponding to a temperature difference approximately equal to -100 K, in contrast with the peak of vibrational under-excitation ($\tilde{T} - \tilde{T}_V \approx 1000$ K). These orders of magnitude may result in many local events of under-excitation which shift the distribution towards high positive values. Comparing figures 5.29(c) and (d), no particular differences are found for strong and weak compressions, the distributions being equally wide. On the other hand, high vibrational under-excitation is less probable in presence of strong expansions (distribution less skewed towards positive values). Even if this correlation is weak, since the distributions start to deviate for events with probability lower than 10^{-3} , this result is in accordance with what happens for homogeneous isotropic turbulence. Zheng *et al.* (2020) have found a correlation between compressions and positive Q_{TV} , and expansions and negative Q_{TV} , in particular when these events are significantly intense. As a result, we verified that such a tight coupling does not exist in boundary-layer configurations, since i) the compressibility effects are much less stronger and ii) the aerodynamic heating deriving from the presence of the wall plays a major role in redistributing the energy contributions. For further confirmation, the same analysis presented by Zheng *et al.* (2020) has been performed. The joint p.d.f.s of Q_{TV} and normalized divergence are shown in figure 5.30, at $\text{Re}_\theta = 6200$. At both stations, the distributions show no particular correlation with compressions or dilatations, since they are nearly symmetric with respect to null divergence.

5.2. RESULTS

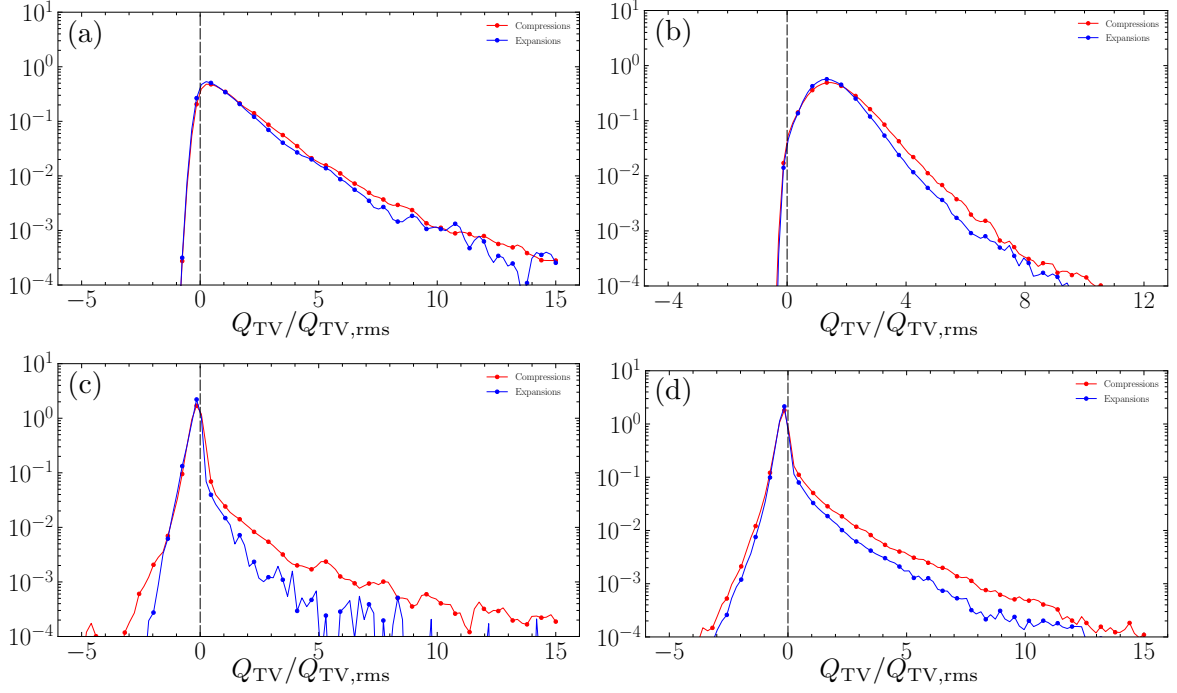


Figure 5.29: Conditional p.d.f. of normalized translational-vibrational energy exchange at $\text{Re}_\theta = 6200$ for $y^* \approx 10$ (first row) and $y^* \approx 1000$ (second row). Strong events (left panels); strong compressions $\theta/\theta_{\text{rms}} < -2$, strong expansions $\theta/\theta_{\text{rms}} > 2$. Weak events (right panels); weak compressions $-2 < \theta/\theta_{\text{rms}} < 0$, weak expansions $0 < \theta/\theta_{\text{rms}} < 2$.

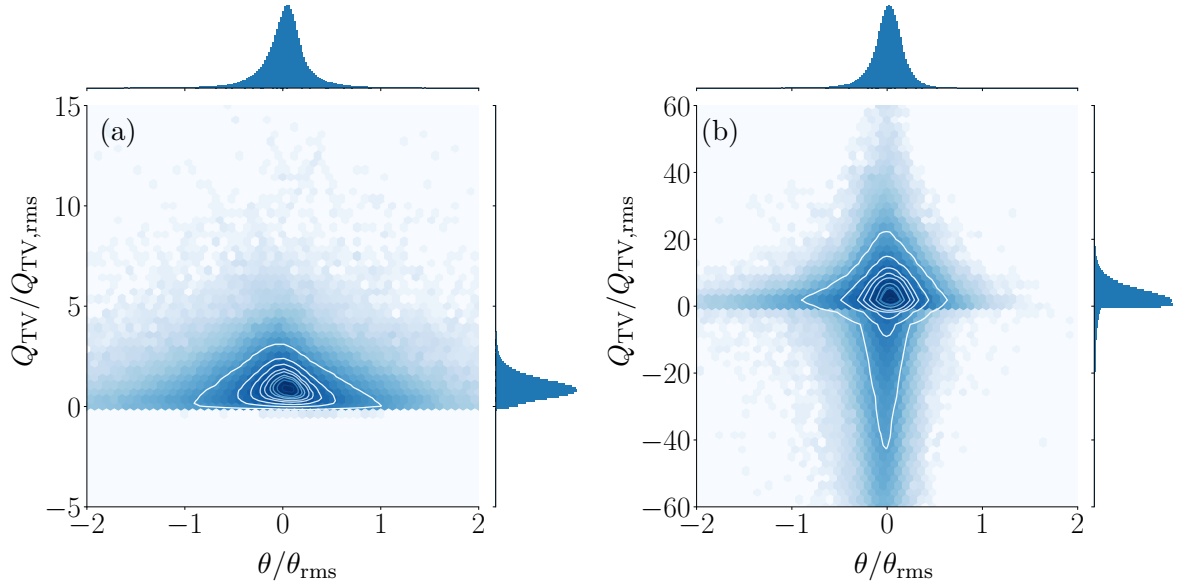


Figure 5.30: Joint p.d.f. of normalized divergence and normalized Q_{TV} at $\text{Re}_\theta = 6200$ for $y^* \approx 10$ (a) and $y^* \approx 1000$ (b).

SUMMARY

The DNS of a hypersonic cold-wall spatially-developing turbulent boundary layer has been performed. The interaction between thermochemical non-equilibrium effects and turbulent quantities is investigated, with specific insights on the vibrational-relaxation impact.

- Streamwise evolution of wall quantities:
 - Same trend for roto-translational contribution of wall heat flux and skin friction.
 - Nearly constant evolution for vibrational heat flux; one order of magnitude smaller with respect to the roto-translational one.
- Dynamic field investigation:
 - Classical transformations for the streamwise velocity result being in a discrete agreement with the logarithmic law whereas a perfect collapse is found for the newest total-stress-based transformation of [Griffin *et al.* \(2021\)](#).
- Thermal non-equilibrium dynamics:
 - Flow in the near wall region is vibrationally frozen; thermal non-equilibrium persists up to the edge of the boundary layer.
 - Molecular nitrogen is responsible for vibrational non-equilibrium, both molecular oxygen and nitric oxide relaxing much faster.
 - Vibrational excitation is sustained by turbulent mixing and a tight coupling with sweep and ejection events is observed.
 - Turbulent transport term in the vibrational energy budgets plays a major role; this term can be modeled through a vibrational turbulent Prandtl number.
 - Significant turbulence/relaxation interaction is found in the buffer layer and accurate modeling is needed in RANS context.
- Chemical activity:
 - Extremely weak chemical activity and mass fractions fluctuations.
 - Mean species mass fractions exhibit a monotonic trend, due to turbulent diffusion. Peak of reaction rates at the maximum turbulent intensity.
 - Turbulent Schmidt number values close to unity is acceptable, despite wall-cooling.
 - Positive correlation between undissociated species and streamwise velocity fluctuations, whereas the opposite for wall-normal velocity fluctuations. An inverse behavior is found for reaction products.
- Second-order statistics:
 - Classical trend of Reynolds stresses.
 - Temperature turbulent fluctuations exhibit a peak on each side of the maximum of mean temperature location, the outer peak being predominant.
 - Vibrational temperature fluctuations exhibit no local minimum in turbulent stations.
- Compressibility effects:
 - Expansion and compression events mostly balanced.
 - Strong expansions or compressions induce a more intense translational-vibrational energy exchange.
 - No peculiar correlation between compressions/expansions and vibrational under-/over-excitation.

Chapter 6

Conclusions and Perspectives

The results illustrated in this thesis represent a contribution towards the knowledge of confined compressible turbulence of hypersonic flows and provide insights on some physical phenomena which simultaneously coexist in high-speed gas dynamics. Turbulent flows of high-enthalpy gases represent a significant research field for numerous applications, ranging from practical engineering challenges to purely theoretical understanding of the physics. To this purpose, a numerical study of the influence of high-temperature effects triggered by hypersonic conditions on turbulent air mixture flows has been carried out. Our study deals with flows surrounding hypersonic vehicles with the following characteristics: i) the freestream Mach number is high enough to preserve strong hypersonic conditions downstream of the bow shock; ii) accordingly, thermal energy exceeds in a way that vibrational and chemical effects are triggered and air is a reacting mixture of nitrogen, oxygen and nitric oxide; iii) the Reynolds number is such that a turbulent regime could be induced and sustained. In such conditions, the gas behavior departs from the one of classical low-temperature calorically perfect gases. The most meaningful differences are obtained for flow time scales comparable to relaxation and chemical time scales, promoting an interplay between confined compressible turbulence and thermochemical phenomena.

To have an idea of the mechanisms underneath such flows, we employed a DNS study of an idealized configuration of a spatially-evolving flat plate boundary layer, yet representative of many practical applications; adiabatic and wall-cooled setups have been investigated, from the laminar up to the fully turbulent regime. The computations of multicomponent hypersonic turbulent flows by means of high-fidelity simulations require a non-negligible effort in terms of computational cost. As a result, the models adopted to close the conservation equations are rather classical ones, yet still faithful for the cases under investigation in this work. Additionally, difficulties are related to the need for numerical schemes to be robust enough to handle strong, unsteady discontinuities, while ensuring low amount of artificial dissipation. To this aim, a central high-order scheme is used, supplemented with highly selective dissipative techniques.

The most meaningful results obtained are listed in the following. Compressible wall-bounded turbulence of hypersonic gases, including high-temperature effects, was found to share some similarities with configurations under cryogenic conditions. Despite the high temperatures reached in both the adiabatic and wall-cooled boundary layers, the chemical activity resulted relatively weak. Consequently, the large chemical time scales caused a slight decoupling between chemical phenomena and the dynamic field, leading to mean velocity and turbulent intensity profiles similar to those encountered in

low-enthalpy hypersonic flows, once properly scaled with semi-local quantities. For the same reason, transition and breakdown to turbulence remain qualitatively similar to those expected for a perfect non-reacting gas, the redistribution of modal energy due to changing mixture composition being the most significant difference. On the other hand, the part of energy drained to trigger dissociation caused a global reduction of turbulent fluctuations of the streamwise component of the Reynolds stresses and temperature, whereas mean and fluctuating quantities of density were not altered. The other aspect that must be taken into account is the change of thermophysical properties due to the varying species mass fractions; transport and thermodynamic properties may significantly deviate from their frozen values, modifying the impact of the diffusive fluxes compared to the turbulent ones. Globally, turbulence dynamics and chemical activity were found to be one-way coupled, in the sense that turbulence mixing, together with molecular diffusion, redistributes the gas and affects the composition. At the same time, for wall-cooled configurations, the peak of temperature is smoothed by mixing, further reducing chemical activity. More tight is the influence of turbulence dynamics on thermal nonequilibrium. The latter was found to occur and persist because of sweep and ejection events promoted by velocity fluctuations. The finite vibrational relaxation times cause a delay in the flow to equilibrate with new gas brought by turbulent motion, leading to different vibrational and translational temperatures; the majority of nonequilibrium was found to be under-excited. Strong compressibility effects further promote this gap, but this effect is less marked with respect to unconfined configurations. Moreover, the coexistence of chemical and thermal nonequilibrium must not be neglected, since the internal energy is redistributed in a different way and some mechanisms may be more preponderant than others. As a confirmation of the interplay between turbulence and high-temperature effects, turbulence/chemistry and turbulence/relaxation interaction terms have been quantified. The results of this analysis have pointed out that this coupling is not negligible and is more significant in the buffer layer. As a consequence, attention must be paid to the development of turbulence models in the context of hypersonic flows, both for the closure of classical turbulent transport terms and for the unclosed terms deriving from species and vibrational energy equations.

6.1 Future work

The present analysis is a first step for understanding complex thermochemistry triggered by hypersonic conditions in turbulent flows. However, several aspects require further research efforts; among them we can cite the following:

- The DNS database produced in this thesis does not hold the answers to all the open research questions. What would happen with a more intense chemical activity? What if the wall heat flux was higher? Different free-stream conditions would lead to different turbulence dynamics? Unfortunately, we cannot draw general and universal conclusions with a “scarce” quantity of reliable data. The different combination of operating conditions, such as altitude, stagnation enthalpy and wall-cooling rate may trigger one phenomenon more intensely than another. For example, turbulent regime is most likely to occur at lower altitudes, whereas vibrational relaxation phenomena would dominate the flow behavior higher in the atmosphere. At the same time, higher densities and higher kinetic energy promote molecular collisions, which may result in a more intense chemical activity. There are still many fundamental mechanisms which remain undiscovered; from here the necessity of performing further simulations of hypersonic turbulent flows, spanning a wider range of control parameters.

6.1. FUTURE WORK

- A massive amount of high-fidelity data is the starting point for the calibration of RANS and LES closure models. When performing computationally expensive simulations is infeasible, turbulence modeling may be the way but there is still a source of uncertainty in the prediction of global quantities. In the existing models, the assumption of calorically perfect gases is usually made, as well as low to moderate temperature and Mach number values. Taking into account hypersonic conditions may lead to the failure of such models. For instance, in Chapter 5 we have ascertained that the hypothesis of a constant turbulent Schmidt number equal to one fails for atomic nitrogen; therefore, this assumption could lead to an over or underestimation of the species turbulent transport for configurations in which N_2 dissociates significantly. Further *a priori* analyses and comparisons against experiments would elucidate the weakness and the strength of turbulence models and clarify the range of usage. Furthermore, modern machine learning techniques may be helpful for learning improved models from high-fidelity data.
- The behavior of the wall in terms of participation to the chemical processes is of utmost importance. The hypothesis of non-catalytic surface should not be taken for granted, since the materials adopted for the TPSs become catalytic with certain degrees of dissociation and temperature values. Finite-rate catalysis must take into account the dependence on surface material, chemical species and interplay between species and catalyst adsorption sites. The recombination mechanism dictated by the wall could have an impact on turbulence dynamics: the turbulent mixing of recombined species may largely contribute to increasing species mass fractions fluctuations and, consequently, turbulence/chemistry interactions. Thermal non-equilibrium conditions would also be altered, since the higher concentration of molecules should be accounted for in the vibrational energy of the system; moreover, during the recombination process, a certain amount of energy is used to pump the last vibrational level of molecules (Armenise *et al.*, 2006). At the same time, when dealing with ablative TPSs, material removal causes defects on the surface that could induce different transition-to-turbulence scenarios, to be added to the effect of wall roughness. The mechanical erosion would also release carbon fibers that would participate to the chemical processes.
- More complex geometries should be investigated, taking into account wall curvature or sharp leading edges. Non-equilibrium state occurs more likely in presence of strong discontinuities, since abrupt changes in thermodynamic quantities do not allow chemical and relaxation processes to rapidly adapt to the new post-shock conditions. Future work will address ramp-like geometries similar to new vehicle concepts, including the presence of shock waves.
- Finally, quite classical models have been used to describe the thermochemical processes and the transport properties. More sophisticated approaches could be adopted, at least for more critical configurations, in order to faithfully describe the phenomena at hand.

Bibliography

- ANDERSON, J. D. 2006 *Hypersonic and high temperature gas dynamics*. American Institute of Aeronautics and Astronautics.
- ANDERSSON, P., BRANDT, L., BOTTARO, A. & HENNINGSON, D. S. 2001 On the breakdown of boundary layer streaks. *Journal of Fluid Mechanics* **428**, 29–60.
- ARMENISE, I., BARBATO, M., CAPITELLI, M. & KUSTOVA, E. 2006 State-to-state catalytic models, kinetics, and transport in hypersonic boundary layers. *Journal of thermophysics and heat transfer* **20** (3), 465–476.
- ARMENISE, I., CAPITELLI, M., COLONNA, G. & GORSE, G. 1996 Nonequilibrium vibrational kinetics in the boundary layer of re-entering bodies. *Journal of thermophysics and heat transfer* **10** (3), 397–405.
- BERTIN, J. J. & CUMMINGS, R. M. 2006 Critical hypersonic aerothermodynamic phenomena. *Annu. Rev. Fluid Mech.* **38**, 129–157.
- BHAGATWALA, A. & LELE, S.K. 2009 A modified artificial viscosity approach for compressible turbulence simulations. *Journal of Computational Physics* **228** (14), 4965–4969.
- BITTER, N. P. & SHEPHERD, J. E. 2015 Stability of highly cooled hypervelocity boundary layers. *Journal of Fluid Mechanics* **778**, 586–620.
- BLOTTNER, F. G., JOHNSON, M. & ELLIS, M. 1971 Chemically reacting viscous flow program for multi-component gas mixtures. *Tech. Rep.*. Sandia Laboratory.
- BONELLI, F., PASCAZIO, G. & COLONNA, G. 2021 Effect of finite-rate catalysis on wall heat flux prediction in hypersonic flow. *Physical Review Fluids* **6** (3), 033201.
- BONELLI, F., TUTTAFESTA, M., COLONNA, G., CUTRONE, L. & PASCAZIO, G. 2017*a* An MPI-CUDA approach for hypersonic flows with detailed state-to-state air kinetics using a GPU cluster. *Computer Physics Communications* **219**, 178–195.
- BONELLI, F., TUTTAFESTA, M., COLONNA, G., CUTRONE, L. & PASCAZIO, G. 2017*b* Numerical Investigation of High Enthalpy Flows. *Energy Procedia* **126**, 99–106.
- BORRELLI, R. & MARTUCCI, A. 2011 Scirocco plasma wind tunnel: synergy between numerical and experimental activities for tests on aerospace structures. In *Wind Tunnels and Experimental Fluid Dynamics Research*. IntechOpen.

BIBLIOGRAPHY

- BURCAT, A., RUSCIC, B. & OTHERS 2005 Third millenium ideal gas and condensed phase thermochemical database for combustion (with update from active thermochemical tables). *Tech. Rep.*. Argonne National Laboratory (ANL).
- CANDLER, G. 2019 Rate effects in hypersonic flows. *Annual Review of Fluid Mechanics* **51**, 379–402.
- CASSEAU, V., ESPINOZA, D. ER, SCANLON, T. J. & BROWN, R. E. 2016 A two-temperature open-source cfd model for hypersonic reacting flows, part two: multi-dimensional analysis. *Aerospace* **3** (4), 45.
- CHEN, S., SUN, Q., KLIOUTCHNIKOV, I. & OLIVIER, H. 2019 Numerical study of chemically reacting flow in a shock tube using a high-order point-implicit scheme. *Computers & Fluids* **184**, 107–118.
- COLONNA, G., BONELLI, F. & PASCAZIO, G. 2019 Impact of fundamental molecular kinetics on macroscopic properties of high-enthalpy flows: The case of hypersonic atmospheric entry. *Physical Review Fluids* **4** (3), 033404.
- COLONNA, G., TUTTAFESTA, M., CAPITELLI, M. & GIORDANO, D. 1999 Non-Arrhenius NO formation rate in one-dimensional nozzle airflow. *Journal of thermophysics and heat transfer* **13** (3), 372–375.
- COOK, A. & CABOT, W. 2004 A high-wavenumber viscosity for high-resolution numerical method. *Journal of computational physics* **195**, 594–601.
- DARU, V. & TENAUD, C. 2009 Numerical simulation of the viscous shock tube problem by using a high resolution monotonicity-preserving scheme. *Computers & Fluids* **38** (3), 664–676.
- DI GIOVANNI, A. & STEMMER, C. 2018 Direct numerical simulations of roughness-induced transition in the boundary layer of a hypersonic spherical forebody under consideration of high-temperature gas effects. In *2018 Fluid Dynamics Conference*, p. 4046.
- DI RENZO, M. & URZAY, J. 2021 Direct numerical simulation of a hypersonic transitional boundary layer at suborbital enthalpies. *Journal of Fluid Mechanics* **912**.
- DUAN, L., BEEKMAN, I. & MARTÍN, M. P. 2010a Direct numerical simulation of hypersonic turbulent boundary layers. Part 2. Effect of wall temperature. *Journal of Fluid Mechanics* **655**, 419–445.
- DUAN, L., BEEKMAN, I. & MARTÍN, M. P. 2011 Direct numerical simulation of hypersonic turbulent boundary layers. Part 3. Effect of Mach number. *Journal of Fluid Mechanics* **672**, 245–267.
- DUAN, L. & MARTÍN, M. P. 2009 Effect of Finite-rate Chemical Reactions on Turbulence in Hypersonic Turbulence Boundary Layers. In *47th AIAA Aerospace Sciences Meeting Including The New Horizons Forum and Aerospace Exposition*, p. 588.
- DUAN, L. & MARTÍN, M. P. 2011 Direct numerical simulation of hypersonic turbulent boundary layers. Part 4. Effect of high enthalpy. *Journal of Fluid Mechanics* **684**, 25–59.
- DUAN, L., MARTÍN, M. P. & BEEKMAN, I. 2010b Direct numerical simulation of hypersonic turbulent boundary layers with varying freestream Mach number. In *48th AIAA Aerospace Sciences Meeting Including the New Horizons Forum and Aerospace Exposition*, p. 353.

BIBLIOGRAPHY

- DUCROS, F., FERRAND, V., NICOUD, F., WEBER, C., DARRACQ, D., GACHERIEU, C. & POINSOT, T. 1999 Large-eddy simulation of the shock/turbulence interaction. *Journal of Computational Physics* **152** (2), 517–549.
- FAN, Y., LI, W. & PIROZZOLI, S. 2019 Decomposition of the mean friction drag in zero-pressure-gradient turbulent boundary layers. *Physics of Fluids* **31** (8), 086105.
- FAY, J. A. & RIDDELL, F. R. 1958 Theory of stagnation point heat transfer in dissociated air. *Journal of the Aeronautical Sciences* **25** (2), 74–85.
- FEDOROV, A. 2011 Transition and stability of high-speed boundary layers. *Annual review of fluid mechanics* **43**, 79–95.
- FIÉVET, R., VOELKEL, S., RAMAN, V. & VARGHESE, P. L. 2019 Numerical investigation of the coupling of vibrational nonequilibrium and turbulent mixing using state-specific description. *Physical Review Fluids* **4** (1), 013401.
- FOYSI, H., SARKAR, S. & FRIEDRICH, R. 2004 Compressibility effects and turbulence scalings in supersonic channel flow. *Journal of Fluid Mechanics* **509**, 207–216.
- FRANKO, K. J. & LELE, S. K. 2013 Breakdown mechanisms and heat transfer overshoot in hypersonic zero pressure gradient boundary layers. *Journal of Fluid Mechanics* **730**, 491–532.
- FRANKO, K. J., MACCORMACK, R. & LELE, S. K. 2010 Effects of chemistry modeling on hypersonic boundary layer linear stability prediction. In *40th Fluid Dynamics Conference and Exhibit*, p. 4601.
- FU, L., HU, X. Y. & ADAMS, N. A. 2017 Targeted ENO schemes with tailored resolution property for hyperbolic conservation laws. *Journal of Computational Physics* **349**, 97–121.
- GATSKI, T. B. & ERLEBACHER, G. 2002 Numerical simulation of a spatially evolving supersonic turbulent boundary layer. *NASA Tech. Memo* **211934**, 2002.
- GHOSH, S., FOYSI, H. & FRIEDRICH, R. 2010 Compressible turbulent channel and pipe flow: similarities and differences. *Journal of Fluid Mechanics* **648**, 155–181.
- GIOVANGIGLI, V. 1999 *Multicomponent Flow Modeling*. Birkhäuser Berlin.
- GLOERFELT, X. & CINNELLA, P. 2019 Large Eddy Simulation Requirements for the Flow over Periodic Hills. *Flow, Turbulence and Combustion* **103** (1), 55–91.
- GLOERFELT, X. & ROBINET, J-C 2017 Silent inflow condition for turbulent boundary layers. *Physical Review Fluids* **2** (12), 124603.
- GLOERFELT, X., ROBINET, J-C, SCIACOVELLI, L., CINNELLA, P. & GRASSO, F. 2020 Dense-gas effects on compressible boundary-layer stability. *Journal of Fluid Mechanics* **893**.
- GNOFFO, P. A., GUPTA, R. N. & SHINN, J. L. 1989 Conservation equations and physical models for hypersonic air flows in thermal and chemical nonequilibrium. *Tech. Rep.*. NASA Technical Paper 2867.
- GOTTLIEB, S. & SHU, C.-W. 1998 Total Variation Diminishing Runge-Kutta schemes. *Mathematics of Computation* **67** (221), 73–85.

BIBLIOGRAPHY

- GRIFFIN, K. P., FU, L. & MOIN, P. 2021 Velocity transformation for compressible wall-bounded turbulent flows with and without heat transfer. *Proceedings of the National Academy of Sciences* **118** (34).
- GROSSMAN, B. & CINNELLA, P. 1990 Flux-split algorithms for flows with non-equilibrium chemistry and vibrational relaxation. *Journal of Computational Physics* **88** (1), 131–168.
- GUARINI, S. E., MOSER, R. D., SHARIFF, K. & WRAY, A. 2000 Direct numerical simulation of a supersonic turbulent boundary layer at Mach 2.5. *Journal of Fluid Mechanics* **414**, 1–33.
- GUPTA, R. N., YOS, J. M., THOMPSON, R. A. & LEE, K. P. 1990 A review of reaction rates and thermodynamic and transport properties for an 11-species air model for chemical and thermal nonequilibrium calculations to 30000 K .
- HERBERT, T. 1988 Secondary instability of boundary layers. *Annual review of fluid mechanics* **20** (1), 487–526.
- HIRSCHFELDER, J. O. & CURTISS, C. F. 1969 *Molecular theory of gases and liquids*. John Wiley and Sons.
- HIRSCHFELDER, J. O., CURTISS, C. F. & BIRD, R. B. 1954 *Molecular theory of gases and liquids*. Wiley and Sons.
- HUANG, J., NICHOLSON, G. L., DUAN, L., CHOUDHARI, M. M. & BOWERSOX, R. D. 2020 Simulation and modeling of cold-wall hypersonic turbulent boundary layers on flat plate. In *AIAA Scitech 2020 Forum*, p. 0571.
- HUANG, P. G., COLEMAN, G. N. & BRADSHAW, P. 1995 Compressible turbulent channel flows: DNS results and modelling. *J. Fluid Mech.* **305**, 185–218.
- HUDSON, M. L., CHOKANI, N. & CANDLER, G. V. 1997 Linear stability of hypersonic flow in thermochemical nonequilibrium. *AIAA journal* **35** (6), 958–964.
- IANNELLI, J. 2003 Direct computation of thermodynamic properties of chemically reacting air with consideration to CFD. *International Journal for numerical methods in fluids* **43**, 360–406.
- JAMESON, A., SCHMIDT, W. & TURKEL, E. 1981 Numerical solutions of the Euler equations by finite volume methods using Runge-Kutta time stepping schemes. *AIAA Journal* **81** (1259).
- JOHNSON, H. & CANDLER, G. V. 2005 Hypersonic boundary layer stability analysis using pse-chem. In *35th AIAA Fluid Dynamics Conference and Exhibit*, p. 5023.
- KAWAI, S., SANTHOSH, K & LELE, S. K. 2010 Assessment of localized artificial diffusivity scheme for large-eddy simulation of compressible turbulent flows. *Journal of Computational Physics* **229** (5), 1739–1762.
- KAWAI, S. & TERASHIMA, H. 2010 A high-resolution scheme for compressible multicomponent flows with shock waves. *International Journal for numerical methods in fluids* **66**, 1207–1225.
- KHURSHID, S. & DONZIS, D. A. 2019 Decaying compressible turbulence with thermal non-equilibrium. *Physics of Fluids* **31** (1), 015103.

BIBLIOGRAPHY

- KIANVASHRAD, N. & KNIGHT, D. 2017 Effect of vibrational temperature boundary condition of isothermal wall on hypersonic shock wave laminar boundary layer interaction of a hollow cylinder flare. In *Proceedings of the 7th European Conference for Aeronautics and Aerospace Sciences*.
- KIANVASHRAD, N. & KNIGHT, D. 2019 Nonequilibrium effects on prediction of aerothermodynamic loading for a double cone. *AIAA journal* **57** (7), 2946–2963.
- KIM, J.W. & LEE, D.J. 2001 Adaptive nonlinear artificial dissipation model for Computational Aeroacoustics. *AIAA Journal* **39** (5), 810–818.
- KLEBANOFF, P. S., TIDSTROM, K. D. & SARGENT, L. M. 1962 The three-dimensional nature of boundary-layer instability. *Journal of Fluid Mechanics* **12** (1), 1–34.
- KLINE, H. L., CHANG, CL & LI, F. 2019 Multiple boundary layer instability modes with nonequilibrium and wall temperature effects using lastrac. In *AIAA Aviation 2019 Forum*, p. 2850.
- KNISELY, C. P. & ZHONG, X. 2019a Impact of thermochemical nonequilibrium effects on the supersonic mode in hypersonic boundary layers. In *AIAA Scitech 2019 Forum*, p. 1132.
- KNISELY, C. P. & ZHONG, X. 2019b Significant supersonic modes and the wall temperature effect in hypersonic boundary layers. *AIAA Journal* **57** (4), 1552–1566.
- LAGHA, M., KIM, J., ELDREDGE, J. D. & ZHONG, X. 2011 A numerical study of compressible turbulent boundary layers. *Physics of fluids* **23** (1), 015106.
- LAX, P. D. 1954 Weak Solutions of Nonlinear Hyperbolic Equations and their Numerical Computation. *Communications on Pure and Applied Mathematics* **7** (1), 159–193.
- LEES, L. 1956 Laminar heat transfer over blunt-nosed bodies at hypersonic flight speeds. *Journal of Jet Propulsion* **26** (4), 259–269.
- LEFIEUX, J., GARNIER, E., BRAZIER, J-P, SANDHAM, N. D & DURANT, A. 2021 Roughness-induced instabilities and transition on a generic hypersonic forebody at mach 6. *AIAA Journal* pp. 1–17.
- LI, W., FAN, Y., MODESTI, D. & CHENG, C. 2019 Decomposition of the mean skin-friction drag in compressible turbulent channel flows. *Journal of Fluid Mechanics* **875**, 101–123.
- LIU, Y., PANESI, M., SAHAI, A. & VINOKUR, M. 2015 General multi-group macroscopic modeling for thermo-chemical non-equilibrium gas mixtures. *The Journal of chemical physics* **142** (13), 134109.
- LUMLEY, J. L. 1979 Computational modeling of turbulent flows. In *Advances in applied mechanics*, , vol. 18, pp. 123–176. Elsevier.
- MACK, K. L. 1969 Boundary layer stability theory. *Tech. Rep.* 900-277. Jet Propulsion Laboratory, California Institute of Technology, Pasadena, CA, USA.
- MAGIN, T. E. & DEGREGZ, G. 2004 Transport algorithms for partially ionized and unmagnetized plasmas. *Journal of Computational Physics* **198** (2), 424–449.
- MALIK, M. R. & ANDERSON, E. C. 1991 Real gas effects on hypersonic boundary-layer stability. *Physics of Fluids A: Fluid Dynamics* **3** (5), 803–821.

BIBLIOGRAPHY

- MARTÍN, M. P. & CANDLER, G. 2001 Temperature fluctuation scaling in reacting boundary layers. In *15th AIAA Computational Fluid Dynamics Conference*, p. 2717.
- MARXEN, O., IACCARINO, G. & MAGIN, T. E. 2014 Direct numerical simulations of hypersonic boundary-layer transition with finite-rate chemistry. *Journal of Fluid Mechanics* **755**, 35–49.
- MARXEN, O., MAGIN, T. E., SHAQFEH, E. S. G. & IACCARINO, G. 2013 A method for the direct numerical simulation of hypersonic boundary-layer instability with finite-rate chemistry. *Journal of Computational Physics* **255**, 572–589.
- MILLIKAN, R. C. & WHITE, D. R. 1963 Systematics of vibrational relaxation. *Journal of chemical physics* **39**, 3209–3213.
- MIRÓ MIRÓ, F. & PINNA, F. 2021 Decoupling ablation effects on boundary-layer stability and transition. *Journal of Fluid Mechanics* **907**.
- MIRÓ MIRÓ, F., PINNA, F., BEYAK, E. S., BARBANTE, P. & REED, H. L. 2018 Diffusion and chemical non-equilibrium effects on hypersonic boundary-layer stability. In *2018 AIAA Aerospace Sciences Meeting*, p. 1824.
- MODESTI, D. & PIROZZOLI, S. 2016 Reynolds and mach number effects in compressible turbulent channel flow. *International Journal of Heat and Fluid Flow* **59**, 33–49.
- MONKEWITZ, P. A. 2017 Revisiting the quest for a universal log-law and the role of pressure gradient in “canonical” wall-bounded turbulent flows. *Physical Review Fluids* **2** (9), 094602.
- MORKOVIN, M. V. 1962 Effects of compressibility on turbulent flows. *Mécanique de la Turbulence* **367** (380), 26.
- MORKOVIN, M. V. 1994 Transition in open flow systems—a reassessment. *Bull. Am. Phys. Soc.* **39**, 1882.
- MORKOVIN, M. V. & FAVRE, A. 1962 Mécanique de la turbulence. *CNRS, Paris* pp. 367–380.
- MORTENSEN, C., H. & ZHONG, X. 2016 Real-gas and surface-ablation effects on hypersonic boundary-layer instability over a blunt cone. *AIAA Journal* **54** (3), 980–998.
- NAGIB, H. M. & CHAUHAN, K. A. 2008 Variations of von kármán coefficient in canonical flows. *Physics of Fluids* **20** (10), 101518.
- NEVILLE, A. G., NOMPELIS, I., SUBBAREDDY, P. K. & CANDLER, G. V. 2014 Effect of thermal non-equilibrium on decaying isotropic turbulence. In *AIAA AVIATION 2014-7th AIAA Theoretical Fluid Mechanics Conference 2014*. American Institute of Aeronautics and Astronautics Inc.
- NEVILLE, A. G., NOMPELIS, I., SUBBAREDDY, P. K. & CANDLER, G. V. 2015 Thermal non-equilibrium effects in turbulent compressible shear flows. In *45th AIAA Fluid Dynamics Conference*, p. 3218.
- PANESI, M., JAFFE, R. L., SCHWENKE, D. W. & MAGIN, T. E. 2013 Rovibrational internal energy transfer and dissociation of $n_2(1\sigma_g^+)-n(4s_u)$ system in hypersonic flows. *The Journal of chemical physics* **138** (4), 044312.

BIBLIOGRAPHY

- PARK, C. 1988 Two-temperature interpretation of dissociation rate data for N₂ and O₂. In *26th Aerspace Sciences Meeting*, p. 458.
- PARK, C. 1989 Assessment of two-temperature kinetic model for ionizing air. *Journal of Thermophysics and Heat Transfer* **3** (3), 233–244.
- PARK, C. 1990 *Nonequilibrium Hypersonic Aerothermodynamics*. John Wiley and Sons.
- PARK, C. 1993 Review of chemical-kinetic problems of future NASA missions. I-Earth entries. *Journal of Thermophysics and Heat transfer* **7** (3), 385–398.
- PASSIATORE, D., SCIACOVELLI, L., CINNELLA, P. & PASCAZIO, G. 2021 Finite-rate chemistry effects in turbulent hypersonic boundary layers: A direct numerical simulation study. *Physical Review Fluids* **6** (5), 054604.
- PERRAUD, J., ARNAL, D., DUSSILLOLS, L. & THIVET, F. 1999 Studies of laminar-turbulent transition in hypersonic boundary layers at ONERA. In *Aerothermodynamics for space vehicles*, , vol. 426, p. 309.
- PIROZZOLI, S. 2011 Numerical methods for high-speed flows. *Annual Review of Fluid Mechanics* **43**, 163–194.
- PIROZZOLI, S. & BERNARDINI, M. 2011 Turbulence in supersonic boundary layers at moderate Reynolds number. *Journal of Fluid Mechanics* **688**, 120–168.
- PIROZZOLI, S., BERNARDINI, M. & GRASSO, F. 2008 Characterization of coherent vortical structures in a supersonic turbulent boundary layer. *Journal of Fluid Mechanics* **613**, 205.
- PIROZZOLI, S., GRASSO, F. & GATSKI, T.B. 2004 Direct numerical simulation and analysis of a spatially evolving supersonic turbulent boundary layer at $M = 2.25$. *Physics of Fluids (1994-present)* **16** (3), 530–545.
- POGGIE, J., BISEK, N.J. & GOSSE, R. 2015 Resolution effects in compressible, turbulent boundary layer simulations. *Computers & Fluids* **120**, 57–69.
- POINSOT, T. & LELE, S. K. 1992 Boundary conditions for direct simulations of compressible viscous flows. *Journal of computational physics* **101** (1), 104–129.
- POINSOT, T. & VEYNANTE, D. 2005 *Theoretical and numerical combustion*. R.T. Edwards, Inc.
- RENARD, N. & DECK, S. 2016 A theoretical decomposition of mean skin friction generation into physical phenomena across the boundary layer. *Journal of Fluid Mechanics* **790**, 339–367.
- SAYADI, T. & MOIN, P. 2012 Large eddy simulation of controlled transition to turbulence. *Physics of Fluids* **24** (11), 114103.
- SCHLATTER, P. & ORLU, R. 2010 Assessment of direct numerical simulation data of turbulent boundary layers. *Journal of Fluid Mechanics* **659**, 116–126.
- SCHMID, P. J. 2010 Dynamic mode decomposition of numerical and experimental data. *Journal of fluid mechanics* **656**, 5–28.
- SCIACOVELLI, L., CINNELLA, P. & GLOERFELT, X. 2017 Direct numerical simulations of supersonic turbulent channel flows of dense gases. *Journal of Fluid Mechanics* **821**, 153–199.

- SCIACOVELLI, L., GLOERFELT, X., PASSIATORE, D., CINNELLA, P. & GRASSO, F. 2020 Numerical investigation of high-speed turbulent boundary layers of dense gases. *Flow, Turbulence and Combustion* **105** (2), 555–579.
- SCIACOVELLI, L., PASSIATORE, D., CINNELLA, P. & PASCAZIO, G. 2021 Assessment of a high-order shock-capturing central-difference scheme for hypersonic turbulent flow simulations. *Computers & Fluids* **230** (105134), 1–23.
- SIVASUBRAMANIAN, J. & FASEL, H. F 2014 Numerical investigation of the development of three-dimensional wavepackets in a sharp cone boundary layer at mach 6. *Journal of Fluid Mechanics* **756**, 600–649.
- SOD, G. A. 1978 A survey of several finite difference methods for systems of nonlinear hyperbolic conservation laws. *Journal of Computational Physics* **27** (1), 1–31.
- STEMMER, C., BIRRER, M. & ADAMS, N. A 2017 Hypersonic boundary-layer flow with an obstacle in thermochemical equilibrium and nonequilibrium. *Journal of Spacecraft and Rockets* **54** (4), 899–915.
- STETSON, K. F & KIMMEL, R. L 1992 Example of second-mode instability dominance at a mach number of 5.2. *AIAA journal* **30** (12), 2974–2976.
- TRETTEL, A. & LARSSON, J. 2016 Mean velocity scaling for compressible wall turbulence with heat transfer. *Physics of Fluids* **28** (2), 026102.
- URZAY, J. & DI RENZO, M. 2021 Engineering aspects of hypersonic turbulent flows at suborbital enthalpies. *Annual Research Briefs, Center for Turbulence Research* pp. 7–32.
- VAN DRIEST, E. R. 1956 *The problem of aerodynamic heating*. ARC.
- VENTURI, S., SHARMA, M. P., LOPEZ, B. & PANESI, M. 2020 Data-inspired and physics-driven model reduction for dissociation: Application to the $\text{o}_2^+ \text{o}$ system. *The Journal of Physical Chemistry A* **124** (41), 8359–8372.
- WALZ, A. 1969 *Boundary layers of flow and temperature*. MIT press.
- WENZEL, C., SELENT, B., KLOKER, M. & RIST, U. 2018 DNS of compressible turbulent boundary layers and assessment of data/scaling-law quality. *Journal of Fluid Mechanics* **842**, 428–468.
- WILKE, CR 1950 A viscosity equation for gas mixtures. *The Journal of Chemical Physics* **18** (4), 517–519.
- XU, D., WANG, J., WAN, M., YU, C., LI, X. & CHEN, S. 2021 Compressibility effect in hypersonic boundary layer with isothermal wall condition. *Physical Review Fluids* **6** (5), 054609.
- ZHANG, C., DUAN, L. & CHOUDHARI, M. M. 2018 Direct numerical simulation database for supersonic and hypersonic turbulent boundary layers. *AIAA Journal* **56** (11), 4297–4311.
- ZHENG, Q., WANG, J., NOACK, B. R., LI, H., WAN, M. & CHEN, S. 2020 Vibrational relaxation in compressible isotropic turbulence with thermal nonequilibrium. *Physical Review Fluids* **5** (4), 044602.

Appendix A

Analytical computation of mixture composition for air at equilibrium conditions

It is known that the thermodynamic state of a system at equilibrium conditions is uniquely described by any set of two independent variables. In general, compressible CFD solvers have direct access to the density ρ and specific internal energy e , and therefore these thermodynamic properties represent the natural choice for computing all the remaining ones. To this aim, the analytical method proposed by [Iannelli \(2003\)](#) allows to compute the species mass fractions Y_i , the temperature T and pressure p starting from ρ and e , via a simple procedure which can be easily coupled with any CFD code. The first equation to be solved is the conservation of mass species, which gives:

$$\sum_{i=1}^5 Y_i = 1. \quad (\text{A.1})$$

Afterwards, the conservation of the mole proportion 21/79 between oxygen and nitrogen nuclei is imposed:

$$\frac{1}{21} \left(\frac{Y_{\text{O}}}{\mathcal{M}_{\text{O}}} + \frac{Y_{\text{NO}}}{\mathcal{M}_{\text{NO}}} + 2 \frac{Y_{\text{O}_2}}{\mathcal{M}_{\text{O}_2}} \right) = \frac{1}{79} \left(\frac{Y_{\text{N}}}{\mathcal{M}_{\text{N}}} + \frac{Y_{\text{NO}}}{\mathcal{M}_{\text{NO}}} + 2 \frac{Y_{\text{N}_2}}{\mathcal{M}_{\text{N}_2}} \right). \quad (\text{A.2})$$

Further relations express the equilibrium of three independent chemical reactions; specifically, two dissociation reactions and one recombination reaction:

$$\frac{Y_{\text{O}}^2}{Y_{\text{O}_2}} = \frac{\mathcal{M}_{\text{O}}}{2} \frac{K_1(T)}{\rho}, \quad \frac{Y_{\text{N}}^2}{Y_{\text{N}_2}} = \frac{\mathcal{M}_{\text{N}}}{2} \frac{K_2(T)}{\rho}, \quad \frac{Y_{\text{NO}}^2}{Y_{\text{O}_2} Y_{\text{N}_2}} = \frac{\mathcal{M}_{\text{NO}}^2}{\mathcal{M}_{\text{O}_2} \mathcal{M}_{\text{N}_2}} K_3(T), \quad (\text{A.3})$$

with $K_i(T)$ the equilibrium functions reported by [Iannelli \(2003\)](#). The last two equations are the thermal and caloric equations of state, which read:

$$p = \rho T \sum_{i=1}^5 \frac{Y_i}{\mathcal{M}_i} \quad \text{and} \quad e = T \sum_{i=1}^5 c_{v,i} Y_i + \sum_{i=3}^5 e_{V,i} + \sum_{i=1}^5 Y_i h_{f,i}^0, \quad (\text{A.4})$$

with $c_{v,i}$ the heat capacity at constant volume. Combining the preceding equations, one can write:

$$Y_{\text{O}} = \alpha_{10} - \alpha_{13}Y_{\text{NO}} - Y_{\text{O}_2} \quad (\text{A.5})$$

$$Y_{\text{N}} = \alpha_{20} - \alpha_{23}Y_{\text{NO}} - Y_{\text{N}_2} \quad (\text{A.6})$$

$$Y_{\text{O}_2} = \alpha_{10} - \alpha_{13}Y_{\text{NO}} + \frac{\mathcal{M}_{\text{O}}}{2} \frac{K_1(T)}{2\rho} - \left[\frac{\mathcal{M}_{\text{O}}}{2} \frac{K_1(T)}{\rho} \left(\alpha_{10} - \alpha_{13}Y_{\text{NO}} + \frac{\mathcal{M}_{\text{O}}}{2} \frac{K_1(T)}{4\rho} \right) \right]^{1/2} \quad (\text{A.7})$$

$$Y_{\text{N}_2} = \alpha_{20} - \alpha_{23}Y_{\text{NO}} + \frac{\mathcal{M}_{\text{N}}}{2} \frac{K_2(T)}{2\rho} - \left[\frac{\mathcal{M}_{\text{N}}}{2} \frac{K_2(T)}{\rho} \left(\alpha_{20} - \alpha_{23}Y_{\text{NO}} + \frac{\mathcal{M}_{\text{N}}}{2} \frac{K_2(T)}{4\rho} \right) \right]^{1/2} \quad (\text{A.8})$$

with

$$\alpha_{10} = \frac{0.21\mathcal{M}_{\text{O}}}{0.21\mathcal{M}_{\text{O}} + 0.79\mathcal{M}_{\text{N}}}, \quad \alpha_{13} = \frac{\mathcal{M}_{\text{O}}}{\mathcal{M}_{\text{NO}}}, \quad \alpha_{20} = \frac{0.79\mathcal{M}_{\text{N}}}{0.21\mathcal{M}_{\text{O}} + 0.79\mathcal{M}_{\text{N}}}, \quad \alpha_{23} = \frac{\mathcal{M}_{\text{N}}}{\mathcal{M}_{\text{NO}}}. \quad (\text{A.9})$$

The equations (A.5)–(A.8) for the four species mass fractions only depend on $Y_{\text{NO}}(\rho, e)$, $T(\rho, e)$ and $p(\rho, e)$. Therefore, by fixing the thermodynamic pair (ρ, e) , a complete solution for equations (A.1), (A.2) and (A.3) is obtained when both Y_{NO} and T are determined. In order to compute the latter quantities, we solve the following two-equation system, given by the Y_{NO} equilibrium equation (A.3) and the calorical equation of state:

$$\begin{cases} f_1(\rho, Y_{\text{NO}}, T) = Y_{\text{NO}} - \mathcal{M}_{\text{NO}} \left[\frac{Y_{\text{O}_2} Y_{\text{N}_2}}{\mathcal{M}_{\text{O}_2} \mathcal{M}_{\text{N}_2}} K_3(T) \right]^{1/2} = 0 \\ f_2(\rho, Y_{\text{NO}}, T) = e - T \sum_{i=1}^5 c_{v,i} Y_i - \sum_{i=3}^5 e_{v,i} - \sum_{i=1}^5 Y_i h_{f,i}^0 = 0. \end{cases} \quad (\text{A.10})$$

With the two auxiliary variables $Q = \{Y_{\text{NO}}, T\}^T$, the system is cast as

$$F(\rho, e, Q) = F(\rho, e, Y_{\text{NO}}, T) = \begin{bmatrix} f_1(\rho, Y_{\text{NO}}, T) \\ f_2(\rho, e, Y_{\text{NO}}, T) \end{bmatrix} = 0. \quad (\text{A.11})$$

The Newton's algorithm used to solve this system reads

$$Q^{k+1} = Q^k - \left[\frac{\partial F}{\partial Q} \Big|_{\rho, e} \right]^k \{F^s\}, \quad (\text{A.12})$$

where the superscript k denotes the iteration index. For a given flow state, the partial derivatives in the Jacobian matrix in equation (A.12) are expressed as

$$\left[\frac{\partial F}{\partial Q} \Big|_q \right] = \begin{bmatrix} \frac{\partial f_1}{\partial Y_{\text{NO}}} \Big|_T & \frac{\partial f_1}{\partial T} \Big|_{Y_{\text{NO}}} \\ \frac{\partial f_2}{\partial Y_{\text{NO}}} \Big|_T & \frac{\partial f_2}{\partial T} \Big|_{Y_{\text{NO}}} \end{bmatrix} \quad (\text{A.13})$$

The procedure here described generates the thermodynamic properties of air with density and internal energy as independent variables. Similar developments can also deliver thermodynamic properties for any other set of independent variables (e.g., pressure and temperature). Further details can be found in Iannelli (2003).

Appendix B

Similarity solutions for chemically-reacting boundary layers

The boundary-layer equations for a steady, compressible, multicomponent, reacting, two-dimensional flow without pressure gradient write:

$$\frac{\partial(\rho u)}{\partial x} + \frac{\partial(\rho v)}{\partial y} = 0 \quad (\text{B.1})$$

$$\rho u \frac{\partial u}{\partial x} + \rho v \frac{\partial u}{\partial y} = \frac{\partial}{\partial y} \left(\mu \frac{\partial u}{\partial y} \right) \quad (\text{B.2})$$

$$\rho u \frac{\partial h}{\partial x} + \rho v \frac{\partial h}{\partial y} = \frac{\partial}{\partial y} \left(\lambda \frac{\partial T}{\partial y} \right) + \frac{\partial}{\partial y} \left(\sum_n \rho_n u_n^D h_n \right) + \mu \left(\frac{\partial u}{\partial y} \right)^2 \quad (\text{B.3})$$

$$\rho u \frac{\partial Y_n}{\partial x} + \rho v \frac{\partial Y_n}{\partial y} = \frac{\partial}{\partial y} \left(\rho_n u_n^D \right) + \dot{\omega}_n \quad (\text{B.4})$$

Independent variable transformations are introduced as follows (see, for instance [Lees, 1956](#)):

$$\xi = \rho_e \mu_e U_e x = \xi(x), \quad \eta = \frac{u_e}{\sqrt{2\xi}} \int_0^y \rho dy = \eta(x, y). \quad (\text{B.5})$$

Considering the definition of the stream-function

$$\frac{\partial \psi}{\partial y} = \rho u \quad \frac{\partial \psi}{\partial x} = -\rho v \quad (\text{B.6})$$

and the equivalent expression in terms of transformed variables

$$\frac{\partial \psi}{\partial \xi} = \frac{1}{\sqrt{2\xi}} f(\eta) \quad \frac{\partial \psi}{\partial \eta} = \sqrt{2\xi} f'(\eta), \quad (\text{B.7})$$

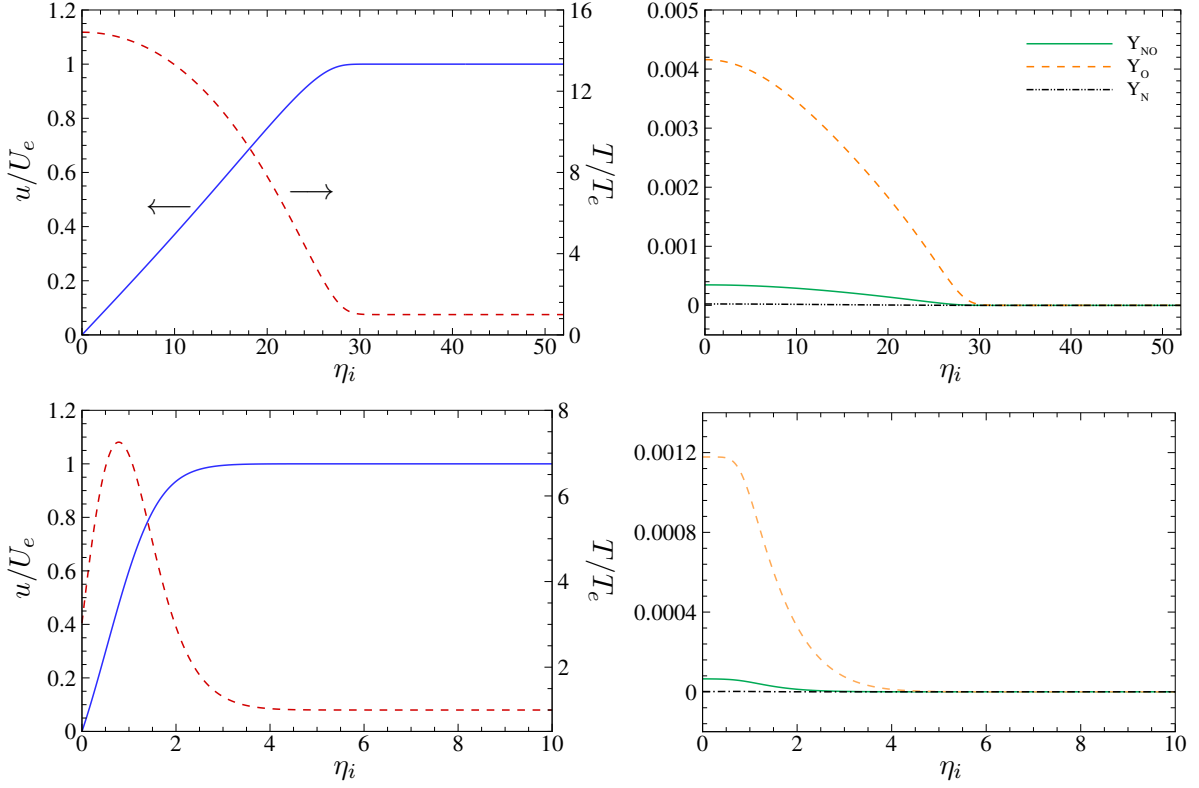


Figure B.1: Evolution of normalized velocity and temperature (left column) and species mass fractions (right column), at the inflow of the simulation in section 4.1 (top) and simulation in section 5 (bottom). In the right column, Y_{N_2} and Y_{O_2} are not shown being outside the range.

with $f' = u/U_e$, one can manipulate the boundary-layer equations and obtain their formulation in the self-similar coordinate system:

$$(Cf'')' + ff'' = 0 \quad (\text{B.8})$$

$$\left[\frac{\rho^2 D_n}{\rho_e \mu_e} \left(Y_n' - Y_n \sum_{i=1}^{\text{NS}} \frac{D_i}{D_n} Y_i' \right) \right]' + fY_n' + \frac{2\xi \dot{\omega}_n / \rho}{\rho_e \mu_e u_e^2} = 0 \quad (\text{B.9})$$

$$\frac{T_e}{h_{0,e}} \left(\frac{C\lambda}{\mu} \theta' \right)' + fg' + \frac{u_e^2}{h_{0,e}} ff'f'' + \frac{u_e^2}{h_{0,e}} (Cf'f'')' + \left[\sum_{n=1}^{\text{NS}} \frac{h_n}{h_{0,e}} \frac{\rho^2 D_n}{\rho_e \mu_e} \left(Y_n' - Y_n \sum_{i=1}^{\text{NS}} \frac{D_i}{D_n} Y_i' \right) \right]' = 0 \quad (\text{B.10})$$

Here, $g = h/h_{0,e}$ and $\theta = T/T_e$ are the self-similar parameters for enthalpy and temperature, $h_{0,e}$ and T_e being the edge stagnation enthalpy and edge temperature, respectively; moreover, $C = \rho\mu/\rho_e\mu_e$ is the Chapman-Rubesin parameter. In case of frozen chemistry or chemical equilibrium conditions, the only ξ -dependent term in equation (B.9) vanishes and the resulting equations become globally self-similar. The equations system (B.8)–(B.10) can be integrated numerically, subjected to the following

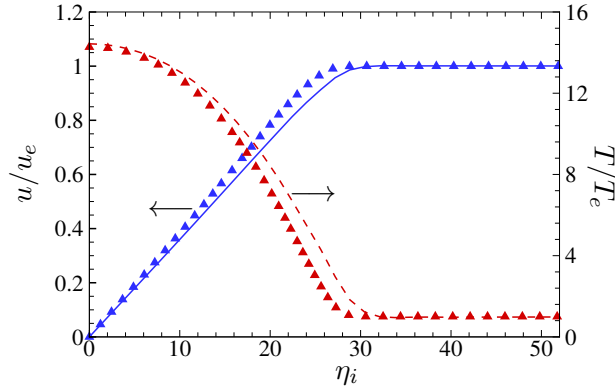


Figure B.2: Wall-normal profiles of normalized velocity and temperature at $x = 0.05$ m. Comparison between the Navier–Stokes solution (line) and locally self-similar solution (symbols).

boundary conditions:

$$f' = f = 0, \quad Y_n' = 0, \quad g' = 0 \quad \text{or} \quad g = g_w \quad \text{for} \quad \eta = 0 \quad (\text{B.11})$$

$$f' = 1, \quad Y_n = Y_{n,e}, \quad g = 1 - \frac{1}{2} \frac{u_e^2}{h_{0,e}} \quad \text{for} \quad \eta \rightarrow \infty. \quad (\text{B.12})$$

At the wall, the boundary condition is imposed on the first derivative of g ($g' = 0$) if the wall condition is adiabatic or on the direct quantity ($g = g_w$) if the wall condition is isothermal. In the test case of Chapter 4, considering a distance from the leading edge equal to $x = 0.01$ m, we obtain the inflow profiles of normalized temperature, normalized velocity and species mass fractions, shown in figure B.1 (top) as a function of the incompressible similitude variable $\eta_i = y\sqrt{\text{Re}_x}/x$. These profiles are imposed as inlet solution for the simulation of section 4.1. For the computation of Chapter 5, we imposed as inlet solution the profiles reported in figure B.1 (bottom), at a distance of $x = 0.027$ m from the leading edge. Finally, for the simulation in section 4.1, we also report a comparison between the locally self-similar solution and the solver numerical solution in figure B.2, where the wall-normal evolution of the dimensionless velocity and temperature values at $x = 0.05$ m are shown.

Appendix C

DMD methodology

DMD is a data-driven technique (Schmid, 2010) useful to analyze the dynamic of nonlinear systems, well suited to post-process both experimental and numerical data. In fluid mechanics, this tool is helpful to reduce a complex and multidimensional problem, such as the dynamics of transitional and turbulent flows, in a set of significant modes associated to a fixed frequency. From an analytical standpoint, it basically consists in the linearization of a given nonlinear system. The collection of data in a sequence of snapshots allows to assemble a data matrix \mathbf{D} with $\mathbf{D}(x_i, t_k) = \mathbf{D}[i, k] \in R^{n_s \times n_t}$:

$$\mathbf{D} = \begin{bmatrix} d_1[1] & \cdots & d_k[1] & \cdots & d_{n_t}[1] \\ \vdots & \vdots & \vdots & \vdots & \vdots \\ d_1[n_s] & \cdots & d_k[n_s] & \cdots & d_{n_t}[n_s] \end{bmatrix} \quad (\text{C.1})$$

where n_t and n_s are the total number of snapshots and grid points, respectively. Each column coincides with a snapshot and thus represents the temporal evolution of the system, whereas the rows describe its spatial evolution. The first step is to construct two different matrices, \mathbf{D}_1 and \mathbf{D}_2 , of dimension $n_s \times n_t - 1$, with $\mathbf{D}_1 = [1 : n_s, 1 : n_t - 1]$ and $\mathbf{D}_2 = [1 : n_s, 2 : n_t]$. The aim of the present decomposition is to find a matrix \mathbf{S} , such that $\mathbf{D}_2 = \mathbf{S}\mathbf{D}_1$. By performing a Singular Value Decomposition (SVD), the matrix \mathbf{D}_1 can be written as product of other matrices, therefore:

$$\mathbf{D}_1 = \mathbf{U}\mathbf{\Sigma}\mathbf{V}^T \quad (\text{C.2})$$

where both \mathbf{U} and \mathbf{V} are orthogonal and orthonormal, i.e. $\mathbf{V}\mathbf{V}^T = \mathbf{U}\mathbf{U}^T = \mathbf{I}$. An important aspect is that, given the orthogonality, these matrices are full-rank and therefore no column can be obtained as a linear combination of the others. $\mathbf{\Sigma}$ is a diagonal matrix in which each element is indicated as σ_i and corresponds to one singular value. Once the SVD is performed, we can rearrange the results and obtain the matrix \mathbf{S} :

$$\mathbf{S} = \mathbf{D}_2\mathbf{D}_1^T = \mathbf{D}_2\mathbf{V}\mathbf{\Sigma}^{-1}\mathbf{U}^T.$$

By observing the singular values, one can alternatively truncate the data to the most significant ones, since not all the data are necessarily representative of the flow dynamics, obtaining a lower rank r . As a consequence, the matrix \mathbf{S} can be approximated by a lower rank matrix which reads:

$$\tilde{\mathbf{S}} = \mathbf{U}^T\mathbf{S}\mathbf{U} = \mathbf{U}^T\mathbf{D}_2\mathbf{V}\mathbf{\Sigma}^{-1}. \quad (\text{C.3})$$

We can now perform an eigenvalue analysis obtaining

$$\tilde{\mathbf{S}}\mathbf{W} = \mathbf{\Lambda}\mathbf{W}, \quad (\text{C.4})$$

where \mathbf{W} denotes the right eigenvectors and $\mathbf{\Lambda}$ the array of the eigenvalues. Finally, the spatial basis, or equivalently the DMD modes, are expressed as

$$\Phi = \mathbf{U}\mathbf{W}. \quad (\text{C.5})$$

Each DMD mode represents a spatial structure which is associated to a single frequency.

Appendix D

Complementary results of adiabatic boundary layers simulations

This chapter reports some complementary results related to the adiabatic boundary layers simulations performed in section 4.2.2, discussed here for the sake of completeness.

The modified Crocco's relation derived by Walz (1969) is used to relate the mean temperature and velocity in zero-pressure-gradient, flat-plate boundary layers. In previous studies with high-Mach numbers, cold walls and high-enthalpy conditions (Duan *et al.*, 2010a; Duan & Martín, 2011), it was found that such a relation deviates from the exact ratio $\overline{T}/\overline{T}_\delta$ resulting from the DNS data (the subscript $(\bullet)_\delta$ indicating a quantity evaluated at the boundary layer edge). In order to remove the explicit dependence on thermal and chemical models, Duan & Martín (2011) proposed an analogous enthalpy-based equation, which reads

$$\frac{\overline{h}}{\overline{h}_\delta} = \frac{\overline{h}}{\overline{h}_w} + \frac{\overline{h_{aw}} - \overline{h}_w}{\overline{h}_\delta} f\left(\frac{\overline{u}}{\overline{u}_\delta}\right) - r \frac{\overline{u}_\delta^2}{2\overline{h}_\delta} \left(\frac{\overline{u}}{\overline{u}_\delta}\right)^2, \quad (\text{D.1})$$

where \overline{h}_w is the wall enthalpy, $r = 0.9$ the recovery factor and $\overline{h_{aw}} = \overline{h}_\delta + \frac{1}{2}r\overline{u}_\delta^2$. The function $f(\overline{u}/\overline{u}_\delta)$ has to be independent of free-stream conditions, wall temperature and surface catalysis (if any). For calorically perfect gases, equation (D.1) reduces to the classical temperature-based equation, apart from the term $f(\overline{u}/\overline{u}_\delta)$ which is equal to u/u_δ in the classical formulation. By curve-fitting the DNS data, Duan & Martín (2011) obtained the following relation for $f(\overline{u}/\overline{u}_\delta)$:

$$f\left(\frac{\overline{u}}{\overline{u}_\delta}\right) = 0.1741 \left(\frac{\overline{u}}{\overline{u}_\delta}\right)^2 + 0.8259 \left(\frac{\overline{u}}{\overline{u}_\delta}\right). \quad (\text{D.2})$$

Figure D.1 plots this modified Walz's equation for both CN and FR cases. An excellent collapse is found for the FR simulation, whereas it is shown to slightly overestimate the exact ratio for low-to-mean values of $\overline{u}/\overline{u}_\delta$ in the CN case.

The budgets for the turbulent kinetic energy, defined as $K = \frac{1}{2}\widetilde{u_i''u_i''}$, are given by:

$$\frac{\partial \rho K}{\partial t} = -C + P + T + \Pi + D + M - \rho \varepsilon, \quad (\text{D.3})$$

where the terms C , P , T , Π , D and M represent, respectively, the contributions due to convection, production by mean velocity gradients, turbulent transport, pressure dilatation, viscous diffusion and

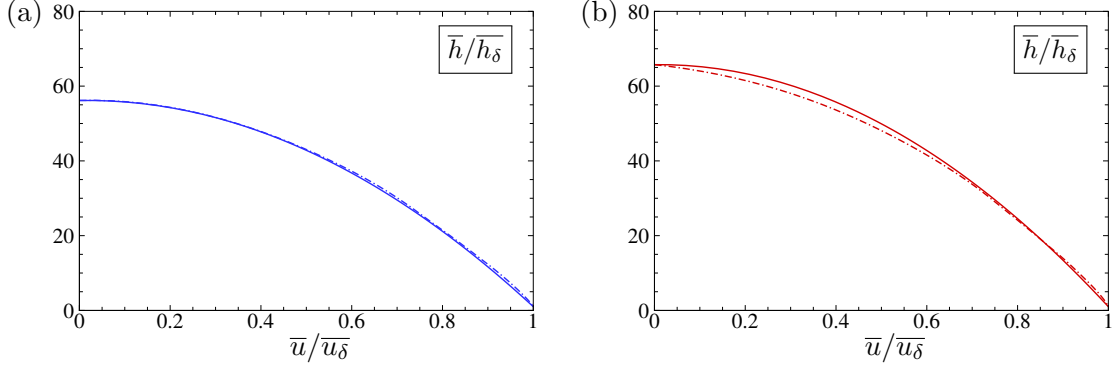


Figure D.1: Modified Walz's equation (solid lines) for the frozen (a) and the chemically-reacting simulation (b), at $\text{Re}_\tau = 185$. Dash-dotted lines indicate the exact ratios of DNS data.

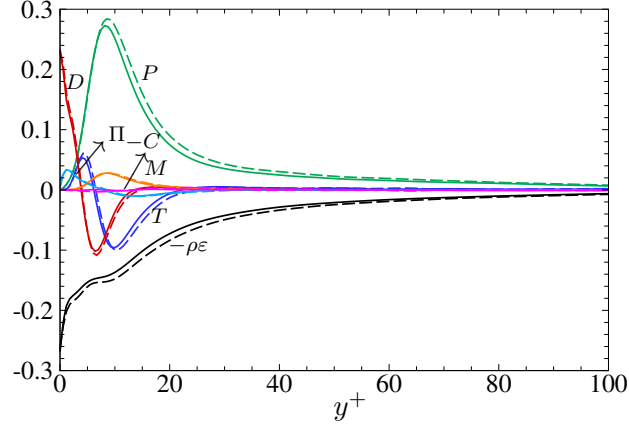


Figure D.2: Turbulent kinetic energy budgets, at $\text{Re}_\tau = 185$. (----), frozen simulation; (—), chemically-reacting simulation.

mas flux contribution associated to density fluctuations. The last term, $\rho\varepsilon$, represents the dissipation and accounts for the sum of the solenoidal, dilatational and inhomogeneous contributions (the last one being usually negligible). The formulation of these terms is as follows:

$$C = \frac{\partial \bar{\rho} \tilde{u}_j K}{\partial x_j}, \quad P = -\bar{\rho} \widetilde{u_i'' u_j''} \frac{\partial \tilde{u}_i}{\partial x_j}, \quad T = -\frac{1}{2} \frac{\partial}{\partial x_j} \left(\bar{\rho} \widetilde{u_i'' u_i'' u_j''} \right), \quad \Pi = \overline{p' \frac{\partial u_i'}{\partial x_i}} - \frac{\partial}{\partial x_j} (\overline{p' u_i' \delta_{ij}}), \quad (\text{D.4})$$

$$M = \bar{\rho} u_i'' \left(\frac{\partial \overline{\tau_{ij}}}{\partial x_j} - \frac{\partial \bar{p}}{\partial x_i} \right), \quad D = \frac{\partial}{\partial x_j} (\overline{\tau_{ij}' u_i'}), \quad \bar{\rho}\varepsilon = -\overline{\tau_{ij}' \frac{\partial u_i''}{\partial x_j}}. \quad (\text{D.5})$$

Figure D.2 shows the profiles of these terms normalized in inner scaling by $\overline{\tau_w^2}/\bar{\mu}$ according to Foyisi *et al.* (2004). It is found that chemical reactions have a mild influence on kinetic energy budgets, with slightly smaller values at the location where turbulent kinetic energy peaks for the CN case.

To complete the spectral analysis of section 4.2.2.3, figure D.3 shows premultiplied energy spectra of the fluctuating wall-normal velocity, streamwise velocity and temperature as a function of the normalized spanwise wavenumber λ^+ , for FR case. The three spectra are similar to those obtained for the CN simulation, hence chemical reactions seem not to alter significantly the spectral contents

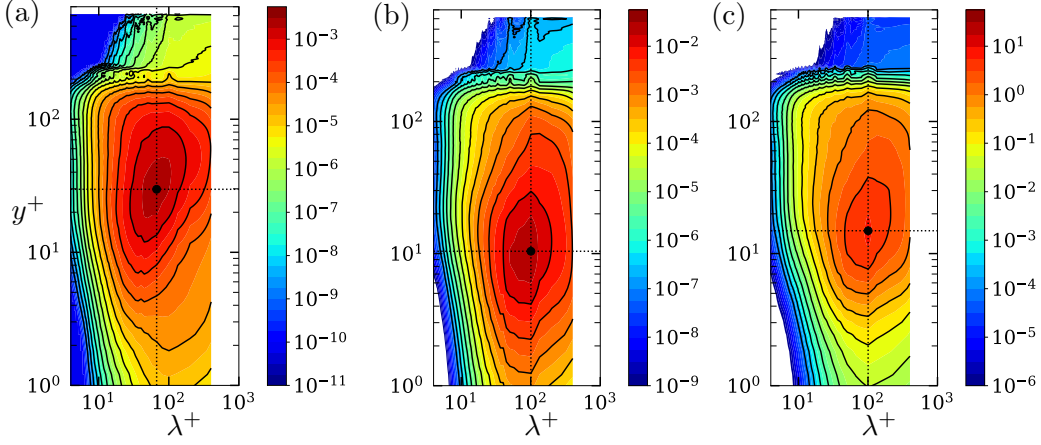


Figure D.3: Premultiplied spanwise spectra $k_z E_{v'v'}/u_\infty^2$ (a), $k_z E_{u'u'}/u_\infty^2$ (b) and $k_z E_{T'T'}/T_\infty^2$ (c) for frozen simulation, computed on a plane in the fully turbulent zone.

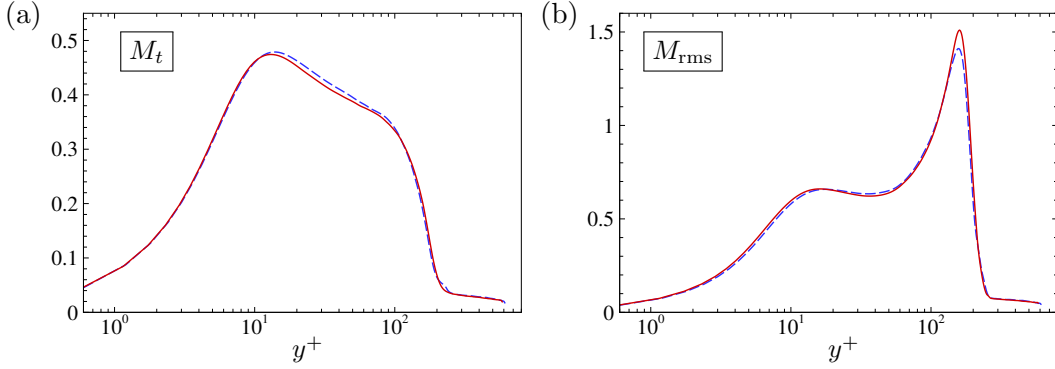


Figure D.4: Wall-normal distribution of the turbulent (a) and fluctuating (b) Mach numbers, and fluctuating speed of sound (c) at $\text{Re}_\tau = 185$. (---), frozen simulation; (—), chemically-reacting simulation.

of such quantities.

Compressibility effects, investigated in section 5.2.5 for the cold-wall case, can be evaluated by means of the turbulent and fluctuating Mach numbers, shown in figure D.4. Despite the high free-stream Mach number, M_t is found to be always smaller than 0.5 for both simulations. The peak of M_{rms} , achieved at the boundary layer edge, is slightly larger for CN even if the velocity fluctuations are smaller. This behavior is attributed to the slight smaller temperature in CN case (i.e., smaller speed of sound). Globally, the small differences in the dynamic fields confirm that the influence of the chemical activity is mostly restricted to the modification of thermodynamic properties. As further confirmation, figure D.5 displays the Reynolds stress anisotropies, defined as:

$$a_{ij} = 2 \frac{\overline{\rho u_i'' u_j''}}{\rho \bar{K}} - \frac{2}{3} \delta_{ij}. \quad (\text{D.6})$$

The trend and the order of magnitude of these terms, appearing in the formulation of turbulence models, are coherent with the results shown by Zhang *et al.* (2018). The a_{ii} components (panel a)

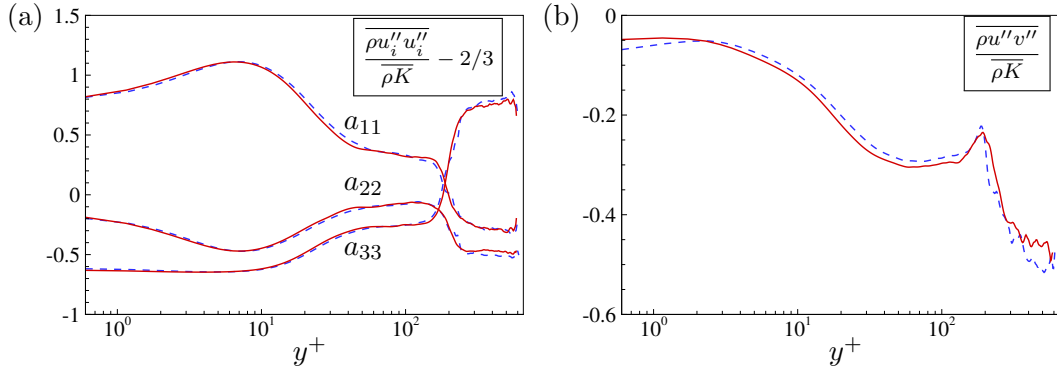


Figure D.5: Distribution of the normal Reynolds stress anisotropies (a) and Reynolds shear stress anisotropy (b) at $Re_\tau = 185$. (---), frozen simulation; (—), chemically-reacting simulation.

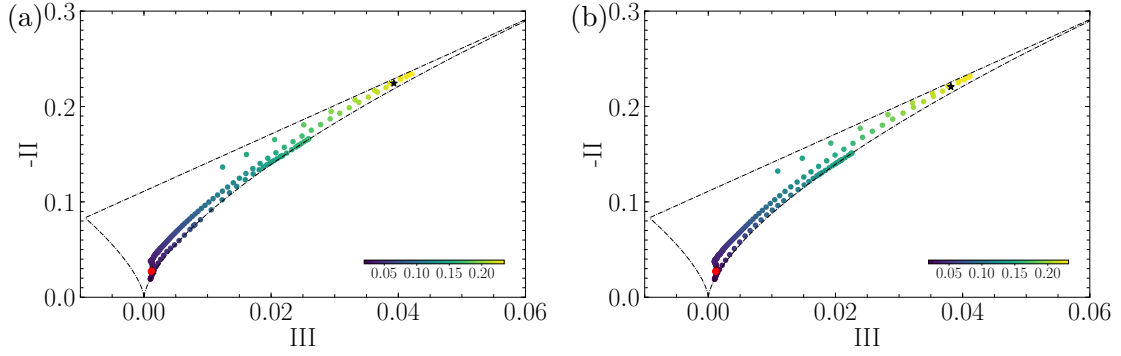


Figure D.6: Anisotropy invariants map for frozen simulation (a) and chemically reacting simulation (b), at $Re_\tau = 185$.

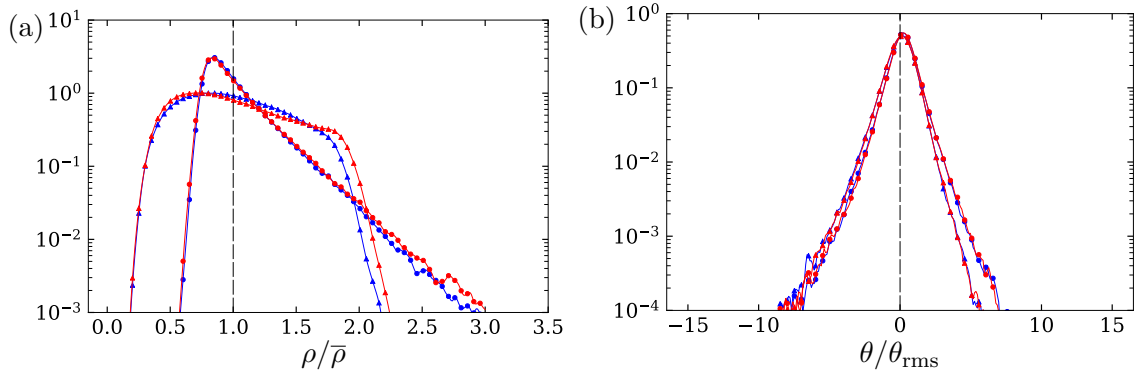


Figure D.7: Probability density function of normalized density (a) and normalized dilatation (b), for FR case at $y^+ \approx 10$ (—●—) and $y^+ \approx 150$ (—▲—) and for CN case at $y^+ \approx 10$ (—●—) and $y^+ \approx 150$ (—▲—).

are perfectly superposed, whereas marginal changes are shown in the a_{ij} ones (panel b) in the near-wall region. Starting from the expression of these terms, the second and the third invariants of the

Reynolds stress anisotropies can be computed (the first being identically zero) as:

$$\text{II} = a_{ij}a_{ij} \quad \text{and} \quad \text{III} = a_{ij}a_{jk}a_{ki}. \quad (\text{D.7})$$

According to Lumley (1979), the evolution of turbulent flow structures can be quantified using the anisotropy invariant map, defined by the aforementioned invariants. These results are reported in figure D.6 and show the classical behavior of a zero-pressure flat plate boundary layer. The star and the circle symbols mark the end of the linear zone and of the logarithmic zone, respectively. Lastly, figure D.7 shows the probability density functions (p.d.f.) of density and velocity divergence at two different wall-normal positions, corresponding to the peak of u_{rms} and of M_{rms} (at $y^+ \approx 10$ and $y^+ \approx 150$), for both simulations. Concerning the p.d.f. of $\rho/\bar{\rho}$, the profiles are shown to be strongly skewed towards large density values close to the wall and then tend to become more symmetric approaching the boundary layer edge. Differently, the behavior of the $\theta/\theta_{\text{rms}}$ p.d.f.s do not exhibit any clear differences between the two cases.

Résumé : Les effets de haute température survenant lors des vols hypersoniques ont un impact sur les performances aérodynamiques d'un véhicule. En outre, la transition d'un régime laminaire à un régime turbulent peut se produire dans des conditions de vol réelles. La prédiction du couplage bidirectionnel de la turbulence compressible et des processus thermochimiques déclenchés par la haute température est un sujet partiellement inexploré. Dans ce travail, le comportement des couches limites de plaques planes dans des conditions hypersoniques est examiné, au moyen de Simulations Numériques Directes (SND). Des configurations avec parois adiabatiques et refroidies sont étudiées, du régime laminaire au régime entièrement turbulent. L'air est modélisé comme un mélange réactif à cinq espèces, dans le but final d'étudier l'effet de la chimie et de la relaxation vibrationnelle des couches limites turbulentes fortement compressibles. On constate que l'activité chimique a un impact sur les propriétés de transport, les grandeurs thermodynamiques et les fluctuations turbulentes. Le transport turbulent entretient le non-équilibre thermique. Les fluctuations de vitesse jouent un rôle majeur dans le mélange des gaz chauds et froids, ce qui conduit à des décalages de l'énergie vibrationnelle par rapport à sa valeur d'équilibre. Les quantités thermodynamiques moyennes et fluctuantes sont affectées par ce mécanisme.

Mots clés: écoulements hypersoniques, couches limites, turbulence compressible, effets à haute température, non-équilibre thermochimique.

Abstract : High-temperature effects arising in hypersonic flights have a major impact on aerodynamic performance of a vehicle. In addition, the boundary layer transition from a laminar to a turbulent regime may occur in real flight conditions. The accurate prediction of the two-way coupling of wall-bounded compressible turbulence and thermochemical processes triggered by the high temperature at stake is a subject partially unexplored. In this work, the behavior of spatially evolving flat-plate boundary layers in hypersonic conditions is inspected by means of Direct Numerical Simulations (DNS). Adiabatic and wall-cooled configurations are investigated, from the laminar up to the fully turbulent regime. A five-species air mixture model is considered, with the final aim of studying the effect of finite-rate chemistry and vibrational relaxation on high compressible turbulent flows. It is found that chemical activity has an impact on transport properties, thermal fields and turbulent fluctuations. Turbulent transport is found to sustain thermal non-equilibrium. Velocity fluctuations have indeed a major role in the mixing of hot and cold gases, which lead to the excitation of all energetic modes and lags in the vibrational energy with respect to its equilibrium value. Accordingly, thermal mean and fluctuating quantities are affected by this mechanism.

Keywords: hypersonic flows, boundary layers, compressible turbulence, high-temperature effects, thermochemical non-equilibrium.